NOTE TO USERS

THREE DIMENSIONAL MODELING OF VERTICAL DC CASTING OF ALUMINUM ALLOYS

KAMAL RAMADAN RAGEL

Department of Mining, Metals and Materials Engineering
McGill University
Montreal, Canada

A thesis submitted to the Faculty of Graduate Studies and Research
in partial fulfillment of the requirements for the degree of
Doctor of Philosophy.

March, 2004

Your file Votre référence
ISBN: 0-612-98355-2
Our file Notre référence
ISBN: 0-612-98355-2

ABSTRACT

A three-dimensional mathematical model for the simulation of vertical direct chill (DC) slab casting of aluminum alloys has been developed. The model is based on the solution of the 3D time-averaged turbulent momentum (Navier-Stokes) and energy equations. The momentum equations are modified with a Darcy-type source term to simulate motion of the melt in the mushy region. The buoyancy force term is implemented in the model through the Boussinesq approximation. The low Reynolds number k-ε turbulence model of Launder and Sharma is used to calculate the Reynolds stresses and the turbulent heat fluxes. A variable heat transfer coefficient is used along the ingot surface to account for the different cooling regions. The mathematical model is qualitatively and quantitatively verified by comparing the computed results with a physical water model and a real casting experiment, respectively of independent researchers. Each of the comparisons showed a good agreement. The quantitative verification of the solidification front depths is improved when the thermal buoyancy force effect is included in the model.

A parametric study has been carried on two casters of variable aspect ratio each using a different type of inlet melt distribution system. In the case of the small aspect ratio caster, the physical properties of aluminum Al-3104 are used. For this caster, the studied parameters are the casting speed, the primary cooling rate, the melt superheat and the combo-bag dimensions. Also, the effect of complete blockage of the bottom windows of the distribution bag is studied. An in-depth understanding of some behaviors of the melt flow and solidification profile in the steady state operational phase of the DC casting process is gained. For example, the roles played by the angle flow and the upward component of the vertical recirculation at the wide symmetry plane in controlling both the solidification front depth and the mushy layer thickness at the slab center are ascertained. This study has revealed the influence of the melt stream issued from the bottom window of the bag on the depth and uniformity of the solidification front. The model has successfully identified a faulty design of the short combo bag. This industrially favorite design causes what is called the reverse flow, that is, the melt from the

surrounding sump enters the combo bag through the bottom window. It is to be noted that a similar flow phenomenon in a physical water model, which used a similar distribution system, was reported in a recent literature but never been explained. It is found that an increase in the casting speed decreases the difference in the average thickness of the solidified layer at the slab rolling and narrow faces. In addition, this study shows that the velocity of approach of the melt to the narrow side of the mold is dependent on the dimensions of the distribution bag and is independent of the bottom window blockage.

In the simulation of the DC caster with the large aspect ratio, the physical properties of Al-1050 are used. Three parameters have been tested; namely, casting speed, channel bag dimensions and melt superheat. This study has resulted in some concluding remarks concerning the upward and downward flow of melt within the sump and their effects on the mushy layer thickness and on the solidification front profiles. The importance of optimizing the casting speed to control the outer solidified layer, turbulence level at the free surface and negative segregation at the slab center is addressed. The possibility of getting similar solidification front characteristics using different combinations of the parameters adds a degree of freedom for cast engineers in specifying the operational parameters that best suite the requirement of the production firm. The importance of keeping a moderate temperature superheat, especially when using graphite lining for insulating the adiabatic section of the mold, is clarified. A moderate superheat will allow less wetting of the graphite surface by the molten aluminum, and hence will reduce the chance of formation of carbide-salt inclusions.

The developed mathematical model has been extended to solve the mass concentration equation in three dimensions. It is found that the uniform concentration profile is an indication of good mixing of the melt and it is also an indicator of a high level of turbulence. Large particles are hardly seen affected by the working parameters such as the casting speed and the bag dimensions and/or type. These particles are mainly concentrated around the slab center. Small particles are more uniformly distributed across the sump. The higher the casting speed, the higher is the concentration of inclusion across the sump. Combo bags are more likely to distribute inclusions uniformly over the slab cross-sections than channel bags.

Résumé

Un modèle mathématique tridimensionnel pour la simulation de la coulée semi-continue de brames verticales d'alliages d'aluminium a été développé. Le modèle est basé sur la solution des équations tridimensionnelles de vitesse et d'énergies en régime turbulent Navier-Stokes. Ces dernières ont été modifiées pour inclure un paramètre de type Darcy pour simuler le mouvement du métal liquide dans la région semi-solidifiée. La limite de flottabilité est mise en application dans le modèle par l'approximation de Boussinesq. Le nombre bas de Reynolds k-ε du modèle de turbulence de Launder et Sharma est employé pour calculer l'effort de Reynolds et le flux turbulent de la chaleur. Un coefficient variable de transfert thermique est employé le long de la surface de lingot pour simuler les différentes régions de refroidissement. Le modèle mathématique développé a été vérifié qualitativement et quantitativement en comparant les résultats calculés à partir d'un modèle physique de simulation qui utilise de l'eau et d'une expérience réelle de coulée semi-continue. Ces études ont été menées respectivement par des chercheurs indépendants. Chacune des comparaisons a montré une bonne concordance. La vérification quantitative, basée sur la comparaison des profondeurs de zones de solidification, est améliorée si l'effet thermique de force de flottabilité est aussi pris en considération dans le modèle développé.

Une étude paramétrique a été effectuée sur deux machines de coulée avec des longueurs variables et des systèmes d'alimentation et de distribution de métal liquide différents. Dans le cas de la machine avec la petite longueur, les propriétés physiques de l'aluminium Al-3104 ont été employées. Dans cette machine de coulée, les paramètres étudiés sont la vitesse de bâti, le taux de refroidissement primaire, la surchauffe du métal en fusion, les dimensions de combo-sac. En outre, l'effet du colmatage complet des fenêtres inférieures du sac de distribution a été étudié. Une meilleure compréhension de plusieurs comportements du profil d'écoulement et de solidification dans la phase d'état d'équilibre du processus de bâti de coulée semi-continue a été obtenue. Par exemple, l'influence de l'écoulement d'angle et du composant ascendant de recyclage vertical sur le

cadre étendu de symétrie a été déterminée en évaluant la profondeur d'avancement du front de solidification et l'épaisseur de la zone semi-solide à l'intérieur de la brame. Cette étude a indiqué l'influence du jet de métal liquide issu de la fenêtre inférieure du sac sur la profondeur et l'uniformité du front de solidification. Le modèle développé s'est avéré très utile en identifiant avec succès une conception défectueuse du sac combo court. Cette conception industriellement préférée a causé ce qui s'appelle l'inversion d'écoulement; c.-à-d. le métal liquide du carter de vidange environnant entre dans le sac combo par la fenêtre inférieure. Il doit être noté qu'un phénomène semblable d'écoulement dans un modèle physique de l'eau, en utilisant un système semblable de distribution, a été rapporté mais jamais expliqué. On constate qu'une augmentation de la vitesse de bâti diminue la différence dans l'épaisseur moyenne de la couche solidifiée de la brame. En outre, cette étude prouve que la vitesse d'approche du métal en fusion sur le côté étroit du moule dépend des dimensions du sac de distribution et est indépendante du colmatage inférieur de fenêtre.

Dans la simulation de la machine de coulée semi-continue avec le grand allongement, les propriétés physiques d'Al-1050 ont été utilisées. Trois paramètres ont été examinés ; à savoir, la vitesse, les dimensions de sac de canal et la surchauffe du métal fondu. Cette étude a eu comme conséquence quelques remarques de conclusion au sujet de l'écoulement ascendant et de haut en bas du métal liquide dans le carter de vidange et de leurs effets sur l'épaisseur de la couche semi-solide et sur les profils des fronts de solidification. L'importance d'optimiser la vitesse de bâti pour commander la couche solidifiée externe, la turbulence sur la surface libre et la ségrégation négative au centre de la brame a été examinée. La possibilité d'obtenir des caractéristiques semblables de fronts de solidification en utilisant différentes combinaisons de paramètres fournit un degré de liberté aux ingénieurs de fonderie en indiquant les paramètres opérationnels les plus adéquats pour leur société de production. L'importance de garder la température de surchauffe modérée, particulièrement lors de l'utilisation de revêtement en graphite pour l'isolation de la section adiabatique du moule a été clarifiée. Une surchauffe modérée permettra un mouillage moins important de la surface de graphite par l'aluminium fondu, et par conséquent, réduisant la chance de la formation des inclusions de carbure-sel.

Le modèle mathématique développé a été utilisé pour résoudre l'équation de concentration des masses en trois dimensions. Il a été trouvé que le profil de concentration uniforme est une indication d'un bon mélange du métal en fusion et c'est aussi un signe de turbulence élevée. Les grosses particules sont à peine affectées par les paramètres d'opération tels que la vitesse de coulée, les dimensions du sac et/ou le type. Ces particules sont essentiellement concentrées au centre de la brame. Les petites particules sont plus uniformément distribuées. Plus la vitesse de coulée est rapide, plus la concentration en inclusions est élevée dans le carter. Les sacs-combos permettent de distribuer plus uniformément les inclusions dans la section de la brame que les sacs de canal.

ACKNOWLEDGMENTS

I would like to express my deep appreciation to my thesis supervisor Prof. Mainul Hasan for his guidance, helpful suggestions and constant encouragements during the course of this research.

I would like to thank my family for their sacrifices, unfailing support and unwavering faith without which this work would not have been possible. With ever lasting gratitude, I dedicate this thesis to them as a token of my eternal indebtedness.

I would like to extend my sincere thanks to Dr. Florence Paray for translating the abstract to French.

It is with immense gratitude that I wish to thank Mr. Mohamed Albukhari for his support and encouragement throughout my postgraduate studies.

Finally, I would like to extend my sincere gratitude to the Libyan Ministry of Higher Education for providing me with the scholarship.

TABLE OF CONTENTS

LIST OF FIGURES

Figure

LIST OF TABLES

Table

NOMENCLATURE

A	Darcy coefficient
a_p, a_{nb},b	coefficients in the discretized governing equations
c_1, c_2, c_μ	empirical constants for low Reynolds number model
c_p	specific heat
C	morphology constant
D	nozzle hydraulic diameter
D_k	extra dissipation term in k-equation
E_ε	extra generation term in ε-equation
f_1, f_2, f_μ	empirical constants used in low-Re version of k-ϵ models
f_l	liquid fraction
G	production term in turbulent kinetic energy equation
g	gravitational acceleration
h	sensible heat
H	total heat (sensible and latent)
K'	permeability of porous media
k	turbulent kinetic energy
P	hydrodynamic pressure
Pe	Peclet number
Pr	laminar Prandtl number
Re	Reynolds number
Re_t	turbulent Reynolds number based on the turbulent quantities
S	source term
S_Φ	source term associated with Φ
Sc	Schmidt number
Sc_t	turbulent Schmidt number
T	temperature

T'	fluctuation of temperature
T_{in}	inlet temperature
T_l	liquidus temperature
T_s	solidus temperature
u_i	velocity component in the *i-th* direction; corresponding to u
$\overline{u}_i$	time-average velocity component in the *i-th* direction
u_i'	fluctuation of velocity in the *i-th* direction
u_{in}	inlet velocity
u_s	casting speed

Greek Symbols

ΔH	nodal latent heat
ΔH_f	latent heat of fusion
Γ_Φ	diffusion coefficient associated with Φ
ρ	alloy density
ρ_S	inclusion particle density
φ	generalized dependent variable
μ_e	effective viscosity equal to $\mu_t + \mu$
μ	laminar viscosity
μ_t	turbulent viscosity or eddy diffusivity
Φ	generalized dependent variable
β_T	thermal expansion coefficient
Γ_{eff}	effective diffusivity
ϵ	rate of energy dissipation
ϵ_{in}	inlet rate of energy dissipation
γ	convective heat transfer coefficient
σ_k, σ_ϵ	turbulence model constants

σ_t	turbulent Prandtl number
γ	heat transfer coeeficient

CHAPTER
ONE

Introduction

1.1 Introduction

Direct chill (DC) casting of aluminum slab ingots and billets was first introduced during 1938-1943 and is recognized as an important and efficient method for the semi-continuous production of many non-ferrous alloys such as aluminum, magnesium and copper. DC casting technology is predominantly used in the production of aluminum alloys. DC cast slabs and billets are later used to produce plate, sheet, foil, wire, rod, and bar products by pressing or rolling. The world aluminum production in the year 2001 using DC casting technology was around 20 million tones per annum (tpa). Depending on the mold orientation, DC casters can be classified into two types; namely, vertical (predominant) and horizontal. The schematic of a vertical DC caster, the subject matter of the present research work, is shown in Figure 1.1. It is comprised of a molten-metal-transfer trough responsible for distributing the melt to a mold and/or molds simultaneously, a water cooled mold where the mold shape is forming the cross-sectional shape of the final product, and a bottom block initially positioned inside the mold. The bottom block can vertically be moved by a hydraulic ram. A distribution bag is positioned under a nozzle. The nozzle carries the molten metal from the trough to the mold. Depending on the levels of impurity of the molten aluminum, ceramic filters of different porosity can be used to prevent inclusions from reaching the final product. Figure 1.2 (a) shows a commercial vertical DC caster, and Figure 1.2 (b) shows some ceramic filters in use in DC casting processes.

The vertical DC casting process starts with the introduction of molten aluminum from the trough to the mold through the nozzle. As the liquid metal enters the water-cooled mold region, known as the primary cooling zone, a solidified shell is formed due to contact with the cold surface of the mold. As soon as the solidified shell is strong

enough to embay the molten metal inside, the bottom block is moved vertically downward. The solidified shell grows due to heat extraction as the metal passes down the mold. The lowering speed of the bottom block is gradually increased till it reaches the casting speed, and then it is fixed at that speed. Due to solidification shrinkage, the solidified shell pulls away from the mold, and an air gap is formed. The air gap causes the temperature of the solidified shell to increase due to the reduction in heat transfer from the ingot surface. Once the ingot emerges from the mold, water is directly sprayed (direct chill) on the cast surface. The region starting from the point of contact of the water spray with the ingot surface and below is called the secondary cooling zone.

Unlike the continuous sheet casting process, which is limited to relatively simple alloys of the 1000, 3000 and 5000 series, the DC casting process offers the ability to cast the full range of alloys up to high strength aluminum alloys used in the aircraft industry. This process also enables casting in different shapes and sizes such as huge sheet ingots for rolling mills, round log like billet for extrusion processes, or square billets for production of wires, rods, and bars. The cast ingots could reach up to 12 m in length and could have different cross-sectional areas depending on the final use of the product. Figure 1.3 shows a slab ingot from a vertical DC caster.

To date, commercial casting of ferrous and non-ferrous metals remains a highly empirical technology. In order to improve the quality of the castings and reduce production costs, it has become increasingly important to understand and control the casting process. The production of new castings requires an expensive, time-consuming, trial-and-error experimental diagnostic approach. These experiments need to be repeated for various alloy compositions and cooling rates, a tedious and time consuming task largely neglected by governmentally funded programs which are more in favor of advanced materials research. Therefore, doors for other economically feasible venues in the research and development of the DC casting process have to be explored. Among those venues, and maybe the most important and promising one, is mathematical modeling, especially given the advanced computing power available nowadays.

In this study, a 3D-mathematical model simulating the steady state part of the vertical DC casting of aluminum-alloy-slab ingots has been developed. The model is later

verified, and used to study and analyze the effects of some operational parameters on the ingot quality. The modeled equations are the 3D turbulent Navier-Stokes and energy equations. The momentum equations are modified with a Darcy-type source term dependent on the liquid fraction. This source term is introduced to simulate the fluid motion in the mushy region. The transition from molten alloy to solidified casting is achieved via the extraction of heat by the mold (primary cooling) and direct water spray on the slab surface (secondary cooling). The buoyancy force is introduced in the model through the Boussinesque approximation. The primary and the secondary cooling zones are simulated by changing the heat transfer coefficient on the slab surface. The heat transfer coefficient values are taken from the literature [13]. The k-ε model of Launder and Sharma [29] is implemented to model the turbulence aspect of the flow.

The developed mathematical model has been verified both quantitatively and qualitatively by comparing the computed results with that of Jones et al. [20] real casting and aqueous experiments, respectively. The quantitative verification has been done through the comparison of the solidification front depth predicted by the present developed mathematical model with that measured in the real casting experiments, a good agreement is found. The agreement in the solidification front depth is seen to improve with the addition of the thermal buoyancy force effect in the mathematical model. A complete match in the two solidification fronts, predicted and measured, is observed at the wide-symmetry plane at y = 440 mm from the slab center.

The developed mathematical model is later used in simulating two DC casters of different aspect ratios; namely, 2 and 2.62. In the smaller aspect ratio caster, the combo bag is used as a melt distributor, while the channel bag is used in the large aspect ratio caster. A detailed parametric study of melt flow and solidification is carried out on both casters. The analysis of the computed results helped in understanding and in explaining some of the DC casting phenomena reported and/or not reported in the literature but never been clarified so far.

1.2 Objectives of the Present Study

The main objective of this Ph.D. research work is to develop a three-dimensional mathematical model for the steady state simulation of vertical DC casting of aluminum alloys. The verification of the model has to be done both qualitatively and quantitatively using experimental results available in the literature. Once verified, the model can reliably be used by cast engineers to perform the early parametric study of DC caster design, and to predict, in advance, any faulty design scenario within any section of the DC caster system. Once these two goals are established, the second and third objectives stated below, longing for by all vertical DC caster producing firms, can be attained. The third and forth objectives are the safety and economy issues of the process. Performing the testing of new designs of DC casters using a computer simulation model would achieve the goal of safety. Reaching the optimum design with the minimum number of experimental trials would ensure the cutback in the capital cost of future installation of DC casters.

The model can be used in simulating flow situations that might happen after some operational period of the DC caster such as the partial blockage of the melt distribution system by inclusion. The early prediction of such flow situations will offer the designer a great deal of time in finding a solution to such problems. To achieve the last task, the developed mathematical model is to be extended to solve the 3D-mass concentration equation in order to predict inclusion particles distribution within the sump. In addition, the model can be used by the relevant academic community involved in improving the efficiency of the DC casting process. The model will help in understanding deeply the various transport processes involved in a DC caster as well as in identifying the most important parameters and the extent of their influence on the produced ingot characteristics.

1.3 Overview of the Present Work

The present work is divided into seven chapters. Chapter two is a general review of the vertical DC casting literature including the literature on numerical, physical and real casting experiments. Chapter three is devoted to the mathematical formulation and

the numerical approach used to solve the governing equations. The numerical formulation section covers the listing of the assumptions used in developing the current mathematical model, the development of the equations including the turbulence model, the model used in describing the flow in the mushy region as well as the solidification model, and the boundary conditions. Verification, both quantitative and qualitative, of the mathematical model developed as well as the study of the effects of the thermal buoyancy force on melt flow and solidification heat transfer is carried out in Chapter four. Chapter five is devoted to the parametric study on the small aspect ratio caster using the combo bag as a melt distribution system. The studied parameters are the casting speed, primary cooling rate, melt superheat, combo-bag dimensions, and combo-bag blockage. Chapter six is divided into two main sections; the first section deals with the parametric study on the large aspect ratio caster, while the second section covers the inclusion-distribution study within the sump. The parameters studied in the first section include the casting speed, channel bag dimensions, and melt superheat. In chapter seven, the main conclusions of the present work, statement of originality, and a few suggestions for possible future work are presented.

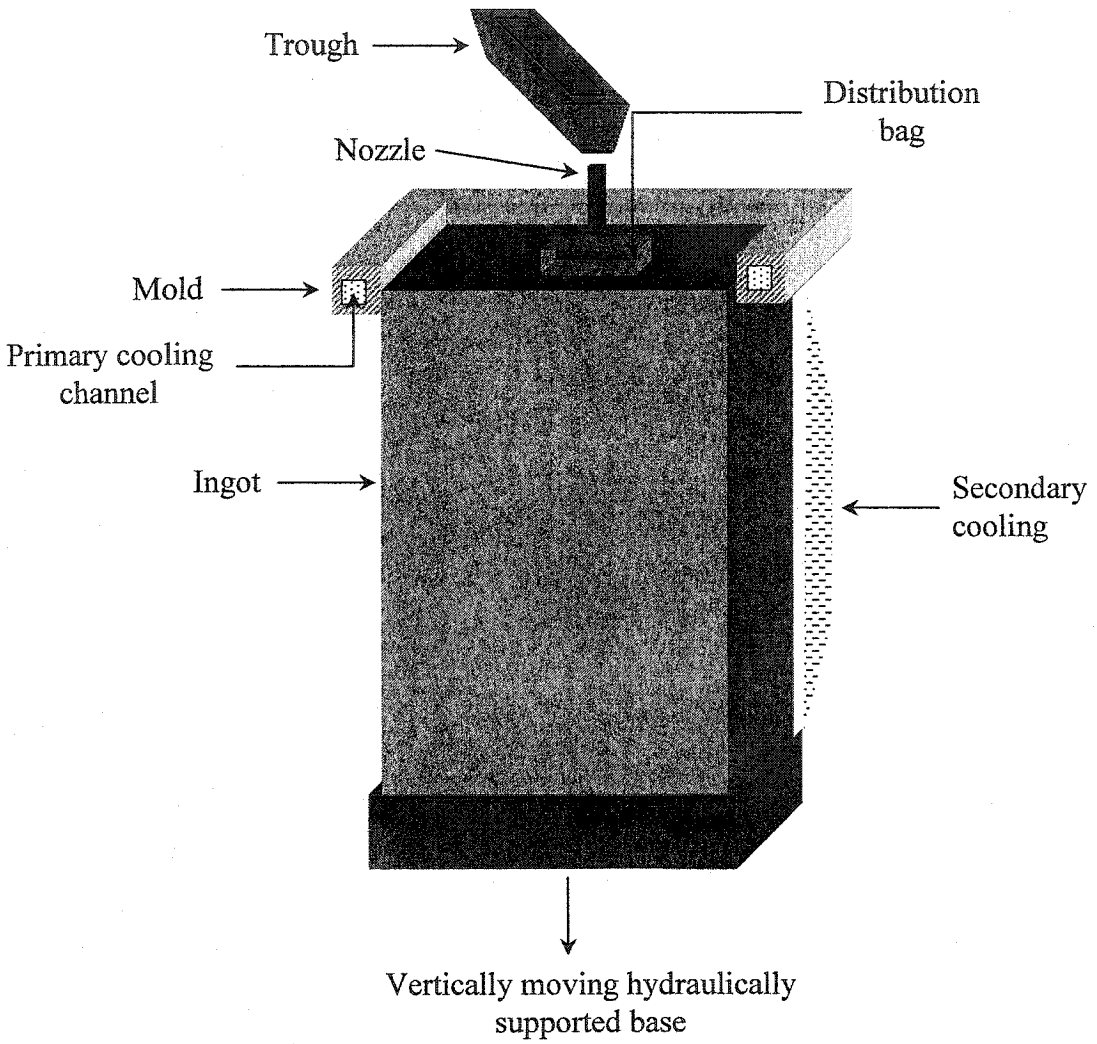

Figure 1.1: Schematic of a DC caster

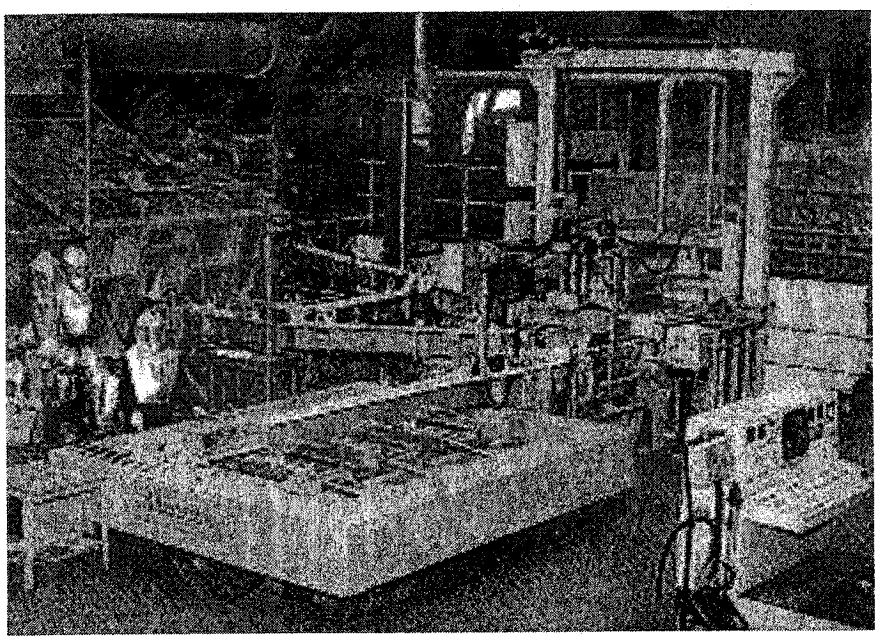

(a) Vertical DC caster

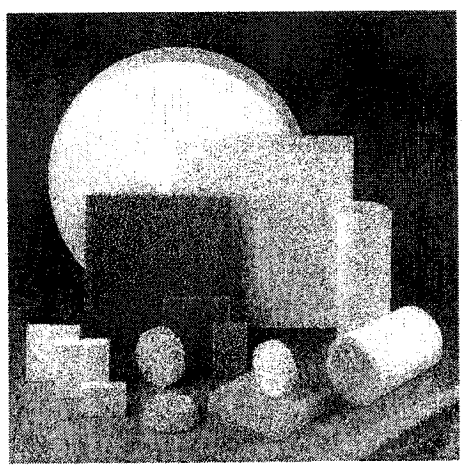

(b) Ceramic filters

Figure 1.2: A vertical DC caster and ceramic filters used in DC casters.

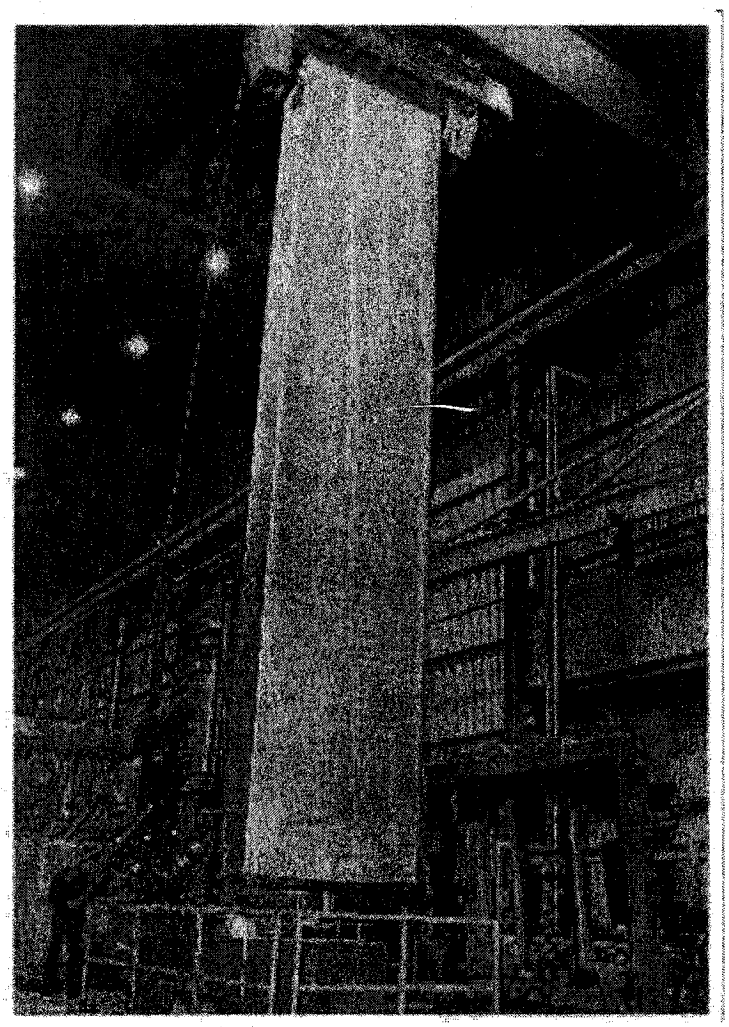

Figure 1.3: An aluminum slab ingot cast using a DC caster.

CHAPTER
TWO

Literature Survey

2.1 Introduction

In this section, a detailed description of the previous work that has a direct relation with the subject matter of the current research is presented. Also, an attempt is made here to shed some light on points where the present work can fill the gap in the surveyed work. The survey is organized in a way that follows the history of the developments of the DC casting technology in a chronological order. This procedure is very helpful in understanding the modern developments in terms of modeling of the DC casting process and also sets the stage for the need of what work will follow.

2.2 Previous Work

One of the early extensive reviews of the past models of the casting process and their assumptions was written by Weckman and Niessen [1]. The review covered the thermal DC casting models in the terms of analytical, numerical, and stress models, for the period ranging from 1947 to 1982. The authors concluded that the numerical models of the process were no longer constrained by the mathematics of the problem but by the lack of proper experimental data, particularly, heat transfer data on the external boundary conditions. These authors emphasized that experimental examinations of the heat transfer mechanisms over the external boundary of the DC cast ingot, in both the primary-cooling zone within the mold and the secondary-cooling zone below the mold, were required. Another review paper was written by Katgerman [2]. The author discussed the major developments in semi-continuous DC casting process and provided detailed process descriptions and metallurgical characteristics of the process. The author also discussed the technical constraints that existed in the period from 1970-1991. The author also emphasized the importance of improved understanding of heat flow during casting and advocated the need for advanced mathematical modeling techniques in order to improve the quality of the as-cast product.

Flood [3] showed the importance of mathematical models used by the aluminum industry in improving the understanding, and eventually, predicting the results of casting processes. The author discussed how the results of a numerical model of heat transfer and fluid flow for the DC casting could be used to optimize casting practices and to explore the transport phenomena within the ingot. To establish this task, the author postulated and explained 'criterion functions' and showed how these functions could be used to predict whether a phenomenon would or would not occur. In addition, the author also showed how the so called 'post-processing functions' could be used to correlate the magnitude of a phenomenon with the macroscopic fields, such as velocity and temperature fields. Furthermore, it was shown how micro-models could be incorporated into macroscopic models to couple small scale metallurgical kinetics with the macroscopic heat transfer and fluid flows.

An early attempt to numerically model the coupled fluid flow and solidification of aluminum alloys in DC casting systems was made by Flood et al. [4]. The CFD package PHOENICS was used to calculate the thermal and fluid flow fields in ingot billets. In their model, in one case, the melt was assumed to have been delivered over entire top surface. In another case, the inlet delivery was restricted to 10% of the billet radius. A good agreement was reported between the solidification front determined by the addition of copper as a tracer during casting and that was determined numerically. Unfortunately, the boundary conditions used in the model were not reported. Natural convection was found to dominate the casting process unless the inlet velocity was very high. In addition, they found that the buoyancy term, when dominated, it produced flat isotherms throughout much of the liquid and also caused steep temperature gradients close to the mushy region.

Tarapore [5] used a series of DC casting experimental trial runs with aluminum alloy 2024 to produce billet and to validate and further to improve a simplified finite element code (TEMPERI) previously developed for the simulation of semi-continuous casting of aluminum. The model was only used to calculate the thermal profiles in semi-continuously cast ingots. The convection of heat transfer in the sump was neglected. However, thermal conductivity of molten aluminum was used to calculate the

temperature in the sump. As a result, the thermal gradients in the sump were found to be significantly larger than the measured gradients. Hansen and Sahm [6], in their effort to improve the same model, used an effective thermal conductivity which took into account the convection effect in the molten metal. The convection in the molten metal was depending on the local superheat conditions. Upon using this procedure, the thermal gradients in the sump and sump depth were found to be in good agreement with measurements. The code TEMPERI was also used by Devadas et al. [7] to model the DC casting of aluminum billets. The results of the model were later compared with the results obtained from the commercial heat transfer and fluid flow package (FIDAP). In the TEMPERI code, slug flow was assumed in the liquid phase, and the convection-diffusion heat transfer equation was solved. At the solid-liquid interface, a planar heat source was assumed to exist. The heat input over this plane was assumed to be proportional to the latent heat of fusion and casting speed. The position of the solid-liquid interface was determined by an iterative process based on the criteria of having adequate thermal gradients to conduct the latent heat away from the fusion interface. The drawback of this model was that it could not handle mushy zones which develop during the solidification of commercial alloys.

Raffourt et al. [8] developed a numerical model to study the influence of different design parameters of the diffuser bag on flow configuration and thermal distribution in the sump. Pressure drop measurements were made in liquid aluminum to ascertain the relationship of pressure drop versus rate of flow through different materials in use for distribution bags. The experimental data so obtained was then employed as an input in a 3D fluid flow and thermal model. The calculations were restricted to the liquid volume of the sump and slabs of relatively low aspect ratio. A simple parallelepiped shape was assumed for the sump which simplified the implementation of the boundary conditions in the model. The solidification front is thus predefined, and its assumed shape was at best speculative and was far from being the shape of a real sump. Two different types of diffuser bags were analyzed by these authors. The first was a bag centrally reinforced by a non-permeable section (type a) and the second was a combo-bag (type b). For the parts of the bags consisting of permeable material, determined experimentally, friction

coefficient versus fluid velocity correlations were introduced into the model. For the non-permeable parts, a very high value was assigned to the friction coefficient. They concluded that in type (b) bag, the flow inside the bag had a direct influence on the flow outside the bag. This was a good example of mixed convection in which the forced convection originating from the diffuser bag competed with the natural convection generated in the neighborhood of the solidification front. The mixed convection flow affected the overall pattern of the liquid sump and, by the same token, the temperature distribution. In case of type (a) bag, the influence of flow inside the bag on external flow was less pronounced and the overall pattern of flow in the sump was dominated by natural convection. Slabs of higher aspect ratios were not considered in their investigation. Complexities of metal feed design were known to be greater for the higher aspect ratio slabs [23]. This is one of the motivations behind developing the 3D-computer code in this study so that one is able to model DC casters of all formats of interest (high and small aspect ratios). Also, the developed model will aid in the design of an optimized distribution bag for each slab format.

El-Demerdash [9] developed a simple-laminar 2D model in cylindrical coordinates to compute the temperature distribution in DC cast aluminum billet ingots. Heat transfer by conduction in the metal and convection at the boundary were studied. The latent heat was taken as a variable which depended on liquid fraction. A variable heat transfer coefficient was used to extract heat from the surface of the ingot in both the primary and secondary cooling zones. The finite difference technique was used to solve the steady-state partial differential equation of heat transfer. The properties of Al6063 were used in the model. The author studied the effects of varying temperature superheat and casting speed for a constant metallostatic head. This author reported that melt pouring temperature between 680°C to 700°C has a minimal effect on the internal temperature distribution in the ingot. On the other hand, the casting speed was found to have a remarkable effect on the temperature contours. The increase in the casting speed caused the solidification front to get deeper and resulted in the mushy zone to expand. A further refinement of the model was recommended through fine-tuning of the heat

transfer coefficient values at different axial surface zones and by the inclusion of the convection terms in the model.

A few analytical studies which tackled the subject of natural convection in aluminum ingots were found in the literature. Among these studies the study by Davidson and Flood [10] is the most advanced. An approximate solution of the integral-momentum equation was established for their model. The model was based on an axisymmetric pool of liquid aluminum of maximum radius R for an aspect ratio of the order of one. The effects of solidification, such as the release of latent heat, were ignored. However, a small inflow of metal at the top surface was allowed. The goal of their study was to predict the temperature distribution and velocity field in the liquid pool. The predictions were compared with the numerical experiments performed using a finite-difference code. The comparison was satisfactory. Both studies showed that the peak velocity was near the stratified region and that the wall jet initially thickened, and later it got thinner over most of the stratified region. Using the simplified model, an overestimation of the peak velocity by 30 % was reported as compared to the peak velocity estimated by the finite-difference code. The overestimation was attributed to the fact that the viscous boundary layer was not taken into account in the model.

El-Raghy et al. [11] developed a simple two-dimensional model to compute the transient and steady state conditions of aluminum DC casting. The finite difference technique was used to solve the model equation. Only conduction heat transfer was considered within the molten metal and inside the mold. Convection heat transfer was assumed at the ingot boundary. The latent heat of solidification was taken as a variable depending on solidified melt fraction and hence on temperature. It was found that increasing the casting speed from 90 mm/min to 105 mm/min decreased the time spent by the melt inside the mold or in the chilling zone and resulted in a lesser heat extraction from the system at a fixed point. Increasing the casting speed caused the temperature contours to shift downwards. A reheating was shown at the ingot surface due to the elimination of vapor and increasing the water temperature.

Buchholz et al. [12] designed a water model to investigate the flow patterns and the influence of different inlet systems. The model comprised of a horizontal spout, a

vertical spout, and a diffuser bag. The water model results were correlated with the results from metallographic analysis. Dynamic similarity was maintained between the water model and a real casting experiment, noting that water between 20°C and 60°C has a kinematic viscosity similar to aluminum at 700°C. Thus, a model of the same geometry can be used at the same flow velocities as in the real casting. The experiments showed that strongly directional melt flow led to overall poor properties in continuously cast slabs, whereas, a distributor bag and a diffuse melt supply arrangement provided more uniform characteristics.

Vreeman and Incropera [13, 14] studied the effects of free-floating dendrites and convection on macrosegregation in DC cast aluminum billets. This study comprised of both analytical and computational modeling parts. Though the specifics of their study are different from the subject matter of the present work, yet the mathematical modeling part has some similarity, particularly with respect to the assumptions of the current study and the boundary conditions employed in the current model. At the billet surface, a no slip boundary condition was applied in the liquid region, and an axially translating boundary was applied in the mushy and solid regions. A variable heat transfer coefficient was implemented at the billet surface. At the air- gap region, the heat transfer coefficient was approximated by weighting two distinct heat transfer coefficients according to the solid and liquid fractions. One coefficient corresponded to the heat extracted through direct mold contact, and the other coefficient corresponded to conduction and radiation across the air gap. The varying heat transfer coefficient along the secondary cooling region was based on measurements done by other researchers [39]. The authors stated that the best method for modeling DC casting would be to extend the computational domain upward, and to include the liquid flow in the distribution bag and/or the trough above the mold assembly. The current developed mathematical model has included the distribution bag within the calculation domain, which was recommended by Vreeman and Incropera. The recommendation for the incorporation of the distribution system in the calculation domain was based on their intuitive understanding that the flow within the sump must be affected by the nature of the flow within the distribution bag.

An extensive work on DC casting was performed by Xu et al. [15-18] and Jones [19,20] at the University of California at Berkeley. Both authors belong to the same group of researchers all of whom worked under the supervision of Professor Evans of the same university. Prof. Evan's group concentrated on simulating electromagnetic (EM) and DC casting processes by constructing physical water models [15]. Particle image velocimetry (PIV) was used to measure the velocity field in the aqueous model by analyzing frame-by-frame of video recordings of the movements of tracer particles. The particles used had nearly the same density as water (the working fluid) so that their rising/settling velocity in the fluid could be neglected. The water model results were compared to the results from a mathematical model which was based on the commercial code FIDAP. Only the fluid flow portion of the problem was modeled. A predefined solidification front was mimicked in their water model which later incorporated in the numerical model also. A good agreement was reported between the measured and calculated results. The PIV system, used in the water model, includes three main subsystems: visualization, photograph, and recording and analysis software. A high-powered laser is needed for satisfactory results, and would be expensive and unsafe due to its powerful laser output. Therefore, a much cheaper and safer normal light source was selected for the illumination system. The basis of the PIV technique is to illuminate a two-dimensional plane of the flow which has been seeded with the tracer particles. These particles are assumed to follow the flow accurately. The illuminated plane is then recorded on photographic film or video camera. The displacements of the flow tracers from one frame of the video camera to the next are extracted from these recordings, and velocities are computed from the time interval between the capturing of the two images and the displacements.

Using their developed physical water model, Xu et al. [15,16] studied the effect of metal-delivery-devices; namely, distribution bags, nozzle placement as well as blockage of the distribution system on the flow in EM and DC casting of aluminum alloys. A combo-distribution bag was found to affect strongly the flows in the liquid pool (sump). The nozzle alone without the distribution bag resulted in a strong downward flow in the center of the pool and also created a deeper solidification front. The velocity of the flow

along the solidification front was found to decrease appreciably. With the employment of the bag, the flow showed different characteristics, which depended on the bag dimensions. The issuing streams from the short combo bag were combined in one stream. The combined streams moved downward and spreaded outward impacting the solidification front at its half height. On the other hand, the long distribution bag with open bottom windows showed four distinct jets issuing from the two bottom and the two side windows. Velocities near the solidification front increased for the long bag. Further changes in the flow field were observed when the bottom windows were eliminated or partially blocked.

As a further development to the above mentioned physical water model, the above authors studied the effect of thermal buoyancy force. In order to generate such a force, a water heater was added in the experimental setup [18]. The water heater was inserted into the flow loop after the pump but before the flow meter, to have a better control over the temperature of the fluid entering the model. To ensure the existence of thermal similarity between a real aluminum caster and a physical water model, the tundish number (ratio of Grashof number to Reynolds number squared) for each system was made equal. The dynamic similarity was established through equating Reynolds number in both systems. It was found that the buoyancy driven flows affected the melt flow in the liquid pool, especially the flow out of the bottom windows, leading to a more uniform flow in the lower regions of the pool. The jet exiting from the end window was found to spread out more under the buoyancy effect. The authors concluded that it is necessary to properly model the thermally induced flow to obtain an accurate description of the flow in the liquid pool. Therefore, based on the last conclusion, the buoyancy term is added in the current developed mathematical model (as will be seen in the model verification chapter of the present work). This step has made the current model more realistic since buoyancy force plays an important role in real DC casters.

As a follow up to the work of Xu et al., Jones et al. [19] used the same physical water model developed by Xu et al. [16] to investigate the effects of disturbances caused by the flow control bags. These bags are typically used in casting of aluminum slab ingots. The study focused on the quantitative characterization of the time averaged flow

patterns that originated from bag defects, such as ones that might occur by human error. An example of such errors was the misplacement and/or tilting of the distribution bag as well as the disturbances caused by the presence of these bags. They concluded that the most desired flow pattern in the balanced (symmetric) position was produced by the shorter bag. Less uniform flow was observed using the larger distribution bag when it was placed in the balanced (neutral) position; however, less change in the flow field was found by placing the bag in a non-symmetric position.

Perhaps the most important work of Jones et al. [20] is the one in which the authors constructed the setup and ran a real DC casting experiment. The importance of this experimental campaign stemmed from two points. The first is that this experiment was among a very few experiments that were accomplished in research centers. The second point is that the results of this experiment have been used in verifying quantitatively the predictions of the present mathematical model. Moreover, the results of a real casting experiment, performed in the research center of a well known DC casting industrial firm[1] which were used to verify the current model gives a high credibility and confidence in the model to be used as a tool in designing new DC casters and improving the product quality. The real casting experiment was carried out to investigate the influence of combo-bag geometry on the fluid flow and the shape of the solidification front of a DC cast aluminum alloy. Experiments were performed on production sized aluminum 3104 ingots. Two different sizes of combo bags were chosen and were subjected to the same casting practice. Sacrificial thermocouples were used to track the steady state thermal field. The study showed that the longer bag resulted in a deeper sump which was up to several centimeters at the center. More thermal fluctuations were noticed in the sump for the shorter bag. These fluctuations were attributed to the increase in turbulence levels usually accompanying shorter bags.

Grun et al. [21,22] contributed two research papers to the DC casting literature. In the first paper [21], the finite element commercial CFD code FIDAP was used to investigate the influence of nozzle-distributor systems on temperature and sump profiles. Natural convection was not considered in their model. They concluded that the flow

[1] The experiments were carried out at Reynolds Metal Company Casting Technology Center, VA.

pattern in the sump as well as the extent of the mushy zone were governed by the aspect ratio (length to width ratio) of the distributor bag. Changing the ingot size and casting speed had only a small effect on the characteristics of the flow field and temperature distributions. They showed that purely thermal calculations were able to predict reasonably the position of the solidification front. In their second paper [22], the performance of four commercial packages in simulating a DC casting process was tested. These packages were ALSIM, PHOENICS, FIDAP and CFX. The comparison was done to evaluate the influence of the chosen fluid flow model, be it laminar or turbulent flow, on the resulting velocity fields and temperature profiles. This study is one of the most recent and comprehensive studies using most of the relevant commercial packages available in the market today. The results were only compared qualitatively with temperature measurements in a liquid pool obtained in an experimental trial program. The temperature contours and the vector field results were presented without putting any dimensions on the figures. Moreover, the vector field arrows were drawn with uniform length. Therefore, even though a lot of efforts were exhausted in the work, yet the way in which the work was presented render it impossible to compare with, or to draw conclusions from out of it. This matter gives the present work its importance in terms of the detailed information on the results that includes vector field, streamlines, and temperature contours. In addition, the current work has the advantage of including the effect of natural convection, and the attempt to explain some of the phenomena reported in the literature that have never been explained, as will be seen in Chapters 4-6.

Gary et al. [23-24] studied the vertical DC casting process and emphasized on the fundamental aspects of the process for the purpose of providing the user with a greater degree of control over a number of operational parameters. Their work was published in two parts. The first paper [23] dealt with the metal distribution, while the second paper [24] presented the heat transfer and the resulting solidification behavior. Their work consisted of physical water model, mathematical modeling and experimental casting trials. In their water model, the flow characterization was achieved by ink injection through the wall of the downspout using Ultrasonic Doppler Velocity Measurements (UVDM). The PIV, as described by Xu et al. [16], was also used in the flow

characterization in the earlier stages of the metal development program. However, at a certain point in their experimental campaign they stopped using the PIV technique due to its time consuming nature in gathering data and the difficulty in obtaining accurate representations of the flow in areas of low velocities. The key performance criteria was to identify some of the basic design features of a distributor influence on the fluid flow, and to investigate which features of the distributor should be modified in water to achieve the desired flow characteristics. Two different ingot sizes and two distribution-bags were tested, namely, a standard-distribution bag and a modified-distribution bag. The main point in comparing the two distributors was to identify the number of dead zones or eddies present, and which would generate more areas of low fluid refreshments. They found out that the modified distributor performed better for the ingot with large aspect ratio than the standard distributor used in the standard ingot.

In the mathematical modeling part, two ingot sizes were considered by the above authors; these were the ingots with 600x1685 mm and 610x2700 mm cross-sections. The ALSIM commercial code was used in the mathematical simulation study. The results correlated well with the established results of their water model. In the case of the 600x1685 mm caster, no explanation was provided for the thickening of the mushy region from the liquidus-temperature side around the slab center. The flow was allowed to occur in the range from the casting temperature to a liquid fraction of 0.8. Below the liquid fraction of 0.8, a rapid convective damping of the inlet flow was assumed. In the experimental casting trials, a number of different distributor bags were tested in a full-scale system. A skewed temperature profile was found due to a misaligned distributor bag, whereas a symmetrical temperature distribution resulted for the balanced positioning of the bag. A 5°C difference was found between the two rolling faces of the slab in the case of the perfectly aligned distribution bag, whereas, a 17°C difference was found using the misaligned distribution bag.

In the aluminum casting industry, which uses ordinary DC casting for highly alloyed aluminum melts for making rolling ingots, it is found in most of the cases that the ingots show heavy surface segregation. In the literature, several authors described this phenomenon. The operating mechanism was generally considered to be an interdendritic

transport of enriched residual melt moving from the center of the solidification front towards the ingot surface and appearing at the surface in the air gap zone. Edge cracking during hot rolling was believed to be strongly related to the ingot subsurface and surface microstructure. Bjorn and Einar [25] investigated numerically the effect of varying the casting parameters such as metal head, water hit point position, heat transfer coefficient in the contact zone, critical shell thickness, and casting speed on the surface segregation (exudation). The temperature models ALSIM2 and ALSIM3 were used for numerical modeling. Their modeling study led to the conclusion that the most effective way to minimize the surface segregation was by decreasing the distance between the primary and secondary cooling zones. No experiment was done to verify their claim. The authors showed that a proper selection of the mold length was critical for the reduction of surface segregation.

Many industrial firms carried out experimental work on their DC casters to improve their ingot quality. Wagstaff et al. [26], worked for Wagstaff Inc., carried out experimental investigation to improve the DC casting technology to get smooth ingot surfaces and to minimize sub-surface segregation. Ingots with such qualities would require less scalping and edge trimming. To achieve the two above mentioned goals, the Low Head Casting (LHC) technology was proposed. The LHC process permits faster casting speeds and minimal lubrication requirements. However, Yves et al. [27] reported that the shell thickness using LHC technique was not low enough to obtain the same beneficial gains as those were achieved using the electromagnetic casting (EMC) technique. In addition, the LHC was limited by:

1- The metal level in the mold and its relation to the casting speed is such that, the slower the casting speed, the higher the metal level in the mold must be to prevent cold folding or overlapping of melt during steady state conditions.

2- The sensitivity of the shell thickness to metal level is such that, any fluctuation of the metal level would change the shell thickness.

3- Safety considerations, where water getting onto the top of the metal head was often seen in production plants using the LHC technique. Rejection of ingots due to severe cold

folding at ingot corners is frequent when the metal level in the mold is kept too low. Starvation of lubricant causing ingot surface tearing is another problem.

The EMC technology is relatively new and had its origins in the USSR, in the mid-sixties, by Getselev et al. [53]. A good review on EMC was written by Evans [40]. In EMC the liquid pool is supported by electromagnetic forces. The forces are produced by the interaction of currents induced in the aluminum, by an inductor surrounding the metal (through which alternating current of a few kA at several kHz is passsed), and the magnetic field produced by the inductor. These forces are moderated by a band of conducting material, typically stainless steel, partially interposed between the inductor and liquid pool and known as a screen or shield. A modified design in which the moderation of electromagnetic forces is achieved by shaping the inductor has been developed to commercial application by Kaiser Aluminum. The EMC technologies still presenting operating problems [54], these problems can be characterized by the fact that there are few conception rules, if any. This is due to the lack of understanding of basic mechanisms; an example is the case of large power inductors. Under such circumstances, a serious attempt to understand and identify relevant parameters is necessary, in order to avoid the giving up of these technologies.

Later, the Alcan Sheet Mold (ASM) [27] was developed to produce ingots with characteristics as the EMC ingots. Using the ASM, a decrease in scalping depth of as much as 50% was achieved. The ASM is based on the optimization of effective mold length defined as the distance between the mold/metal contact point and the bottom of the mold and added to this is the distance between the bottom of the mold and the water impingement point on the ingot surface. The optimization of the effective mold length is achieved by the superposition of both the primary and secondary cooling zones and through the use of a short mold. A higher impingement point on the ingot surface, and the use of an insulation ring at the upper part of the mold addressed the safety issues related to low metal level casting (LMLC). This is achieved in ASM technology by maintaining a liquid reservoir of melt above the primary cooling region. In addition to the improved surface quality, the ASM technology was credited for the significant gains in internal

ingot quality, robustness, and casting productivity. The new design also offers major benefits on mold maintenance and replacement costs.

Sylvain and Martin [45] developed a new distributor for DC sheet ingot casting. The reported work was divided into two sections. The first part dealt with the principle and design of a new Reusable Molten Aluminum Distributor (ReMAD) to replace the standard combo bag. The design of the distributor is based on a full-scale water modeling experiments. In the second part of their paper, the test results of the ReMAD used at ABI to cast AA-1045, AA-3003 and AA-5052 alloys were presented. The research work focused on studying the cast start-up, actual metal flow observations, ingot surface finish and temperature profiles around the mold. Also, the ingot cut slice analyses, PODFA analyses, and results from the rolling plant were considered in their research work. With the use of the ReMAD, they claimed to have obtained a thinner oxide layer at the ingot surface compared to the standard combo bag. They also obtained a better meniscus rolls at the mold interface, less turbulence at the melt free surface, and suggested to remove the skim dam in the mold region. They did not report any numerical modeling work and said that the work was yet to be completed.

2.3 Closure

The above survey shows, to a certain extent, the importance of the role played by numerical models in simulating the process of vertical DC casting of aluminum alloys. From the above review of literature, it is clear that all of the serious attempts made so far to numerically model the vertical DC casting of aluminum alloys are either simple models or models which depended on commercial codes. These commercial codes are too general and are not specifically coded to model DC casting problems [22]. These general purpose fluid dynamic codes are indeed very cumbersome to use and suffer serious convergence difficulties. The latter aspect could be one of the reasons why these CFD codes have not been able to analyze in detail and to provide rational answers to some of the observations and phenomena noticed in DC casting processes. In addition, only a few of the surveyed models were verified, and some of these verifications were conducted using the results of other computer codes that were not verified.

Regarding the experimental attempts, although the DC casting is essentially a solidification problem, it can be noticed that most of the previous research on DC casting were conducted using physical water models. In addition, using a predefined and fixed solidification fronts would not serve the main goal behind building these experiments, and analyzing the fluid flow in the sump. Therefore, a specialized code which can be depended upon in designing, analyzing and answering matters unexplained in the vertical DC casting literature is critically needed at this stage. The supposedly new developed model might be used in the early stages of the most recently developed casting technique, namely the ASM by identifying the optimum operating parameters such as the casting speed, temperature superheat, primary and secondary heat transfer coefficients, etc. In the present numerical modeling work, an attempt is made to develop a 3D CFD model that would enable to answer most of the above mentioned points.

CHAPTER
THREE

Mathematical Model and Numerical Approach

3.1 Introduction

The general characteristics of the DC casting process render the modeling of the process a challenging task. The relatively large ingot formats and the locally high thermal gradients due to the water cooling may induce severe distortions. The direct water cooling is in itself a rather complicated process. The impingement angle, the velocity of the water jet, the quality and the quantity of the water flow, the cast surface roughness, and the temperature of both the water and the cast surface are of importance. Fluid flow is important for the distribution of superheated liquid, especially for large ingot dimensions, and for the microstructure evolution.

Qualitative and quantitative insights could be generated through the use of analytical tools, however, the nonlinear nature and the irregular time dependence of the real-world problems make the technique less accurate. On the other hand, the advancement in developing numerical techniques and the high degree of accuracy of their solutions make the analytical solutions less appealing. In addition, the staggering advancement in the computing facilities and its power, especially the computing speed, makes the numerical solutions more attractive as a tool in solving DC casting problems.

This chapter is devoted to the development of the equations used to model the three-dimensional fluid flow and heat transfer of the vertical DC casting of aluminum alloys. The governing equations are characterized generally as non-linear partial differential equations. These equations consist of the continuity, momentum, and energy equations. The low-Reynolds number k-ε turbulence model of Launder and Sharma [29] is used to simulate the turbulence aspect of the flow. The chapter is divided into two main sections, the mathematical formulation and the numerical approach used to solve the

governing equations. The first section is divided into six sub-sections, the first of which is dedicated to listing the assumptions used in developing the current mathematical model, while the second sub-section is devoted to the development of the equations used to model the turbulence in fluid flow and heat transfer of the DC-casting of aluminum alloys. The third sub-section describes the solidification modeling, and the forth deals with the modeling of fluid flow in the mushy region. The boundary conditions used in solving the governing equations are listed in the fifth sub-section, and the last sub-section is devoted to the non-dimensionalization of the governing equations. The numerical approach section is divided into two sub-sections, the first of which is dealing with the discretization procedure, while the second describes the solution procedure and convergence criteria.

3.2 Mathematical Formulation

In order to model a physical problem numerically, the problem has to be correctly defined. The definition should include specifying the calculation domain, the assumptions used in developing the mathematical model, the physical properties needed, the boundary conditions, and any other constitutive relations deemed to be pertinent to the problem. Transport phenomena in a vertical DC caster are essentially three dimensional in nature. Figure 3.1 shows schematic of the vertical DC caster in which the calculation domain, a quarter of the ingot, is presented as a shadowed block.

3.2.1 Model Assumptions

The assumptions used in developing the current mathematical model are summarized in the following points:

1. The process is steady state with respect to a fixed-coordinate system (Eulerian approach).
2. Molten aluminum behaves as an incompressible Newtonian fluid.
3. Thermophysical properties of aluminum are invariant.
4. Density and thermal conductivity of the solid phase are equal to those of the liquid phase.
5. No viscous dissipation.
6. Variation of liquid fraction in the mushy zone is assumed to be a linear function of temperature.
7. Turbulent viscosity is calculated using a two-equation k-ε turbulent model.
8. Solidification occurs under equilibrium condition.
9. The slag layer is assumed to be flat and fixed at a constant level.

Due to the symmetry of the problem, only a quarter of the domain is considered in the calculations. It is to be noted that the buoyancy force effect has been included in a part of the current study in Chapter Four titled, "Model verification and buoyancy effect study". Therefore, discussion of the mathematical modeling of the buoyancy force is included in the following chapter.

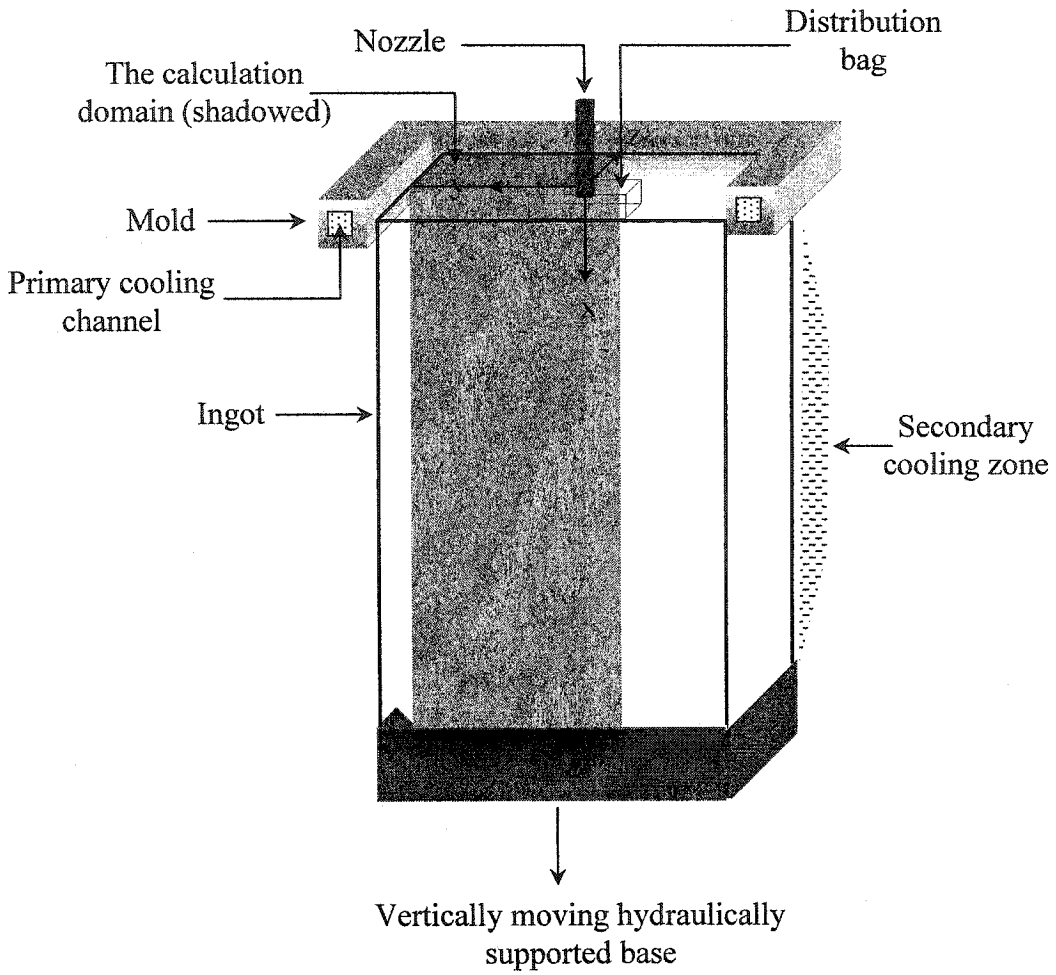

Figure 3.1: Schematic of the DC caster with the yellow part representing the computational domain.

3.2.2 Turbulence Modeling

Turbulent fluid behavior is difficult to describe due to its complexity. This complexity arises from the fact that the various properties of the fluid vary randomly in space and time. Many researchers studied and tried to come up with a general definition for the turbulent motion of fluids, among those researchers is Hinze [28] who defined turbulent fluid motion as an irregular condition of flow in which the various quantities

show a random variation with time and space coordinates, so that statistically distinct average values can be distinguished. Therefore, turbulence is a deterministic phenomenon. Noting that in the current modeled problem Re_j is around $41x10^3$ (turbulence zone). The current turbulence model relies on the solution of the Reynolds-averaged three dimensional turbulent flow and the energy equations. In this model, the instantaneous velocities (u, v, w), pressure (p), and energy (H) are decomposed into time-averaged and fluctuating components as follows:

$$\begin{aligned} u &= \overline{u} + u' \\ v &= \overline{v} + v' \\ w &= \overline{w} + w' \\ H &= \overline{H} + H' \\ p &= \overline{p} + p' \end{aligned} \tag{3.1}$$

where the bar represents average variable quantity, and the second term on the right hand side of each equation represents the fluctuating component of the variables. Substituting equation (3.1) into the laminar form of Navier-Stokes and energy equations, the time-averaged forms of the conservation equations are obtained. These equations can be written in Cartesian-tensor notation as follows:

Continuity equation
$$\frac{\partial(\overline{\rho u_i})}{\partial x_i} = 0 \tag{3.2}$$

Momentum equation
$$\frac{\partial(\rho \overline{u}_i \overline{u}_j)}{\partial x_j} = -\frac{\partial \overline{P}}{\partial x_i} + \frac{\partial}{\partial x_j}\left[\mu\left(\frac{\partial \overline{u}_i}{\partial x_j} + \frac{\partial \overline{u}_j}{\partial x_i}\right) - \rho\overline{u_i' u_j'}\right] \tag{3.3}$$

Energy equation
$$\frac{\partial(\rho \overline{u}_j \overline{H})}{\partial x_j} = \frac{\partial}{\partial x_j}\left(K\frac{\partial \overline{T}}{\partial x_j} - \rho\overline{u_j' H'}\right) \tag{3.4}$$

The over bars represent averaged quantities, while

$$\overline{u_i' u_j'} = \frac{1}{\Delta t}\int_0^{\Delta t} u_i'(t) u_j'(t) dt \tag{3.5}$$

where Δt is longer than any significant period of the fluctuations themselves.

A comparison of equations (3.3) and (3.4) with the corresponding laminar form of Navier-Stokes and energy equations shows the existence of extra terms in the above mentioned equations. These new terms (variables) contain the fluctuation components, and are termed as the Reynolds stress term $\overline{\rho u_i' u_j'}$ in the momentum equations and the turbulent heat flux ($\overline{\rho u_j' H'}$) in the energy equation. The determination of these new variables requires the introduction of a turbulence model.

3.2.2.1 Models of Turbulence

Amongst the many proposed models of turbulence to specify the Reynolds stress and turbulent heat flux quantities in averaged equations, at present two types of models are being used the most; these are known as eddy viscosity models and Reynolds stress models. The eddy viscosity model is widely used in solving engineering problems. It is based on the assumption that Reynolds stress or the turbulent heat flux is proportional to gradients of mean flow variables. The constant of proportionality is the eddy diffusivity, a scalar quantity, and is therefore isotropic. Depending on the number of partial differential equations used to determine the eddy diffusivity, the models can be classified as zero, one, and two-equation models.

In the zero equation models, the turbulence viscosity (eddy diffusivity) is calculated using an empirical relationship as:

$$\mu_t = \mathrm{C}\, \rho\, u\, l \tag{3.6}$$

where u and l are the characteristic velocity and mixing length, respectively. The mixing length and the constant C are determined based on experimental data. The characteristic velocity of turbulence u is proportional to the gradient of the mean flow. The major drawback of these models lay in their prediction of the eddy diffusivity at symmetry planes to be zero, contrary to measurements made in laboratories where it is found that the eddy diffusivity is not zero. On the other hand, in the one equation models, the characteristic velocity of turbulence is considered to be proportional to square root of kinetic energy of turbulence. Therefore, the eddy diffusivity can be expressed as:

$$\mu_t = C_k \rho \, l_m \sqrt{k} \tag{3.7}$$

where k is found by solving a transport partial differential equation for turbulent kinetic energy of the form:

$$\rho \frac{Dk}{Dt} = \frac{\partial}{\partial x_m}\left[\left(\mu + \frac{\mu_t}{\sigma_k}\right)\frac{\partial k}{\partial x_m}\right] + \mu_t\left(\frac{\partial \overline{u}_i}{\partial x_j} + \frac{\partial \overline{u}_j}{\partial x_j}\right)\frac{\partial \overline{u}_i}{\partial x_j} - \frac{C_D \rho k^{1.5}}{l} \tag{3.8}$$

where C_D is an empirical constant, and l is the mixing length. The ratio of momentum turbulent diffusivity to the turbulent diffusivity of kinetic energy is represented by σ_k. The mixing length needs to be specified using empirical relations that are difficult to find for complex flow situations. As a result, two equation models have been proposed so that the length scale can be obtained by two transport equations. The most popular of the two equation models is the k-ε equation model in which k is the kinetic energy of turbulence, and ε is the rate of dissipation of the kinetic energy of turbulence. The k-ε model is based on the eddy diffusivity model in which the eddy turbulent viscosity is correlated using k and ε via the Kolmogorov-Prandtl expression as:

$$\nu_t = C_\mu \frac{k^2}{\varepsilon} \tag{3.9}$$

where C_μ is an empirical constant. The k-ε models can be classified as high and low turbulence model. The high Reynolds number model can not be applied in low Reynolds number regions, such as near the solid boundaries where viscous effects become dominant. To overcome such a problem, two solutions are proposed. The first is based on the use of a special function near the solid boundaries known as wall function. The second is the use of a damping factor to cover the viscous sub-layer. The wall function approach is appropriate for use in simple turbulent flows. In addition, it requires less computational requirement. However, it is difficult to apply the technique in complex flow situations such as turbulent flows with centrifugal force, buoyancy, phase change and flow over spinning surfaces. Moreover, it can not be used in the case of low

Reynolds number flows. The difficulties in applying the high-Reynolds turbulence model become more evident when one deals with phase change problems in which the solid boundaries are not known a priori, which is the case in the current model (DC casting).

The above shortcomings can be resolved by the use of the low-Reynolds-number k-ε model. The model covers the whole flow domain including the buffer and viscous sub-layer. As mentioned earlier, the model works by imposing a damping function proposed by Van Driest [32] for the mixing length model. The purpose of the damping function is to reduce the production of the eddy diffusivity μ_t and to increase the production of the dissipation of the kinetic energy of turbulence ε, so that the turbulence effects are reduced in the viscous sub-layer. A number of such models were proposed by different authors all of which can be found in the literature [33-36]. Many researchers [33, 37] conducted experiments on the various low Reynolds turbulent models to evaluate their accuracy in predicting the turbulent boundary layer. It was found that the model of Lauder and Sharma, Lam-Bremhorst, and Chein all performed fairly well in comparison with experimental results. However, in the models proposed by Lam-Bremhorst and Chein, the distance from the solid boundary is used to calculate the eddy diffusivity. For that reason, these models can not be used in flow situations where the solid boundary is not predefined such as in the case of DC casting. In contrast, the Launder and Sharma model does not depend on the distance from the solid boundaries in finding μ_t. Therefore, the model proposed by Lauder and Sharma [29] is adopted in the current DC casting model. A brief discussion of the model follows.

Launder and Sharma Low Reynolds Number Two-Equation k-ε Model:

The low Reynolds number two equation k-ε turbulence model of Launder and Sharma is based on the assumption of linear isotropic formulation of the eddy viscosity in presenting Reynolds stress terms. The eddy viscosity concept is based upon the observation that the main effect of turbulence is to increase the transport of the conserved properties and dissipation effects with respect to the laminar state. Since for laminar flows, the laminar viscosity of the fluid controls these processes, it is natural to represent

turbulence in a similar way in terms of apparent viscosity (turbulent viscosity) in the form:

$$\overline{\rho u_i' u_j'} = -\mu_t \left(\frac{\partial \overline{u}_i}{\partial x_j} + \frac{\partial \overline{u}_j}{\partial x_i}\right) + \frac{2}{3}\delta_{ij} k \tag{3.10}$$

where k is the turbulent kinetic energy defined as:

$$k = \frac{1}{2}\overline{u_i' u_j'}$$

the Kronecker delta (δ) is defined as:

$$\delta = \begin{cases} 0 & when \quad i \neq j \\ 1 & when \quad i = j \end{cases}$$

The second term on the right hand side in equation (3.10) is added so that the equation can be applicable to homogeneous and isotropic turbulent flows.

Similarly, the turbulence heat flux is obtained using the eddy diffusivity concept to relate the turbulence heat flux to the local mean temperature gradient in what is known as the Turbulence Prandtl Number Approach (TPNA):

$$\frac{1}{c_p}\overline{\rho u_j' H'} = -\frac{\mu_t}{\sigma_t}\frac{\partial \overline{T}}{\partial x_j} \tag{3.11}$$

where σ_t is the turbulent Prandtl number, and μ_t, the turbulent viscosity defined as:

$$\mu_t = \frac{c_\mu f_\mu k^2}{\varepsilon} \tag{3.12}$$

The function f_μ is a damping factor to account for the laminar viscosity onto the turbulent viscosity for the low turbulent Reynolds number flow near the wall (the viscous sublayer and the buffer zone). The variables k and ε, as defined earlier, are the turbulent kinetic

energy and its rate of dissipation, respectively. The values of these variables are obtained from the solution of another two transport partial differential equations. The first equation is the turbulence kinetic energy, while the second is the rate of dissipation of kinetic energy. Since the detailed derivation of these two equations is given by Lam and Bremhorst [30], and Hollworth and Berry [31], only the final form of the equations are given below. Henceforth, the symbols u, v, and w without the over bars represent the average velocities:

(a) Transport equation for turbulence kinetic energy:

$$\frac{\partial(\rho u_j k)}{\partial x_j} = \frac{\partial}{\partial x_j}\left[\left(\mu_t + \frac{\mu_t}{\sigma_k}\right)\frac{\partial k}{\partial x_j}\right] + \mu_t\left(\frac{\partial u_i}{\partial x_j} + \frac{\partial u_j}{\partial x_i}\right)\frac{\partial u_i}{\partial x_j} - \rho(\varepsilon + D_k) \tag{3.13}$$

(b) Transport equation for rate of dissipation of kinetic energy:

$$\overline{\rho}\,\overline{U}_j \frac{\partial \varepsilon}{\partial x_j} = \frac{\partial}{\partial x_j}[(\mu_l + \frac{\mu_t}{\sigma_\varepsilon})\frac{\partial \varepsilon}{\partial x_j}] + c_1 f_1 \frac{\varepsilon}{k} G - c_2 f_2 \frac{\varepsilon^2}{k} + E_\varepsilon \tag{3.14}$$

where ν is the kinematic viscosity. In equation (3.14), the coefficient f_1 is a function that increases the magnitude of the destruction of the kinetic energy of turbulence (ε) near the wall. In Launder and Sharma model the value of f_1 is set to 1, and f_2 is a function that corrects the destruction term of ε in low turbulent Reynolds number flow.

3.2.3 Solidification Modeling

In modeling the DC casting mathematically both the fluid flow that occurs in the molten sump and the related heat transfer that occurs as a result of phase change and external cooling should be considered. In alloys having a freezing range instead of a single melting point, the latent heat release would be a function of the fraction solidified. The major barrier in analyzing phase change problems is the occurrence of an interface whose location is unknown priori, and across which the latent heat is to be released. Also, the phase boundary, continuity of velocity and temperature is required. At the phase boundary, a jump in the heat flux occurs, which is proportional to the latent heat.

There are two main approaches for modeling the solidification of pure metals and alloys, the multiple and single domain approaches. The multiple domain technique is based on dividing the whole domain into discrete regions according to their phases. The transport equations are then solved separately for each region. The conservation equations at the different regions are coupled through a proper interface boundary condition. This makes the technique too difficult to model. The complexity in the modeling using the multiple domain approach stems from the fact that the interface between various regions needs to be traced. Hence, the single domain approach is followed in the present simulation since it does not require the tracking of the unknown interface (solidification front). Among the various fixed domain techniques that take into account the release of latent heat are apparent or effective heat capacity method and enthalpy based method. In the current work, the enthalpy based method is implemented. The technique is characterized by decomposing the enthalpy into sensible and nodal latent heat in the energy equation:

$$H=h+\Delta H \tag{3.15}$$

where h is the sensible heat defined as:

$$\int_{h_{ref}}^{h} dh = \int_{T_{ref}}^{T} c_p dT \tag{3.16}$$

For constant c_p, and taking h_{ref}=0 at T_{ref}, the above equation can be integrated to obtain the sensible heat as:

$$h= c_p (T-T_{ref}) \tag{3.17}$$

In order to establish the region of phase change, the latent heat contribution is specified as a function of temperature, i.e. $\Delta H= f(T)$.

Since the energy equation is valid in the entire calculation domain including solid, liquid, and mushy regions, the nodal latent heat can be related to the liquid fraction. It becomes zero in the solid phase and equals the latent heat of fusion (ΔH_f) in the liquid

phase. In the mushy region, the latent heat can be any function of liquid fraction. In the current model, it is assumed to be linear.

$$\Delta H=\Delta H_f f_l \tag{3.18}$$

where f_l is the liquid fraction, which is related to temperature as:

$$f_l = \begin{cases} 1 & when \quad T \geq T_l, \\ \dfrac{T-T_s}{T_l-T_s} & when \quad T_l \geq T \geq T_s, \\ 0 & when \quad T \leq T_s. \end{cases} \tag{3.19}$$

where T_l and T_s are the liquidus and solidus temperatures, respectively.

The final form of the energy equation is obtained by substituting Equations (3.11) and (3.15) into the energy equation (3.4):

$$\frac{\partial(\rho\overline{u}_j\overline{H})}{\partial x_j} = \frac{\partial}{\partial x_j}\left[\left(\frac{\mu}{\Pr}+\frac{\mu_t}{\sigma_t}\right)\frac{\partial\overline{h}}{\partial x_j}\right] - \frac{\partial(\rho\overline{u}_j\overline{\Delta H})}{\partial x_j} \tag{3.20}$$

The last term in Equation (3.20) represents the latent heat exchange due to solid-liquid phase change resulting from the turbulent convective flow.

3.2.4 Modeling of Fluid Flow in the Mushy Region

In solidifying castings, mushy regions that develop are characterized by the coexistence of both liquid and solid. For a considerable fraction of the solidification period the intermingled liquid (i.e., the interdendritic liquid) can convect through the solid network (i.e., the dendritic solid). It is found that this type of convection is a major cause of macro segregation in cast products. The flow of fluids through porous media is not simple, especially because of the effect of the complex geometry of the solids on the flow. Therefore, most models rely on empirical measurements of a system parameter

known as permeability, or on measurements of friction factors. In the current model, the Darcy law for porous media is adopted to model the flow of liquid metal in the dendritic solid structure. The law is based on the empirical measurement of the permeability. Darcy's law for a porous media can be written as:

$$\overline{u}_i = -\frac{K'}{\mu}\left(\frac{\partial P}{\partial x_i} - \rho g_{xi}\right) \tag{3.21}$$

where K' is the permeability, which is a function of porosity, or in the case of a mushy region of a binary alloy, a function of liquid fraction. The permeability decreases with decreasing liquid fraction ultimately, forces all the velocities to zero in the case of a stationary solid. Incorporating the diffusive and convective momentum flux terms, one can write the modified Darcy equation in the following form:

$$\frac{\partial(\rho\overline{u}_i\overline{u}_j)}{\partial x_j} = \frac{\partial}{\partial x_j}\left[(\mu_l + \mu_t)\frac{\partial \overline{u}}{\partial x_j}\right] - S_{\overline{U}_i} - \frac{\mu}{K'}(\overline{u}_i - u_{i_s}) \tag{3.22}$$

where the coefficient $\frac{\mu}{K'}$ decreases from a large value in the solid phase to zero in the liquid phase. Consequently, the Darcy source term vanishes as the liquid fraction becomes one. The Carman-Koseny equation is adopted for the relation between the permeability and the liquid fraction.

$$\frac{\mu}{K'} = \frac{C(1-f_l)^2}{f_l^3 + q} \tag{3.23}$$

where q is a small positive number introduced to avoid division by zero in numerical calculations. C is a constant that depends on the morphology of the porous media. The value of C has been estimated from the expression given by Minakawa et al. [38] as:

$$C=180/d^2 \tag{3.24}$$

where d is assumed to be constant and is equal to the secondary dendrite arm spacing. The value of d is of the order of $1x\ 10^{-4}$ m. A large C value would force the velocity to be equal to the casting speed.

3.2.5 Boundary Conditions

In order to produce reliable results from simulations, one needs accurate input of boundary conditions and material data. One method to provide such data is to carry out experiments, e.g., thermocouple measurements, and to subsequently apply inverse modeling techniques to extract the desired information. In DC casting, inverse modeling has mostly been applied to find the boundary conditions for water cooling zones. Since the experimental work is not within the budget of the current project, the heat transfer coefficient distribution at the slab surface was taken from the literature [14].

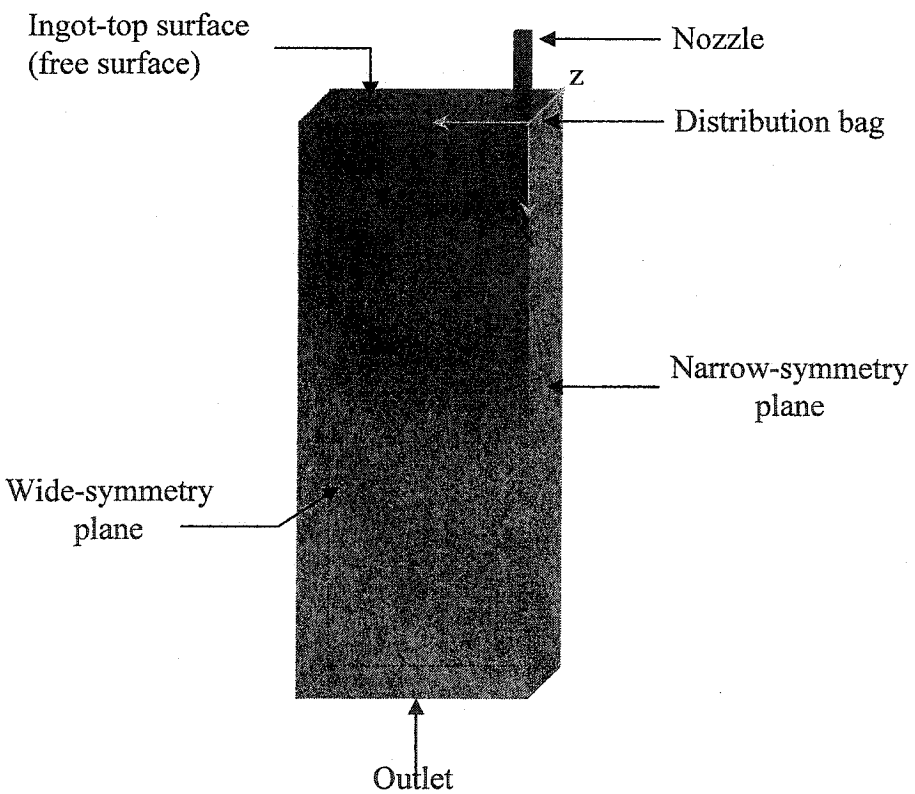

Figure 3.2: Calculation domain showing the boundary surfaces.

As mentioned earlier, only a quarter of the slab is taken as the calculation domain. The boundary conditions, referring to Figure 3.2, are given below:

Free surface

The normal gradient of all variables were set to zero but the velocity component normal to the surface was assumed to be zero.

$$\frac{\partial v}{\partial x} = \frac{\partial w}{\partial x} = \frac{\partial k}{\partial x} = \frac{\partial \varepsilon}{\partial x} = \frac{\partial h}{\partial x} = 0, \qquad u=0 \qquad (3.25)$$

Symmetry planes

At the x-y plane:
$$\frac{\partial u}{\partial z} = \frac{\partial v}{\partial z} = \frac{\partial k}{\partial z} = \frac{\partial \varepsilon}{\partial z} = \frac{\partial h}{\partial z} = 0, \qquad w=0 \qquad (3.26)$$

At the x-z plane:
$$\frac{\partial u}{\partial y} = \frac{\partial w}{\partial y} = \frac{\partial k}{\partial y} = \frac{\partial \varepsilon}{\partial y} = \frac{\partial h}{\partial y} = 0, \qquad v=0 \qquad (3.27)$$

It is to be noted that zero sensible heat gradients at the symmetry planes imply that these planes can be treated as adiabatic surfaces.

Outlet

At outlet, the fully developed boundary condition is imposed, i.e., all gradients normal to the outlet plane are specified to be zero, except for the velocity components parallel to the outlet-plane which are specified to be zero:

$$\frac{\partial u}{\partial x} = \frac{\partial k}{\partial x} = \frac{\partial \varepsilon}{\partial x} = \frac{\partial h}{\partial x} = 0 \qquad (3.28)$$

$$v = w = 0 \qquad (3.29)$$

Moving Walls

At the ingot surface, a no slip boundary condition ($u=0$) is applied in the liquid region, and an axially translating boundary with the casting speed ($u=u_{cs}$) is imposed on the solid and mushy regions, with the assumption that no liquid escapes the computational domain.

$$v = w = k = \varepsilon = 0 \tag{3.30}$$

The energy boundary condition at the slab surface is applied through the use of variable heat transfer coefficient. The governing equation for the heat transfer at the slab surface is given by:

$$\frac{\partial h}{\partial y} = \frac{\partial h}{\partial z} = -\frac{\gamma}{K}(h_s - h_a) \tag{3.31}$$

where γ is the average heat transfer coefficient between the solid surface and the surrounding. h_s represents the enthalpy at the surface and h_a represents the product of ambient temperature and the specific heat of the aluminum.

To account for the variation of heat transfer at the external surface of the slab, variable heat transfer coefficients are assigned to the mold, air gap, and secondary-cooling zones. The simulated casting assembly consists, unless specified otherwise, of a 120 mm adiabatic section followed by a 60 mm mold section. It is known that contraction of the ingot takes place as the ingot is about to emerge from the mold. This contraction allows air to fill in the formed gap between the ingot and the mold. The axial length of the air gap ranges from 10 to 20 mm. To account for the formation of the air-gap, a heat transfer for the gap is assumed. The change of the heat transfer coefficient along the slab outside surface at the secondary cooling region is based on measurements made on DC cast billets [13], where the heat transfer coefficients was observed to exhibit a sharp nearly linear increase in the impinging jet region, and achieved a maximum value within

an axial length of 5 to 10 mm. A subsequent decrease occurred over axial lengths of approximately 30 to 60 mm. An almost uniform value of the heat transfer coefficient was preserved along the remaining length of the slab. Accordingly, the heat transfer coefficient is presumed to increase linearly in the impinging jet region to some maximum value, h_{max}, and then decreases linearly to some uniform value, h_{film}. Generally, unless mentioned otherwise, the heat transfer coefficient is distributed on the slab surface according to the following:

Adiabatic section:	$h(x) = 0.$ kW / m^2 K	$0 \le x < 120$ mm.
Mold region:	$h(x) = 1.5$ kW / m^2 K	$120 \le x < 180$ mm.
Air gap:	$h(x) = 0.15$ kW / m^2 K	$180 \le x < 190$ mm.
Spray zone:	$h(x) = h_{gap} + (x - x_1) / (x_2 - x_1)$ kW / m^2 K	$190 \le x < 200$ mm.
	$h(x) = h_{max} + (x - x_2) / (x_3 - x_2)$ kW / m^2 K	$200 \le x < 240$ mm.
	$h(x) = h_{film}$ kW / m^2 K	$x \ge 240$ mm

where $h_{gap} = 0.15$ kW / m^2 K, $h_{film} = 10.0$ kW / m^2 K, and $h_{max} = 20.0$ kW / m^2 K, $x_1 = 180$ mm, $x_2 = 190$ mm , $x_3 = 230$ mm.

3.2.6 Non-Dimensionalization of the Governing Equations

It is a good practice to non-dimensionalize the governing equations for the sake of generality of the results. The governing partial differential equations are made non-dimensional using the following dimensionless parameters:

$$X = \frac{x}{D},\ Y = \frac{y}{D},\ Z = \frac{z}{D},\ U = \frac{u}{u_{in}},\ V = \frac{v}{u_{in}},\ W = \frac{w}{u_{in}},$$

$$P^* = \frac{P}{\rho_o u_{in}^2},\ k^* = \frac{k}{u_{in}^2},\ \varepsilon^* = \frac{\varepsilon D}{u_{in}^3},\ h^* = \frac{h}{\Delta H_f},\ \Delta H^* = \frac{\Delta H}{\Delta H_f},\ \mu_t^* = \frac{\mu_t}{\mu} \qquad (3.32)$$

where D is the hydraulic diameter of the nozzle, u_{in} is the nozzle's inlet velocity and ΔH_f is the latent heat of fusion. Fortunately, all the conservation equations presented above can be expressed in a general non-dimensional partial differential equation. The Cartesian-tensor form of this equation is:

$$\frac{\partial(\rho U_i \Phi^*)}{\partial X_i} = \frac{\partial}{\partial X_i}(\Gamma_\Phi^* \frac{\partial \Phi^*}{\partial X_i}) + S_\Phi^* \qquad i=1,2,3 \tag{3.33}$$

where, Φ^*, Γ_Φ, and S_Φ are the general dependent variable, the generalized diffusion term, and the source term, respectively. The values of Φ^*, and the associated definition of Γ_Φ^* and S_Φ^*, for all of the transport equations discussed earlier, are listed in Table (3.1). Casting the governing equations in a general form simplifies the development of a general-purpose program for the solution of all the equations. The non-dimensional form of the boundary conditions becomes:

Nozzle inlet

$$U=1, \quad V=W=0, \qquad h^*=h_{in}^*, \qquad k^*=0.01, \quad \varepsilon = c_\mu (0.01)^{3/2}/0.05 \tag{3.34}$$

Free surface

$$\frac{\partial V}{\partial X} = \frac{\partial W}{\partial X} = \frac{\partial k^*}{\partial X} = \frac{\partial \varepsilon^*}{\partial X} = \frac{\partial h^*}{\partial X} = 0 \ , \quad u=0 \tag{3.35}$$

Symmetry planes

at the X-Y plane: $$\frac{\partial U}{\partial Z} = \frac{\partial V}{\partial Z} = \frac{\partial k^*}{\partial Z} = \frac{\partial \varepsilon^*}{\partial Z} = \frac{\partial h^*}{\partial Z} = 0, \quad W=0 \tag{3.36}$$

at the X-Z plane: $$\frac{\partial U}{\partial Y}=\frac{\partial W}{\partial Y}=\frac{\partial k^*}{\partial Y}=\frac{\partial \varepsilon^*}{\partial Y}=\frac{\partial h^*}{\partial Y}=0, \quad V=0 \tag{3.37}$$

Outlet

$$\frac{\partial U}{\partial X}=\frac{\partial k^*}{\partial X}=\frac{\partial \varepsilon^*}{\partial X}=\frac{\partial h^*}{\partial X}=0 \tag{3.38}$$

$$V=W=0 \tag{3.39}$$

Moving walls

$$U=U_s=u_s/u_{in}, \quad V=W=k^*=\varepsilon^*=0, \quad \frac{\partial h^*}{\partial Y}=\frac{\partial h^*}{\partial Z}=-\frac{\gamma D}{K}(h_s^*-h_a^*) \tag{3.40}$$

Table 3.1: Summary of the Non-Dimensional Governing Equations.

Equation	Φ^*	Γ^*_Φ	S^*_Φ
Continuity	1	0	0
U-momentum	U	$\frac{1}{\mathrm{Re}}(1+\mu_t^*)$	$-\frac{\partial P^*}{\partial X}+\frac{\partial}{\partial X_i}\left(\Gamma^*_\Phi\frac{\partial U_i}{\partial X}\right)-\frac{A^*}{\mathrm{Re}}(U-U_S)$
V-momentum	V	$\frac{1}{\mathrm{Re}}(1+\mu_t^*)$	$-\frac{\partial P^*}{\partial Y}+\frac{\partial}{\partial X_i}\left(\Gamma^*_\Phi\frac{\partial U_i}{\partial Y}\right)-\frac{A^*}{\mathrm{Re}}(V-V_S)$
W-momentum	W	$\frac{1}{\mathrm{Re}}(1+\mu_t^*)$	$-\frac{\partial P^*}{\partial Z}+\frac{\partial}{\partial X_i}\left(\Gamma^*_\Phi\frac{\partial U_i}{\partial Z}\right)-\frac{A^*}{\mathrm{Re}}(W-W_S)$
Kinetic Energy	k^*	$\frac{1}{\mathrm{Re}}(1+\frac{\mu_t^*}{\sigma_k})$	$\frac{G^*}{\mathrm{Re}}-\varepsilon-\frac{D_k}{\mathrm{Re}}$
Rate of energy dissipation	ϵ^*	$\frac{1}{\mathrm{Re}}(1+\frac{\mu_t^*}{\sigma_\varepsilon})$	$\frac{1}{\mathrm{Re}}f_1C_1G^*\frac{\varepsilon}{k}C_2f_2\frac{\varepsilon^2}{k}+\frac{E^*\varepsilon}{\mathrm{Re}^2}$
Energy	h^*	$\frac{1}{\mathrm{Re}}(\frac{1}{\mathrm{Pr}}+\frac{\mu_t^*}{\sigma_t})$	$-\left(\frac{\partial U\Delta H}{\partial X}+\frac{\partial V\Delta H}{\partial Y}+\frac{\partial W\Delta H}{\partial Z}\right)$

where:

$$\mathrm{Re}=\frac{\rho u_{in}D}{\mu}$$

$$G^*=\mu_t^*\left(\frac{\partial U_i}{\partial X_j}+\frac{\partial U_j}{\partial X_i}\right)\frac{\partial U_i}{\partial X_j},\qquad D_k^*=2\frac{\partial\sqrt{k^*}}{\partial X_i}\frac{\partial\sqrt{k^*}}{\partial X_i},$$

$$E_\varepsilon^*=2\mu_t^*\left(\frac{\partial^2U_i}{\partial X_j\partial X_k}\right)_t\left(\frac{\partial^2U_i}{\partial X_j\partial X_k}\right),\qquad f_\mu^*=e^{\frac{-3.4}{(1+\mathrm{Re}_t^*/50)^2}},\qquad \mathrm{Re}_t=\mathrm{Re}\frac{k^{*2}}{\varepsilon^*},$$

$$\mu_t^*=\mathrm{Re}\,C_\mu f_\mu^*\frac{k^{*2}}{\varepsilon^*},\qquad f_1=1,\ f_2=1-0.3e^{-\mathrm{Re}_t^2},\qquad A^*=\frac{C^*(1-f_l)^2}{f_l^3+q},$$

$C_\mu=0.09,\ C_1=1.44,\ C_2=1.92,\ \sigma_k=1.0,\ \sigma_\varepsilon=1.3,\ \sigma_t=0.9,\ q=1\times10^{-30}$

3.3 Numerical Approach

Having derived the governing equations, a numerical solution of these equations is sought. In order for this to be achieved, the equations have to be set in an algebraic form, this is called discretization. The discretized equations are derived by integration of the partial differential equations over each control volume of the calculation domain (control volume method). Power-law scheme of Patankar [49] was used to discretize the convection-diffusion terms. A detailed description of the discretization procedure can also be found in Versteeg and Malalasekera [50]. A suitable solution procedure or algorithm for the algebraic equations has to be set. The following section is devoted to explaining the solution procedure.

3.3.1 Solution Procedure and Convergence Criteria

Each of the above derived-discretized equations is cast in the following form:

$$a_p\phi_p = a_E\phi_E + a_W\phi_W + a_N\phi_N + a_S\phi_S + a_T\phi_T + a_B\phi_B + b_\phi \tag{3.41}$$

where a_E, a_W, a_N, a_S, a_T, and a_B are the coefficients of the six neighboring nodes of node P shown in a two-dimensional grid in Figure 3.3. b_Φ is the source term. The coefficients entail the diffusion and convection terms while the source term may involve various terms such as pressure gradient, buoyancy force, and Darcy terms. The developed computer program is an in-house code based on control volume and power-law scheme for the discretization of the diffusion-convection terms. Having established the general discretization equation, a suitable solution procedure (algorithm) is subsequently required. In this study the SIMPLE algorithm, which stands for Semi-Implicit Method for Pressure-Linked Equations, has been employed for the solution of the governing equations. The flowchart for the algorithm is shown in Figure 3.4. The algorithm is described in many articles such those by Patankar and Spalding [46], and Caretto et al. [47], and Patankar [48].

The discretized equations were solved iteratively using an implicit relaxation technique and employing the well known line-by-line Tri-Diagonal Matrix Algorithm

(TDMA) solver until a converged solution was obtained. For convergence to be established, the sum of the residuals for each calculated variable (R_Φ) was less than 0.01.

$$R_\Phi = \sum_{all\ nodes} \left| a_p \Phi_p - \sum_{nb} a_{nb} \Phi_{nb} - b \right| \tag{3.42}$$

Numerical tests were performed on the computer program for each simulated DC caster, the small and large aspect ratio casters, to ensure that the solutions were grid-independent. The axial velocity profiles at the wide symmetry plane at x = 40 mm from the slab free surface for different number of grids were compared. In both the small and large aspect ratio casters, the difference in the values of the axial velocity distribution was less than 5%. Considering the insignificant difference in the results of the velocity distribution and the computational cost, the least number of grids which satisfied the grid independency criterion were used in the calculations. In the case of the DC caster using the combo bag distribution system (the small aspect ratio caster), the grid size used in the calculation was (52x50x24), and for the caster using the channel bag distribution system (the large aspect ratio caster), the grid size was (60x42x24). It is to be noted that in modeling DC casting of aluminum alloys, care has to be taken in distributing the grids, especially in the axial direction, in order to capture the solidification front which is usually located within 400 to 800 mm from the slab free surface. This situation is unlike the situation in the modeling of continuous steel slab casters, where the metallurgical length (solidification front at the slab center) could reach to 30 m from the slab free surface. In continuous steel slab casters, the calculation domain can not be made to cover the solidification front. In the current developed mathematical model, the grids are distributed non-uniformly with more grids at the regions of high gradients and near the expected location of the solidification front. Figure 3.5 shows a typical non-uniform distribution of the grids in the calculation domain. The following chapter will be devoted to the discussion of the code-verification and buoyancy effect.

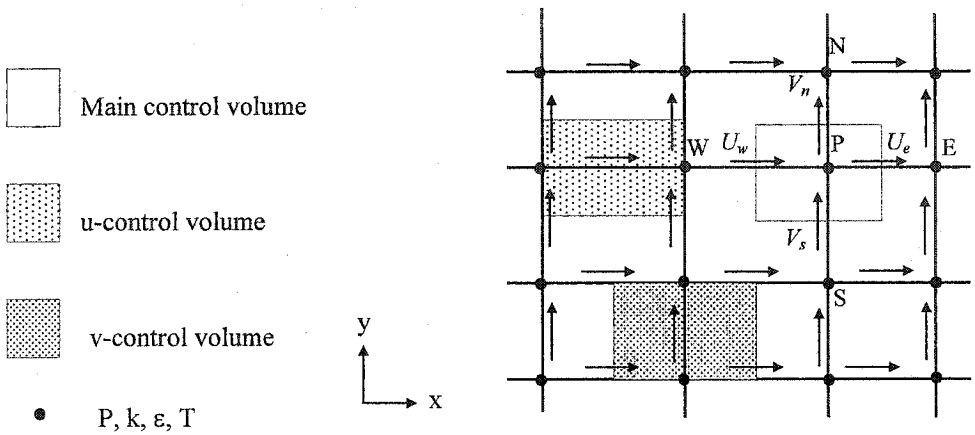

Figure 3.3: Staggered grid

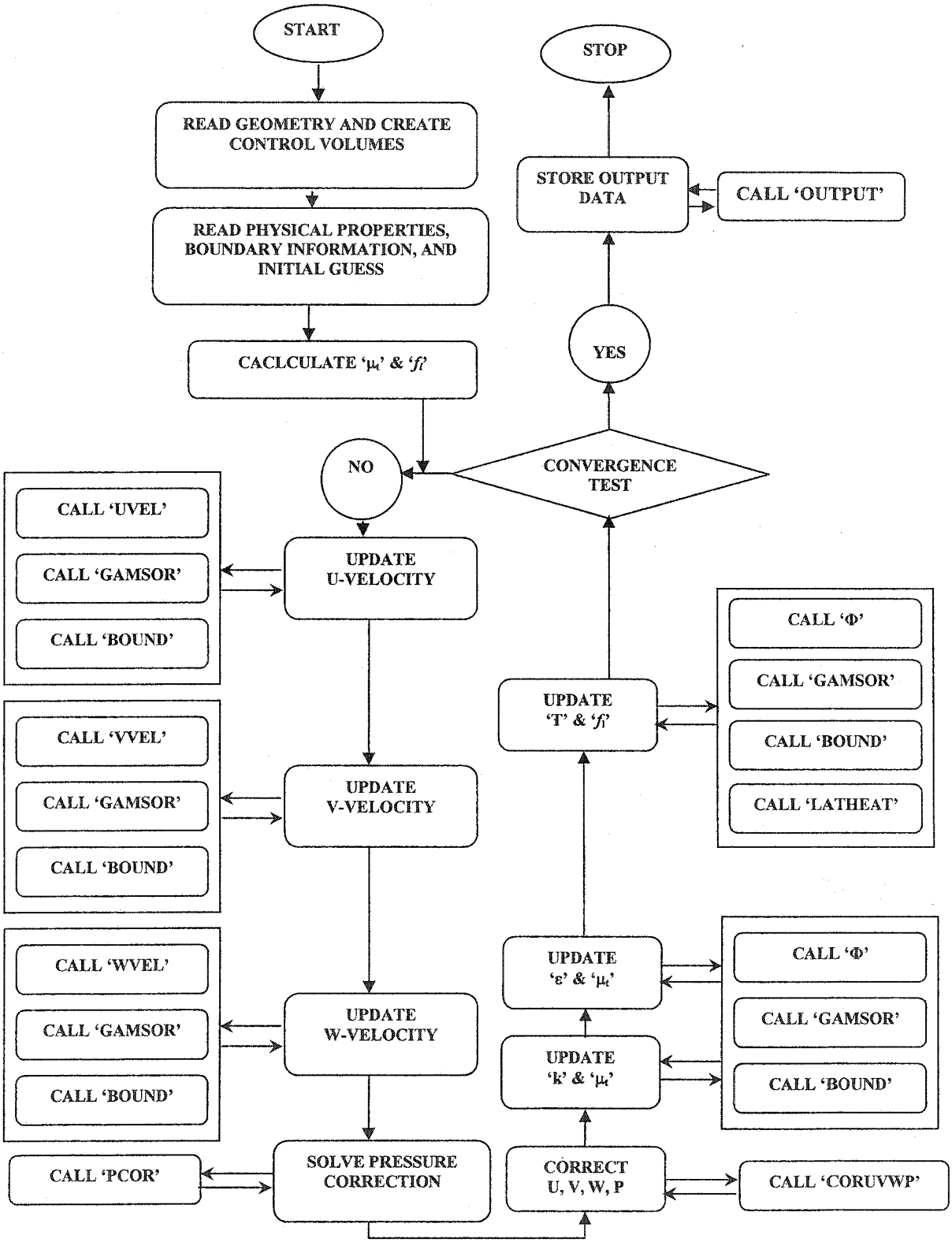

Figure 3.4: Flow chart of the 3-D turbulent fluid flow and solidification code.

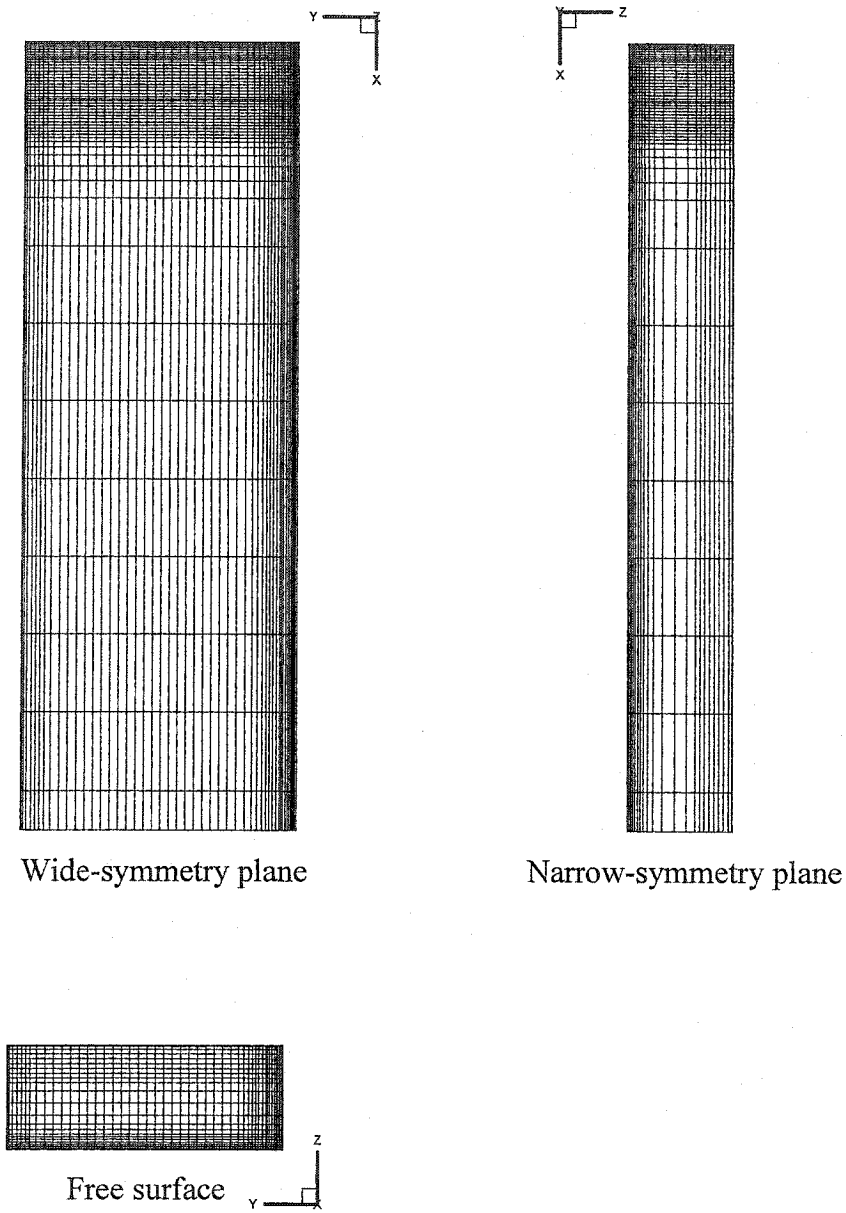

Figure 3.5: A typical non-uniform grids distribution in the calculation domain.

CHAPTER
FOUR

Model Verification and Buoyancy Effect Study

4.1 Introduction

In order for any computer code to be ready for use in any specific and/or general task, the code has to be verified, at least qualitatively. However, a quantitative verification is required for the code to be commercialized as a tool so that it can be used to analyze a specific type of problem, or can be used as a general purpose commercial code. In real metal casting, the opacity of the melt and the high temperatures involved make it difficult to measure, or even observe, the flow patterns resulting from different metal delivery devices. Consequently, mathematical and physical modeling has been extensively used to determine the flows in casters. While mathematical models have been widely accepted, their performance has frequently been judged by their ability to predict flows measured in physical water models. Therefore, water models have been always regarded, in the literature, as standards against which mathematical models are tested. However, no heat transfer and solidification results could be verified by using water models.

A complete verification of a DC casting model requires a comprehensive validation of its fluid flow and thermal results. The most effective way by which these verifications can be done is by comparing the thermal field results of mathematical models with the thermal field results of real casting experiments, and comparing the flow field results of mathematical models with the flow field results obtained from physical water models. The current developed mathematical model has been verified both qualitatively and quantitatively by comparing with the experimental results of Jones et al. [20]. The latter author carried out two kinds of studies. The first study was performed

using a physical water model in which the particle imaging velocimetry (PIV) was used to measure the flow field at specified planes. The PIV results are used for the qualitative comparison with the results of the current developed mathematical model. The second study, a real casting experiment, was carried out using aluminum Al-3104 alloy cast using a production size caster. The intended goal of the second study was to investigate the effect of distribution bag dimensions on the sump depth. Therefore, two different sizes of combo bags were used. Thermal results of the latter experiments are used for the quantitative verification of the current developed mathematical model.

As mentioned earlier, measuring flow field in a real casting experiment is quite a difficult task. Therefore, it is difficult to verify molten metal flow field results obtained from mathematical models with the flow field results of a real casting experiment. Only the thermal results of the mathematical model could be verified using the results of a real caster. To the best of the author's knowledge, the current mathematical model is the first 3D coupled turbulent fluid flow and solidification study simulating the DC casting of ingots and incorporating the buoyancy effect that has been quantitatively verified by comparing its results with the results obtained from a real caster. The quantitative verification is done by comparing the sump profile measured in the real casting experiment of Jones et al. [20] with the results of the current mathematical model.

A commercial graphics software package named TECPLOT (version 7) was used for post processing of the obtained results. It is to be noted that in this software the length of a 3-D vector was measured tangentially to the plane of the paper. Therefore, the reference vector would not give the exact magnitude of the velocity field, since to measure the exact magnitude of the velocity vector, the vector orientation must be taken into account. The vector orientation can not be presented on a 2D paper. However, the latest version of TECPLOT allows the determination of the exact magnitude of velocity directly from the monitor screen. In terms of analyzing the various flow mechanisms that occur in the flow field of a DC caster, this is one of the best ways to present a 3-D vector plot.

4.2 Modeling Buoyancy

Natural convection effects are incorporated into the model verification part of the current study through the use of Boussinesq approximation. In the approximation, the density is assumed to be constant in all terms except the buoyancy term, which is given by:

$$\rho = \rho_{\infty}[1-\beta\,(T-T_{\infty})] \tag{4.1}$$

where β is the thermal volumetric expansion coefficient defined as:

$$\beta = -\frac{1}{\rho}\left(\frac{\partial \rho}{\partial T}\right)_{P} \tag{4.2}$$

For the sake of simplicity, the x-momentum equation is written in the following short form as:

$$\rho_{\infty}(u\frac{\partial u}{\partial x}+v\frac{\partial u}{\partial y}+.....) = -\frac{\partial p}{\partial x}+\rho g+\mu\frac{\partial^2 u}{\partial x^2}+..... \tag{4.3}$$

where the second term on the R.H.S. represents the body force term. The flow of the molten aluminum is gravity driven. Note that the vertical coordinate in the calculation domain is the x-axis, which is increasing in the direction of the action of gravity (downward), therefore the pressure gradient can be written in the following form:

$$\frac{\partial p}{\partial x} = \rho_{\infty}\, g \tag{4.4}$$

From Equation (4.4) substitute in Equation (4.3)

$$\rho_{\infty}(u\frac{\partial u}{\partial x}+v\frac{\partial u}{\partial y}+.....) = g(\rho-\rho_{\infty})+\mu\frac{\partial^2 u}{\partial x^2}+..... \tag{4.5}$$

If Equation (4.1) is substituted into Equation (4.5) and after simplification one gets:

$$\rho_{\infty}(u\frac{\partial u}{\partial x}+v\frac{\partial u}{\partial y}+.....) = -\rho_{\infty} g\,\beta(T-T_{\infty})+\mu\frac{\partial^2 u}{\partial x^2}+..... \tag{4.6}$$

The above equation can be written in a non-dimensional form using the non-dimensional parameters used in the previous chapter, Equation (3.32), noting that $T=\frac{h}{c_p}$, the following equation can be obtained:

$$U\frac{\partial U}{\partial X}+V\frac{\partial U}{\partial Y}+.....=-\frac{\Delta H_f\, g\,\beta\, D}{c_p\, u_{in}^2}(h^*-h_\infty^*)+\frac{\mu}{\rho_\infty\, D u_{in}}(\frac{\partial^2 U}{\partial X^2}+..... \tag{4.7}$$

Multiplying and dividing the first coefficient on the R.H.S. by $D^2.\nu^2$ and rearranging, the above equation can be written in the following form:

$$U\frac{\partial U}{\partial X}+V\frac{\partial U}{\partial Y}+.....=-\frac{Gr}{\mathrm{Re}^2}(h^*-h_\infty^*)+\frac{1}{\mathrm{Re}}(\frac{\partial^2 U}{\partial X^2}+..... \tag{4.8}$$

where Gr is the Grasshof number, which is the ratio of buoyancy forces to viscous forces,

$$Gr=\frac{g\,\beta\,\Delta H_f\, D^3}{c_p\,\nu^2} \tag{4.9}$$

Re is the Reynolds number given by: $\mathrm{Re}=\frac{u_{in}\, D}{\nu}$.

The first term on the R.H.S. of Equation (4.8) represents the buoyancy term. The term is implemented in the model as a linear source term (S) in the x-momentum equation. This source term can be written in the following form:

$$S = S_c + S_p\, \Phi_p \tag{4.10}$$

where S_c stands for the constant part of the source (S), while S_p is the coefficient of Φ_p (the dependent variable). Since in this case, the source term is not a function of the dependent variable (u), therefore it can be linearized in the following way:

$$S_c=\frac{Gr}{\mathrm{Re}^2}(h_\infty^*-h^*), \tag{4.11}$$

and $$S_p = 0.$$

It is to be noted that h^* *and* h_∞^* represent the non-dimensional temperatures of each scalar cell in the calculation domain (variable) and the liquidus temperature, respectively. The buoyancy term in the discretized form can give rise to serious instabilities in the solution processes [50]. Severe under-relaxation is often required in buoyancy related problems. In the actual runs of the current mathematical model with the buoyancy term included, a transient approach was followed for obtaining the steady state solution.

4.3 Problem Definition

The developed computer program has been run with and without the buoyancy term in order to simulate the DC casting of aluminum 3104 alloy under steady state condition. The main purpose of the current runs is to quantitatively verify the current developed mathematical model so that the computer program can confidently be used in systematic parametric studies; which will be carried out in the following chapters. The simulated geometrical dimensions and alloy physical properties used in the model are the same as those used by Jones et al. [20] in his real casting experiment.

Figure 4.1 shows a schematic of the DC caster with the calculation domain illustrated as a shadowed block. It should be noted that the current simulated mold is similar in design to the Alcan Sheet Mold (ASM). The latter mold is a newly developed mold system which came into operation fairly recently after the introduction of the low metal level casting and electromagnetic casting (EMC) [23-24]. The ASM technique is characterized by giving the good surface quality of the EMC and preventing the drawbacks of the low metal level casting which is explained earlier in the literature survey. The ASM is based on the optimization of the effective mold length. The geometrical dimensions and physical properties of aluminum 3104 are listed in Table 4.1. Figure 4.2 shows a schematic of the combo bag used in distributing the molten metal in the mold. The height, length and width (h,l,w) of the bag are listed in Table 4.1. Table 4.2 shows the boundary conditions used in the calculations. In the current developed mathematical model, the heat transfer coefficient at the outside surface of the ingot is axially changing to simulate the different stages of cooling rates the ingot goes through in its descend. In a real casting situation, the surface heat transfer coefficient is not only axially changing but also changing in the transverse direction. Due to the scarcity of experimentally measured heat transfer coefficient in the transverse directions, only the axial change of the coefficient is considered. The functions, by which the heat transfer coefficient is distributed along the ingot-outside surface, are based on the experimental measurements of Weckmann and Niessen [39] and Tarapore [5]. These experimental measurements show a general behavior of heat transfer coefficient distribution along the outside surface in the secondary cooling region. Generally, the heat transfer coefficient is

observed to exhibit a sharp, nearly linear increase in the impinging jet region. A maximum in the heat transfer coefficient (h_{max}) is attained within an axial length of 5 to 10 mm from the impinging jet region of the secondary coolant. A subsequent decrease in the coefficient is detected over an axial length of 30 to 60 mm where the heat transfer coefficient reaches a minimum value. A nearly uniform heat transfer coefficient is maintained along the remaining length of the slab surface (h_{film}), which corresponds to film boiling condition.

Table 4.1: Thermophysical properties of aluminum Al-3103 and geometrical parameters used for the quantitative verification of the code.

Variable	Value
Thermal conductivity	170 w / m K
Specific heat (liquid or solid)	0.88 kJ/kg K
Latent heat of fusion	396.4 kJ/kg
Liquidus temperature	655.0 °C
Solidus temperature	630.0 °C
Viscosity	16.2 x 10-4 kg/m s
Density	2720 kg/m3
liquid thermal expansion coefficient	1.020D-04 1/K
Slab width (y-axis)	1.32 m
Slab thickness (z-axis)	0.66 m
Ingot length simulated (x-axis)	2.5 m
Nozzle port width	30.0 mm
Nozzle submergence length	20.0 mm
Mold length	70.0 mm
Air gap length	10 mm
Combo bag dimensions (h x l x w)[2]	50 x 330 x 152 mm

[2] Refer to Figure 4.2 for the combo bag dimensions.

Table 4.2: Boundary conditions for quantitative verification.

Regions		Dependent variables					
		u	V	w	h	k	ε
Nozzle exit		u_{in}	0	0	h_{in}	$-0.01 \times u^2_{in}$	$c_\mu k_{in}^{3/2} / 0.05\,D$
Free surface		0	$\frac{\partial v}{\partial x} = 0$	$\frac{\partial w}{\partial x} =$	$\frac{\partial h}{\partial x} = 0$	$\frac{\partial k}{\partial x} = 0$	$\frac{\partial \varepsilon}{\partial x} = 0$
Symmetry planes	Narrow	$\frac{\partial u}{\partial y} = 0$	0	$\frac{\partial w}{\partial y} =$	$\frac{\partial h}{\partial y} = 0$	$\frac{\partial k}{\partial y} = 0$	$\frac{\partial \varepsilon}{\partial y} = 0$
	Wide	$\frac{\partial u}{\partial y} = 0$	$\frac{\partial v}{\partial x} = 0$	0	$\frac{\partial h}{\partial x} = 0$	$\frac{\partial k}{\partial x} = 0$	$\frac{\partial \varepsilon}{\partial x} = 0$
Outlet		$\frac{\partial u}{\partial x} = 0$	0	0	$\frac{\partial h}{\partial x} = 0$	$\frac{\partial k}{\partial x} = 0$	$\frac{\partial \varepsilon}{\partial x} = 0$
Ingot outside surface	Melt in contact with mold	0	0	0	h (x)	0	0
	solidified	u_{cs}	0	0	h (x)	0	0

Adiabatic section:		h (x) = 0. kW / m^2 K	0 ≤ x < 75 mm.
Mold region	:	h (x) = 1.5 kW / m^2 K	75 ≤ x < 145 mm.
Air gap	:	h (x) = 0.15 kW / m^2 K	145 ≤ x < 155 mm.
Spray zone	:	$h(x) = h_{gap} + (x - x_1) / (x_2 - x_1)$ kW / m^2 K	155 ≤ x < 175 mm.
		$h(x) = h_{max} + (x - x_2) / (x_3 - x_2)$ kW / m^2 K	175 ≤ x < 215 mm.
		$h(x) = h_{film}$ kW / m^2 K	x ≥ 215 mm.

where $h_{gap} = 0.15$ kW / m^2 K

$h_{film} = 10.0$ kW / m^2 K

$h_{max} = 20.0$ kW / m^2 K

$x_1 = 155$ mm, $x_2 = 175$ mm, $x_3 = 215$ mm.

In the qualitative verification part, a comparison is carried out of a similar but not the same geometrical domain as the one used by Xu et al [18]. in their physical water model. The purpose of the comparison with the physical water model is merely done to show qualitatively the similarity between the vector fields obtained from the current developed model with that of the physical water model, keeping in mind that the main purpose of this work is to mathematically simulate the real casting process not the physical water model. For the verification of the flow field results of the current mathematical model, a physical water model has to be built using the same dimensions of the caster and the same mathematically predicted solidification-front profile. The latter is out of the budget of the current project.

4.4 Mathematical Model Results and Discussion

In this section, a detailed presentation of the results of the developed mathematical model is done through a discussion of the results obtained without incorporating the buoyancy effect. A discussion of the results with the buoyancy term included is followed. In the last part of this section, the results, with and without the buoyancy effect, will be compared to the results of the real casting experiment of Jones et al. [20]. A brief description of the setup used in the real casting experiment, as well as, the procedure followed to measure the solidification front is given at the end of the section.

4.4.1 Model Results Without Thermal Buoyancy Force Effect

Figure 4.3 (a-c) shows a 3D-surface plots for the calculated temperature contours, vector field and streamlines, respectively. The figure presents the calculation domain, which consists of the two symmetric planes, wide and narrow planes, and the slab's top free surface. These results are for the case where the buoyancy term is not included in the model. The casting speed is 50.8 mm/min, and the superheat is 65 °C. The vector-surface plot and the streamline in Figure 4.3 are magnified to clearly show the nature of the flow field, and only the section which contains the liquid sump is shown. Figure 4.3 (b) shows two issuing streams out of the distribution bag. These two streams are issuing from the

bottom and side windows of the combo bag. The melt flow out of the side window is acting as a diffuse jet with most of the momentum directed in the horizontal direction toward the narrow side of the mold. Once the flow hits the upper part of the narrow side of the mold, it splits into two streams. These two streams form two recirculations. One recirculation is vertical and can be seen at the wide symmetry plane of Figure 4.3 (c). The other is a horizontal recirculation which can be seen at the slab top free surface in the same figure. The outer stream of the horizontal recirculation moves along the inside wall of the mold. Once this stream reaches to the narrow symmetry plane of the slab, and due to the symmetry boundary condition of no flow across the symmetry plane, the flow moves parallel to the narrow symmetry plane towards the impervious wall of the distribution bag. As soon as the flow reaches the impermeable wall of the bag, it splits into two other streams, one flows horizontally along the side wall of the distribution bag towards the narrow side of the slab, the other stream goes under the bag forming what is called, henceforth, an angle flow. The angle flow can be seen at the narrow symmetry plane of Figure 4.3 (b,c). Upon reaching the wide symmetry plane, the angle flow splits into two streams, one stream is entrained by the vertical recirculation at the wide symmetry plane as shown in Figure 4.4 (a). The other stream is seen to flow obliquely towards the solidification front.

The vertical recirculation at the wide symmetry plane rotates in a counter clockwise direction as shown if Figure 4.4 (a). The same figure shows the issuing melt flow from the bottom window of the distribution bag. This flow acts as a moderator to the momentum of the melt issuing from the side window by directing a part of the melt towards the inclined region of the solidification front. The extension of the vertical recirculation at the wide symmetry plane to reach to the slab center is a function of the weakness and/or strength of the earlier mentioned angle flow in such a way, that if the downward momentum of the angle flow is stronger than the upward component of the vertical recirculation at the wide symmetry plane, then the angle flow seems to push the recirculation at the wide symmetry plane away from the slab center and towards the narrow side of the ingot. This can clearly be seen in Figure 4.4 (a).

The interaction between the angle flow, resulting from the horizontal recirculation of the melt at the upper region of the mold, and the upward component of the vertical recirculation at the wide symmetry plane around the slab center plays a vital rule in controlling the mushy layer thickness especially at center region of the slab as will be explained later. Figure 4.4 (b) presents the liquidus and solidus temperature contours at the wide symmetry plane. A widening of the mushy region from the liquidus-contour side can be seen at around 300 mm in the y-direction. This extension of the mushy region can be attributed to the upward vector component created by the separation of the vertical recirculation from the solidification front at 300 mm in the y-direction. A low pressure region (wake) is created at that point of separation. The wake region has less effect on the positioning of the solidification contour line. The ability of the current mathematical model to predict in a precise way the position of such a wake region renders the model its recognition as an effective and efficient tool in the design of vertical DC casters.

Figure 4.4 (c) shows the onset of a vortex near the slab free surface at a section parallel to the wide symmetry plane at 150 mm in the z-axis. The vortex is located at y = 200 mm and is spinning in a clockwise direction. The outer-upward component of the vertical recirculation (the left vortex) is entrained by the mentioned new vortex. The entrainment can be attributed to the weakness of the former vertical vortex as it approaches the top left corner of the slab. The continuing weakness of the left vortex is attributed to its constant friction with both the solidification front and the slab shell extending from the narrow side of the ingot. On the contrary, the new vortex is gaining extra momentum as it is developing in a region far from both the solidification front and the outer solidified part of the ingot. The mushy layer at the point of contact of the two upward-vertical components of the mentioned vortices is extending toward the slab free surface as shown in Figure 4.4 (d). Figure 4.4 (e) (z=156 mm) shows how the new mentioned vortex is developing, while the old vortex is weakening. Figure 4.4 (f) shows the corresponding mushy region (z=156 mm.), the effect of the two vortices on the mushy region is continuing to be the same as explained before.

In the absence of a distribution system, there is an inherent tendency for the solidified layer at the corner to be thicker due to the convexity of the corners, and to a

lesser extent at the narrow faces [17]. This can be attributed to the fact that the narrow faces are more distant from the inflow of superheated metal issuing from the nozzle than the wide faces. This tendency is mitigated if the inflowing metal is directed by the bag toward the slab-narrow faces. Figure 4.5 shows the vector/streamline and temperature contours for planes including the slab free surface and parallel to it. Figure 4.5 (a) shows the ingot free surface (x = 0) in which the issuing molten aluminum out of the side window of the distribution bag is directed towards the narrow side of the mold. Since it is assumed that the bag-top surface is blocked, therefore the velocity on the top surface of the bag, the blank rectangle at the corner (y,z) = (0,0), is zero. The corresponding plane for the temperature contours, Figure 4.5 (b), is showing the effect of mixing of the molten aluminum in the adiabatic section of the mold. The temperature is decreasing as the melt passes from the wide-symmetry line and goes along the inside surfaces (narrow and wide) of the mold, yet all of the temperature contours are above the liquidus temperature. The decrease in temperature is attributed mainly to the axial transportation of heat.

Figure 4.5 (c) presents a cross-section at the start of the primary cooling region (x = 85 mm), exactly 10 mm under the start of the mold active section. Figure 4.5 (d) shows that the solidified layer (temperature contour 903 K) on the slab rolling face develops earlier than it does on the narrow side of the slab. This is attributed to the strong momentum by which the hot melt is delivered to the narrow side of the slab. Figure 4.5 (e,f) depicts a cross-section taken near the end of the mold at x = 135. At this axial distance, the average solidified-layer thickness along the slab rolling face is 80 mm, whereas, the average thickness along the narrow side of the slab, the side far from the nozzle, is 35 mm, having a difference of 45 mm between the two layer thicknesses. The difference in the solidified-layer thicknesses on the two sides of the ingot is decreasing as the ingot approaches the end of the mold. This difference can be reduced further by either controlling the primary cooling heat transfer coefficient through the control of coolant flow rate, or by changing the distribution-bag and its window's dimensions, especially the side windows, so that the melt can be delivered to the narrow side of the mold with less momentum. Minimizing the difference between the solidified-layer thicknesses at the narrow and rolling faces of the slab is of vital importance for the consistency and quality

of the slab surface. The latter objective can be handled efficiently by the current developed mathematical model through changing the primary cooling rate and/or identifying the proper design for the inlet melt distribution system.

Figure 4.5 (g,h) shows a slab section that lies in the air-gap region. By looking at the isotherms near the ingot narrow surface, especially the isotherms 903 and 810 K, it can be seen that the isotherms are closely spaced compared with the upper or lower sections of the ingot. This is an indication that the temperature gradient near the slab surface is high due to the accumulation of heat. The later is a direct consequence of the low heat transfer coefficient of the air. Figure 4.5 (d,f,h,j,l) shows the extension of the mushy layer towards the molten core in all the sections positioned in the solidification region. The mushy region extension is taking place at the point of separation of melt recirculation from the solidified shell, as was seen earlier in the discussion of the results of the mushy region at the wide symmetry plane.

Figure 4.6 depicts the vectors/streamlines and the temperature contours in planes parallel to the slab-narrow face starting from a cross-section at the narrow symmetry plane and ending at a plane slightly before the slab-side wall (y=540 mm). Figure 4.6 (a) shows the earlier mentioned strong angle flow coming from the horizontal recirculation at the slab top surface. The hot stream flows around the outside side wall of the distribution bag and along the solidification front. Figure 4.6 (b) shows that the mushy layer near the slab surface is thinner than at the middle of the narrow side of the calculation domain. The thinning in the mushy layer near the slab surface is due to the strong downward vertical momentum of the molten metal created by both the symmetry boundary condition and the impermeable-side wall of the distribution bag. Consequently, this stream suppresses more the mushy layer near the slab surface. The mushy layer thickness at the slab center is partly controlled by the angle flow. The stronger the angle flow, the thinner is the mushy layer at the slab center. This is because the angle flow carries the hot melt from the adiabatic section of the mold (hot top) to the slab center.

Figure 4.6 (c,d) presents a section taken after the side window of the distribution bag. Figure 4.6 (c) shows a counter-clockwise vertical recirculation. Again, the mushy zone extends toward the slab top surface at the region of separation of the recirculation

from the solidified shell as can clearly be seen in Figure 4.6 (d). Figure 4.6 (e,f) depicts a section at 12 cm from the slab side wall (y = 540 mm). Figure 4.6 (e) shows the spreading of the hot stream coming from the side window of the distribution bag as it hits the narrow side of the mold. It can be seen that the mushy region in the corresponding temperature contours, Figure 4.6 (f), is generally thin, and it is thinner at the slab corner ((x,z)=(0,330) mm). This can be attributed to the absence of any recirculation in this plane, and that the flow has a more downward component. The downward characteristic of the flow would suppress the extension of the mushy layer by providing it with hot melt. The thinner mushy region at the corner is attributed to the convexity of the region.

Figure 4.7 shows the axial temperature and its gradient along a line on the ingot side wall (y = 660 mm) at z = 0 mm. The temperature in the outer solidified layer is almost decreasing linearly in the direction of increasing x, while the temperature gradient is slowly decreasing in the mold contact section ($85 \leq x < 135$ mm). A steep decrease in the temperature gradient as the air gap region is approached ($135 \leq x < 145$ mm). A minimum temperature gradient is attained at the air gap region ($145 \leq x < 155$ mm), followed by a sharp increase at the beginning of the secondary cooling zone (spray cooling region) to reach to a maximum at around x = 165 mm. A sharp decrease is followed in the range of ($166 \leq x < 215$ mm). Finally, the temperature gradient is decreasing slowly as the slab enters the film boiling region. It should be noted that the calculated temperature gradient is at the surface of the narrow side of the ingot, solidified shell region. Therefore, the heat transfer mechanism at the outer slab layer is controlled by the heat transfer coefficient of the primary, secondary and air-gap region. Since it is assumed that the heat transfer-coefficient distribution in these three regions is the same for both modeled cases of with and without buoyancy effect, thus, the temperature gradient for the two cases is the same in those particular regions.

The following section is devoted to the discussion of the developed mathematical model results with the buoyancy term included in the x-momentum equation. Therefore, these results are expected to simulate the real vertical DC casting situation more closely than the previously discussed ones. The buoyancy term in the x-momentum equation was derived earlier by applying the Boussinesq approximation.

4.4.2 Model Results Including Thermal Buoyancy Force Effect

Figure 4.8 (a-c) shows a 3D-surface plot for the calculated temperature contours, vector fields and streamlines, respectively. The figure, as in the earlier discussed case, presents the calculation domain, which consists of the two symmetric planes, wide and narrow, and the top surface of the slab. These results are obtained for the same geometrical, operational and boundary conditions as the earlier case discussed as no buoyancy case. For the purpose of conducting a detailed analysis of the model results, the 3D calculation domain is sliced at various sections in the three perspective orthogonal planes. Figure 4.9 (a) shows the wide symmetry plane, it is clear that the flow has changed from largely horizontal to exhibiting a stronger vertical component around the slab center compared to the earlier discussed and corresponding to the case of no buoyancy effect of Figure 4.4 (a). This flow behavior is in agreement with the experimental observation in which the free convection generates typical flow patterns with downward flow along the cold solidification front and side walls and upward flow in the warm center of the pool. The isotherms and the flow direction near the bag outlets have experienced a marked lifting; this is in agreement with the results of Gary et al. [23]. The recirculation at the wide symmetry plane is extended to the slab center. The angle flow at the slab center, resulting from the earlier mentioned recirculation at the slab free surface, is overwhelmed by the upward component of the vertical recirculation at the wide symmetry plane. As a result, the overwhelmed downward flow is pushed to recirculate at the narrow symmetry plane. Whereas in the no buoyancy case, shown in Figure 4.4 (a), the angle flow is entrained by the vertical recirculation at the wide symmetry plane. The extra activity of the flow at the wide symmetry plane, especially around the ingot center, can be attributed to the momentum gained by the upward flow component of the vertical recirculation. This enhancement in momentum is the result of the thermal buoyancy force, the latter is generated at the solid-liquid interface.

Both, the angle flow resulting from the horizontal recirculation at the ingot top surface, and the upward flow resulting from the vertical recirculation at the wide symmetry plane have a direct effect on thickening and/or narrowing of the mushy layer according to the following; whenever the upward component of the recirculation at the

wide symmetry plane overwhelms the angle flow, the mushy region becomes thicker and expands toward the ingot top surface as can be seen in Figure 4.9 (a-d). It is to be noted that a part of the main flow coming from the side window and circulating in the wide symmetry plane is cooled down as it flows along the solidification front. This results in a thicker mushy zone. On the other hand, if the angle flow overcomes the upward component of the vertical circulation at the wide symmetry plane, then the mushy layer will be thin as shown earlier in the case of no buoyancy of Figure 4.4 (a,b). This is because the angle flow carries hot aluminum melt from the adiabatic section of the mold. The hot melt causes the mushy layer to shrink. It is known that the longer the mushy zone the more difficult it becomes to compensate for the solidification shrinkage through melt feeding from the liquid sump [51]. This leads to the stress build up, and results in hot cracks. Therefore, it is advised to design the distribution system in such a way so as to keep the mushy layer as thin as possible. The later can be achieved, as shown earlier, by promoting the angle flow to overcome the upward flow component of the vertical recirculation, which is enhanced by the buoyancy force. Katgerman [51] demonstrated that a strong vertical component opposing the upward flow in the slab center caused by natural convection would prevent the settlement of depleted grains. The practical implication of this is that the mold-distribution system can be designed in such a manner that macrosegregation patterns can be largely improved. The latter can efficiently be done by extending the current developed mathematical model to incorporate macrosegregation.

The solidification front at the wide symmetry plane with the buoyancy effect included is deeper and more uniform than that in the case of no buoyancy. This is in consistence with the observations made by Dong et al. [16], that the strong flow of hot melt from the windows at the end of the bag toward the short sides of the ingot was beneficial in yielding a uniform solidification front. Therefore, the solidification-front profile at the slab center can be said to have been accurately predicted by the current developed mathematical model. In fact, the general shape of the predicted solidification profile of the current developed mathematical model is in agreement with the general shape of the designed and predefined solidification profiles used in most physical water models such as the one designed by Dong et al. [16]. These physical water models are, in

turn, designed according to the solidification profiles measured in real vertical DC casters. The metallurgical length, the solid front depth at the slab center, for the case where the buoyancy effect is included in the model, is located at 510 mm from the ingot top surface, whereas for the case of no buoyancy, it is located at 492 mm, with a difference of 18 mm. Figure 4.9 (c) shows the formation of a new vortex near the slab outside surface. This type of vortex is a characteristic of a flow inside a cavity. In this case, the cavity is confined by the slab top surface, the mold and the side-solidified layer. The corner vortex is spinning in a counter clockwise direction, and is developing more with the increase in distance in the z direction. On the other hand, the vertical vortex is decaying with the increase in distance in the z-direction. Ultimately, the vertical vortex is entrained by the corner vortex as can be seen in Figure 4.9 (e). Figure 4.9 (b,d,f) shows that the outer profile of the outer solidified layer as almost an inclined straight line with a negative slope, and the solidification front is almost a horizontal straight line. It can be seen that there is a considerable portion of the sump with a uniform temperature. This is no doubt due to the good mixing effect of the convective currents seen in Figure 4.9 (a,c,e). In general, natural convection causes the mushy layer to get thicker over most of the planes parallel to the slab rolling face. This can be attributed to the strong upward flow created by the buoyancy force over the slab center. On the other hand, in the case of no buoyancy, the mushy region gets thicker in places of separation of the vertical vortex from the solidification front.

Figure 4.10 (a-f) shows results for cross-sections parallel to the slab free surface for the vector/streamlines and temperature contours. Figure 4.10 (a) shows the spreading of the melt stream, coming from the distributor-bag outlet facing the mold narrow side, and proceeding toward the rolling face of the ingot. This plane is located at the adiabatic section of the mold, therefore, the temperature contours are above the liquidus temperature as shown by the corresponding temperature contours plot of Figure 4.10 (b). The decrease in temperature is attributed to the vertical mixing of the melt. The vertical mixing causes the transport of heat from the hotter upper region to the cooler lower region of the sump. At the beginning of the primary cooling region, [Figure 4.10 (c,d)], the melt is primarily solidified at the outside corner and at the slab rolling face. The

strong mixing is causing a large portion of the slab layer to have the same temperature. At around the end of the mold primary cooling section, [Figure 4.10 (e,f)], the solidified shell develops around the entire slab periphery. The solidified layer thickness at the narrow face is less than that at the slab rolling faces. For the prevention of surface segregation, it is important to keep the solidified thickness, in the mold section, as minimum as possible, yet strong enough to withstand the metallostatic head of the sump. As mentioned earlier, to get the best ingot-surface characteristics, the solidified layer thickness at the slab periphery should develop equally and uniformally.

Figure 4.11(a-f) shows vector/streamline and temperature contours in cross-sections parallel to the slab narrow side. Figure 4.11 (a,b) presents the narrow symmetry plane. It is clear that the mushy region, confined between the 903 K and 928 K temperature contours, is extended due to the upward flow of the relatively cold melt coming from the vertical recirculation at the wide symmetry plane. The momentum of the cold stream is enhanced by the influence of the buoyancy force, to the point where it overcomes the angle flow, thereby, forcing the latter to form a vortex in the narrow symmetry plane at ((x,z)=(40,200) as can be seen in Figure 4.11 (a). Figure 4.11 (c,d) shows the vortex development in a section laying after the end of the distribution bag in the y-direction. Figure 4.11 (e,f) depicts a section 120 mm from the ingot-side wall, the vortex is overwhelmed by the strong horizontal flow along the mold surface. It is clear that the mathematical model was able to predict the vortices and their depth in all perspective directions, a task even the particle imaging velocimetry (PIV) would fail to accomplish, especially in regions characterized by low velocities. Predicting recirculations, vortices and separation regions is a key point of note when comparing different distributors, since mapping out these flow mechanisms would help in specifying eddies and/or dead zone locations, which would indicate areas of low fluid refreshment [23].

4.5 Quantitative Verification of the Developed Mathematical Model

Having discussed the results of the model for the two cases of with and without the thermal buoyancy force, these results need to be verified quantitatively so that the model can confidently be used in carrying out the parametric study which will be done in

the next chapter. Therefore, the coming section is devoted to the code's quantitative verification; this task would be preceded by a brief description of the real casting experiment used for the validation of the code.

4.5.1 Description of the Real DC Casting Experiment

The real DC casting experiment, used to verify the current mathematical model, was performed at Reynolds Metal Company Casting Technology Center, Chester, VA, by Jones et al. [20]. A T-shaped bar was secured on the top of a 0.66×1.32 m mold to guide thermocouples (TC) as shown in Figure 4.12. The average inlet temperature was 700°C, and the casting speed was 50.8 mm/min. A combo bag was used to redistribute the aluminum (Al 3104) melt. The sump profile was measured by setting the time equal to zero when the thermocouple first read the temperature of the liquid metal. By measuring the time interval for the thermocouples to reach the solidification front, and multiplying the time intervals by the drop speed, the solidification front depth could be calculated. Only thermocouple TC1, TC2, TC3 and TC4, parallel to the rolling face, were used for the verification, since thermocouple 5 failed to measure the depth of the solidification front. It was not possible to use thermocouple results in the transverse direction, i.e. (TC6, TC7, TC8), in the code verification, because there was a geometrical scale-type of mistake in reporting the results from these thermocouples.

4.5.2 Quantitative Verification Results and Related Discussion

Figure 4.13 shows a plot of the solidification fronts using the results of the real casting experiment [20] and the present developed mathematical model. In this figure, the two numerical prediction curves correspond to the two cases of with and without the buoyancy effect. The axial distance is measured relative to the top of the mold. The measurement is taken at the ingot wide symmetry plane. Failure in measuring the temperature from thermocouple (TC5) during the real casting experiment caused the comparison to be done starting at a distance of 310 mm from the slab center. In their experimental work, the authors did not measure the thermal boundary conditions. Therefore, the boundary conditions imposed in the developed mathematical model were

those reported and in common use in the DC casting literature [13]. These boundary conditions are based on experimental measurements.

Generally, the predicted-sump profile with the buoyancy effect taken into consideration is linear in nature, and is showing a better agreement with the experimental profile than the predicted sump profile without the buoyancy effect. The agreement between the predicted profile with the buoyancy effect included and the real experiment is enhanced near the slab center than that near the narrow side of the slab surface, with the two profiles match at around 440 mm from the slab center. As mentioned earlier, the sump profile near the narrow side surface of the slab is more affected by the imposed boundary condition. Whereas, the sump profile at and around the slab center is more affected by the melt flow behavior. Therefore, the metallurgical depth at and around the slab center is taken as a measure for such verification of the mathematical model, unless the boundary conditions of the experimental work are accurately known or specified.

The relative difference in the sump depth between thermocouple number four (TC4), which is at a distance of 310 mm from the ingot center, and the mathematical prediction with the buoyancy effect included at the same position is just 8.8 %. Whereas, the relative difference at the same position between the real experiment and the prediction results without the buoyancy effect is 18.8 %. Therefore, the mathematical model is demonstrated to give a very good prediction towards the slab center, where all the mechanisms of fluid flow and heat transfer are taking place. These mechanisms include turbulence effect, conduction and convection with phase change. At the edges, the mechanism of heat transfer is much simpler than that at the rest of the slab, and is mostly limited to a conduction type of heat transfer within the solidified layer. It is expected that the current mathematical model would provide very good predictions at the edges too once accurate heat transfer boundary conditions are supplied. The solidification profile with the buoyancy force included follows approximately an average path between the other two profiles, the real casting experimental profile and the prediction profile without buoyancy. An accurate prediction of the solidification front is of paramount importance for the casting engineer, since the centerline macrosegregation increases with

the increase in sump depth [20]. A shallower sump is preferable in terms of reducing macrosegregation.

The solidus temperature contour at the wide symmetry plane, for the case where the buoyancy effect is included, demonstrates that the solidified contour line is falling almost on a straight line with a steeper-negative slope from the ingot-side wall up to a point located at around the middle of the calculation domain. This straight line profile is followed by most researchers in designing there water models, as will be seen later in describing the physical water experiments of Xu et al. [18]. The steepness in the solidification profile with the buoyancy included can be attributed to the strong downward flow component of the recirculation at around half a distance from the slab-side wall with reference to the calculation domain. This strong flow was shown earlier in the vector field in Figure 4.9 (a). At a distance of 360 mm from the side wall, at the wide symmetry plane, the solidification front is horizontally flattening out until the slab center is reached. Whereas in the case of no buoyancy effect, the solidification front follows an average smooth parabolic path from the side wall of the slab until the slab center as shown earlier in Figure 4.6 a.

4.6 Verification of the Mathematical Model with a Water Model

The qualitative verification of the model is built on the comparison of the current developed numerical model with the physical water model of Xu et al. [18]. It should be noted that the intended goal of the qualitative comparison is merely to show the similarity in the two vector fields of the numerical model and the physical water model, once similar geometrical characteristics are being used. Exact numerical simulation of the physical water model requires imposing of the predefined solidification front into the numerical model and canceling thereby the energy equation from the numerical model. Achieving the last task is not the intended goal for the current developed mathematical model. The model was built to achieve the goal of simulating the real DC casting process.

In the following section, a brief description of the physical water model and an explanation upon which the justification of using physical water model to verify and simulate the aluminum DC casting process is presented.

4.6.1 Brief Description of the Physical Water Model

The physical water experiment used in the code qualitative verification was designed by Xu et al. [18]. The study was conducted to investigate the role of thermal buoyancy driven flows in a laboratory scale model of an aluminum caster. The horizontal dimensions of the physical water model were 0.762 m x 0.305 m. The experiment concentrated more on studying flows in the liquid metal pool at the head of an electromagnetic (EM) or direct-chill (DC) caster. The setup consisted of an inverted pyramid of Lexan, simulating the solid front, within a PVC tank as shown in Figure 4.14. The Lexan had 10 mm diameter holes with a 17 mm distance between the hole centers. These holes are made to allow the fluid touching the surface to slip through the holes into a tank in order to imitate what happens in a real casting situation, where the melt in contact with the solidified surface solidifies and takes the velocity of that surface. The setup consisted of a reservoir, a pump, a flow meter and a heater positioned between the pump and the flow meter. The water heater was added so that the water temperature entering the model could be precisely controlled. A thermocouple was inserted into the side of the nozzle to measure the temperature of the flow upon exit. The reservoir temperature was measured and the difference between the temperature of the water in the reservoir and the water entering the model was set as the superheat. In the water model, the superheat was set at 15°C. This temperature superheat corresponds to 65°C in aluminum as will be shown in the coming section.

In the developed mathematical model, a configuration similar to that used in the water model is simulated. The ingot has dimensions of 2.5 x 1.73 x 0.33 m in the x, y and z directions, respectively, as shown in Figure 4.1. Due to symmetry considerations, a quarter of the ingot is taken as the calculation domain. The shaded part in Figure 4.1 represents the section modeled. A combo type of bag, as shown in Figure 4.2, is used to distribute the molten aluminum and is located at the mold center as shown in Figure 4.1. The bag has dimensions of 50 x 102 x 76 mm in the x, y, and z, respectively. The end windows extend along the whole thickness of the bag, and the bottom windows have dimensions of 20 x 40 mm in the y and z directions, respectively. The mold is 80 mm in length. In the current mathematical model, the solidification front is not predefined as in

the case of the water model, but rather is the result of the iterative calculation of the combined continuity, momentum, energy, and turbulence equations. The qualitative comparison of the results of both the mathematical model and the physical water model is merely to show that both exhibits the same flow behavior once similar combo bags are used. The other reason for making this qualitative comparison between the two systems using the flow field results is because of the earlier mentioned difficulty of doing such a comparison with the real casting experiment. The difficulty is manifested in the complexity of measuring the flow field in real casting experiments.

4.6.2 Justification of Using Physical Water Model to Simulate a Real Aluminum DC Casting

From the fundamentals of dimensional analysis in general, and the similarity principle in particular, physical water models can be used to simulate real aluminum caster only if dynamic and thermal similarities are proven to exit between the two. To ensure the existence of both conditions of similarity, the Tundish number, for thermal similarity, along with the Reynolds number, for dynamic similarity, of the water model were matched with operational properties of an actual aluminum caster [20]. The Tundish number is defined by the following equation.

$$Tu = \frac{Gr}{\mathrm{Re}^2} = \frac{g L \beta \Delta T}{U^2} \tag{4.12}$$

where g is the gravity, L is the characteristic length of the system, β is the volumetric thermal expansion coefficient. ΔT is the superheat, which in the water model experiment represents the difference in temperature between the water in the reservoir and the inlet water temperature at the nozzle, and U is a characteristic velocity. Therefore;

$$Tu_{al} = Tu_{w} \tag{4.13}$$

Since L and g are constants, therefore,

$$\frac{\beta_w \Delta T_w}{U_w^{\ 2}} = \frac{\beta_{al} \Delta T_{al}}{U_{al}^2} \tag{4.14}$$

where the subscript w and al stand for water and aluminum, respectively. Due to flow restrictions and superheat limitations, the maximum flow rate in the water model that can be achieved was

$$U_w^2 = 0.64\ U_{al}^2 \tag{4.15}$$

Substituting U_w^2 from equation (4.15) into equation (4.14), the following equation can be derived,

$$\Delta T_w = 0.64 \frac{\beta_{al}}{\beta_w} \Delta T_{al} \tag{4.16}$$

Values of the volumetric thermal coefficient were taken as $\beta_w = 3.21\text{x } 10^{-4}\ \text{K}^{-1}$ and $\beta_{al} = 1.02\text{ x } 10^{-4}\ \text{K}^{-1}$. Substituting these values in equation (4.16) leads to the following equation:

$$\Delta T_w = 0.2\ \Delta T_{al} \tag{4.17}$$

Therefore, for example, in order to model a superheat of 65°C in the aluminum caster, the superheat in the water model must be set approximately at 13°C. Both dynamic and thermal similarity criteria were respected in arriving at the above superheat temperature of water. The above explanation is also the basis upon which the comparison between the water model and the real casting experiment was founded. That is the same reason why these two models (the water model and the real casting experiment) are taken as a reference for the comparison with the results of the current developed mathematical model.

4.6.3 Verification of the Results and Related Discussion

Figure 4.15 (a, b) shows the flow field at the wide symmetry plane for both the water model of Jones et al. [18] and the current developed mathematical model, respectively. In both cases [Figure 4.15 (a,b)] two jets of molten aluminum can be seen exiting from the vertical and horizontal windows of the combo bags. The issuing stream from the side window goes along the wide symmetry plane toward the narrow side of the mold. Once it hits the narrow side of the mold, the stream recirculates at the slab-outside corner in a counter clockwise fashion. The other stream, coming from the bottom window, is impacting the solid front in both cases. In the mathematical prediction, the jet stream hits the solid front, and splits into two streams. One stream is entrained by the corner recirculation, and the other goes down along the solidification front, and recirculates at the slab center. The center recirculation can not be seen in the physical water model due to the difficulty in capturing the vector field in a weak velocity region using the PIV technique. The two velocity vector field results, presented by the physical water model and the current mathematical model, clearly show the similarity.

Gary et al. [24] stated that a key point of comparing the performance of melt distributors with any standard distributor is the identification of the number of dead zones or eddies present within the sump. These dead zones or eddies represent areas of low fluid refreshment. The inability of the PIV in capturing low velocity regions constitutes another advantage of using mathematical models in simulating a DC casting process in the sense that by using mathematical models, the flow field results can be analyzed at any region and corner at any section in the three orthogonal planes, no matter how weak the flow field is there. Thus, the DC caster can be numerically modeled without incurring much expense until the optimum theoretical design is arrived at.

4.7 Closure

The current mathematical model has been verified both quantitatively and qualitatively. The quantitative verification is made by comparing the sump depths, with and without the buoyancy effect incorporated in the model, with that of the real casting

experiment of Jones et al. [20]. The agreement between the predicted and the real experiment sump profiles is found to be more favorable with the addition of the buoyancy term in the mathematical model. The agreement of the two mentioned profiles is increasing with the increase in the distance away from the slab side wall. A complete match in the sump depths of the mathematical model with the buoyancy term included and the real casting experiment is achieved at 440 mm from the slab center. The good agreement in the sump profiles is an indication that the heat transfer (conductive, convective, and solidification) and turbulent aspects of the DC casting process are well incorporated in the mathematical model. Due to the lack of information about the boundary conditions used in the real casting experiment, the agreement in the sump profiles of the mathematical predictions with the real casting experiment is less as the slab side wall is approached. Regarding the Verification of the Mathematical Model with Water Model, it is clearly demonstrated that once similar geometrical configurations are used in both the mathematical and the physical water models, similar flow characteristics are obtained.

The phenomenon of increasing and/or decreasing of the mushy layer at the slab center, observed in the literature but never being explained earlier, is analyzed in detail by the current model. In addition, the factors controlling this phenomenon are delineated. The factors are expressed in terms of the upward component of the vertical recirculation and the angle flow. Effects of each of these two factors can be enhanced and/or reduced through the proper design of the melt-distribution system. Controlling the mushy layer thickness is one of the most important aspects in the design of vertical DC casters. The mushy layer thickness at the slab center is known to be of importance in terms of controlling macrosegregation and hot cracks. A strong angle flow would produce minimum macrosegregation.

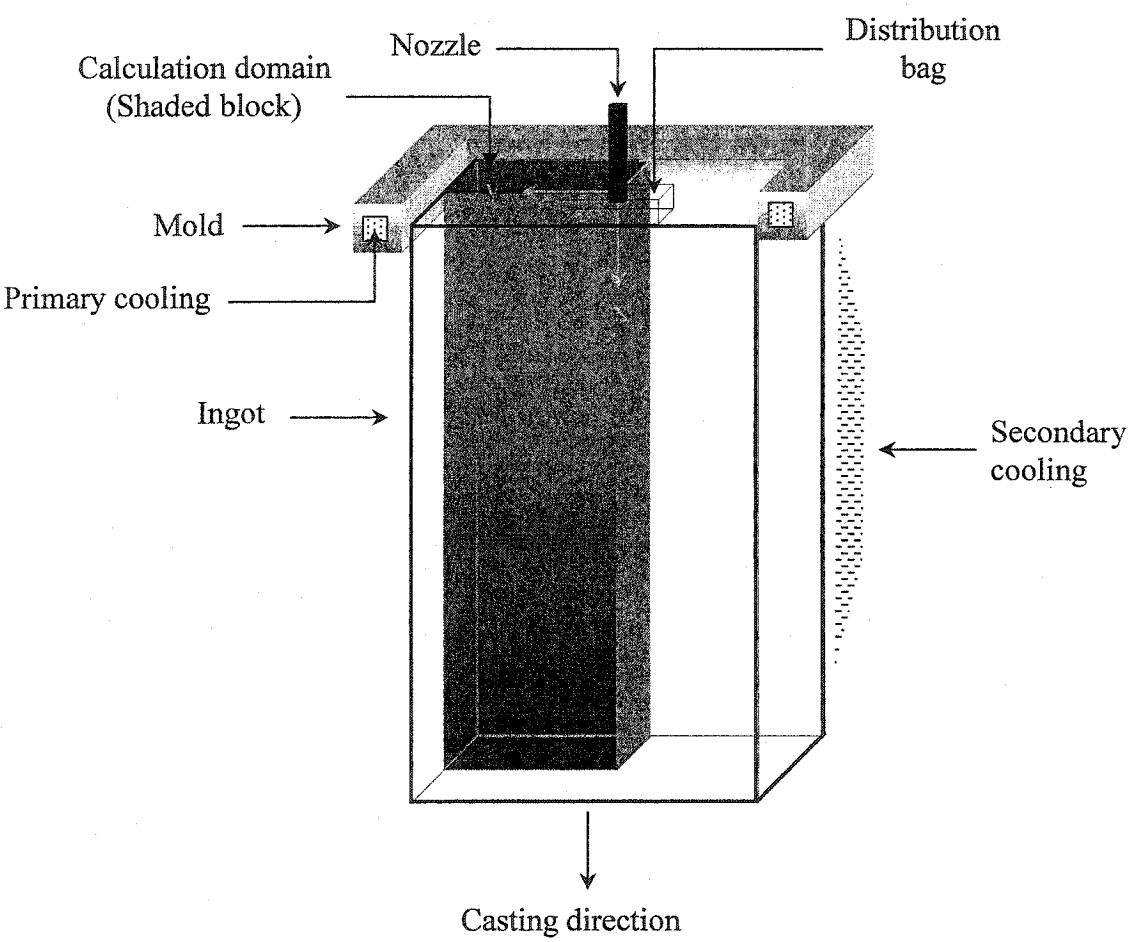

Figure 4.1: Schematic of a vertical DC caster with the calculation domain

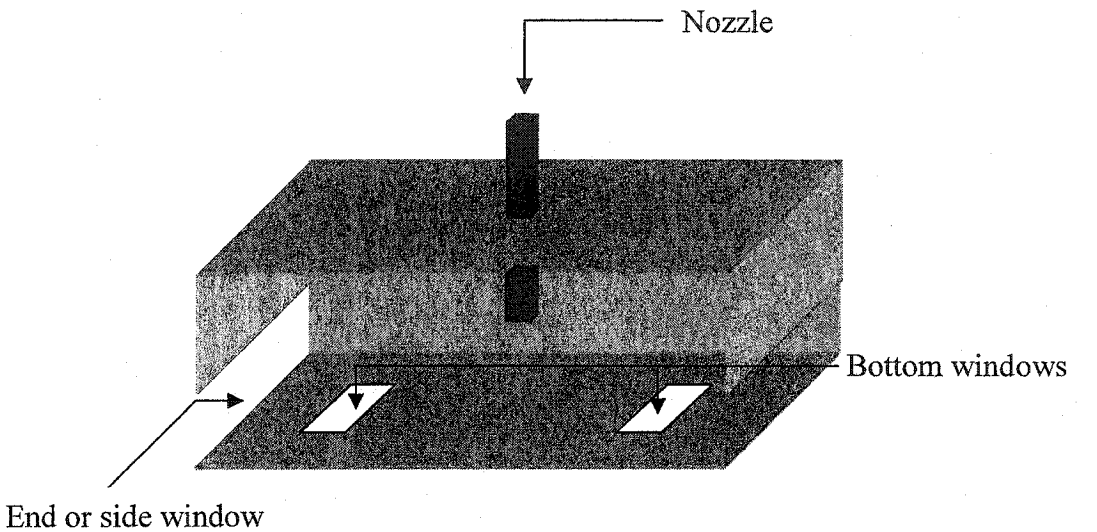

(a) Combo bag

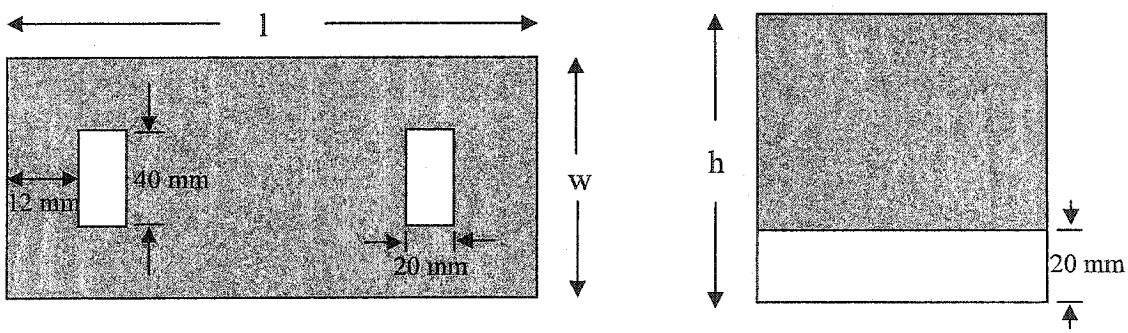

(b) Bottom view (c) Side view

Figure 4.2: Schematic of a combo-distribution bag

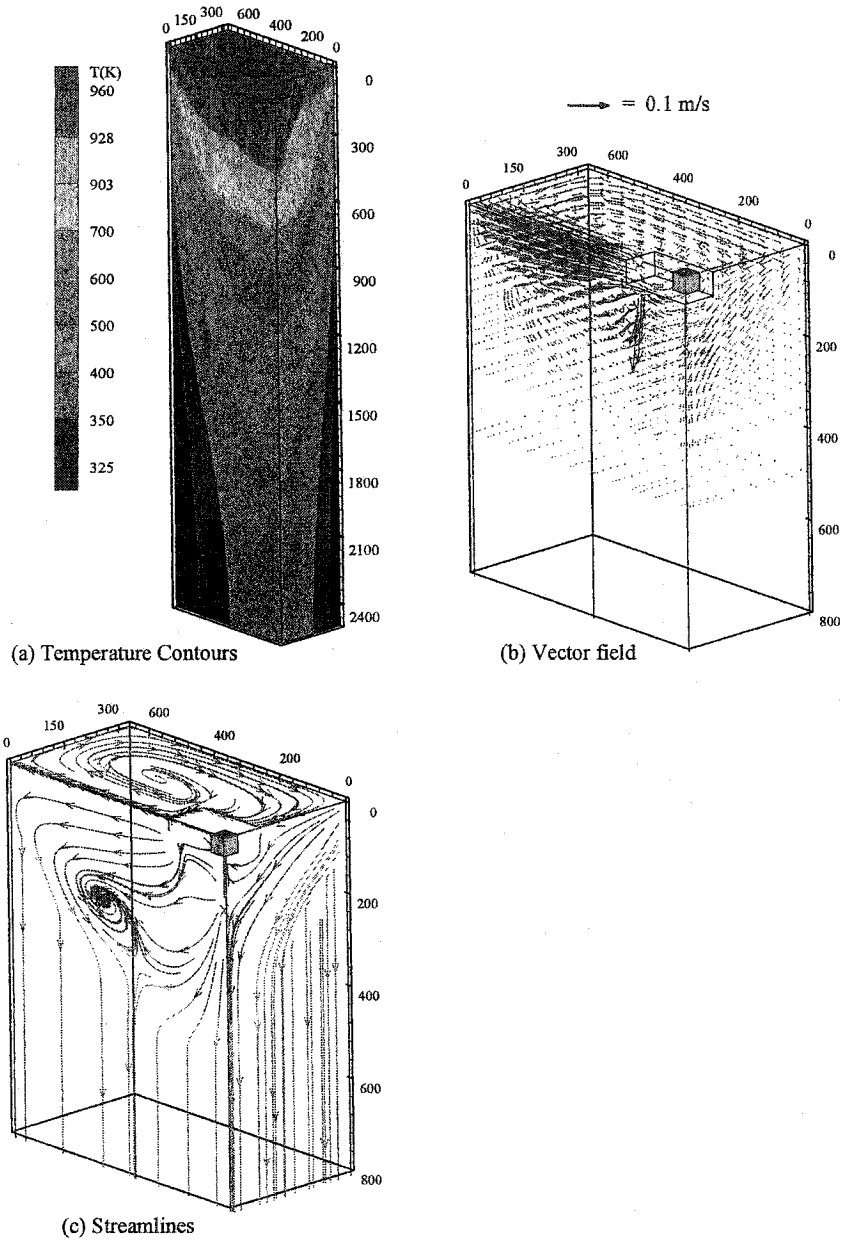

Figure 4.3: 3D-surface plot using the combo bag, casting speed = 50.8 mm/min, temperature superheat = 65°C, no buoyancy.

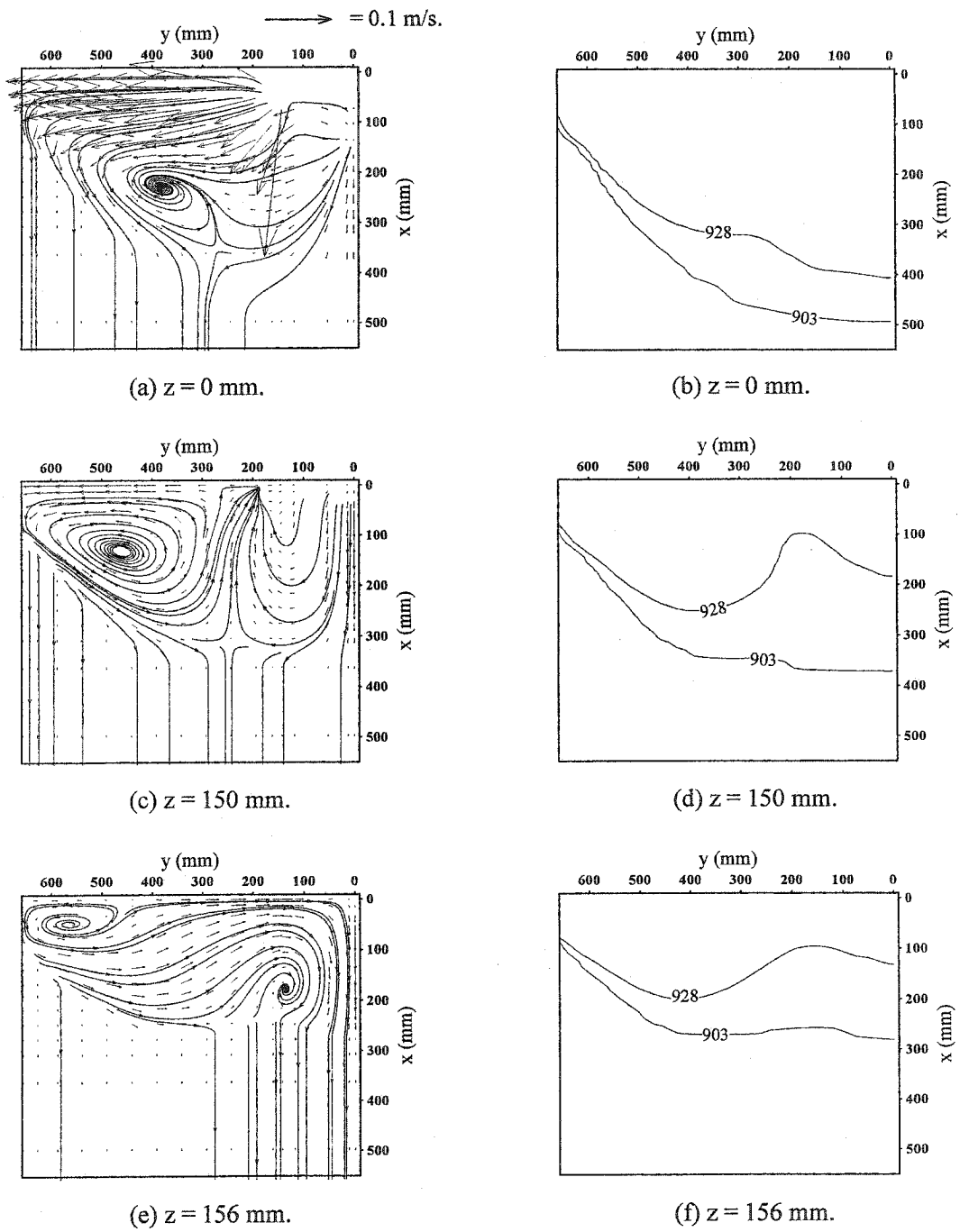

(a) z = 0 mm. (b) z = 0 mm.

(c) z = 150 mm. (d) z = 150 mm.

(e) z = 156 mm. (f) z = 156 mm.

Figure 4.4: Computed results parallel to the slab rolling face using the combo bag, casting speed = 50.8 mm/min, temperature superheat = 65 °C. (a,c,e) vector and streamlines plot, (b,d,f) solidus and liquidus temperature contours in Kelvin.

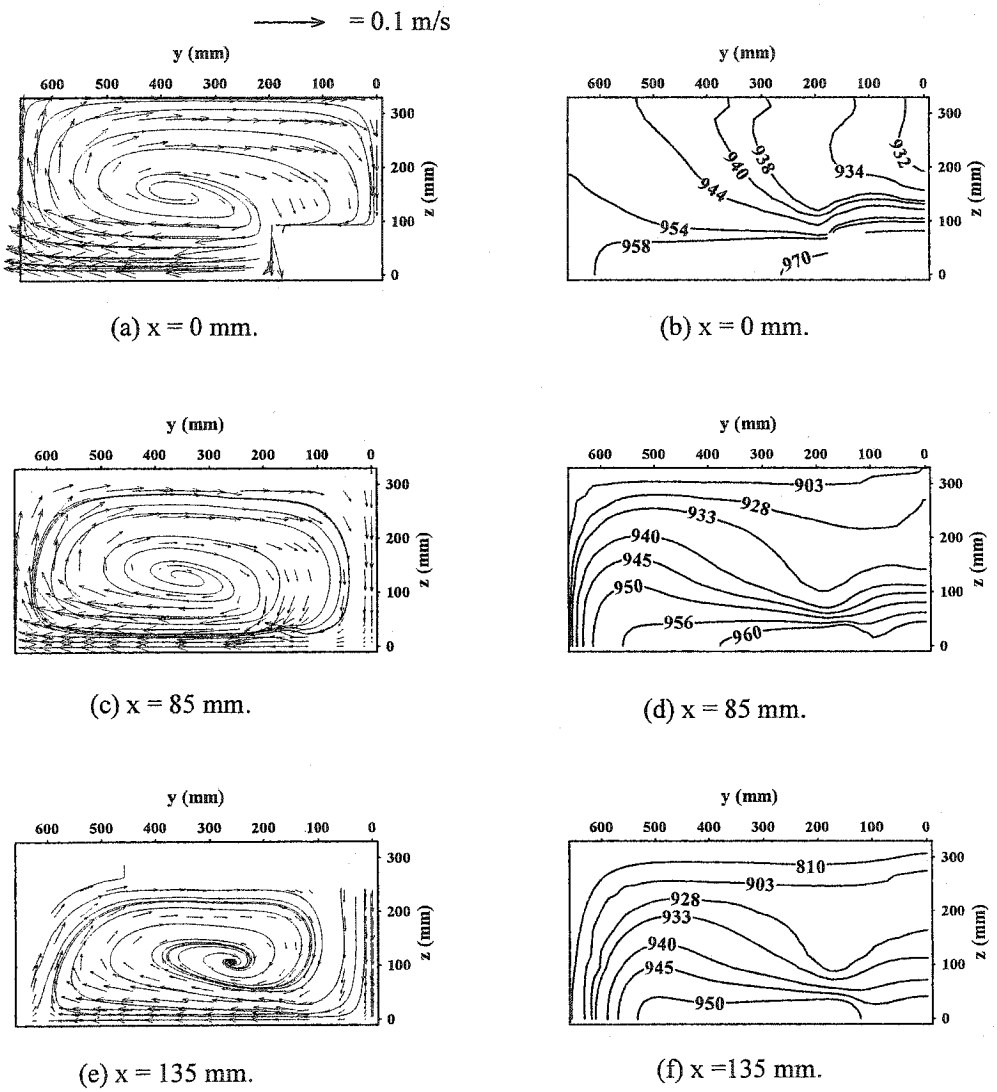

Figure 4.5: Computed results parallel to the slab free surface using the combo bag, casting speed = 50.8 mm/min, temperature superheat = 65 °C, (a,c,e) vector and streamlines plots, (b,d,f) temperature contours in Kelvin.

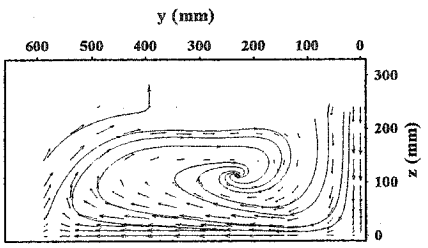

(g) x = 155 mm.

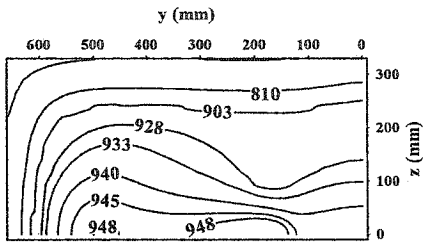

(h) x =155 mm.

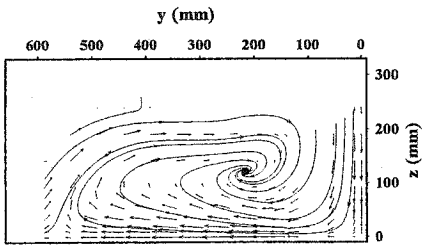

(i) x = 165 mm.

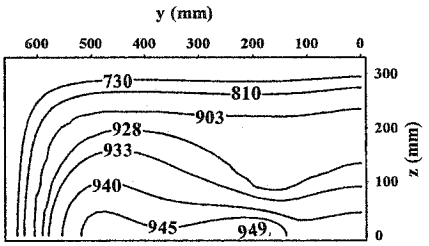

(j) x = 165 mm.

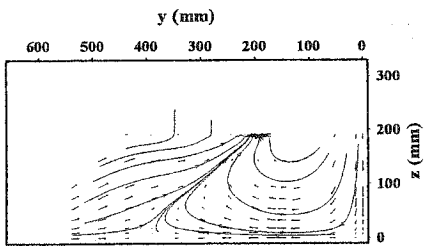

(k) x = 225 mm.

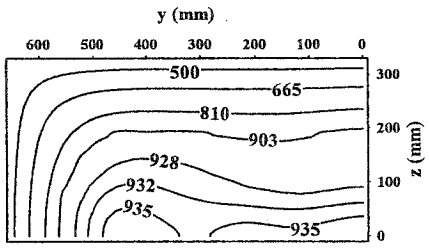

(l) x =225 mm.

Figure 4.5 (continue): (g,i,k) vector and streamlines plots, (h,j,l) temperature contours in Kelvin.

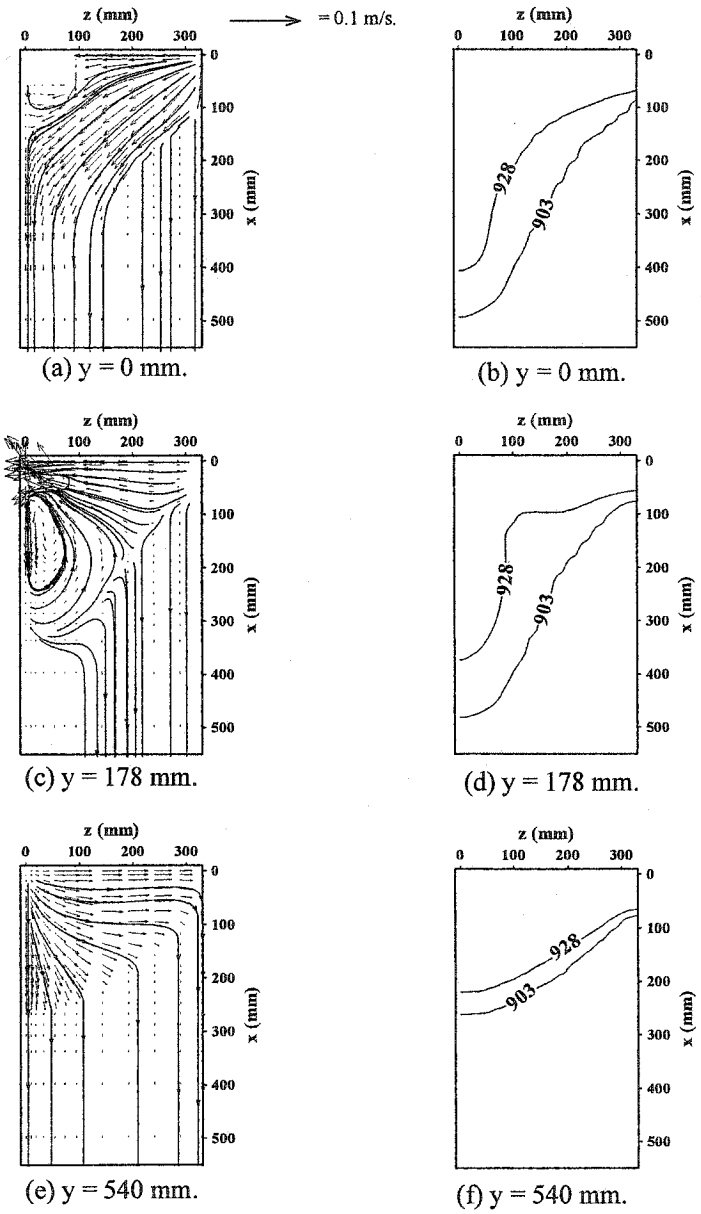

Figure 4.6: Computed results parallel to the slab narrow surface using the combo bag, casting speed = 50.8 mm/min, temperature superheat = 65 °C. (a,c,e) vector plot and streamlines, (b,d,f) temperature contours in Kelvin.

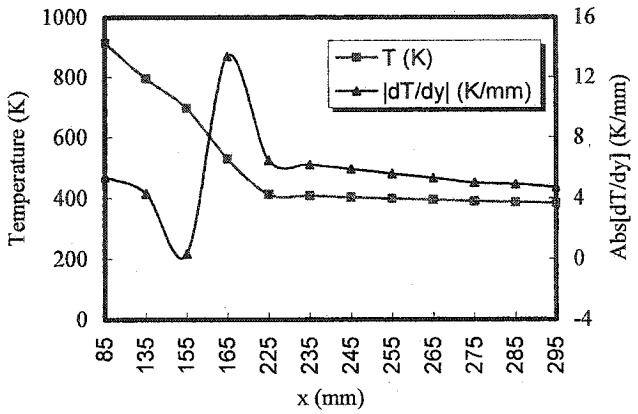

Figure 4.7: Axial temperature and its gradient along the ingot side wall at the wide symmetry plane (z = 0)

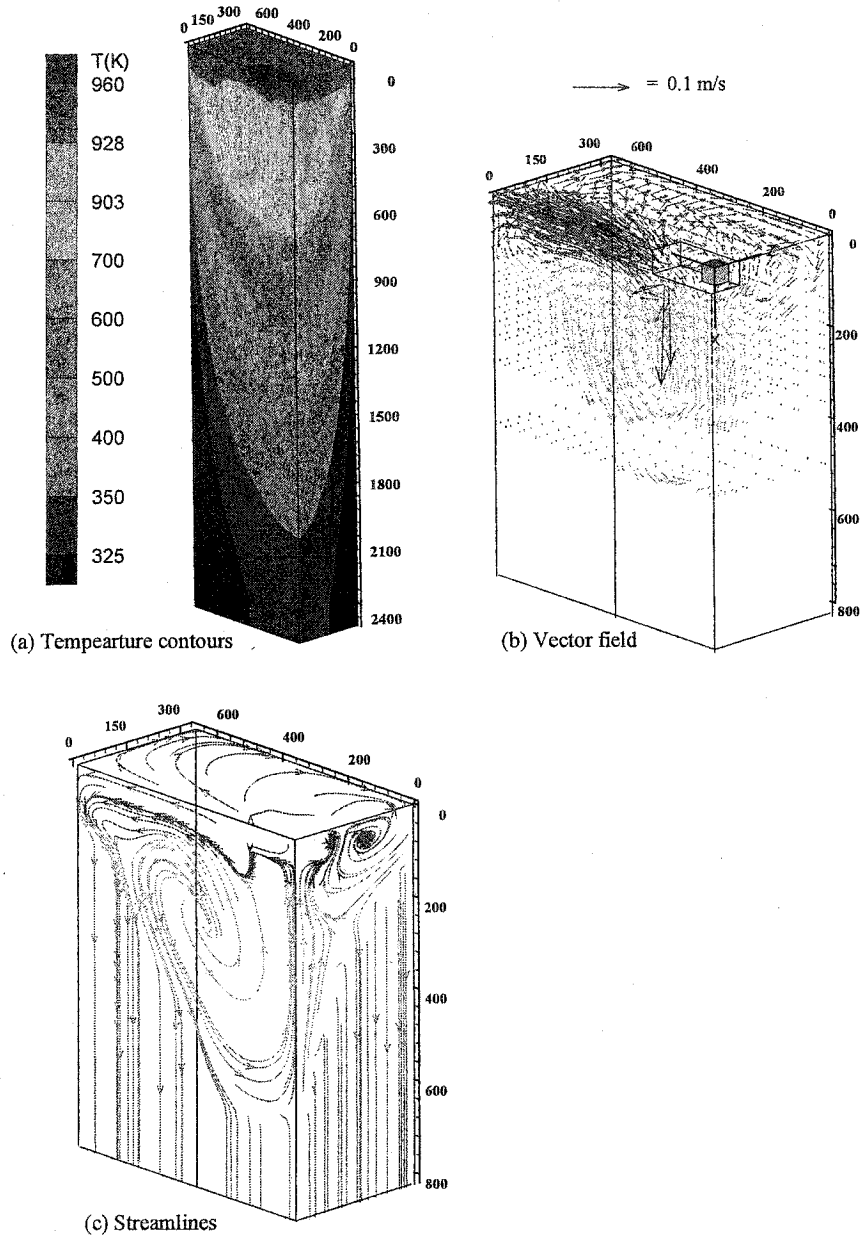

Figure 4.8: 3D-surface plot using the combo bag, casting speed = 50.8 mm/min, temperature superheat = 65 °C, including buoyancy.

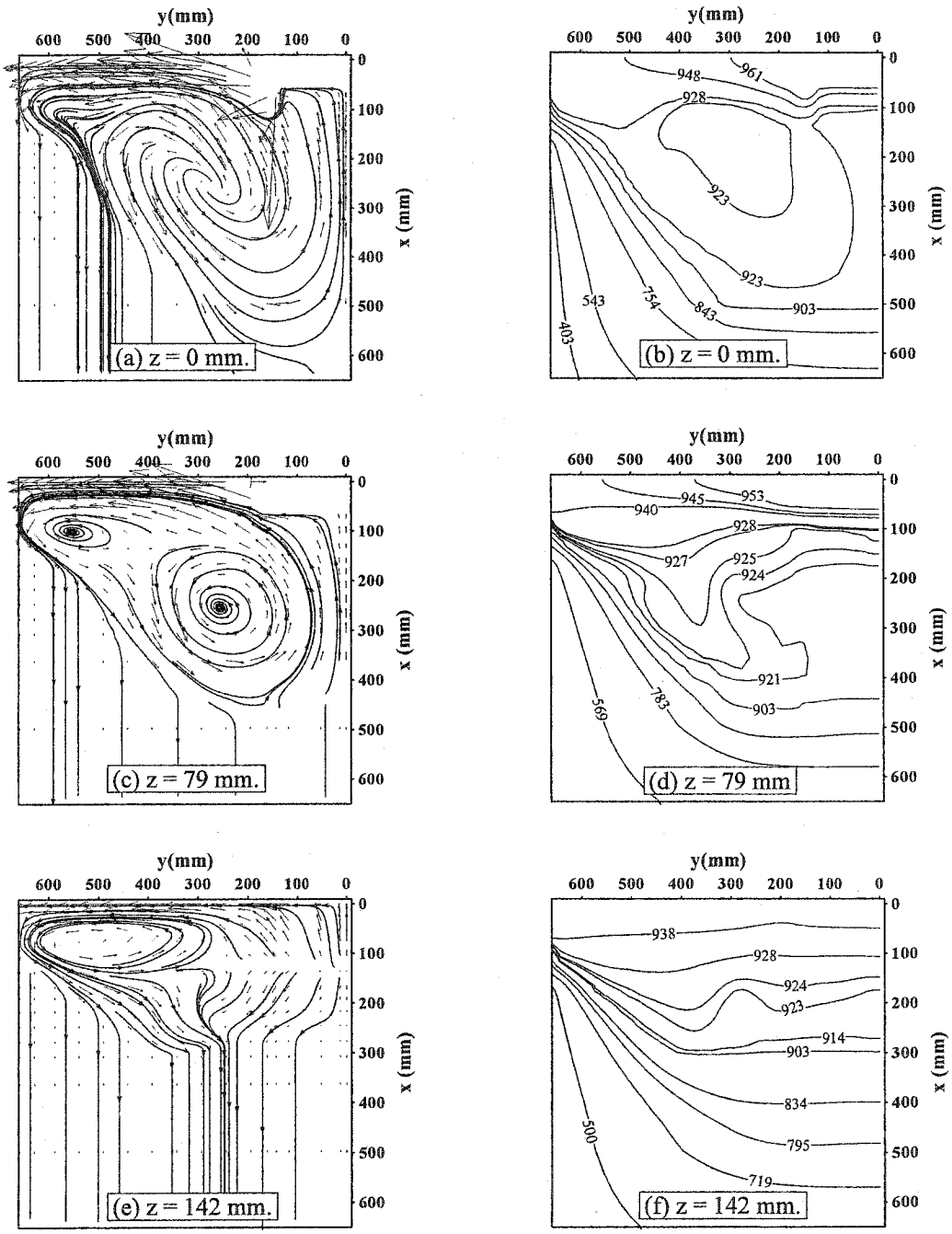

Figure 4.9: Computed results parallel to the slab rolling face using the combo bag, casting speed = 50.8 mm/min, temperature superheat = 65°C. (a,c,e) vector/streamlines plot, (b,d,f) temperature contours in Kelvin, including buoyancy.

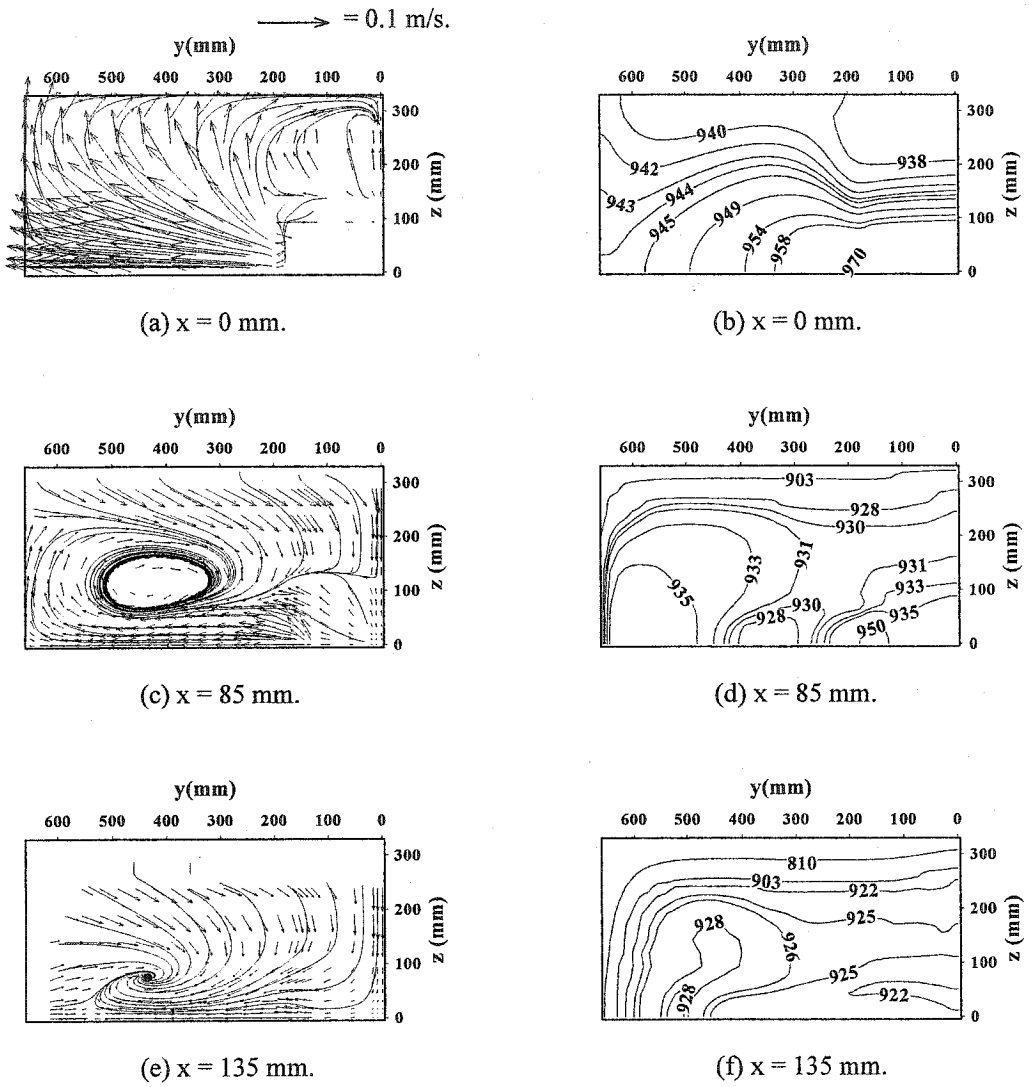

(a) x = 0 mm. (b) x = 0 mm.

(c) x = 85 mm. (d) x = 85 mm.

(e) x = 135 mm. (f) x = 135 mm.

Figure 4.10: Computed results parallel to the slab free surface using the combo bag, casting speed = 50.8 mm/min, temperature superheat = 65 °C. (a,c,e) vector/streamlines plot, (b,d,f) temperature contours in Kelvin, including buoyancy.

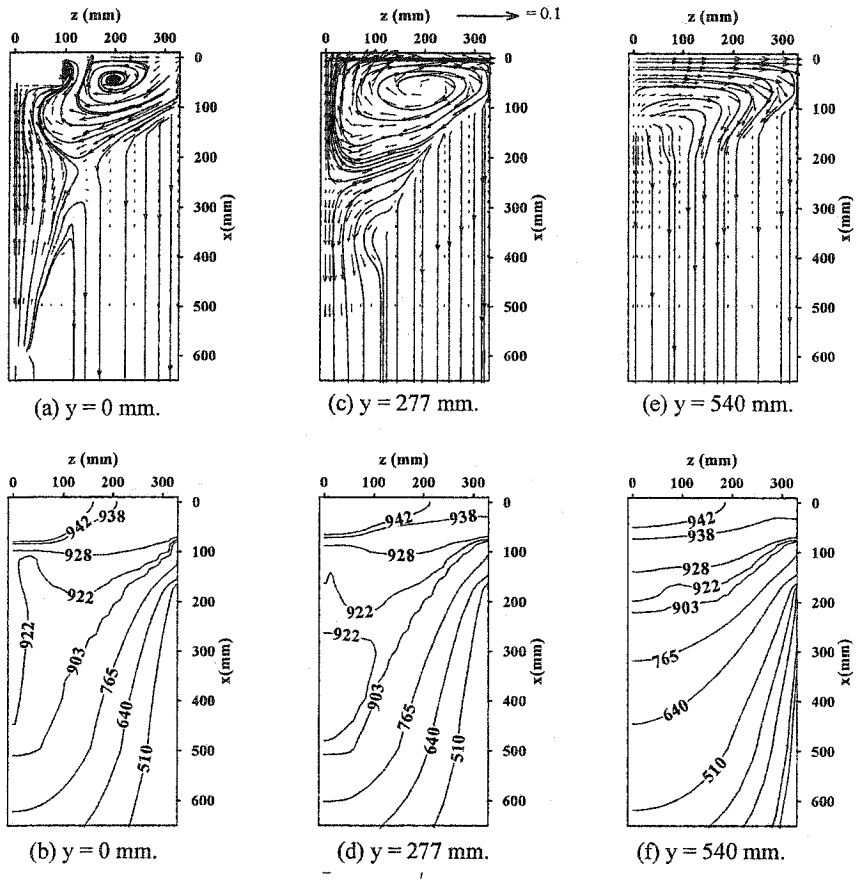

Figure 4.11: Computed results parallel to the slab narrow surface using the combo bag, casting speed = 50.8 mm/min, temperature superheat = 65 °C. (a,c,e) vector plot and streamlines, (b,d,f) temperature contours in Kelvin, including buoyancy.

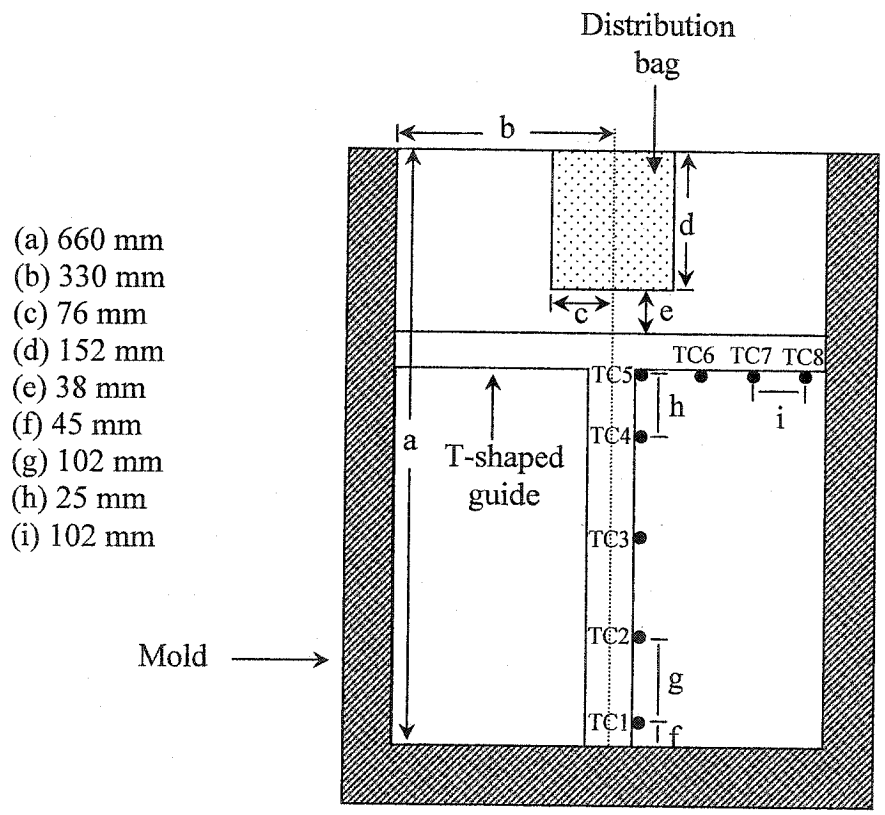

Figure 4.12: Top view of the real casting experiment showing thermocouples distribution.

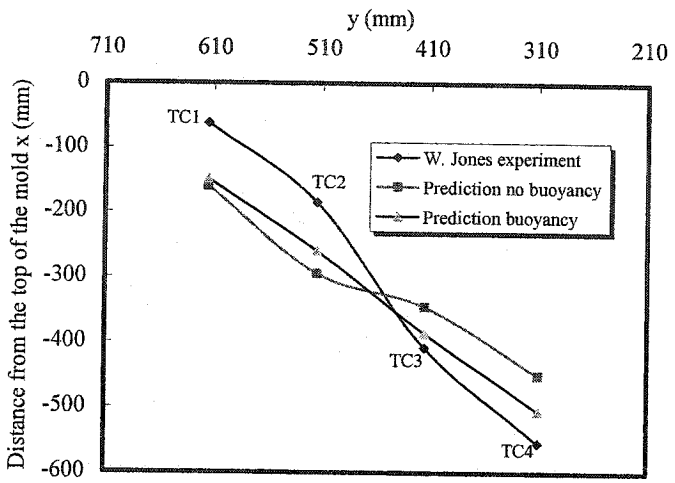

Figure 4.13: Sump profiles at the wide-symmetryplane determined from experimental and numerical predictions

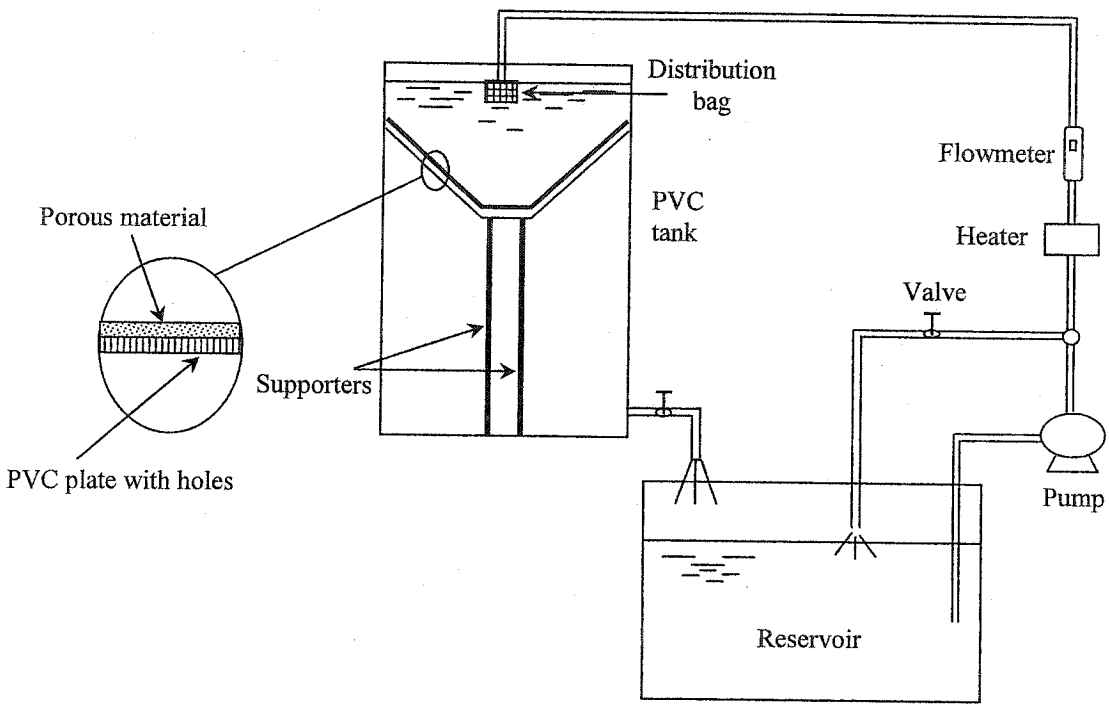

Figure 4.14: Schematic of the physical water model designed by D. Xu.

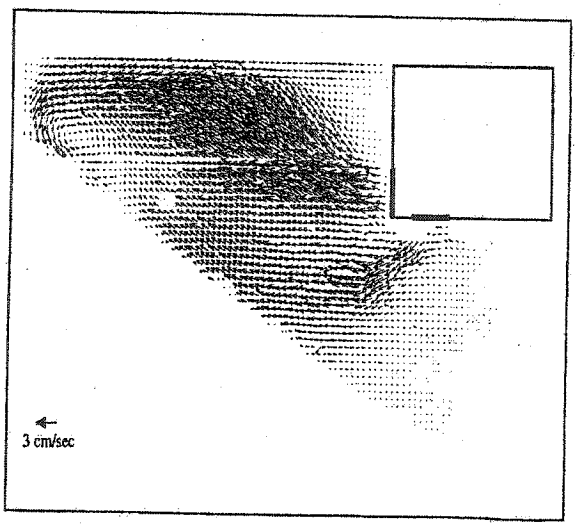

(a) Physical water model vector field at the symmetry plane.

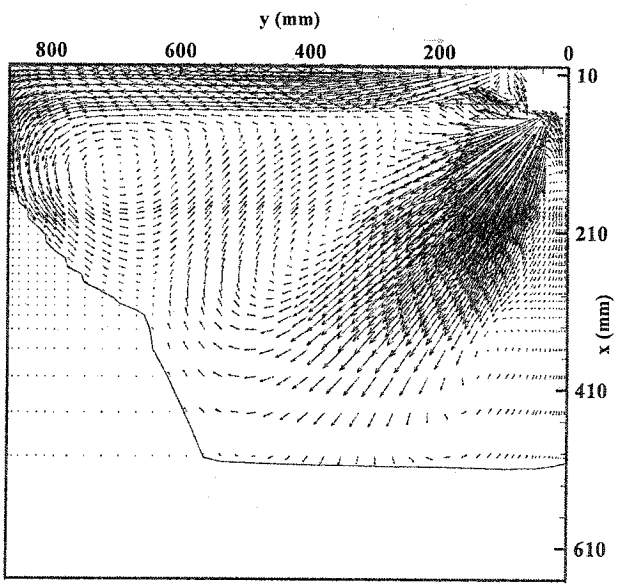

(b) Computed vector field at the symmetry plane using the developed mathematical model.

Figure 4.15: Vector field results of both the physical water model of Jones [18] and the current developed mathematical model.

CHAPTER
Five

A Parametric Study for the Combo-Bag Distribution System and Blockage Study

5.1 Introduction and Problem Definition

Having verified the developed mathematical model, both qualitatively and quantitatively, a parametric study is carried out using the same geometrical configuration [Figures 4.1-2] of the DC caster and physical properties of the aluminum alloy listed in Table 4.1. The importance of this parametric study stems from the fact that end users of direct chill (DC) cast aluminum slabs are demanding better and more uniform physical properties from these products. Macrosegregation, for example, is a source of non-uniformity of aluminum slabs produced via DC casting. In addition, macrosegregation can not be mitigated through processing of the casting after solidification is completed. Therefore, understanding macrosegregation and defining factors that promote and/or resist macrosegregation is essential to treat it beforehand. There comes the importance of the parametric study in identifying these factors and determining the extent of their importance in enhancing and/or diminishing a certain phenomenon. And thus, trying to come up with the optimum operational conditions and design that suit the needs of the industry.

For reasons of getting fast convergence, most of the calculations in this chapter were made using a converged input data as an initial guess. The procedure involves the introduction of better approximations into the program by imposing a certain flow field and solidification front as an initial guess, and then running the program so that the newly imposed boundary conditions are sensed by the calculation domain. In return, the convergence time is reduced by 80% of the time the program usually takes to converge

running from a set of arbitrary initial guessed values of the field parameters. Moreover, running the program from arbitrary set of values would require a lot of efforts in getting the right grid distribution before convergence could be attained. The error introduced by following the procedure of supplying the program with a converged result as an initial guess is very minimal, and after all, it is still within the engineering accuracy. The above mentioned procedure is found to be an excellent way of simulating physical-water models with the energy equation and the buoyancy term still included in the mathematical model.

The parametric study reported here covers the effects of casting speed, primary cooling rate, melt superheat, combo-bag dimensions, and combo-bag blockage on fluid flow and solidification of a 3104 aluminum alloy. Regarding the casting speed effect, the code was run for three casting speeds; namely, 40, 60 and 80 mm/min, all for a fixed initial superheat of 65°C. Concerning the effect of bag dimensions, two combo-bags were simulated, the standard combo-bag with dimensions of 50 x 330 x 152 mm, and the small combo-bag with dimensions of 50 x 166 x 152 mm in the x, y, and z directions, respectively.

It is well known to the industry that after some operational time, the combo-bag windows are often get blocked that ranges from partial to complete blockage due to particles deposition. Many plants use ceramic filter units as well as degassing units to remove solid particles from the molten aluminum. A filter unit comprises of a ceramic foam or sponge which can be cast into various configurations and porosities depending on the metal flow rate and type of particles in the melt. As the metal flows through the internal passages of the filter, the complex eddies and currents created there causes solid particles to be deposited thus cleaning the metal. The metal level on each side of the filter is monitored via non-contacting sensors so that it is possible to check whether the filter is becoming blocked up and change the filter is necessary to avoid possible metal spillage. For the purpose of studying the effect of blockage on the melt flow and solidification, the worst case scenario of window blockage has been simulated using the presently developed mathematical model. The scenario is illustrated in the complete blockage of the bottom windows of the standard combo-bag. Melt flows are allowed only through the

side windows facing the narrow sides of the mold. In the blockage study, the casting speed is fixed at 60 mm/min, while the temperature superheat is set at 65°C.

The effect of changing the primary coolant rate is implemented in the mathematical model through changing the heat transfer coefficient of the primary coolant. In addition to the standard primary coolant heat transfer coefficient of 2.5 kW/m^2K, used widely in the literature, two other coefficients are studied; these are the 0.5 and 8.0 kW/m^2K. In studying the effects of this parameter, the standard combo bag is used, the temperature superheat is fixed at 65°C, and the casting speed is set at 50.8 mm/min. With regard to the temperature superheat, the effect of three different inlet temperatures, corresponding to the 32, 65 and 100°C superheat, is investigated.

5.2 Assumptions

The assumptions used in the current parametric study are summarized in the following points:

1. The process is steady state with respect to a fixed-coordinate system (Eulerian approach).
2. Molten aluminum behaves as an incompressible Newtonian fluid.
3. Thermophysical properties of aluminum are invariant.
4. Density and thermal conductivity of the solid phase are equal to those of the liquid phase.
5. No viscous dissipation.
6. Variation in liquid fraction in the mushy zone is assumed to be linear.
7. Turbulent viscosity is calculated using low Reynolds two-equation k-ε turbulent model.
8. Solidification occurs under equilibrium condition.
9. The slag layer is assumed to be flat and fixed at a constant level.

5.3 Results and Discussion

All calculations were carried out for a grid size of 52 x 50 x 24, i.e., the total number of non-linear discretized equations that have to be solved for each of the seven dependent variables is 62400/iteration. The dependent variables are the pressure, the three velocity components, the kinetic energy of turbulence (k) and its rate of dissipation (ε), and the energy. The grids are unevenly but arbitrarily distributed with more grids located at the distribution-bag region and near the moving surface of the slab, as well, near the expected position of the solidification front. Due to the huge volume of output data and the difficulty of handling such data, only few typical cases of the 3D-surface plots are presented. However, the discussion will mainly focus on comparing 2D cross-sectional plots for different values of the parameters showing the most important effects the studied parameter has on the melt flow and solidification. A typical run, starting from a converged result as an input data, takes around 24 hrs on a 333 MHz PC machine.

Figure 5.1 shows a typical 3D-surface plot for the calculation domain (a quarter of the aluminum slab) using the standard combo bag. The results are shown in terms of the vector field, the streamlines and the temperature contours in which the casting speed is 80 mm/min and the temperature superheat is 65°C. In presenting the vector and streamline results, only the parts showing the sump are presented and magnified for the purpose of clarifying the results. Figure 5.1 (a) shows the general characteristics of the melt flow in the liquid sump using the combo bag as the melt distribution system. These flow characteristics include the two streams of hot melt issuing from the side and bottom windows of the bag. The figure shows also the two recirculations, vertical and horizontal, caused by the deflection of the hot stream, coming from the side window of the bag, by the inside surface of the mold. The vertical recirculation can clearly be seen at the wide symmetry plane (xy-plane) in the streamline plot of Figure 5.1 (b). The stream of hot melt coming from the bottom window helps in placing the center of the vertical recirculation at any place within the wide-symmetry plane. The present mathematical model results, for the first time, explains the critical role played by the downward stream of melt issued from the bottom window of the combo bag in shaping the solidification front as will be explained later. The horizontal recirculation can clearly be seen at the slab

free surface in Figure 5.1 (b), while the angle flow can be seen at the narrow-symmetry plane (xz-plane) of the same figure. Figure 5.1 (c) shows the temperature contours in a flooded format for the entire calculation domain including the liquidus (928 K) and solidus (903 K) temperature contours. The mushy layer is located between these two temperatures.

5.3.1 Effect of Casting Speed

Figure 5.2 depicts the computed results for the 40, 60 and 80 mm/min casting speeds at the wide symmetry plane. The results are presented in terms of velocity vectors, streamlines, and temperature contours using the standard combo bag. The temperature superheat is fixed at 65°C. Figure 5.2 (a, d, g) shows that an increase in the casting speed causes the velocity field within the liquid sump, in general, to be increased so that the mass flow is conserved. The increase in the velocity field can clearly be seen in the increased length of the velocity vector issued from the bottom window of the combo bag.

Figure 5.2 (c,f,i) shows that an increase in the casting speed causes the solidification front, presented by the 903 K contour line, to be pushed deeper. The solidification profile is departed from having the classical parabolic profile, the profile taken if only conduction is considered, to the more horizontally-uniform profile at and around the slab central region. The parabolic profile is the one used by most of the researchers in designing the pre-defined solidification front in their physical water model experiments. This profile is based on real casting experimental measurements. Therefore, the general shape of the solidification front is successfully predicted by the current mathematical model. For the 40 mm/min casting speed, the almost horizontally-flat part of the solidification front is extending to around 180 mm in the y-direction from the slab center, whereas, in the case of 60 mm/min and 80 mm/min, the same sections of the solidification front are extending to 350 and 400 mm from the slab center, respectively. The increased uniformity of the solidification front with the increase in the casting speed is a very desirable metallurgical characteristic in DC casting for the following reasons. First, increasing the casting speed implies the increase in the production rate of aluminum slabs. Second, an increase in the flat part of the solidification front implies uniform heat

transfer is taking place over increased surface of the solidification front. The latter would allow the slab to have more homogeneous metallurgical characteristics. The increase in length of the almost-horizontally-flattened solidification front is attributed mainly to the stream of melt issued from the bottom widows of the combo bag, henceforth called the vertical jet. An increase in the casting speed causes the speed of the vertical jet to be increased. The vertical recirculation is pushed toward the solidification front by the action of the vertical jet. Consequently, the streamlines of melt traveling downward between the solidified periphery of the slab and the outer edge of the vertical recirculation are squeezed due to the downward movement of the vertical recirculation. Actually, the melt in touch with the outer edge of the vertical recirculation is accelerated more by the dragging effect of the downward component of this recirculation. The same thing happens to the melt in touch with the solidified periphery of the slab, since the later is moving downward with the casting speed. As a result, the velocity of the melt confined in between the two edges, the vertical recirculation and the outer solidified layer, is increased as shown in Figure 5.2 (a,d,g). In other words, the hot melt traveling along the solidified layer at the slab periphery is accelerating due to the fact that it is passing along a geometry which looks like a diverging-converging channel with downward moving edges. The channel is formed by the solidified layer at the slab-side periphery and the outer edge of the vertical recirculation shown clearly by the streamline cross-sections in Figure 5.2 (b,e,h). The accelerated hot stream of melt traveling downward causes the solidified front at and around the slab center to be pushed deeper, flatter, and extending horizontally more along the wide symmetry plane of the slab as shown in Figure 5.2 (c,f,i).

Looking at the point of onset of solidification on the narrow side of the slab of Figure 5.2 (c,i), it can be seen that an increase in the casting speed from 40 mm/min to 80 mm/min causes an axial delay in the onset of solidification by approximately 30 mm. A delay of this amount in the onset of solidification is considered substantial knowing that the axial active mold length is 70 mm. Moreover, in designing DC casters, it is very important to choose the proper casting speed which will produce a solidified layer capable of holding the pool of melt once the slab passes the mold region. In the case of

80 mm/min casting speed and 65°C superheat and with the specified geometrical configuration, the slab starts to solidify at 115mm in the axial direction from the free surface as seen by Figure 5.2 (i). Figure 5.3 shows the solidified layer thickness at the axial end of the mold (x = 145 mm) at the wide symmetry plane (z = 0) as a function of the casting speed. It is clear that with an increase in the casting speed, the solidified-layer thickness decreases. Thus, by the time the slab reaches the end of the mold for a casting speed of 80 mm/min, the solidified layer thickness is seen to be 31 mm.

Figure 5.4 presents 2D-cross sections parallel to the slab free surface for the same three casting speeds stated earlier. Figure 5.4 (a,d,g) shows the vector plot for the 40, 60, and 80 mm/min at a section 10 mm below the start of the active mold section[3] (x = 75 mm). As can be seen, the hot stream of melt issued from the side window of the distribution bag attains more momentum with the increase in the casting speed. In the case of 40 mm/min, the slab periphery is almost completely solidified. Whereas, in the case of 60 and 80 mm/min casting speeds, the slab rolling face and part of the narrow side are completely solidified. The part of the narrow side of the slab facing the side window of the distribution bag is the last to solidify due to the direct feeding of that part with the hot melt from the distribution bag.

Figure 5.4 (j-r) illustrates a cross-section taken at the axial end of the mold (x = 145 mm). As seen, the solidified layer is completely extending along the slab periphery regardless of the casting speed as shown by Figure 5.4 (l,o,r). The solidified layer at the slab-rolling face is thicker than the layer at the narrow side of the slab. However, the difference in the average thickness of the layers at the rolling face and the narrow face of the slab decreases with an increase in the casting speed. This difference, in the case of 40 mm/min casting speed, is approximately 20 mm, whereas it is only 5 mm in the case of 80 mm/min casting speed. Therefore, the higher the casting speed, the more uniform is the internal heat transfer along the entire surface of the slab at a certain axial distance. The last phenomenon is very much desired in DC casters for the production of slabs that have homogeneous surface characteristics. Establishing of a uniform heat transfer rate

[3] The active mold section is the mold length starting from the primary cooling and ending at the end of the mold.

around slab surface is one of the most important reasons why inlet melt distribution systems are important and included in DC casters.

5.3.2 Effect of Primary Coolant Heat Transfer Coefficient

Figure 5.5 illustrates part of the wide-symmetry plane, the part containing the liquid sump, for three different values of primary coolant heat transfer coefficient. Figure 5.5 (a-c) depicts the computed results for the lowest heat transfer coefficient of 0.5 kW/m^2K, while Figure 5.5(d-f) presents the computed results for the standard heat transfer coefficient of 2.5 kW/m^2K used in all the previous simulations. Figure 5.5 (g-i) demonstrates the results for the 8.0 kW/m^2K. The temperature superheat is fixed at 65°C, and the casting speed is maintained at 50.8 mm/min. Changing the value of the heat transfer coefficient of the primary coolant shows a little effect on the solidification front at the middle region of the slab, as would be expected due to small heat extraction area of the primary cooling region. However, it exerts more effect on the onset of solidification at the melt/mold contact region as well as on the distribution of temperature contours above the solidification temperature as shown by Figure 5.5 (c,f,i). An increase in the primary coolant heat transfer coefficient causes the point of onset of solidification to be shifted upward towards the slab free surface.

Figure 5.6 shows the point of start of solidification at the wide symmetry plane as a function of the primary coolant heat transfer coefficient. It is known that as more solidification takes place in the mold, the worst the slab surface characteristics become and vice versa [2]. Thus, the perfect surface characteristics would be achieved when solidification takes place with no mold existing at all such as in Electro-Magnetic Casting (EMC), where the electro-magnetic field replaces the mold in holding the molten surface. Due to the operational difficulties facing the EMC technology, most of the aluminum casters in the world, nowadays, are based on DC casting technology with the goal of achieving the same or almost the same surface characteristics of EMC. Among the many approaches followed to achieve this goal, the approach followed by Alcan Canada named as Alcan Sheet Mold (ASM), which was explained in the literature survey, seems to be

most promising. The approach can be summarized in delaying the solidification process in the mold and making most of the solidification to take place under high heat transfer rate at the secondary cooling region. Therefore, the reduction of the heat transfer of the primary coolant as well as the use of the shortest mold possible is desirable, yet a strong solidified layer capable of holding the molten aluminum core has to be established before the slab gets out of the mold. The figure shows that, starting from a low heat transfer coefficient, an increase in the coefficient will produce a relatively significant upward shift in the axial position of the point of onset of solidification up until a value of 2.5 kW/m^2K, beyond this value of the coefficient, a change in the coefficient will produce a minor change in the point of onset of solidification.

An increase in the heat transfer coefficient causes the mushy region at and around the slab center to expand toward the slab free surface. The mushy layer thickness at the slab center for h = 0.5 kW/m^2K is 200 mm, whereas the thickness for h = 8.0 kW/m^2K is 260 mm as can be seen Figure 5.5 (c,i). The extension of the hump of the mushy layer for the three values of the heat transfer coefficient is affected directly by the value of the upward component of the vertical recirculation in such away that an increase in the upward component of the vertical recirculation causes the hump of the mushy layer to expand toward the slab-free surface. An increase in the heat transfer coefficient causes the wake region, confined by the stream separated from the vertical recirculation, part of the angle flow [4] moving toward the solidification front and the entrained part of the angle flow by the vertical recirculation, to be shifted toward the slab center as shown in Figure 5.5 (b,e,f). For example, in the case of h =0.5 kW/m^2K, the wake region is located at 150 mm from the slab center, while for h=8.0 kW/m^2K, the same region is located at 84 mm from the center.

Figure 5.7 shows cross-sections taken at x= 85 mm (10 mm below the start of the mold active section) parallel to the calculation domain's free surface for the same parameter discussed above. Being the worst in terms of cooling, the slab corners are usually the first regions to solidify (solidification contour line 903 K) as shown in Figure 5.7 (c). Complete solidification of the outer slab surface is achieved at the same section

[4] Look at the definition of the angle flow in Chapter 4, page 59.

using the higher values of the heat transfer coefficient (h = 2.5 and h = 8.0 kW/m^2 K) as shown in Figure 5.7 (f,i). At the solidified section the v and w components of the velocity vector are zero, and the solidified section travels with the casting speed, which is normal to the plane of the paper, therefore the solidified region is shown as a blank space with no velocity vectors existing as shown by Figure 5.7 (d,g).

Figure 5.7 (j-r) illustrates a section taken at the end of the active mold section. At this section, the solidified layer covers the entire slab periphery for the three simulated values of the primary coolant heat transfer coefficient. The ratio of the average solidified layer thickness at the rolling surface to the average solidified layer at the narrow surface of the ingot is referred to as $\bar{l}$. A value of $\bar{l}$=1, meaning the two layers are equal, a situation the most desired in terms of getting good slab surface characteristics. The value of this ratio for the three simulated heat transfer coefficients is ranging from 0.5 to 0.6. Thus, not much can be established with regard to the uniformity of the thickness of the outside slab layer through the control of the primary heat transfer coefficient. However, it is known from experimental measurements in industry that the heat transfer coefficient in the transverse direction do not remain uniform. Due to the unavailability of reliable measured data for the heat transfer coefficient in the transverse direction, it is assumed to be uniform in all the simulated runs reported here.

5.3.3 Effect of Superheat

Figure 5.8 illustrates the effect of temperature superheat at the wide-symmetry plane for a fixed casting speed of 50.8 mm/min. The three simulated temperature superheats are, 32, 65, and 100°C. Not much can be drawn from the vector field and streamline figures which look more or less the same. It is to be noted that most of the energy released by aluminum during solidification comes from the release of latent heat. The sensible part of the heat forms only a small fraction of the total heat released. It is clear that an increase in the temperature superheat causes a little bit of delay in the onset of solidification at the mold as shown by Figure 5.8 (c,f,i). An increase in the temperature superheat causes the mushy layer thickness at the middle region of the slab to decrease. In the case of the 100°C superheat, a slight increase in the extension of the almost

horizontal solidification front at the slab center region is observed as shown in Figure 5.8 (i).

Figure 5.9 shows cross-sections parallel to and including the slab free surface for the three temperature superheats. Figure 5.9 (a,d,g) shows the spreading of the temperature contours at the free surface. Figure 5.9 (b,eh) illustrates cross-sections taken at x =95 mm. This figure shows that the onset of solidification is delayed for the 65°C and 100°C superheat melt only in the region of impingement of the hot stream on the narrow side of the mold presented by (y,z)=(660, ≤50). Excluding the impingement region on the narrow side of the mold, the temperature superheat has no effect on the onset of solidification as well as the solidified layer thickness at the rest of the narrow side and the wide side of the mold. Figure 5.9 (c,f,i) depicts a cross-section at the end of the mold region (x = 145 mm). The solidified layer is developed over the entire slab surface with almost the same thickness for the three temperature superheats. Therefore, the effect of the temperature superheat is only confined in the adiabatic–section and the upper region of the active section of the mold. This is in agreement with the experimental observations and reality as mentioned earlier that most of the heat in the melt is stored as a latent heat; the ratio of sensible to latent heat for Al-3103 is around 14%.

5.3.4 Effect of Comb-bag Dimensions

As mentioned in the introduction, the two combo bag distribution systems were simulated. The standard combo bag with dimensions of 50 x 330 x 152 mm and the small bag with dimensions of 50 x 166 x 152 mm in the x, y, z, respectively. The dimensions of the windows as well as the position of the bottom windows relative to the side wall of the bag are kept the same as the combo bag used in chapter four for both distribution bags. Figure 5.10 shows the computed results for both bags at the wide symmetry plane. The casting speed and the temperature superheat are fixed at 60 mm/min and 65°C, respectively. The figure shows a significant change in the flow field of the two bags. The standard bag is showing the two regular melt streams issued from the side and bottom windows as shown in Figure 5.10 (a). Whereas in the case of the small bag, a change in the course of the melt going through the bottom window is noticed, i.e. a melt stream

from the sump is found to be going through the bottom window of the bag into the bag instead of going out of it as shown in Figure 5.10 (d). This stream, henceforth, will be called the reverse flow. The reverse flow is enhanced by the position of the bottom window in the bag. This position is happened to coincide with the wake created by the melt coming through the inlet nozzle, as this melt bounces up after hitting the inside-bottom-impervious surface of the combo bag. As a result, a positive axial pressure gradient is created across at more than half of the areas of the bottom window.

Figure 5.11 shows the positive pressure across the bottom window of the bag. It is clear from the figure that more than half of the bottom window's area as well as most of the rest of the bag up until the side window are located under the positive pressure. The staggered position of the bottom window relative to the positive pressure shown in Figure 5.11 is the reason behind the tilting in the direction of the vector arrows of the reverse flow shown in Figure 5.10 (d). The other factor which contributed to the flow of melt from outside the bag into the bag is that the position of the bottom window is located exactly on top of the upward component of the vertical recirculation at the wide symmetry plane. Therefore, the reverse flow is caused by a combination of a positive-axial-pressure gradient across the bottom window and an upward flow of melt under the bottom window. Eventually, the location of the bottom window within the small bag is the motive behind the action of the two mentioned factors (positive pressure and upward flow outside the bag) in producing the reverse flow. It is interesting to mention here that Xu et al. [16] reported, in their physical water experiment on a small combo bag having the same dimensions as the one modeled by the current developed mathematical model, that the issuing streams from the short combo bag were combined in one stream, i.e. they observed only one single stream coming out of the combo bag. Considering the fact that in their physical water experiment, it was impossible to analyze the fluid motion inside the bag, therefore, the reverse flow could have been the reason behind their observation of one single stream of fluid coming from the combo bag, which is the stream coming out from the side window. A flow situation of this type is to be avoided when designing a DC caster distribution system. This shows one of the powerful abilities of the current mathematical model in predicting undesired flow characteristics within the DC caster

such as the one explained by the phenomenon of reverse flow. If such a situation is predicted, an adjustment in the design of the combo bag has to be carried out to prevent this phenomenon from taking place.

As a further illustration in the differences in the flow fields for the two distribution bags, the v-component of velocity distribution for both bags are drawn in Figure 5.12. This figure presents the transverse distribution of the v-component of velocity, starting from the slab center to the slab side wall, along a line passing through the middle of the side window of the bag (x=37 mm). There are many observations that can be withdrawn from the mentioned figure. Firstly, the flow field results can be investigated at any place within the ingot such as inside the combo bag itself. Secondly, the v-component distribution using the standard combo bag is starting from zero at the slab center where the u-component having its maximum value. For both bags, as the observer moves along the positive y-direction, the v-velocity increases rapidly to reach a maximum value of 23333 mm/min at around 25 mm from the slab center. This region corresponds to the point where the flow spreads out horizontally after hitting the impervious inside-bottom surface of the bag. The rapid increase and decrease in the v-velocity (first peak) is a characteristic of a vertical recirculation within the bag. Subsequently, for the standard bag, a minimum in the v-velocity of 2400 mm/min at 80 mm from the slab center is rapidly attained, followed by a smaller peak located at 125 mm from the slab center. Finally, a gradual decrease in the velocity is observed along the rest of the transverse line until the slab side wall. Whereas, in the case of the small bag, there is neither a minimum nor a small maximum in the v-velocity curve after the first peak, but rather a sudden drop followed by a gradual decrease is occurring after the first peak. The v-velocity curve has a small bulging after the first peak due to the earlier explained reverse flow. The melt issued via the side window of the bag losses momentum faster than that in the case of the standard bag. This can be seen in the v-velocity distribution curve for the melt out of the small bag, the curve lies under the v-velocity distribution curve of the standard bag. Due to this, the narrow side wall of the mold is approached with a higher velocity using the standard bag, whereas in the case of the

small bag the velocity is almost zero due to the early mixing of the melt with the melt in the surrounding sump.

Figure 5.13 shows the computed results at cross-sections parallel to the slab free surface. Figure 5.13 (a-c) illustrates the velocity vectors, streamlines and temperature contours using the standard combo bag at the free surface, while Figure 5.13 (d-f) depicts the same results using the small-combo bag. Once more, the vector field results for both bags show clearly the early dispersion of the issued melt using the small bag through the closeness of the recirculation center at the free surface from the narrow-symmetry plane, whereas, the center in the standard combo bag case is far from the narrow-symmetry plane as shown in Figure 5.13 (a,b,d,e). The early dispersion of the issued melt in the case of the small bag causes the temperature contours to have a more transverse distribution as compared to the temperature contours caused by the standard bag in which the temperature contours are characterized by a more like longitudinal distribution as can be seen in Figure 5.13 (c,f) by the 958 and 950 K temperature contours. This small bag feature can be utilized in increasing of the heat transfer through the slab rolling face and decreasing it through the slab-narrow face.

Figure 5.13 (g-l) depicts the computed results at a section positioned at the middle of the molds active region (x = 115 mm). In case of the small bag, the sump core is cooled faster than in the case of the standard bag as seen by the temperature contours in Figure 5.13 (i,l). Moreover, the solidified layer at the narrow side of the slab is thicker in the case of the small bag than in the case of the standard bag. The narrowness of the solidified layer for the standard combo bag can be attributed to the stronger downward currents of hot melt. These currents are the result of deflection of the issued stream from the side window as the later stream hits the narrow side of the mold as seen in Figure 5.13 (g,j). The early mixing of the melt stream, coming from the side window of the small-combo bag, with the surrounding sump prohibits this hot stream from reaching the narrow-side of the mold, and causing the solidified layer to be thicker.

5.3.5 Combo Bag Blockage Study

The combo-bag blockage study is conducted to show that not only can the current developed mathematical model be used in the early stages of DC caster and distribution system design, but it can also be used in simulating the anticipated flow situations that result from a long working period of the DC caster, such as those ensuing from the blockage of the bottom windows of the combo bag. In the current blockage study the standard combo bag is used as the melt distribution system. A complete blockage of the bottom windows is simulated. The casting speed and temperature superheat are fixed at 60 mm/min and 65°C, respectively. Figure 5.14 shows a 3D-surface plot of the computed results without blockage, while Figure 5.15 illustrates the results for the case of complete blockage of the bottom windows. The results are presented in terms of the velocity vector fields, streamlines, and temperature contours. The part consisted of the sump is magnified and presented in the vector and streamline figures. The full calculation domain is shown for the temperature-contour plots.

Looking at the vector and streamline figures, it is clear that the most affected region, as a result of the blockage, is the wide symmetry plane. Figure 5.15(a) shows that the jet stream has disappeared from the bottom of the combo bag. Consequently, the melt inside the combo bag is forced to exit the bag through the side window. The increase in the momentum of the side-window stream causes two recirculations; the vertical recirculation zone at the wide symmetry plane and the horizontal recirculation zone at the slab-free surface. The increase in momentum causes the two recirculations to rotate with higher speeds as can be seen from the vector field. As a result, the vertical recirculation is axially extended as compared to the case of no blockage of Figure 5.14 (b). The melt flowing along the wide side of the mold reaches the narrow symmetry plane, and then, it turns toward the slab center due to the symmetry boundary condition. Upon arriving at the slab center, the flow splits into two streams. One recirculates at the slab free surface, and the other forms the angle flow which can be seen at the narrow-symmetry plane of Figure 5.15 (b). Once the angle flow arrives at the wide-symmetry plane, it changes course to travel toward the narrow side of the slab, and splits into two other streams. One stream is entrained by the vertical recirculation at the wide symmetry plane, and the other

is directed toward the solidification front as seen from the wide symmetry plane in Figure 5.15 (b). The center of the vertical recirculation at the wide-symmetry plane is pushed more toward the side wall of the slab, as compared to the case of no blockage of Figure 5.14 (b).

Figure 5.16 reveals the computed results at the wide symmetry plane for the previously shown calculation domains for blocked and unblocked bottom window conditions. This plane is exclusively presented since it is the most affected region in the ingot. Figure 5.16 (a) shows the stream of melt issued through the bottom window of the combo bag. The bottom jet of melt is completely disappeared from Figure 5.16 (d) due to the complete blockage of the respective window, and the region is replaced by the entrained melt coming from the slab center. Since the melt stream from the side window is issued with a higher momentum as a result the vector arrows are longer. Figure 5.16 (b) illustrates the streamlines at the wide symmetry plane for the unblocked bag. It can be seen that the bottom jet is acting as a shield and is preventing the melt coming from the slab center from being entrained by the stream of melt issued from the side window. Moreover, the melt coming from the slab center is dragged by the stream issued from the bottom window. Consequently, the vertical recirculation is pushed down toward the solidification front, and its center is made to approach the slab center. While in the case of window blockage, the melt stream coming from the slab center under the distribution bag is entrained by the melt issued from the side window, causing the center of the vertical recirculation to be slightly lifted up and out toward the side wall of the slab as shown in Figure 5.16 (e). In addition, the vertical recirculation is axially extended. Figure 5.16 (c,f) reveals the effect of unblocking and/or blocking of the bottom windows on the mushy region at the wide symmetry plane. An inclined swelling in the mushy layer from the liquidus side is formed in the case of the blocked bag. The inclined hump in the mushy layer is parallel to the upward-tilted part of the vertical recirculation shown in Figure 5.16 (e). However, in the case of the unblocked bag, the mushy layer is squeezed from the liquidus side due to the jet stream of melt coming from the bottom window of the bag.

Figure 5.17 demonstrates the v-velocity distribution at the wide symmetry plane along a line passing along the middle of the side window (x = 37 mm) for the unblocked and blocked bottom window cases. The side window stream is acting in a similar manner to a side-aligned-submerged jet, where the melt stream is directly injected to a miscible atmosphere. The figure is presented due to the crucial information that can be drawn out of it, such as the different experiences the side window stream goes through as it mixes with the sump. These experiences include:

a- the initial mixing region,

b- the established jet region,

c- the stagnation region,

d- the wall jet region.

A complete definitions of the above terms and a comprehensive study of submerged jets can be found in Kamal [52]. The figure shows that the two curves beginning from the center and going in the increasing y-direction are in a complete match until the start of the bottom window opening at y = 133 mm. At that stage, a slight increase is followed by a decrease in the v-velocity as the stream passes over the bottom window for the no blockage case. Right after the small peak, located at around y = 135 mm in the no blockage case, larger peaks are appearing now for both cases of with and without blockage. The two peaks is a characteristic of the flow when going through an opening in the bag, in this case it is the side window of the bag. The hump corresponding to the blockage case is located over the no blockage hump due to the loss in momentum incurred earlier by the no blockage stream when part of this stream goes through the bottom window. Whereas, in the case of blockage, the side window is approached with a higher momentum, and thereby, resulting in a bigger v-velocity hump. As the melt travels along the y-direction, a gradual decay in the v-velocity is seen to take place in both cases due to the mixing with the surrounding sump. The narrow side of the mold is approached with almost the same velocity in both cases, unlike the case discussed earlier concerning the bag dimensions, where it was seen that the narrow side wall of the mold, in the case of the standard bag, was approached with a higher velocity than that in the case of the

small bag as shown earlier in Figure 5.12. Therefore, the bottom window blockage has almost no effect on the velocity of approach to the narrow-side wall of the mold.

5.4 Closure

A comprehensive parametric study of five influential factors on the melt flow, heat transfer and solidification in a vertical DC casting mold using a combo bag as a metal distribution system has been carried out. The studied parameters are the casting speed, primary cooling rate, melt superheat, combo-bag dimensions, and complete blockage of the bottom windows of the distribution bag. A more in depth understanding of some of the behaviors of the fluid flow and solidification in the steady state phase of the DC casting process is achieved such as:

- The role played by the melt stream issued from the bottom window of the bag in controlling the position of the vertical recirculation, where this jet is found, to a certain extent, to be responsible in pushing the vertical recirculation downward.

- The role played by the position of the vertical recirculation within the sump in accelerating and/or decelerating the stream of melt confined between the outer edge of this recirculation and the outer solidified periphery of the slab. The depth and the horizontal extension of the solidification front are greatly affected by the strength of the momentum of the latter stream. The greater the momentum of the hot stream is, the deeper the solidification front will be.

- The prediction of the reverse flow as well as the explanation of the reasons behind this undesirable flow phenomenon.

- The relation between the casting speed and the thickness of the outer solidified layer is clearly demonstrated. This relation would help the DC cast designer in specifying an upper and a lower bound for the casting speed.

- The difference between the average thickness of the solidified layer at the slab rolling face and the average thickness of the solidified layer at the slab narrow face, and the relation of this difference to the casting speed.

- The velocity of approach of the melt issued from the side window to the narrow side of the mold and its dependence on the bag dimensions and its near independence on the blockage.

The author is not aware of any other mathematical model whereby predictions and explanations are provided for most of the above mentioned points, especially, the first three points. The above and other phenomena explained earlier in the current parametric study shows how strong prediction abilities the current developed mathematical model could provide to the DC cast designer. Using the model, either in the early stages of the DC caster design or after some operational time, the designer can easily and safely adjust and optimize the design parameters in the shortest time possible and without going through a heavy financial burden. A further demonstration of the use of the current developed mathematical model is provided by simulating a DC caster that produces ingots with a larger aspect ratio. The latter study is carried out in the following chapter. In the following study, a channel bag is used as a melt distribution system instead of a combo bag.

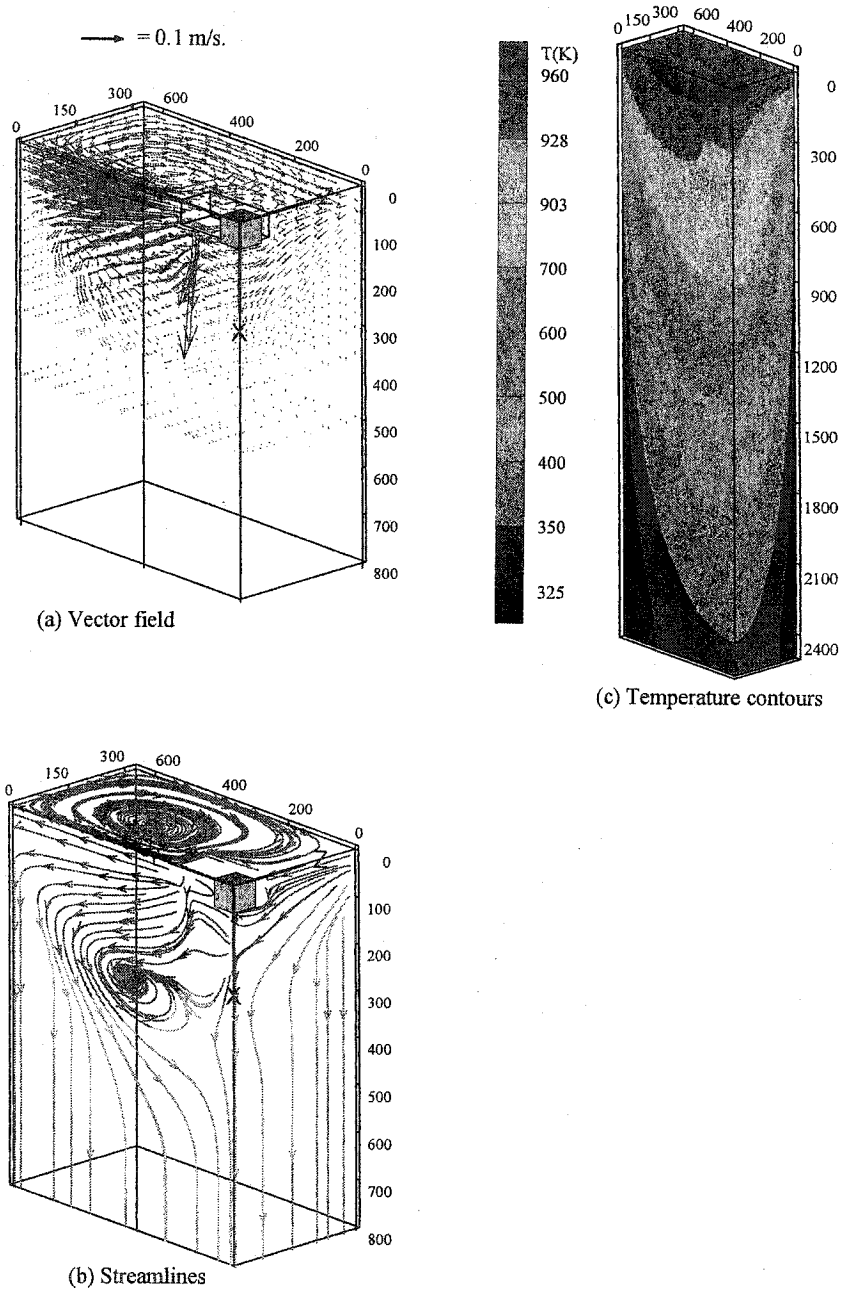

Figure 5.1: 3D-surface plot for the computed results using the standard combo bag, casting speed = 80 mm/min, temperature superheat = 65 °C.

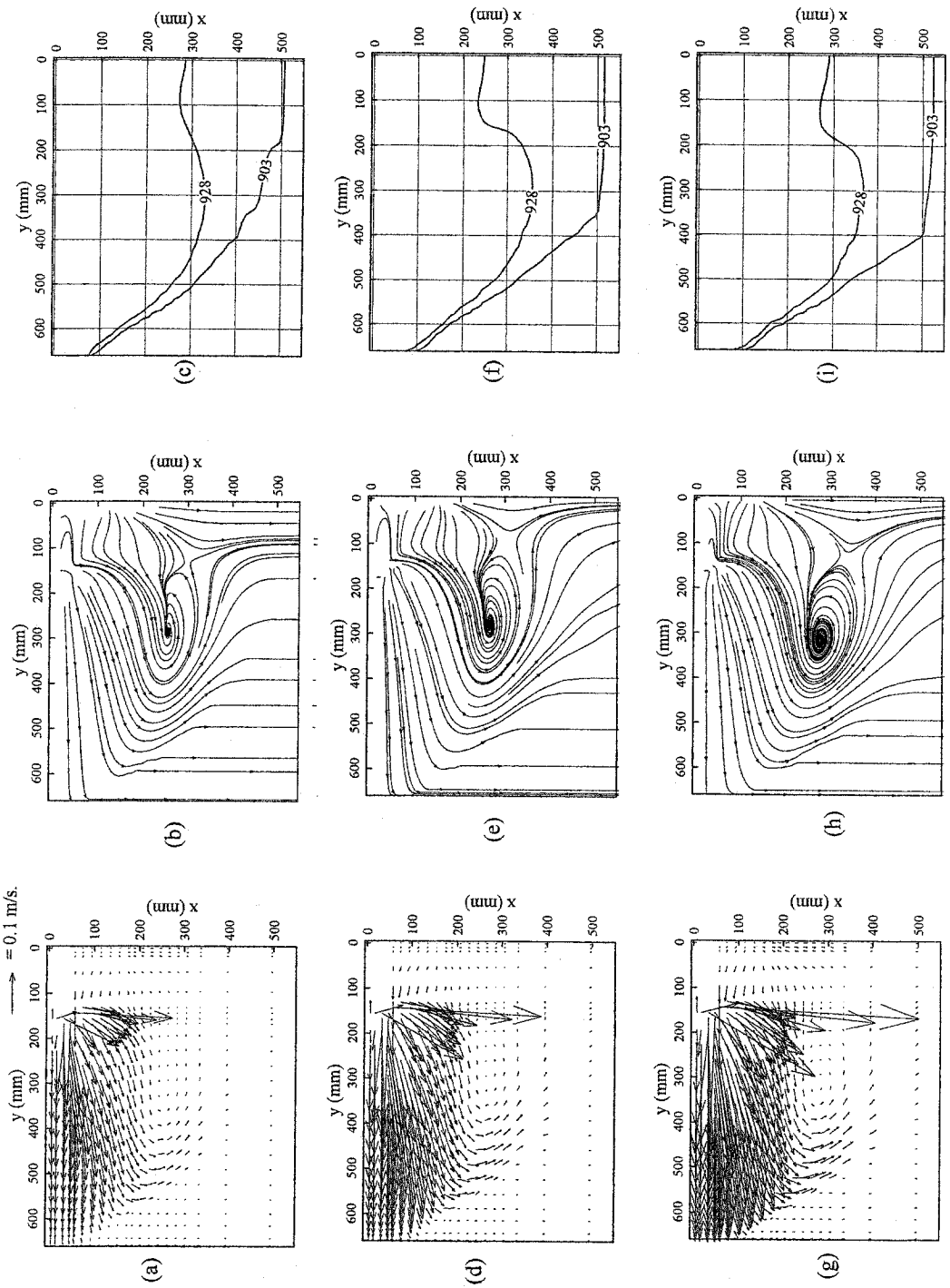

Figure 5.2: Computed results for three casting speeds at the wide symmetry plane: (a,b,c) casting speed =40 mm/min, (d,e,f) casting speed = 60 mm/min, (g,h,i) casting speed = 80 mm/min. Temperature superheat = 65°C.

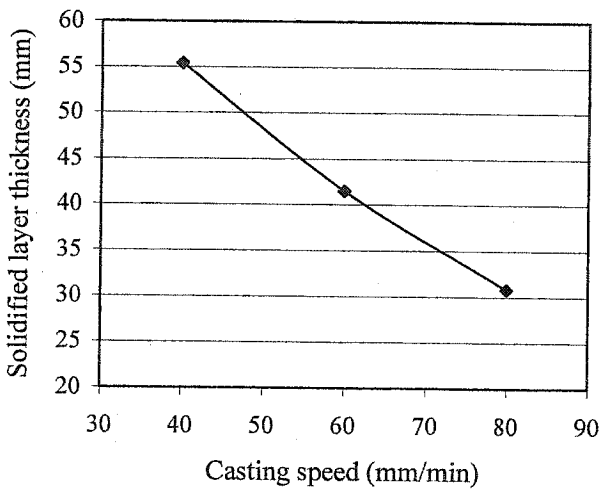

Figure 5.3: Solidified layer thickness versus casting speed at the axial end of the mold (x =145 mm), at the wide symmetry plane.

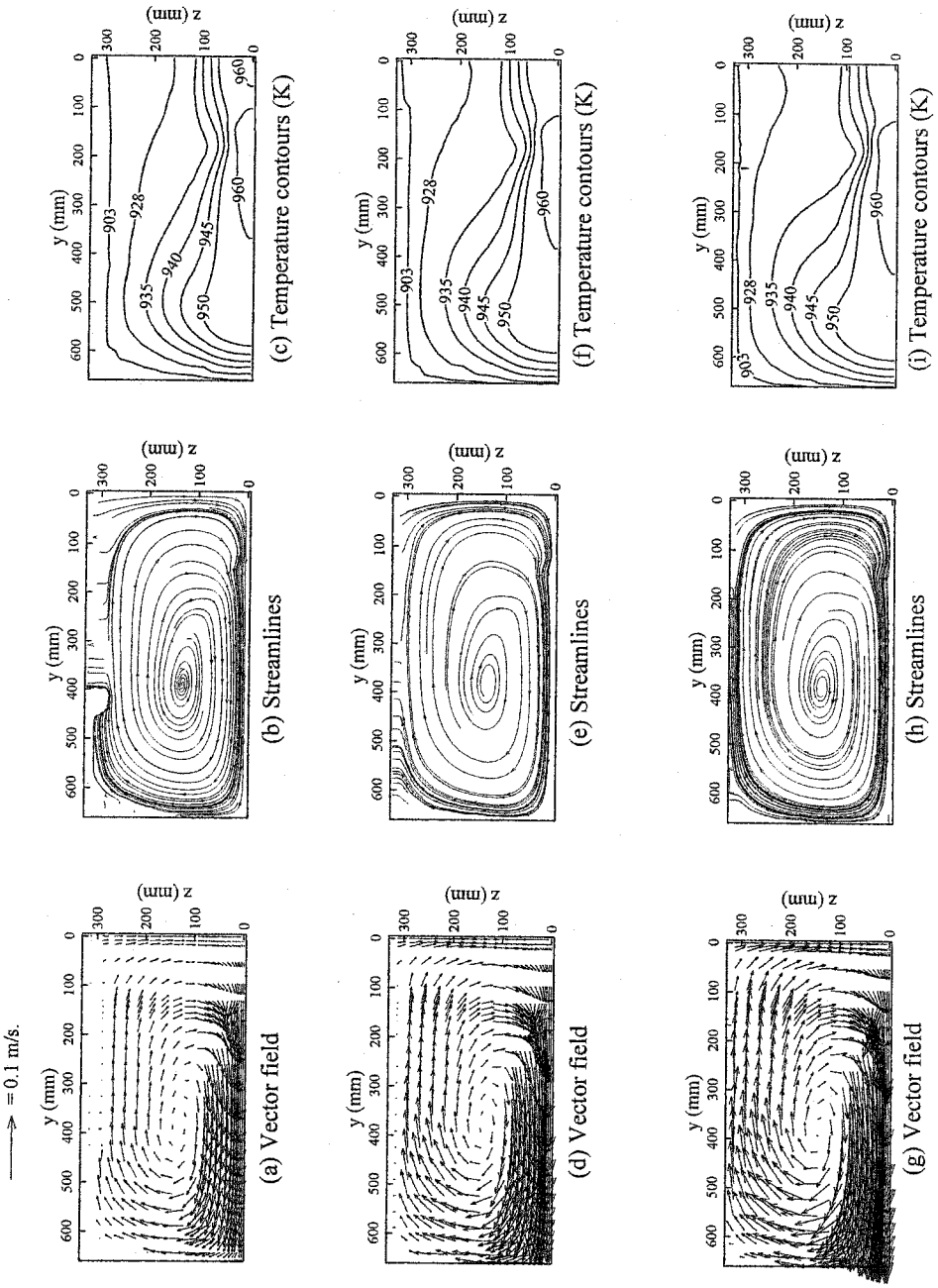

Figure 5.4: Computed results for three casting speeds at x = 85 mm, temperature superheat = 65°C (Mold region). (a,b,c) casting speed = 40 mm/min, (d,e,f) casting speed = 60 mm/min, (g,h,i) casting speed = 80 mm/min.

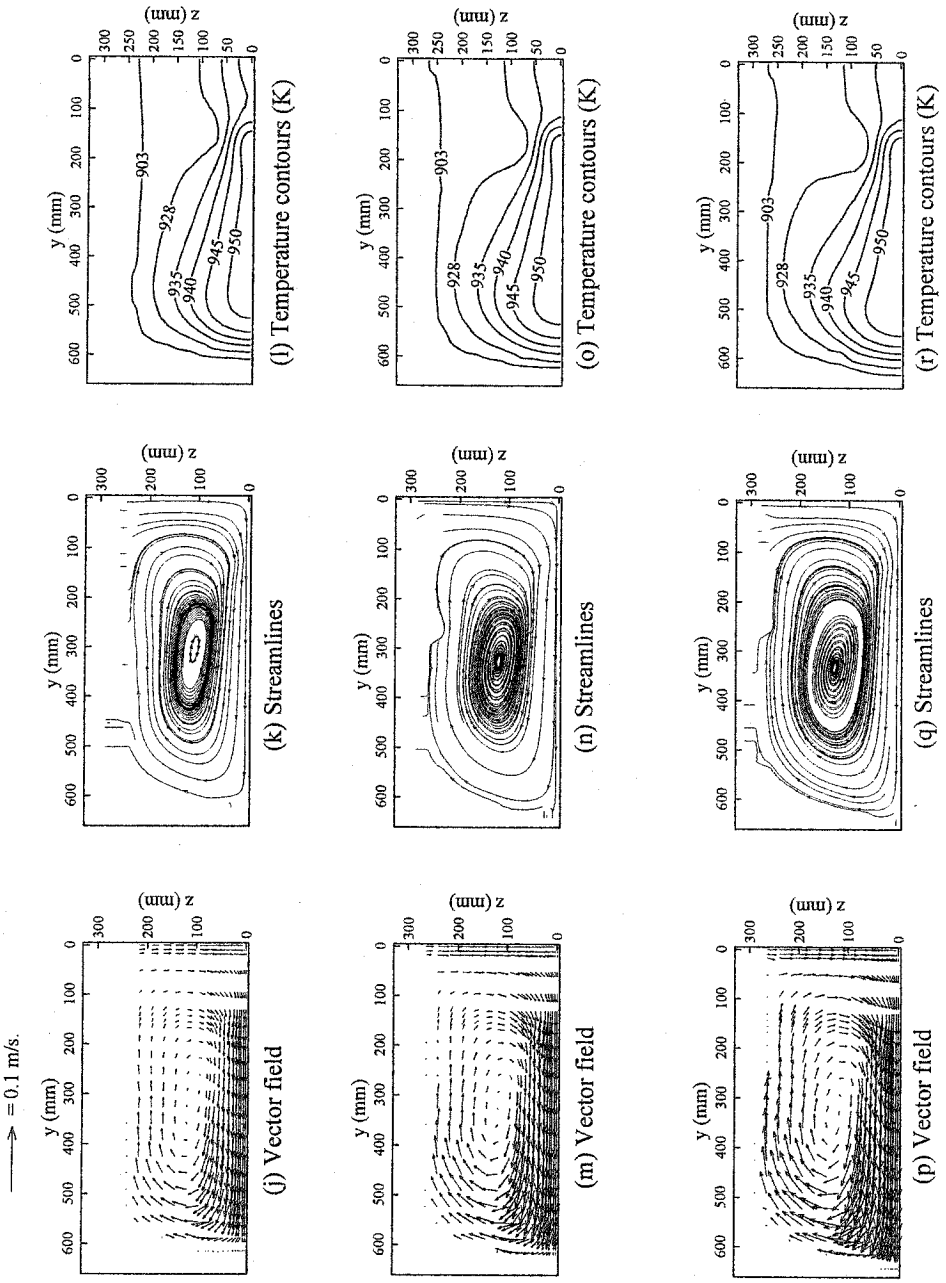

Figure 5.4 (continue): computed results for three casting speeds at x = 145 mm, Temperature superheat = 65°C. (j,k,l) casting speed = 40 mm/min, (m,n,o), casting speed = 60 mm/min, (p,q,r) casting speed =80 mm/min.

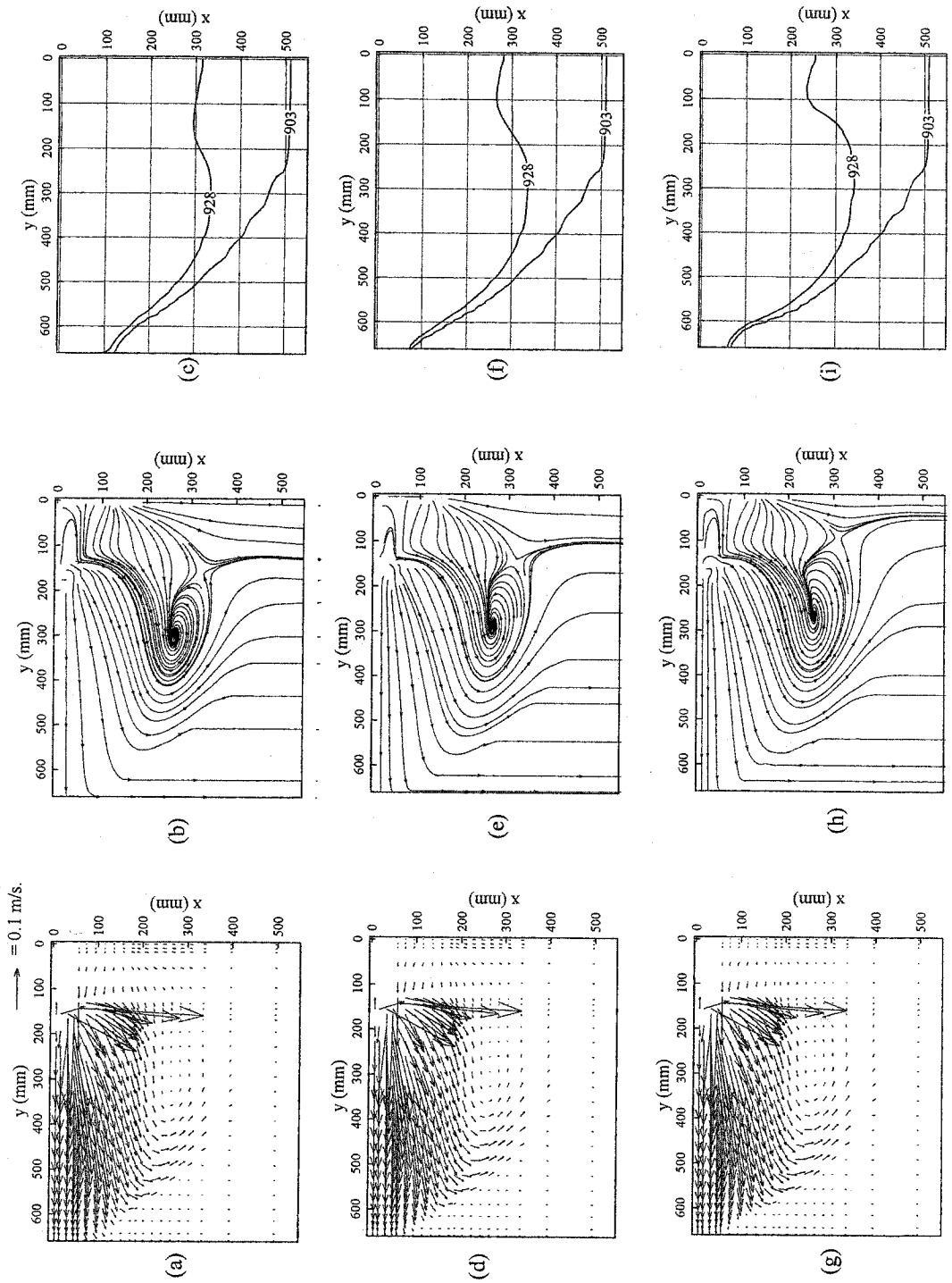

Figure 5.5: Effect of primary coolant heat transfer coefficient at the wide-symmetry plane. Casting speed = 50.8 mm/min, temperature superheat = 65 °C, (a,b,c) h = 0.5 kW/m^2 K , (d,e,f) h = 2.5 kW/m^2 K, (g,h,i) h = 8.0 kW/m^2 K.

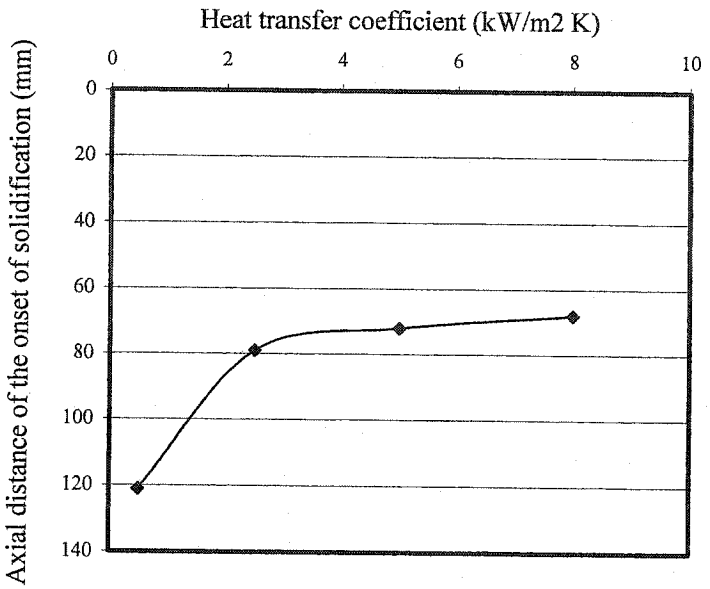

Figure 5.6: Effect of primary heat transfer coefficient on the onset of solidification along the narrow face of the slab at the wide symmetry plane

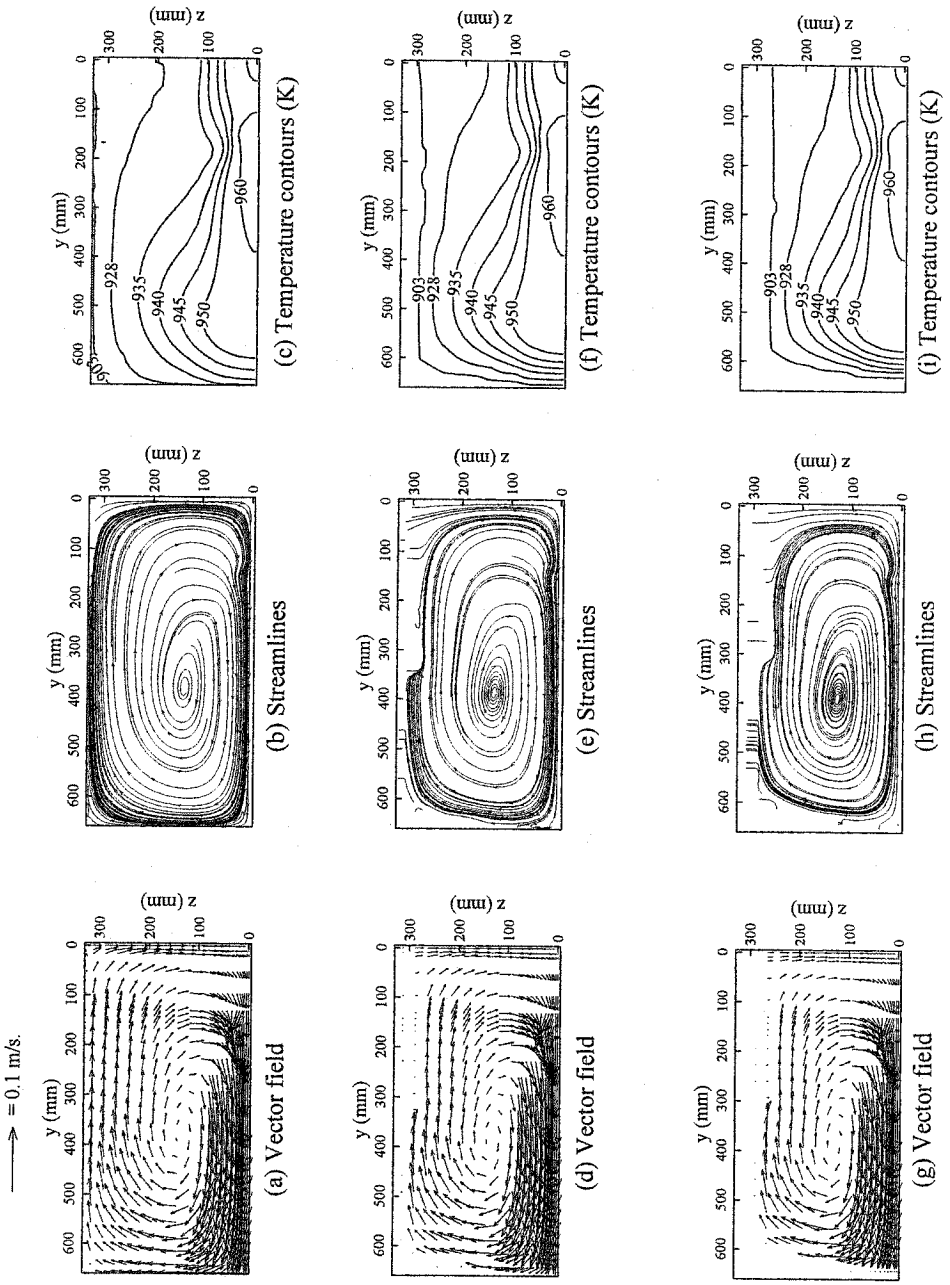

Figure 5.7: Effect of primary coolant heat transfer coefficient at x = 85 mm. Casting speed = 50.8 mm/min, temperature superheat = 65 °C, (a,b,c) h = 0.5 kW/m^2 K, (d,e,f) h = 2.5 kW/m^2 K, (g,h,i) h = 8.0 kW/m^2 K.

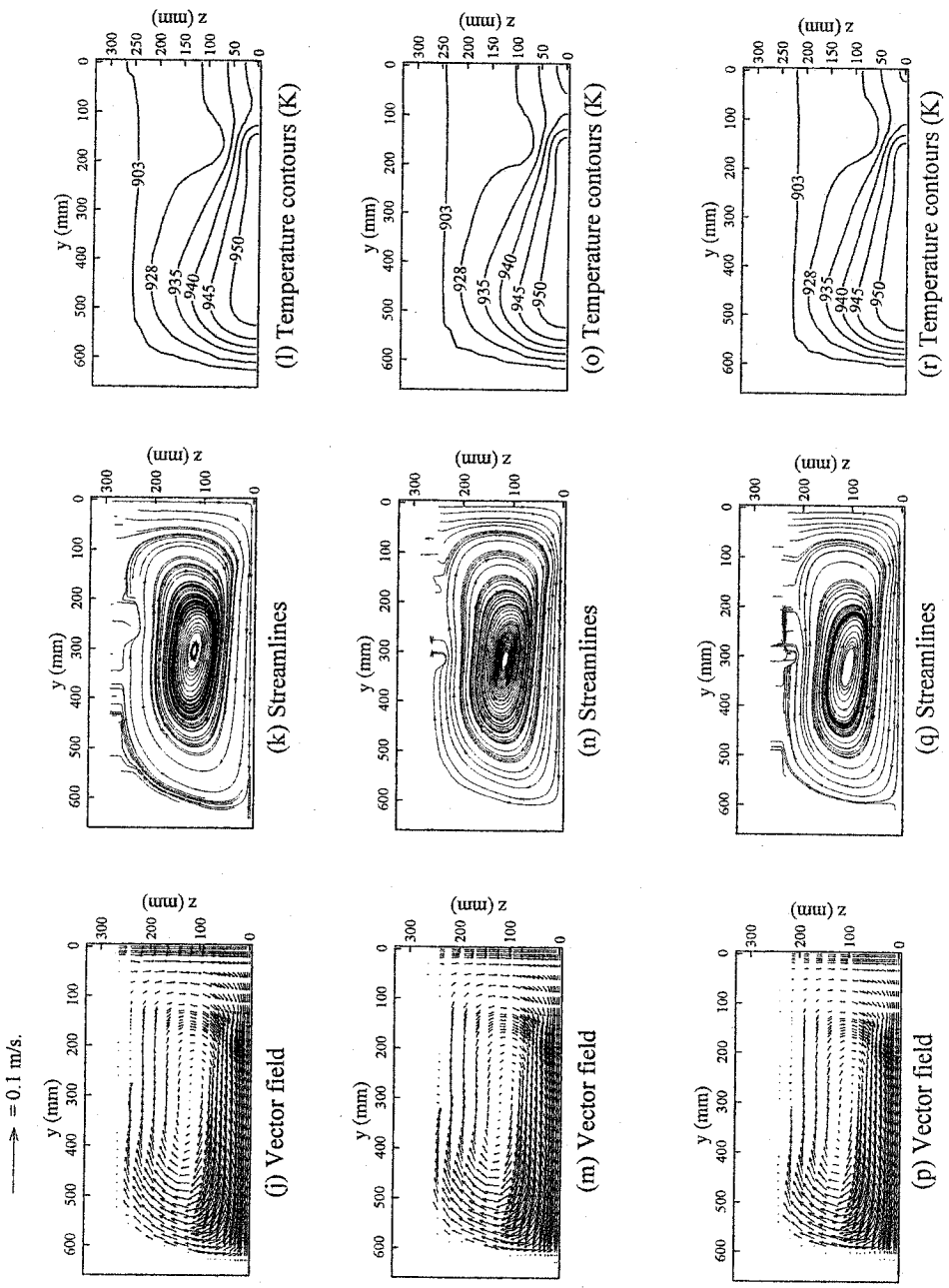

Figure 5.7 (continue): Effect of primary coolant heat transfer coefficient at x = 145 mm. Casting speed = 50.8 mm/min, temperature superheat = 65°C, (j,k,l) h = 0.5 kW/m^2 K, (m,n,o) h = 2.5 kW/m^2 K, (p,q,r) h = 8.0 kW/m^2 K.

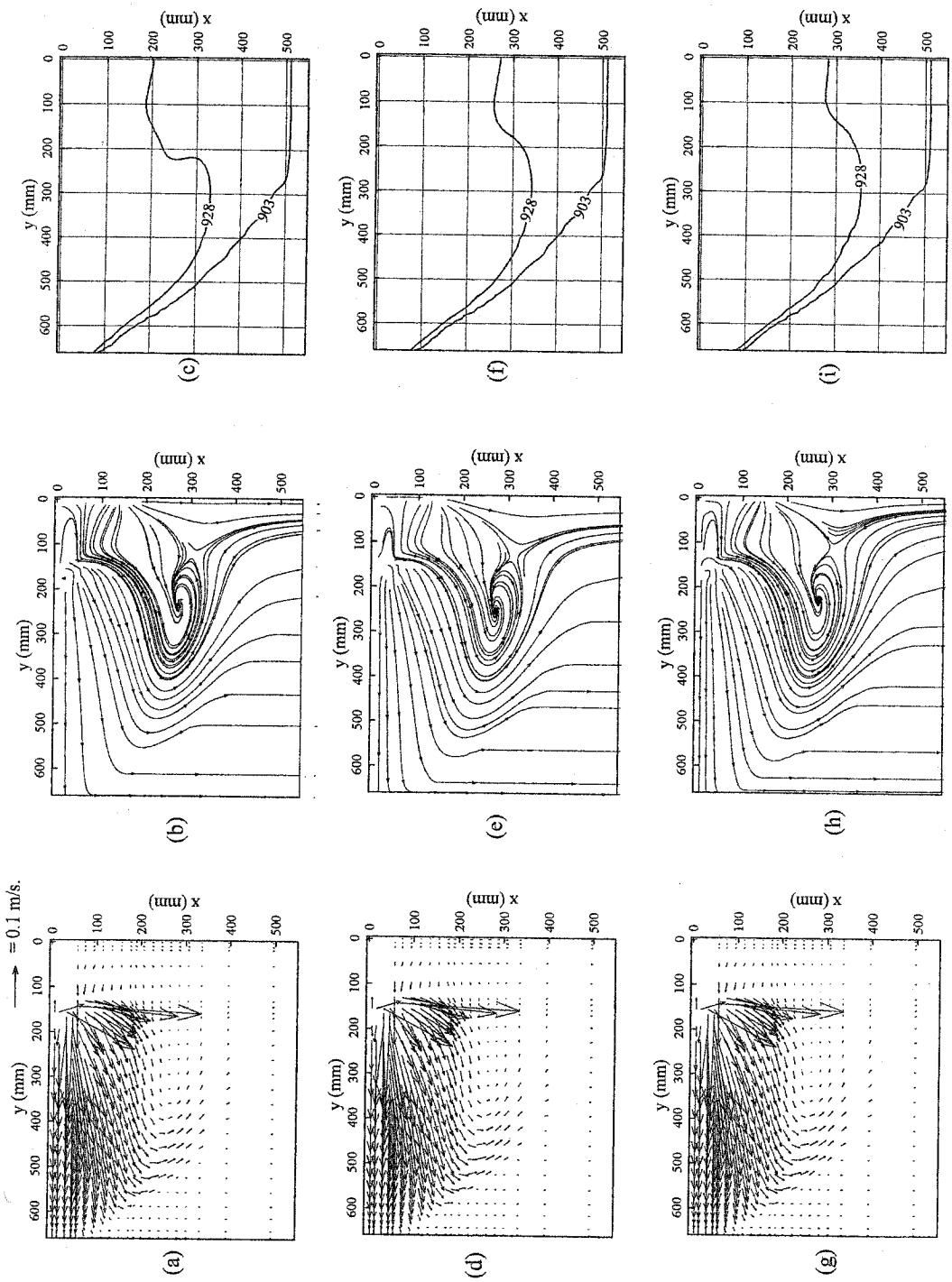

Figure 5.8: Temperature superheat effect at the wide symmetry plane, casting speed = 50.8 mm/min., (a,b,c) temperature superheat = 32°C, (d,e,f) temperature superheat = 65°C, (g,h,i) temperature superheat = 100°C.

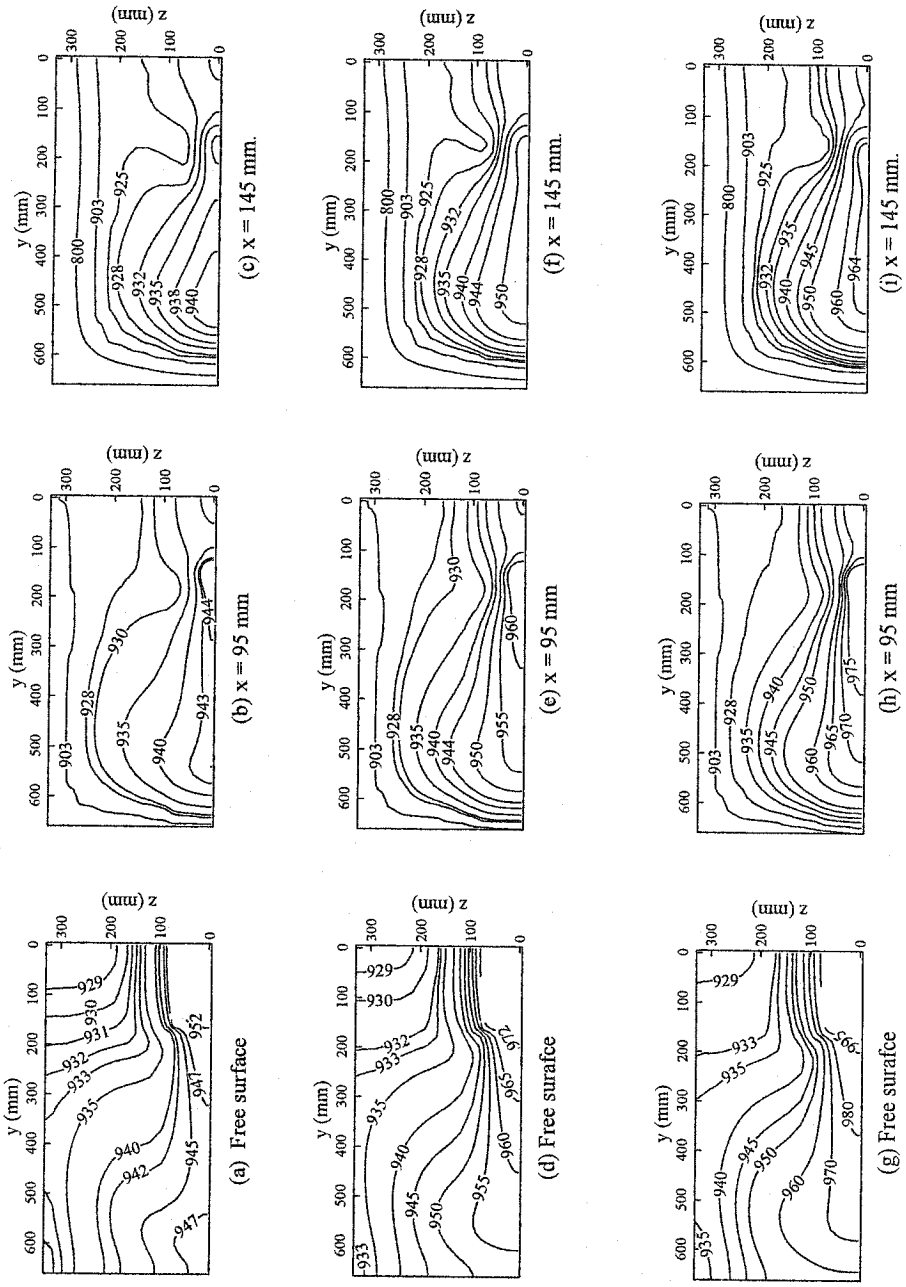

Figure 5.9: Temperature superheat effect at cross-sections parallel to the slab free surface, casting speed = 50.8 mm/min, (a,b,c) temperature superheat = 32°C, (d,e,f) temperature superheat = 65°C, (g,h,i) temperature superheat = 100°C.

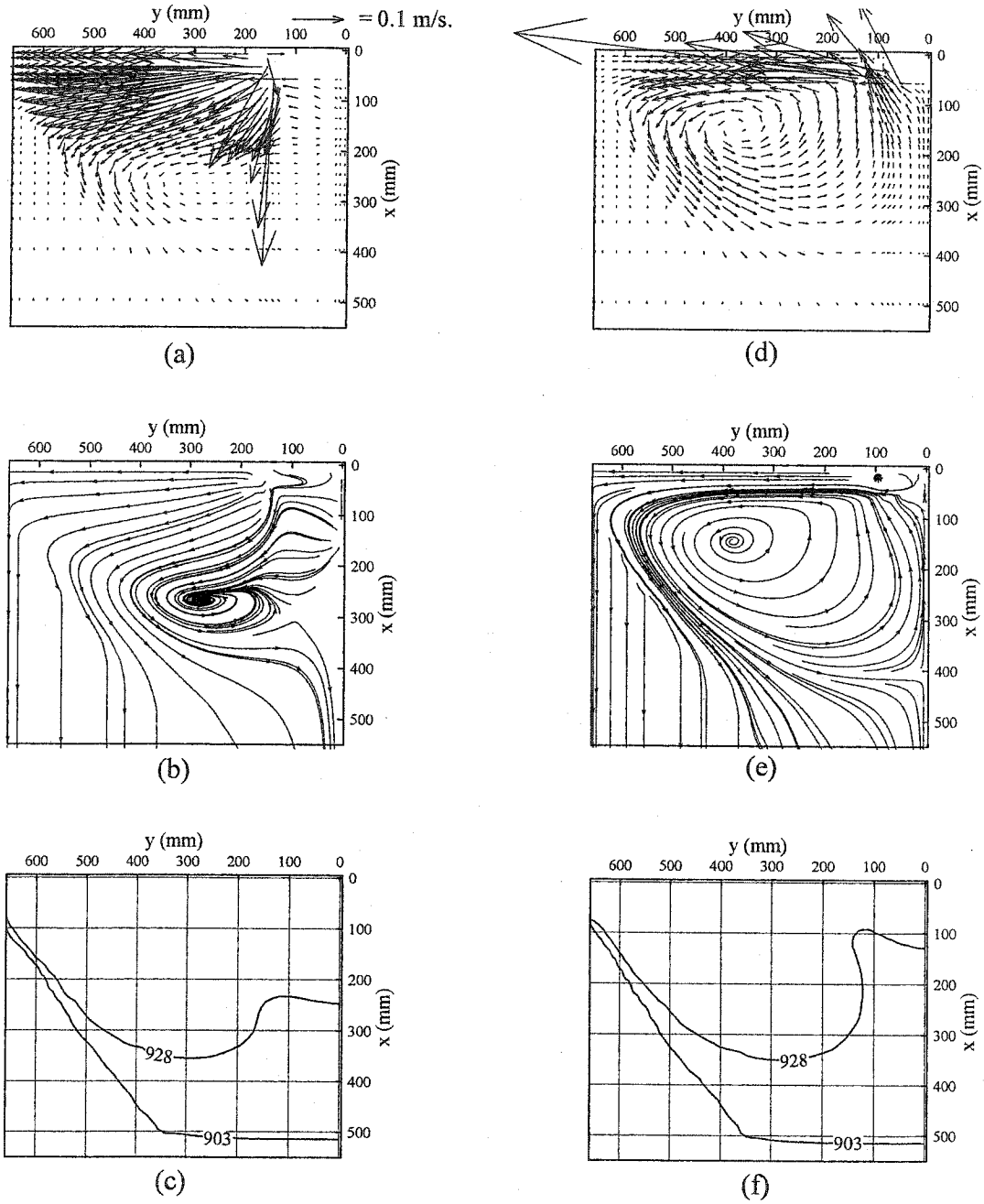

Figure 5.10: Effect of bag dimension at the wide symmetry plane; (a,b,c) standard-combo bag; (d,e,f) small bag. Casting speed = 60 mm/min;temperature superheat = 65°C.

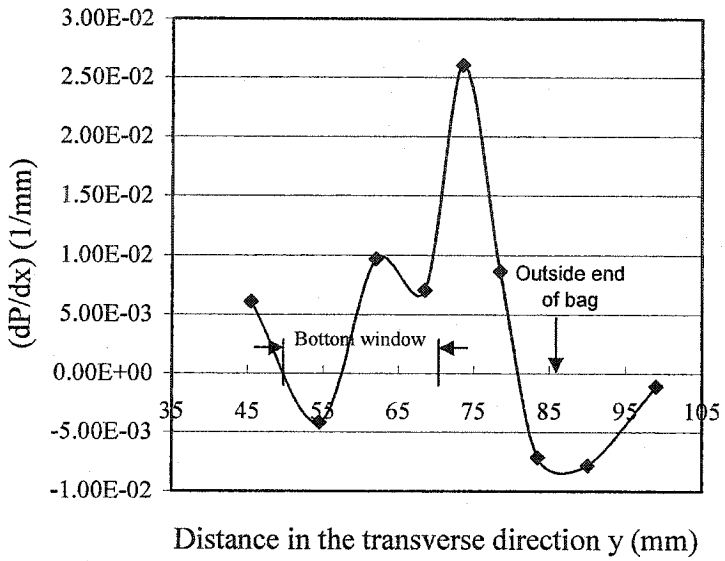

Figure 5.11: The Pressure gradient across the region bounded by the two transverse lines above and under the bottom surface of the small distribution bag.

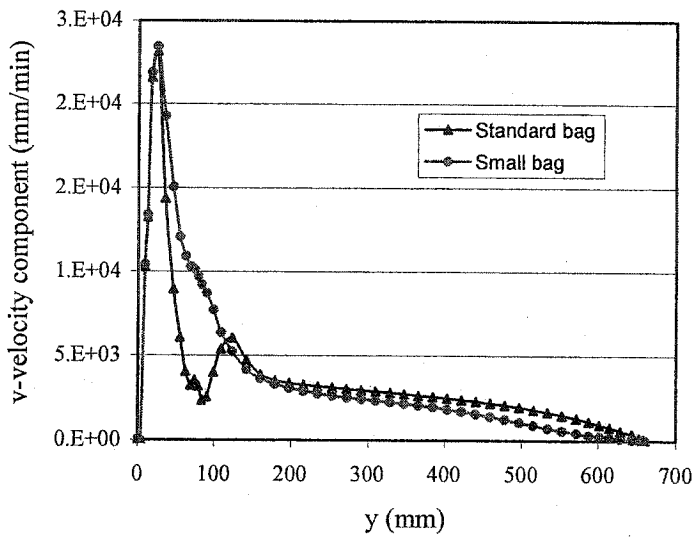

Figure 5.12: Effect of bag dimensions on v-velocity distribution at the wide symmetry plane, at x=37 mm. Castingspeed = 60 mm/min, superheat = 65C.

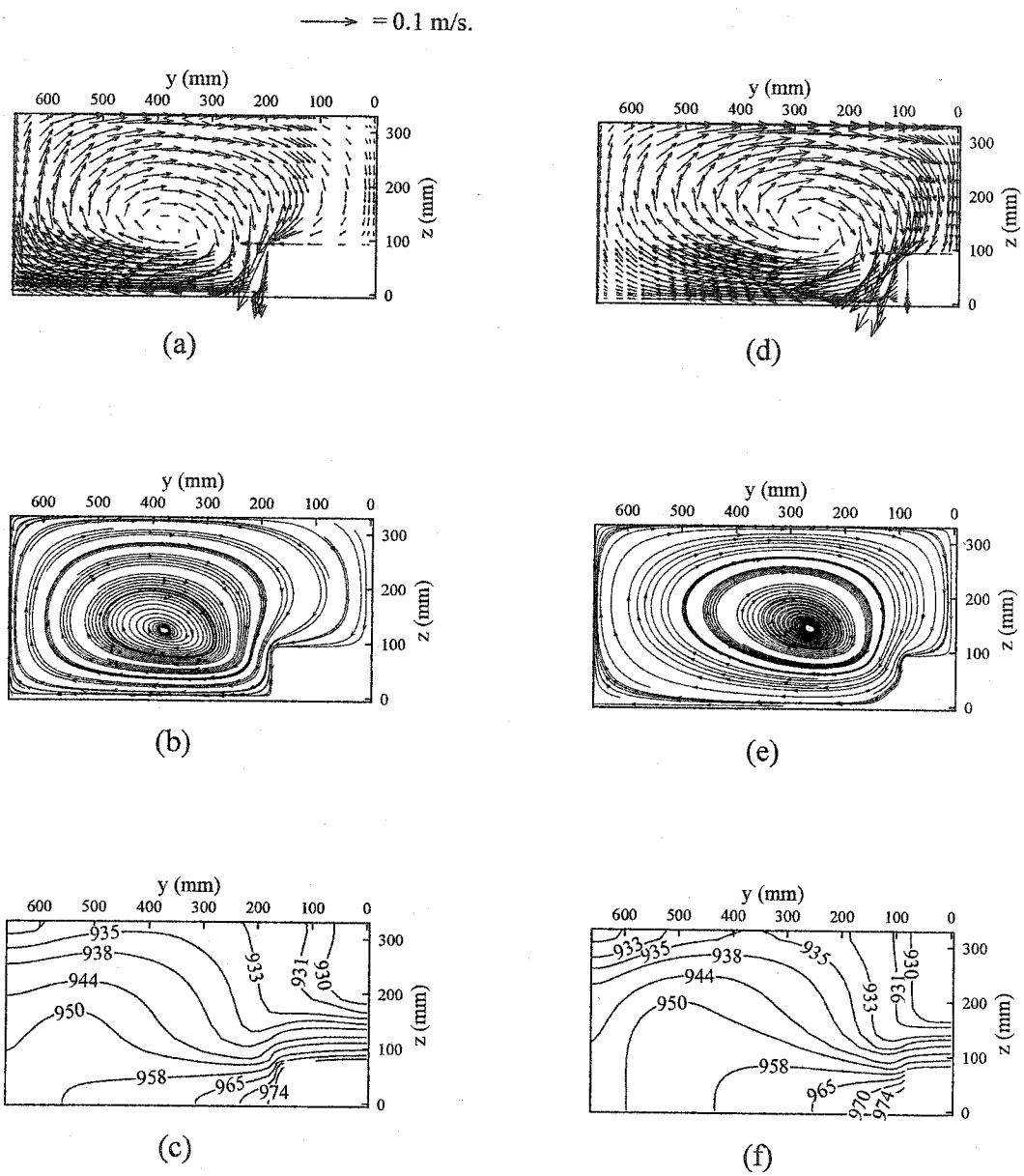

Figure 5.13: Computed results at the slab free surface using two combo-bag sizes, (a,b,c) standard combo-bag, (d,e,f) small bag. Casting speed = 60 mm/min, temperature superheat = 65°C.

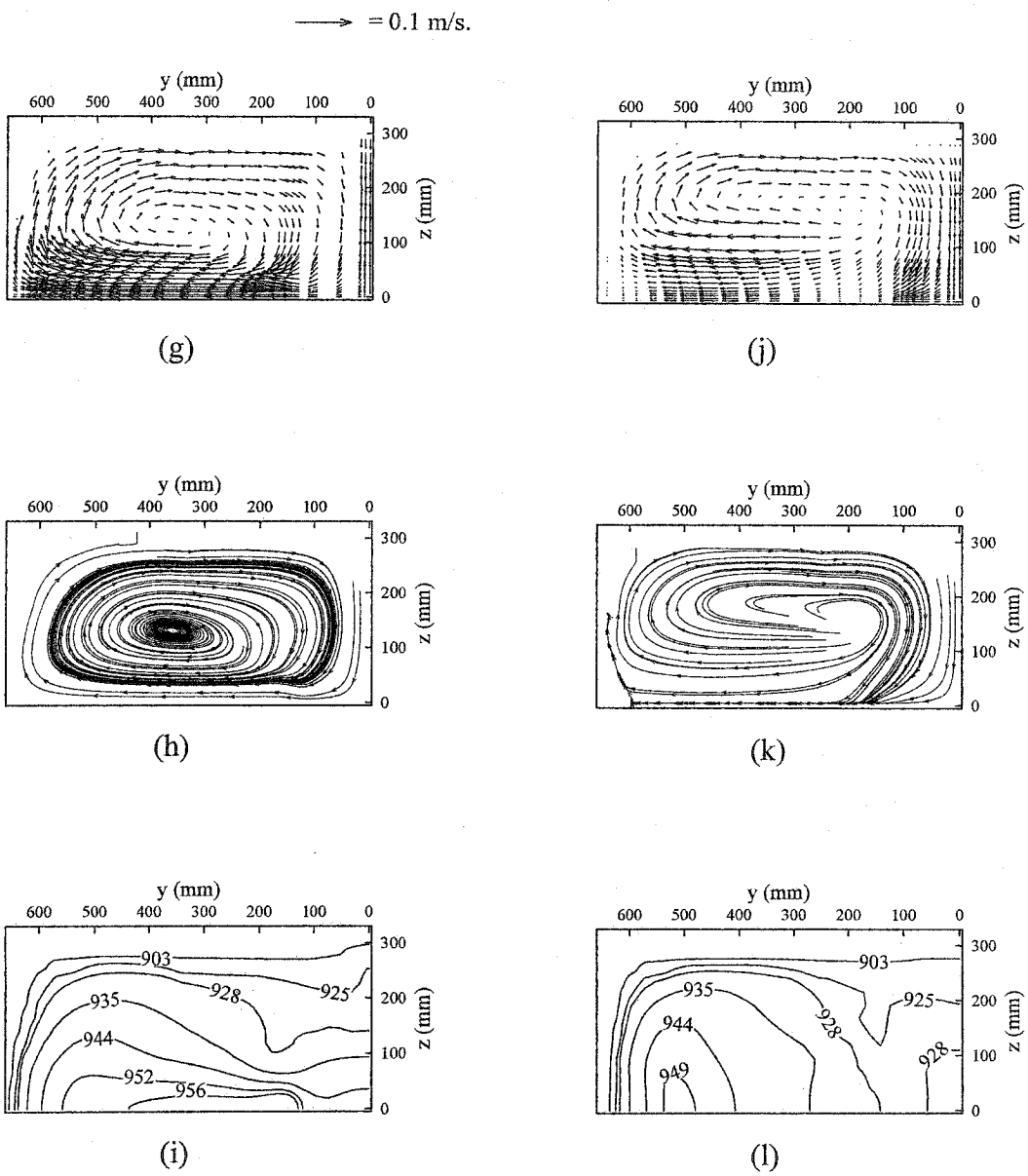

Figure 5.13 (continue): Effect of combo-bag dimension at x = 115 mm, (g,h,i) standard combo-bag, (j,k,l) small bag. Casting speed = 60 mm/min, temperature superheat = 65°C.

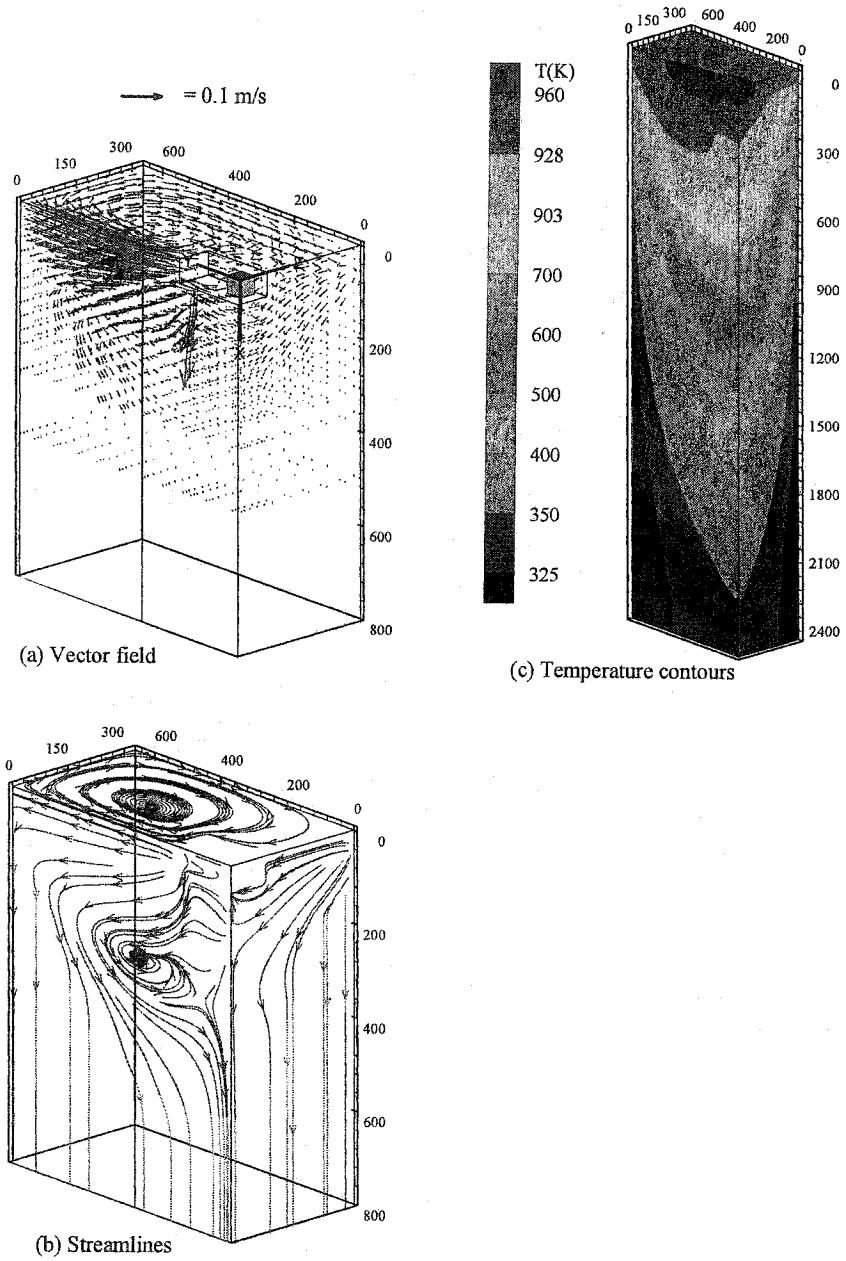

(a) Vector field

(b) Streamlines

(c) Temperature contours

Figure 5.14: Computed results for the combo bag without blockage, casting speed = 60 mm/min, temperature superheat = 65 °C.

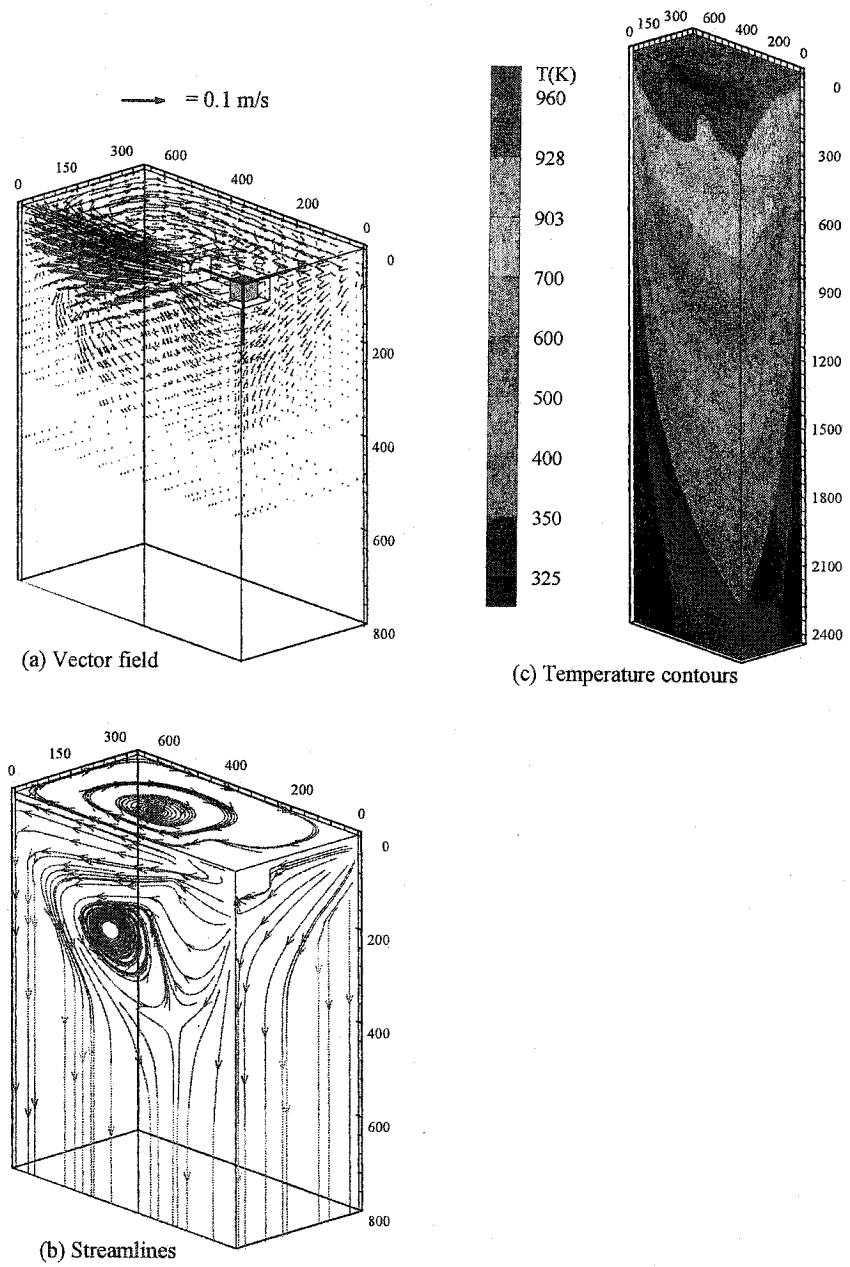

Figure 5.15: Complete blockage of the bottom windows, casting speed = 60 mm/min, temperature superheat = 65 °C.

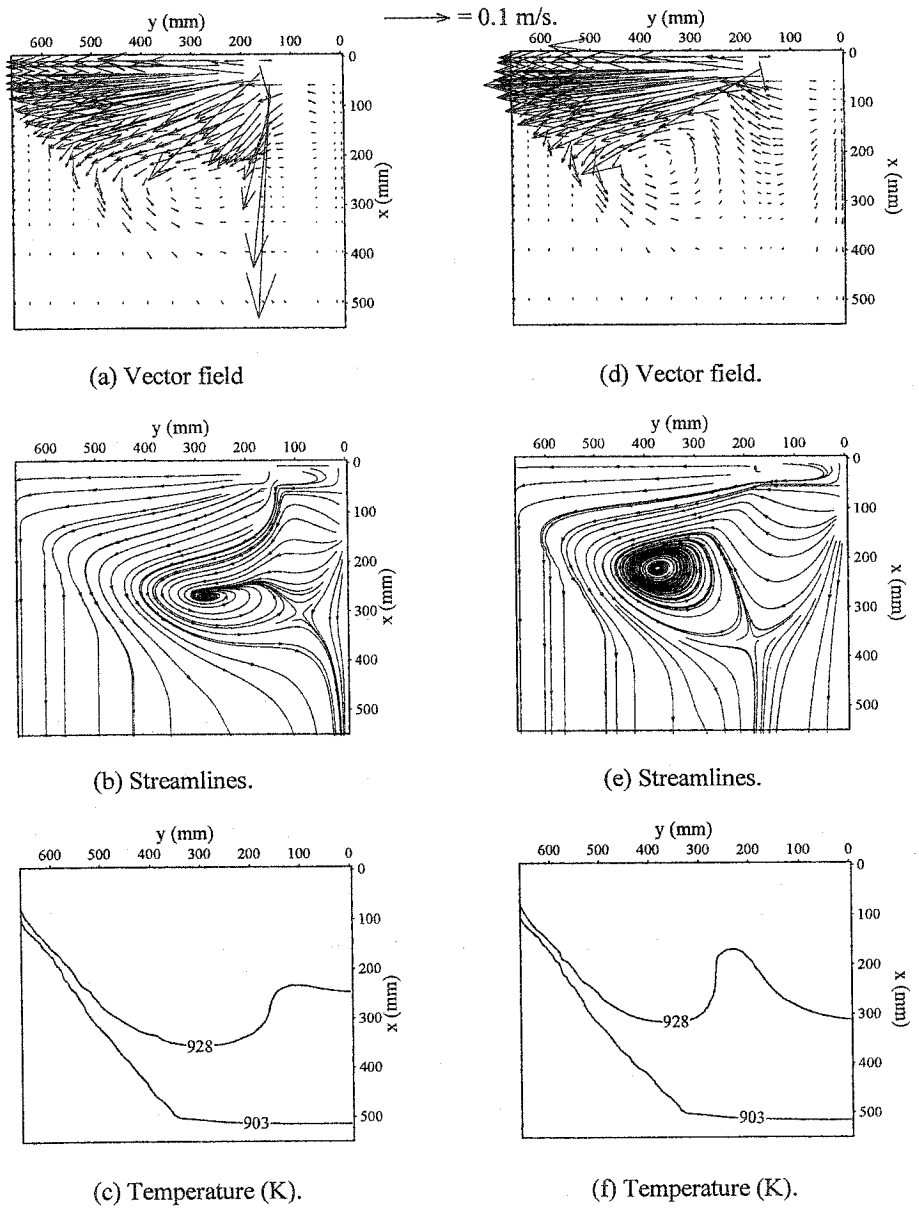

(a) Vector field

(d) Vector field.

(b) Streamlines.

(e) Streamlines.

(c) Temperature (K).

(f) Temperature (K).

Figure 5.16: Computed results at the wide symmetry plane using the combo bag, casting speed = 60 mm/min, temperature superheat = 65 °C. (a,b,c) no blockage, (d,e,f) complete blockage of the bottom windows.

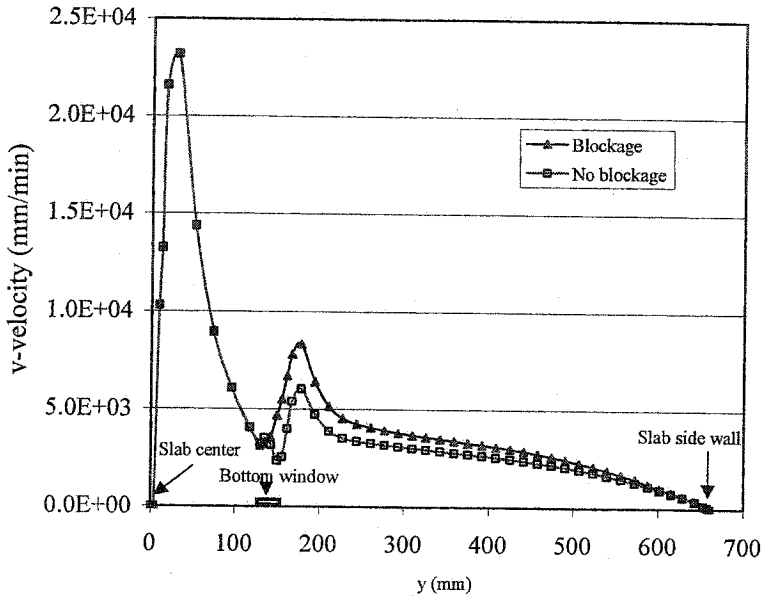

Figure 5.17: v-component of velocity distribution at the wide symmetry plane, along a line passing by x=37 mm,casting speed = 60 mm/min, superheat = 65 C .

CHAPTER
SIX

Ingot Casting Using Channel Bag Distribution System and Inclusion Study

6.1 Introduction

This chapter is divided into two main sections. The first section reports on the study of channel bag distribution systems and their effects on the melt flow and solidification characteristics of vertical DC cast ingots. The second section is devoted to the study of inclusion distribution inside the sump using the previously and currently computed steady state velocity fields.

6.2 Modeling of Vertical Ingot Casting Using the Channel Bag Distribution System

There are two widely used types of distribution systems in use in commercial vertical DC casters. The first is the formerly studied system represented by the combo bag, and the second is a channel bag. The channel bag distribution system is usually used in caster systems which produce aluminum slabs of large aspect ratios. The aspect ratio of the current modeled slab is 2.62, whereas, the aspect ratio of the previously modeled slab using the combo bag was 2. This section is devoted to the analysis of the effect of using the channel bag distribution system on the ingot characteristics under a steady state condition. The channel bag is simply a channel which is sealed from all sides except the sides facing the mold-narrow edges as shown in Figure 6.1. Two different sizes of channel bags are modeled. A long channel bag which has dimensions of 50 mm × 300 mm × 100 mm, and a short one has dimensions of 50 mm × 150 mm × 100 mm in the x, y, and z, respectively. The bags are placed at the mold center. The melt is delivered into the bags from an overhead trough through a nozzle having a cross-sectional area of 225

mm^2. The nozzle is immersed in the liquid metal pool to a depth of 20 mm. The two simulated distribution systems, short and long channel bags, are tested using three casting speeds; namely the 40, 50 and 60 mm/min. The modeled ingot has dimensions of 2500 × 1730 × 660 mm in the x, y and z directions, respectively. Due to symmetry reasons, only a quarter of the whole domain is considered as the calculation domain (refer to Figure 4.1). The physical properties of aluminum 1050, commercially pure aluminum, are used in the current simulation. The properties of aluminum 1050 and the geometrical dimensions incorporated in the mathematical model are summarized in Table 6.1.

Table 6.1: Physical properties of Al-1050 and DC caster geometrical parameters.

Variable	Value
Thermal conductivity	199 w / m K
Specific heat (liquid or solid)	1.056 kJ / Kg K
Latent heat of fusion	396.4 kJ / Kg
Liquidus temperature	657.0 °C
Solidus temperature	646.0 °C
Viscosity	16.2 X 10^{-4} Kg / m s
Density	2700 Kg / m^3
Slab width (parallel to rolling face)	1730.0 mm
Slab thickness	660.0 mm
Slab length simulated	2500.0 mm
Mold length	60.0 mm
Nozzle port width	30.0 mm
Nozzle submergence length	20.0 mm

The modeled DC caster is based on the Alcan Sheet Mold (ASM) technique. This technique has been found to produce ingots with improved surface characteristics and reduced shell thickness. The ASM involves the use of an insulation ring with certain axial length starting from the mold top surface. The insulation ring is used to reconcile the safety issues related to the low metal level casting (LMLC). These safety issues were explained in the literature survey, and are based on maintaining a liquid metal reservoir above the primary cooling section of the mold. Therefore the casting assembly consists of 120 mm adiabatic section followed by 60 mm mold section (the section of the primary

cooling region). The heat transfer coefficient in the primary cooling section is 1500 W/m^2 K. An air gap spanning 10 mm in the axial direction is adopted in the model to account for the shrinkage of the ingot as it emerges from the mold. The rest of the slab surface is located in the secondary cooling region, where water is sprayed directly onto the ingot surface. In this region, an axially variable heat transfer coefficient taken from experimental measurements reported in the literature [13] is adopted. The functions by which the heat transfer coefficient changes along the slab surface in the axial direction are given by the following equations:

$$h(x) = h_{gap} + \frac{x - x_1}{x_2 - x_1}\left(h_{\max} - h_{gap}\right) \qquad (180 \le x < 190 \text{ mm}) \qquad (6.1)$$

$$h(x) = h_{\max} + \frac{x - x_2}{x_3 - x_2}\left(h_{film} - h_{\max}\right) \qquad (190 \le x < 230 \text{ mm}) \qquad (6.2)$$

$$h(x) = h_{film} \qquad (x \ge 230 \text{ mm}) \qquad (6.3)$$

where x_1 = 180 mm, x_2 = 190, and x_3 = 230 mm. In the current study, the air-gap heat transfer coefficient (h_{gap}) is 150 W/m^2 K, while the maximum heat transfer coefficient (h_{max}) is assigned a value of 20,000 W/m^2 K and h_{film} = 10,000 W/m^2 K. The boundary conditions for the momentum, energy and turbulence variables are the same as those given earlier in Table 4.2.

The aim of the current study is to come up with general suggestions for the studied parameters which would produce good slab characteristics. In trying to come up with the optimum distribution system for a particular caster, the designer has to make sure that the general objectives, beside the special ones, is fulfilled by the employed melt distribution system. These objectives include the ability of the system to feed metal to all parts of the mold while minimizing the temperature gradient between the hottest and coldest areas. Noting that the areas identified as being of significant importance with regard to metal feed refreshment are the corners, short sides and the center of the rolling face. Another condition that has to be accomplished is that the distribution system has to deliver the required amount of metal without generating oxides through increased levels of

turbulence. Increasing the turbulence levels especially at the melt free surface was found to be the principle reason behind the generation of oxide inclusions [23].

6.2.1 Results and Discussion

The computed results are presented in terms of 3D surface plots as well as in 2D cross-sections. The 2D cross-sections are taken in the three orthogonal planes over the entire calculation domain. The discussion of the results will cover the velocity field, streamlines, and temperature contours. It is to be noted that only the longer distribution bag is used in studying the effects of casting speed and temperature superheat.

6.2.1.1 Casting Speed Effect

Figure 6.2 (a-c) shows a 3D-surface plot of the computed results for the 40 mm/min casting speed and 32°C superheat. The figure shows the calculation domain which consists of the two symmetry planes [wide (x-y plane) and narrow (x-z plane)] of the ingot as well as the top surface of the ingot. The streamlines are used to illustrate the nature of the velocity field in a particular region of the plot. Figure 6.2 (c) shows the mushy region which is confined by the solidus (919 K) and liqidus (930 K) temperature contours. The 3D-vector field is magnified, and only the section containing the liquid sump is shown. The solidified portion of the ingot, according to the model assumptions, is traveling axially downward with the casting speed. Figure 6.2 (a) shows the deflection of the molten metal, from the axial direction to the horizontal direction toward the narrow side of the mold, by the distribution bag. After reaching the narrow side of the slab, the horizontal flow of hot melt is split into two streams. One stream is forming a counter clockwise vortex at the wide symmetry plane, hence forth, will be called the vertical vortex or recirculation. The other stream follows the two inside surfaces of the mold (narrow and wide) as can be seen from the top surface of the ingot in Figure 6.2 (a, b).

Figure 6.3 (a-c) shows explicitly a 2D vector field, streamline, and temperature contours at the wide symmetry plane. The cross-sections are taken from the computed results of Figure 6.2. It is clear that the vertical recirculation is positioned between the middle of the calculation domain and the narrow side of the slab as shown in Figure 6.3

(b). The flow coming from under the distribution bag, the angle flow, is entrained by the vertical vortex at the wide symmetry plane. The angle flow can clearly be seen by the streamlines at the narrow symmetry plane (x-z plane) of Figure 6.2 (b). This flow directs a relatively hot stream of melt toward the middle region of the slab, forcing both the solidification front and the liqidus contour line in that region to take a negative slope as can be seen in Figure 6.3 (c). The same figure reveals that at the middle region of the calculation domain, the solidification front is almost aligned horizontally, whereas the mushy layer is slightly extended toward the top surface of the slab. This extension is reported in the literature, and can be attributed to the low pressure region (wake) created at the point of separation of the vertical recirculation from the solidification front (Figure 6.3 (b) at (x,y) = (320,380) mm). The entrained stream, seen approaching from the slab center, is originally coming from the angle flow as this flow changes course once it reaches the wide symmetry plane, to finally travel parallel to the latter plane towards the narrow side of the slab. Figure 6.3 (d-f) shows a cross-section taken at z = 90 mm from the wide symmetry plane in which the effect of the vertical eddy is more pronounced. This effect is demonstrated in the expansion of the mushy layer toward the slab top surface, and the horizontal flattening of the solidification front in the transverse direction. The current study shows that the last two observations presented in terms of the flattening of the solidification front and the extension of the mushy layer from the liquidus temperature side are accompanying any eddy that is vertical and touching the solidification front. The same phenomena were observed in the real casting experimental trials and the physical water model of Gary et al. [23], yet no clear explanation was provided. The current model is able to predict the location and depth of the eddy and can also describe the consequences of forming such an eddy. These numerical predictions of vortices and their consequences can be taken as guiding signs not only in designing real casters, but also in constructing physical water models to promote or to avoid certain vortices in specific locations.

The streamlines in Figure 6.3 (e) show the onset of separation of the entrained stream from the vertical vortex. Once this stream is separated, it forms a vertical-clockwise recirculation near the slab center as demonstrated by Figure 6.3 (g,h). As a

consequence of the formation of the latter vortex, the mushy region is again expanding toward the slab surface at the region of separation of the vortex from the solidification front as seen by the temperature contours of Figure 6.3 (i). Figure 6.3 (j-k) depicts a cross-section taken at 212 mm in the z-direction. At this section, the flow travels horizontally toward the slab center, once this flow reaches the slab center, it moves vertically downward causing the solidification front in this region to get deeper in the upward direction as shown in the corresponding temperature contour in Figure 6.3 (l).

Figure 6.4 presents results for transverse cross-sections (y-z plane) including and parallel to the slab-free surface. Figure 6.4 (a-c) shows cross-sections for the slab-free surface. The rectangle at the corner of (y,z) = (0,0) in Figure 6.4 (a) shows the top surface of the distribution bag. The bag is sealed from the top therefore there is no flow in that region. The same figure illustrates the strong stream of hot melt that is issuing from the distribution-channel-side opening. This stream is heading towards the narrow side of the mold. The temperature distribution can be seen through the temperature contours of Figure 6.4 (c) in which the temperature is seen decreasing along the wide symmetry line, and along the two inside surfaces of the mold. The decrease in temperature, as mentioned earlier, is mainly because of the vertical conduction and convection within the melt itself, and not because of the heat transfer through the mold since this section of the slab is located in the adiabatic region of the mold. Figure 6.4 (d-f) portrays a section taken at around the middle of the axial length of the adiabatic section of the mold (x = 75 mm). This section is below the distribution bag bottom surface, therefore the vector field covers the whole section as shown in Figure 6.4 (d,e). Figure 6.4 (g-i) illustrates cross-sections taken 5 mm below the start of the primary cooling region of the mold. A solidified layer is formed along the rolling face and the outside corner of the slab, while the narrow face of the slab is still liquid. The formation of the solidified layer along the rolling face of the slab can be attributed to the weak flow of melt along that side as can be seen by Figure 6.4 (g). The slow moving melt along the rolling section allows more heat to be extracted by the primary coolant of the mold. Whereas, the high momentum melt stream delivered to the narrow side of the mold through the side opening of the distribution bag has delayed the formation of the solidified layer in that part.

Figure 6.4 (j-l) presents a section taken at 215 mm from the slab top surface. This section is positioned in the secondary cooling region, which starts according to the boundary conditions at x =180 mm from the slab top surface. Here, the solidified layer is formed all over the outside periphery of the slab, and the thickness of the solidified layer at the rolling face is thicker than that at the slab narrow face. In an actual DC casting process it is well known that the heat transfer coefficient, as in the axial direction, also varies in the transverse directions, that is along the z and y axes. The highest value of the heat transfer coefficient is located at the point first contact of the hot stream coming from the channel bag which happens to be the middle of the narrow side of the mold, and then it decreases along the z-direction to have its lowest value at the outside corner of the slab. From that point on, the heat transfer coefficient increases up until the middle of the slab rolling face. This change in the heat transfer along the transverse direction has not been implemented in the current mathematical model due to the lack of values in the literature of the proper heat transfer coefficient functions that describe this change. Therefore, it is expected, once appropriate heat transfer coefficient functions are implemented along the transverse directions, an almost uniform thickness of solidified layer will be achieved along the entire slab surface. This goal, once achieved, will guarantee good ingot surface characteristics.

Figure 6.5 depicts results for longitudinal cross-sections parallel to the x-z plane. The results are for cross-sections parallel to and including the narrow symmetry plane. Figure 6.5 (a,b) portrays the angle flow as it travels parallel to the narrow symmetry plane coming from the horizontal recirculation in the mold region, as mentioned earlier. The square at the left top corner of Figure 6.5 (a-c) represents a cross-section for the distribution bag. Figure 6.5 (d-f) depicts a cross-section taken right after the distribution channel opening (the opening is facing the mold narrow side). A counter-clockwise vortex is formed right after the channel opening as shown in Figure 6.5 (d,e). The melt flowing down along the solidified surface and the stream bouncing up from the solidification front are entrained by the mentioned vortex. At the point of separation of these two streams from the solidified side front, the mushy layer gets thicker. Figure 6.5 (g-i) shows a section taken at y = 248 mm from the narrow symmetry plane. In this

section, the onset of a clockwise vortex is seen as a result of the separation of part of the upward flow from the earlier mentioned corner vortex. As can be seen from the vector field in Figure 6.5 (g), the newly formed vortex is very weak, therefore, it disappears completely in the following section taken at y = 355 mm as shown in Figure 6.5 (j,k). Figure 6.5 (m-a1) depicts in detail the development of both the corner vortex and the temperature contours at cross-sections taken normal to the rest of the y-axis. The vortex center has moved from the corner to the location (x,z) = (95 mm,95 mm) as shown in Figure 6.5(n). As the narrow side of the slab is approached, the vortex center goes toward the free surface (Figure 6.5(q)), and after traveling along the free surface it moves towards the outside corner (Figure 6.5(t,w)). Finally, this vortex is completely disappeared by the sweeping momentum of the melt stream coming from the channel bag as this stream impinges on the narrow side of the mold as shown in Figure 6.5 (y,z). The mushy region in this section is at its narrowest thickness due to the disappearance of eddies.

In the case of 50 mm/min casting speed, the vertical vortex at the wide-symmetry plane is merely extended to the slab center as seen in Figure 6.6 (a,b). This can be attributed to the fact that as the casting speed increases, the flow rate of the melt from the nozzle increases so that at steady state the mass is conserved. This results in a higher melt flow rate out of the channel bag and causes the narrow side of the mold to be hit with a high temperature melt stream. As mentioned earlier, this stream of high temperature melt splits into two other streams, one stream forms the vertical recirculation at the wide-symmetry plane, and the other instigates the horizontal recirculation at the upper part of the mold. The vertical recirculation has a higher momentum and is faster in reaching the slab center than the angle flow coming from the horizontal recirculation. The horizontal recirculation loses momentum in two occasions, the first is upon coming in contact with the inside surface of the mold, and the second is upon the impact with the impervious outside wall of the channel bag at the narrow symmetry plane region, not considering the momentum lost due to friction within the melt itself. Considering all of the above, the vertical recirculation arrives at the slab center with a higher momentum causing this recirculation to extend to the slab center. The upward flow component of the vertical

recirculation overcomes and entrains a part of the angle flow coming from the top recirculation as soon as the angle flow reaches the wide symmetry plane. The solidification front exhibits a more uniform shape over most of the middle region of the calculation domain, except at the slab center region where it displays a negative slope as can be seen in Figure 6.7 (c). As mentioned earlier, the entrainment of part of the angle flow by the vertical recirculation barely happens at the wide-symmetry plane. Actually, for the case of 50 mm/min casting speed, the vertical recirculation is detached from the slab center at z = 63 mm from wide symmetry plane. Therefore, by looking into a cross section parallel to the wide symmetry plane, Figure 6.7 (d-f), at z = 109 mm, the vortex diameter decreases. Consequently, the angle flow is entrained by the vertical vortex not at the slab center but at around 200 mm in the y-direction. The point of separation of the vertical eddy from the solidification front is located at around 200 mm in the y-direction. Therefore, similar to the case of 40 mm/min casting speed, the solidification front takes an a flatter shape, and the mushy region extends more toward the slab free surface as seen in Figure 6.7 (f). As cross-sections are taken deeper in the calculation domain from the top, the liquid sump becomes shallower, the vortices get weaker, and the flow of melt exhibits a horizontal component toward the slab center as shown by Figure 6.7 (g-l).

Figure 6.8 (a-l) illustrates cross sections parallel to and including the slab top surface. Figure 6.8 (a-c) shows the horizontal recirculation and the temperature contours at the free surface. At the free surface as well as at a section 75 mm below this surface (Figure 6.8 (b,e)), the horizontal recirculation is covering the whole section, and is not affected by the upward component of the vertical recirculation at the slab wide-symmetry plane. In other words, the upward component of the vertical recirculation, shown in Figure 6.7 (b), does not have enough momentum to reach the slab free surface, but rather recirculates at the wide symmetry plane below the free surface. This is not the case for the 60 mm/min casting speed as it will be shown later. Figure 6.8 (g-h) depicts a cross-section 5 mm after the start of the primary cooling region of the mold. Solidification at the rolling face side of the slab develops faster than at the narrow side of the slab as shown by the solidification temperature contour (919 K) in Figure 6.8 (i). Figure 6.8 (j-l) shows a cross section positioned at x = 215 mm from the slab top surface. This section is

located in the secondary cooling region. At this section, the outer surface of the ingot is completely solidified; the solidified layer is thicker at the rolling face than that at the narrow side of the slab.

Figure 6.9 (a-a1) presents cross-sections taken through the narrow side of the slab starting with the narrow symmetry plane for the case of 50 mm/min casting speed and 32°C superheat. Figure 6.9 (b) shows clearly how the angle flow is entrained by the vertical recirculation, and that the vertical recirculation is prevented from reaching the free surface of the slab as explained earlier. Figure 6.9 (d-a1) shows cross-sections taken subsequent to the end of the channel opening. As the slab side wall is approached, the upward component of the vertical vortex is diminished as shown by Figure 6.9 (e,h). The mushy layer thickness at the wide symmetry line decreases with the decrease in the value of the upward component of the vertical vortex as shown by Figure 6.9 (f,i). At y = 503, the upward component of the vertical vortex is replaced by a relatively strong downward flow of melt. In this region, the solidification front is pushed down at the place of higher downward flow as shown by Figure 6.9 (k,l). Figure 6.9 (p-a1) shows a change in the melt flow direction from downward to horizontal as the narrow side of the slab is approached.

Figure 6.10 (a-b) shows 3D-surface results for the 60 mm/min casting speed using the same channel bag dimensions (50 x 300 x 100 mm) and temperature superheat as the above discussed cases. Figure 6.10 (a,b) shows clearly that the vertical vortex not only extends to the slab center, but also engulfs the angle flow, and reaching to the slab free surface. Consequently, the horizontal vortex at the slab free surface is pushed to recirculate in the region closer to the narrow side of the mold. A region of low melt refreshment is formed at the point of separation of the horizontal vortex from the mold wide surface at around (x,y) = (0,175) mm as shown by Figure 6.10 (a,b). This region, as expected, is characterized by a low temperature as will be shown later. The higher exit velocities at the distribution channel opening, attained by the increase in the casting speed, would have the tendency to increase the momentum of the vertical vortex to reach to the slab free surface. The later, once happened, increases the turbulence at the slab free surface. Turbulence at the free surface causes the melt to have a high melt surface area-

to-volume ratio, which in turn increases the oxidation of the aluminum. In addition, this turbulence thoroughly mixes the surface oxide films with the molten sump and leads to the increase of oxide inclusions in the melt underneath the free surface. The higher exit velocities at the channel opening would also have the tendency to drive inclusions trapped by the ceramic filters out into the sump. Therefore, a flow situation of this nature is to be avoided in DC casting unless two conditions are met. The first is that the slab free surface is protected by an inert gas to avoid the formation of oxide layer. The second is that the melt has to be originally clean, so that not much of inclusions trapped in the ceramic filter are infiltrated into the sump.

Figure 6.10 (a) shows a strong flow of melt from the slab narrow side along the solidification front and toward the slab center. This flow is responsible for pushing the solidification front deeper in the axial direction along most of the symmetry plane. The mushy layer (between 919 K and 930 K) around the center of the slab gets thicker as can be seen in Figure 6.10 (c). Figure 6.11 shows cross-sections taken parallel to and including the wide-symmetry plane of Figure 6.10. The effect of the vertical vortex is felt through deeper sections in the z-direction as can be seen in Figure 6.11 (d-f) (z = 109 mm) in which the solidification front is almost uniform and the mushy region around the slab center is thicker. As the slab rolling surface is approached, the liquid sump becomes shallower and the flow develops from recirculating to horizontally directed as demonstrated by Figure 6.11 (g-l). Figure 6.12 presents cross-sections taken in the 3D calculation domain of Figure 6.10 parallel to the slab free surface. The region of low melt refreshment can clearly be seen at the slab free surface by the vector plot and streamlines of Figure 6.12 (a,b). This low melt refreshment region is located around (x,y) = (0,150) mm at the rolling face of the slab. As far as the heat transfer is concerned, this region of low melt refreshment is not important, since it is located in the adiabatic section of the mold. However, as far as the inclusions are concerned, these regions play an important role in distributing impurities inside the ingot. Figure 6.12 (d-f) is positioned in the secondary cooling region (x = 215 mm.). At this region, the outer solidified layer develops very fast due to the high heat transfer coefficient provided by the direct contact of the water with the outer slab surface and the relatively high thermal conductivity of

aluminum. The temperature contours are taking the shape of the calculation domain, and the solidified section moves in the axial direction with the casting speed. Figure 6.13 illustrates cross-sections normal to the y-axis of the 3-D calculation domain of Figure 6.10. The upward component of the vertical recirculation can clearly be seen by the streamlines at the narrow symmetry plane of Figure 6.13 (b). As mentioned earlier, the effect of such flow behavior would cause the mushy region at the slab center to get thicker as can be seen by the corresponding contour lines of Figure 6.13 (c). Figure 6.13 (d-f) presents a cross-section taken right after the channel bag opening. The surrounding melt at this section is entrained by the issuing stream from the channel-bag opening [Figure 6.13 (d,e)]. The issued stream is exiting from the channel bag in the form of a counter-clock wise spinning vortex. As the slab narrow side is approached, the flow changes and becomes more horizontal, and causes the mushy layer to be thinner [Figure 6.13 (g-h)].

A calculation is carried out using the solidification front temperature profile to find the average sump depth ($\bar{x}$) at the wide symmetry plane. The following formula is used to find the average sump depth:

$$\bar{x} = \frac{\int_0^{y_l} x(y)\, dy}{\int_0^{y_l} dy} \tag{6.88}$$

where

$$y_l = Y_L - y_b \tag{6.89}$$

where Y_L is the width of the symmetry plane of the calculation domain, and y_b is the thickness of the base of the outer solidified layer as shown schematically in Figure 6.14. The value of y_l is taken to be constant for the three considered casting speeds and is equal to 650 mm. The results are plotted in terms of the three modeled casting speeds versus the average sump depth in Figure 6.15. It is clear that the depth of the solidification front is increasing with the increase in the casting speed.

Figures 6.16-6.18 consist of the temperature contours and streamlines for the three casting speeds (40, 50, and 60 mm/min) at the three orthogonal planes represented by the wide symmetry plane, the slab-top surface and the narrow symmetry plane,

respectively. These figures are listed in this way in order to establish two goals. The first is to make comparison between the three casting speeds much easier. The second is to conclude the discussion of the most important parameter in vertical DC casting, which is the casting speed. Figure 6.16 illustrates the effect of the casting speed on the extension of the vertical vortex. As the casting speed increases, the vortex extends more toward the slab center, the solidification front gets deeper and exhibits a more uniform profile. Moreover, the mushy layer thickness at the center increases with the increase of the casting speed. This is in agreement with the observations stated by Xu et al. [16]. Figure 6.17 shows cross-sections taken parallel to the slab free surface at the same depth (x = 105 mm) from the slab-top surface for the three casting speeds. For the 40 mm/min casting speed [Figure 6.17 (a,b)], the outer solidified layer develops over most of the slab rolling face, whereas in the case of 50 mm/min shown in Figure 6.17 (c,d), the solidified layer is just developed in a region around the middle of the calculation domain at the side of the rolling face. On the other hand, for the case of the 60 mm/min casting speed [Figure 6.17 (e,f)], the solidification seems not started there. This confirms that the increase in the casting speed delays the onset of solidification process down the axial direction. This can be attributed to the fact that the increase in casting speed causes more of hot melt to be delivered to the mold for the mass to be conserved, and since it is assumed that the heat transfer coefficient at the slab surface is the same for the three casting speeds, therefore at the 60 mm/min casting speed, the melt has not been allowed enough contact time with the primary cooling region of the mold for the heat of fusion to be released. Therefore, when increasing the casting speed two things have to be watched. The first is to make sure that the ingot has developed a solidification layer capable of holding the molten sump before leaving the mold. The second is to make sure that the vertical recirculation does not reach to the slab free surface so that the oxide inclusions at the ingot surface do not mix with the melt underneath.

In addition to the above, the strong convective currents, such as the one created by the vertical recirculation, are found to be a major cause of negative segregation at the ingot center [44]. This solute-lean region is formed by solute-lean grains that are carried by convective currents along the mushy interface of the sump to the center of the ingot.

These grains then settle out of the molten sump and become entrained by the advancing solidification front. The rejection of solute (microsegregation) from grains formed by nucleation or dendrite shearing is taking place at the lower portion of the molten sump. Settling of the solute-lean grains at the bottom of the sump and their displacements by solute rich liquid results in a negative segregation at the center of the ingot. The displaced solute-rich liquid is then carried by convection up and out toward the surface of the ingot. It then recirculates with the incoming melt, floods the rigid portion of the mushy zone, and results in a positive segregation region near the slab surface [43]. Therefore, reducing these convective currents resulting from the vertical recirculation by reducing the casting speed will alleviate this problem.

Figure 6.18 shows the narrow symmetry plane for the three simulated casting speeds. One of the major contributions of the current work is shown by these cross-sections of the narrow symmetry planes. This contribution can be summarized in the explanation of the two major streams which control both the depth of the solidification front at the slab center and the thickening and/or narrowing of the mushy layer at the same location. These two streams are the upward component of the vertical vortex at the wide symmetry plane and the angle flow coming from the horizontal recirculation at the slab top surface. At the casting speed of 40 mm/min, Figure 6.18 (a,b), the upward component of the vertical vortex is completely overwhelmed by the angle flow. As a result, the mushy layer at the center is narrowing, and the solidification front at the same location is relatively deepening. For the case of 50 mm/min, part of the upward component of the vertical vortex is prevented from reaching the slab top surface, but is rather forced to recirculate at the wide symmetry plane by the angle flow as shown by Figure 6.18 (d). The other part of the upward component of the vertical recirculation is forced to change course toward the solidification front at the slab center. Consequently, the solidification front at the slab center is pushed deeper in the axial direction. The extreme case is presented by the 60 mm/min casting speed. At this speed, the angle flow is completely engulfed by the upward component of the vertical vortex, and the latter stream reaches the slab top surface. Accordingly, the horizontal recirculation at the slab

free surface is pushed to recirculate further from the slab center and more toward the narrow side of the mold as shown earlier in Figure 6.17 (f).

6.2.1.2 Effect of Bag Dimensions

Distribution bags are mainly used to redistribute molten metal as this melt enters the cast through the nozzle. The redistribution of melt is controlled so that a comparatively homogenous distribution of temperature isotherms is achieved over the slab surfaces. Thus, uniform heat transfer can be attained at each section orthogonal to the axial direction. Control of flow outside the bag is possible if the bag is correctly sized and placed. In this section, a study of the effect of distribution-bag dimensions on both the flow behavior and temperature distribution in the sump is carried out. Two channel bags with different sizes are tested; namely, the long channel bag with dimensions of 50 x 300 x 100 mm, and the short channel bag with dimensions of 50 x 150 x 100 mm in the x, y, and z directions, respectively. It is to be noted that all the other parameters are fixed including the temperature superheat, which is kept at 32°C and the casting speed at 50 mm/min. In order to avoid repeating descriptions of the general flow behavior within the sump, the following discussion will be limited to showing and clarifying the differences in melt flow and heat transfer results using the two simulated channel bags.

Figure 6.19 shows 3-D surface plot of the velocity vectors, streamlines and temperature contours for the 50 mm/min casting speed for the case of short distribution bag. It is to be noted that the lower segment of the calculation domain is cut, and the upper segment is magnified for the purpose of presenting the results in a clear way. A quick comparison of these results with the previously discussed results of the long channel bag (Figure 6.6) reveals the importance of the role played by changing the size of distribution bags in changing not only the melt flow behavior, but also the temperature contours within the ingot. Figure 6.20 shows the vector plot, streamlines, and temperature contours for the liquidus and solidus temperatures at the symmetry plane for both the short (a,b,c) and long (d,e,f) channel bags. An early spreading of the melt stream, coming out of the short channel bag in the surrounding sump is observed. This dispersion can be

seen in both the wide symmetry plane shown by Figure 6.20 (a,b), and the slab free surface as will be shown later. Whereas, in the case of the long-channel bag of Figure 6.20 (d,e), the melt stream coming out of the bag is less dispersed and more focused toward the narrow side of the mold. The dispersion of the melt stream in the case of the short-bag is attributed to the early mixing of the outer boundary of the jet stream with the melt in the sump. The mixing rate determines the potential core length, which is defined as the distance from the point where the issuing melt leaves the bag to the point where the centerline velocity of the stream is 95% of the issuing velocity. The earlier the mixing is, the shorter the potential core length will be. When the separation distance from the bag outlet to the side of the mold is longer than the potential core length, the surrounding molten fluid penetrates the jet and reaches the centerline of the jet. This causes the centerline velocity to decrease as the jet spreads. This region is called the established jet region. That is the reason for the weak velocity of the melt as it hits the side wall of the mold in the case of the short distribution bag which is shown by the short vector arrows in Figure 6.20 (a). In other words, early mixing means shorter potential core length and a rapid decrease in the momentum of the issued molten stream. Whereas, in the case of the longer channel bag, the issuing melt experiences less mixing with the surrounding sump. Therefore, the potential core in this case is longer, and the melt stream reaches the side wall of the mold with higher momentum. The early dispersion of the melt issued from the short distribution bag causes part of the hot stream to be directed vertically downward toward the middle region of the solidification front. Accordingly, most of the momentum and heat of the later stream are dissipated toward deepening the solidification front along most of the middle region of the calculation domain ($640 \geq y \geq 280\ mm$). This is shown by the solidification-temperature contour (919 K) in Figure 6.20 (c). In addition, the mushy layer around the slab center gets thicker as compared to the corresponding case of the long channel bag. In general, the solidification front at the 50 mm/min casting speed using the short bag is more uniform than that when using the long distribution bag at the same casting speed.

Figure 6.21 shows the computed results for both the short (a,b,c) and long (d,e,f) channel bags at the slab free surface for the 50 mm/min casting speed. Similar to what

has happened at the symmetry plane, the issuing melt stream out of the short-channel bag is scattered over most of the slab free surface. Therefore, no recirculation is experienced by the melt at this surface as shown by Figure 6.21 (a,b). In the case of the long channel bag, the molten stream issued from the channel bag hits the center of the narrow side of the mold, and then recirculates at the slab free surface as shown by Figure 6.21 (d,e). This difference in the flow behavior caused by the two channel bags (long and short) is translated in producing two different distribution characteristics of the temperature contours as shown in Figure 6.21 (c,f). In the case of the short bag, the temperature contours exhibit a nearly longitudinal shape. Whereas, in the case of the long distribution bag, the temperature contours demonstrate a more elliptical like shape.

Another interesting observation is that the shorter distribution bag at the 50 mm/min casting speed produced almost similar uniform temperature profile for the solidification front at the wide symmetry plane, shown in Figure 6.20 (c), to the solidification profile obtained by using the long distribution bag at the 60 mm/min casting speed as depicted in Figure 6.11 (c). The only clear difference between the two mentioned cases is that the solidification front for the longer bag at the 60 mm/min casting speed is deeper in the axial direction as compared to the shorter bag at the 50 mm/min casting speed by about an average of 50 mm. Thus, it is possible to produce similar solidification profiles using different casting speeds with different distribution bag dimensions. This gives a degree of freedom to cast designers to get the required specifications using different parameter combinations.

6.2.1.3 Effect of Temperature Superheat

In investigating the effect of melt superheat on the sump, two temperatures superheat are considered; namely, the 16°C and 60°C. The casting speed is maintained at 60 mm/min using the long channel bag. Figure 6.22 depicts the vector field as well as the temperature contours (solidus and liquidus) at the wide symmetry plane for the two temperatures superheat. In both cases, the temperature superheats do not have much of an effect on either the solidification profile or on the vector field at the wide symmetry plane. The only influence detected is in the increase in the thickness of the mushy layer

from the liquidus contour side, especially around the middle of the calculation domain for the 16°C temperature superheat as seen in Figure 6.22 (b). Figure 6.23 demonstrates cross-sections including and parallel to the slab free surface. At the slab free surface, Figure 6.23 (a-d), the temperature contours for the 16°C and 60°C superheat show completely different distributions. This is attributed to the fact that these sections are located at the adiabatic region of the mold. The temperature of the melt there, in both cases, is distributed according to the inlet temperature of the melt. The higher is the inlet temperature, the greater is the temperature at the whole section. That is not the case at a section located at the primary cooling region (x = 145 mm) as shown by Figure 6.23 (e-h). In this figure, the solidus temperature contours (919 °C) for the 16 and 60°C superheats have almost the same profile, and they differ only in the liquidus contour. The thickening and/or narrowing of the mushy layer according to the inlet temperature superheat could be utilized in relation to the impurity content of the alloy to be cast as follows: if the impurity content of the melt is high, then raising the inlet temperature would cause the mushy layer to be thin and almost uniform, this would allow less impurities to be trapped in the mushy layer and more uniformly distributed within the sump. On the other hand, care has to be taken in raising the inlet temperature as it is known that raising the temperature of the melt increases the oxidation rate exponentially. A "rule of thumb" states that for every 10-12 °C increase in melt temperature, the rate of oxidation will double [42]. In addition, higher melt temperatures cause increased melt contact with carbon sources due to improved wetting. And since in the current model, the upper part of the mold is insulated, and the material that is normally used in the insulation is made of carbon, therefore, improved wetting due to higher melt superheat would cause the aluminum to react with carbon and form carbide-salt inclusions. Because of the aforementioned negative impact on melt quality, the inlet temperature superheat of the melt has to be looked at very carefully when designing molds, especially, those using graphite linings as insulators for the adiabatic section of the mold.

6.3 Spatial Distribution of Inclusions

Metallic and non-metallic inclusions have long been recognized as one of the most important quality issues for aluminum in general, and specifically aluminum can-body alloys in particular. In general, inclusions in the melt can lead to various problems, ranging from the reduction of mechanical properties, excessive tool wear, increased porosity, poor surface finish to lack of pressure tightness. In particular, existence of the inclusions is often the cause of pinholes and high tear-off rate especially in the can-making process. They also impose severe complications for alloy down-gauging. Modeling of deformation hardening and recovery as well as recrystallization requires knowledge of the distribution in size and space of the inter-metallic particles.

The determination of size distribution can be made by measuring particle areas on a polished cross-section using optical or scanning electron microscopy or in a thin foil using transmission electron microscope (TEM). The TEM instruments have very high resolution, but the technique is expensive since good statistics are required. Good statistics requires good automation, and the automation is very difficult to carry out [41]. To determine the 3D distribution of the particles, the thickness of the foil must be known at each measurement. The distribution can also be determined by dissolving the matrix, filtering off the particles and measuring their size.

In order to predict the spatial distribution of inclusion particles within the sump, the current mathematical model is extended to solve the dimensionless convective-diffusive mass transport equation within the sumps of an ingot cast by the vertical DC casting process. The inclusions distribution is predicted at steady state for different particle sizes. In order to do this, the computed steady vector fields obtained in the current and previous chapters, for different melt distributors and casting parameters, are used as an input data to solve the inclusion distribution equation. Inclusion distribution is predicted for particle sizes ranging from 50 to 200 μm diameters. The results can be utilized in understanding the mechanism of inclusion distribution and the parameters that would affect the most this distribution within the sump. All the calculations are based on the assumption that inclusions are infiltrated through the ceramic filters. The

mathematical modeling would try to predict which of the distribution bags would distribute the inclusions more homogeneously in the ingot.

6.3.1 Problem Definition and Boundary Conditions

A prediction of inclusion distribution within the sump is carried out using the converged steady state velocity field. This filed is implemented in the convective-diffusive mass concentration partial differential equation. The equation is then solved iteratively. The inclusion particles are considered to enter the mold through the nozzle. The particles are assumed to be spherical in shape and fine enough but not so numerous as to affect the flow field. The dispersion of particles of a specific size introduced into the mold can be expressed by the dimensionless steady-state-convective-diffusive mass transport equation:

$$\frac{\partial}{\partial x}[(u-U_{st})c]+\frac{\partial vc}{\partial y}+\frac{\partial wc}{\partial z}=\frac{1}{\mathrm{Re}}\left[\frac{\partial}{\partial x}(\Gamma_{eff}\frac{\partial c}{\partial x})+\frac{\partial}{\partial y}(\Gamma_{eff}\frac{\partial c}{\partial y})+\frac{\partial}{\partial z}(\Gamma_{eff}\frac{\partial c}{\partial z})\right] \tag{6.1}$$

where U_{st} is the stock rising velocity defined as:

$$U_{st}=(\rho_f-\rho_p)\,g\,d_p^2/18\mu\,u_i \tag{6.2}$$

ρ_f and ρ_p represent the melt and the particle densities, respectively. The particle density (ρ_p) is assumed to be 3500 kg/m^3, and g is the gravity. u_i is the jet inlet velocity. The effective diffusion coefficient is defined as:

$$\Gamma_{eff}=\frac{1}{Sc}+\frac{\mu_t}{Sc_t} \tag{6.3}$$

where Sc_t is the turbulent Schmidt number, and is assumed to be 1. The laminar part of the effective diffusivity is negligible compared to the turbulent part. Note that the unsteady term in equation (6.1), $(\frac{\partial c}{\partial t})$, is dropped since the interest is in the calculation of the steady state distribution of the particles. The computed velocity fields obtained in the current and last chapters are used in equation (6.1), and the latter equation is solved

iteratively using the finite volume technique. The convergence criterion is based on the following criterion:

$$Max\left| c^{n+1} - c^{n} \right| \leq 10^{-5} \tag{6.4}$$

where c^{n+1} and c^{n} are the values of the normalized concentration at the (n+1)-th and n-th iteration, respectively. The normalized concentration of inclusions at the nozzle port is set to 1. The flux at all boundaries is set to zero. It is assumed that the particles passing through the mushy zone are entrapped and move downward with the solidifying front at the casting speed. Given the low value of the particle volumetric concentration, the effect of the particles on the turbulent flow field is considered to be negligible.

6.3.2 Results and Discussion Using Combo Bag

Figure 6.24 shows the effect of the casting speed on the spatial distribution of particles at the wide symmetry plane. The particle diameter is 50 μm, and the temperature superheat is 65°C. The particle distribution is shown at 37 mm below the slab free surface. At this depth, the transverse line is almost passing through the middle of the side window facing the narrow side of the mold. Therefore, this depth would be a suitable location to show the effect of the discussed parameter on the concentration distribution. The figure shows, in general, that the concentration is the highest under the nozzle opening, and then it drops sharply from 1 to 0.275 within a transverse distance of 80 mm from the slab center. In the case of 60 and 80 mm/min casting speed, an almost constant concentration profile is established, after the sudden drop, over a distance of 43 mm. This constant concentration profile is an indication of a good mixing of melt within the bag. The latter is attributed to the high degree of turbulence in that region. Another sudden drop in the concentration can be seen over most of the bottom window of the bag as a result of the escape of some inclusions through its opening. The drop in concentration continues up until the end of the bag is reached (y=150 mm). As the melt emerges from the side window of the bag, a uniform concentration profile is maintained over a small distance followed by a small rise to another peak at y =200 mm. Then, a gradual decrease in the concentration is taking place over the rest of the wide symmetry plane. It can be seen that the concentration for the three casting speeds follows the same trend, except in

the case of the 40 mm/min where the concentration after the first sudden drop is dropping gradually instead of staying constant as in the other two casting speeds. It is clear that the higher the casting speed is, the higher the concentration distribution across the sump will be.

Figure 6.25 depicts the concentration distribution of particles with diameter of 250 μm at the same location as in the previous case for the same distribution system and temperature superheat. It is clear that with the increase in the inclusion size, the casting speed as well as the bottom window have less effect on the spatial-concentration distribution, as will be seen later in the discussion of the effect of particle size. The concentration is almost exponentially dropping to zero right after the bag side opening. Figure 6.26 presents the effect of particle size on the spatial-concentration distribution at the wide symmetry plane at an axial distance of 37 mm from the slab free surface. The distribution is computed at a temperature superheat of 65°C using the standard combo bag. The smaller particle with diameter of 25 μm is affected the most by the bag openings and distributed more uniformly over the slab length in the transverse direction. Whereas, with the increase in the particle size, the spatial distribution of the concentration is less affected by the bag openings and unevenly distributed with most of the particles concentrated around the slab center. Figure 6.27 shows that the bottom window blockage has less effect on the particle concentration, especially when these particles have small diameters. Here, the casting speed of 60 mm/min, a relatively high value, plays a significant role in drifting the particles with a gradual decrease in concentration over the entire symmetry plane.

Figures 6.28 and 6.29 illustrate the effect of bag dimensions on the transverse particle concentration at the wide symmetry plane for 100 and 500 μm particles, respectively. It is clear for small particles (Figure 6.28) the concentration distribution is affected by the bag dimensions. Whereas, the large particles show almost the same concentration distribution intensifying around the slab center, and the bag size has no influence on the particle concentration distribution as shown in Figure 6.29. In the case of 100 μm diameter particle shown in Figure 6.28, the concentration using the small combo bag is dropping sharply more than that in the case of the standard bag at the region

surrounding the slab center. This drop in the concentration can be attributed to the reverse flow explained in Chapter Five in which the molten aluminum outside the combo bag is entering inside the bag through the bottom window. The particle concentration of the molten aluminum inside the small bag is diluted by the reverse flow causing the concentration to drop more than that in the case of the standard bag which has no reverse flow problem. The particles failed to escape from the bottom window of the small bag and thereby cause the concentration along the rest of the wide symmetry plane of the slab to be higher than in the case of the standard bag.

6.3.3 Results and Discussion Using Channel Bag

Figure 6.30 presents the effect of casting speed on the transverse distribution at the wide symmetry plane using the long channel bag. The concentration distribution profile is taken at x = 37 mm below the slab free surface. The particle size is 100μm, and the temperature superheat is 32°C. In general, there is a big difference in the concentration profile when using the combo bag (refer to Figure 6.24) and when using the channel bag. For the channel bag, the concentration distribution profile is a strong function of the casting speed as can be clearly seen in the figure. The profile for the 60 mm/min casting speed shows a more uniform distribution around the middle region of the calculation domain (180 mm- 600 mm). This is an indication of increased levels of turbulence which enhances mixing around that region. Over the same region for the 40 mm/min casting speed, the concentration profile is almost linearly decreasing.

Figure 6.31 depicts the effect of particle size on the concentration profile at the wide symmetry plane using the long channel bag. As in the case of the combo bag, for the larger particle size, the higher concentration is around the slab center. Figure 6.32 illustrates the effect of channel bag dimensions on the concentration profile at the same location and using the same parameters as in the previous case. The particle diameter is 100 μm. The early mixing of the issued melt from the short bag with the surrounding sump is the reason for the lower concentration across the wide symmetry plane. This is a clear indication that the short channel bag is suitable for distributing the inclusions more uniformly over the slab cross-section than the long channel bag.

6.4 Closure

Some general concluding remarks can be made from the current parametric study that would enable the foundryman to have a better control over the flow and solidification characteristics of aluminum slabs cast using the vertical DC casting technique. This chapter's concluding remarks are summarized by the following points:

- Generally, the upward flow causes the mushy region thickness to extend from the liquidus side, while the downward flow causes the mushy layer to be thin, and might push the solidification front deeper or might cause it to be horizontally uniform.
- The importance of optimizing the casting speed so that the following objectives can be achieved:

  1- A guarantee that the outer solidified layer is able to hold the molten core once the slab emerges from the mold.

  2- Avoid turbulence at the slab free surface, such as the one generated by the 60 mm/min casting speed, in order to eliminate, or at least, minimize aluminum oxide detachment from the free surface. In addition, avoiding turbulence at the slab free surface reduces the oxidation rate through reducing the melt surface to volume ratio.

  3- Minimize both the problem of negative segregation at the ingot center and the positive segregation at the slab surface as explained earlier.

  4- It is recommended in DC casting under steady state condition to have a shallow sump with uniform solidification front, such as the one obtained with the 50 mm/min casting speed using the short channel bag.

- The possibility of getting similar solidification front characteristics using different parameter combinations will provide a degree of freedom to cast engineers in specifying operational parameters that best suite the requirements of the production firm. This has been shown in the similarity of the solidification-front profiles attained in the case of the long-channel bag with a casting speed of 60 mm/min to that obtained with the short bag with the casting speed of 50 mm/min.
- Temperature superheat has to be kept moderate but not too high especially when using graphite lining as insulation at the upper region of the mold. Keeping the inlet melt

superheat low would allow less wetting of the graphite surface by the molten aluminum, and hence, reducing the chance of formation of carbide-salt inclusions.

Regarding the inclusions distribution:

- Uniform concentration profile is an indication of good mixing of melt. Good mixing in turn is an indication of high levels of turbulence.
- Large particles are hardly affected by the operational and geometrical parameters such as casting speed, bag dimensions and/or type. These particles are mainly concentrated around the slab center.
- Small particles are more uniformly distributed within the sump.
- A higher casting speed leads to a higher concentration of inclusion across the sump.
- Combo bags are more likely to uniformly distribute inclusions over the slab cross-sections than channel bags.

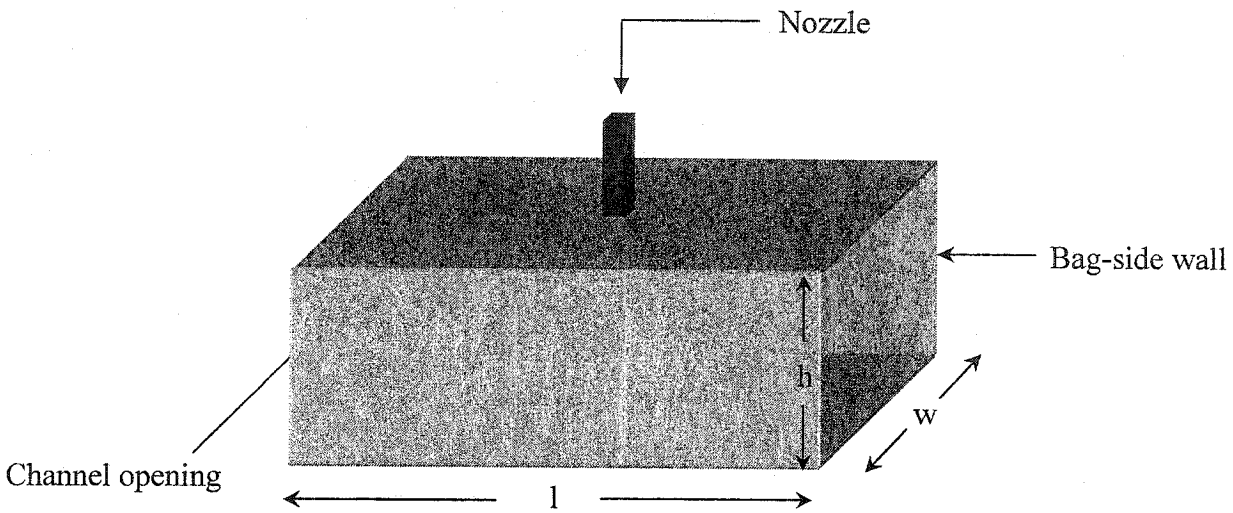

(a) Channel bag

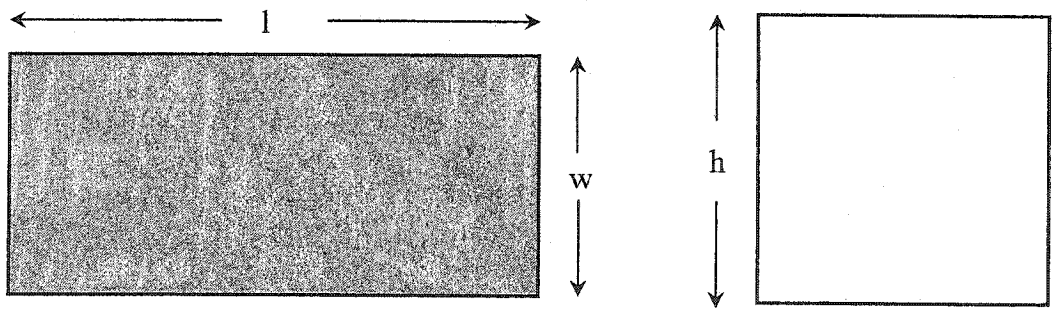

(b) Bottom view

(c) Side window

Figure 6.1: Schematic of a channel bag

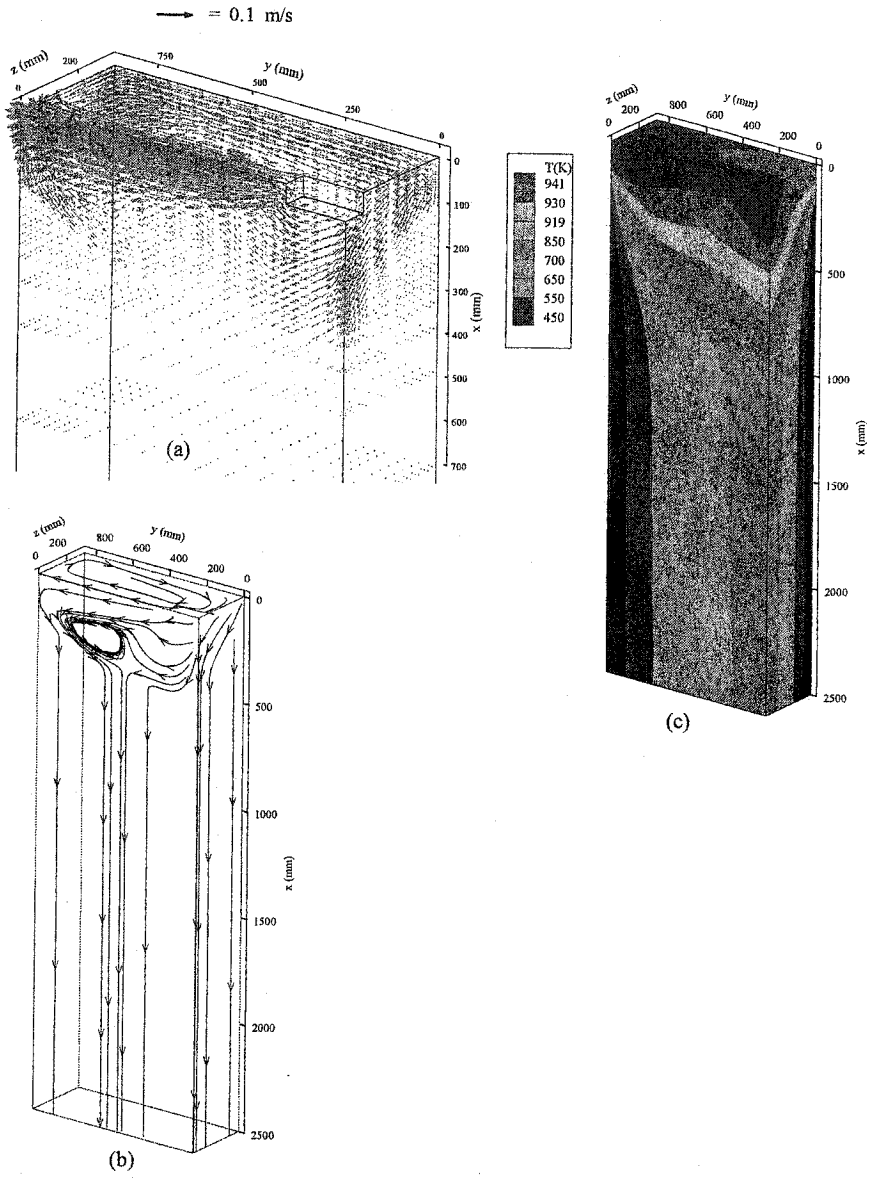

Figure 6.2: 3D-surface plot using the long-channel bag, casting speed = 40 mm/min, temperature superheat = 32 °C. (a) Vector field, (b) Streamlines, (c) Temperature contours.

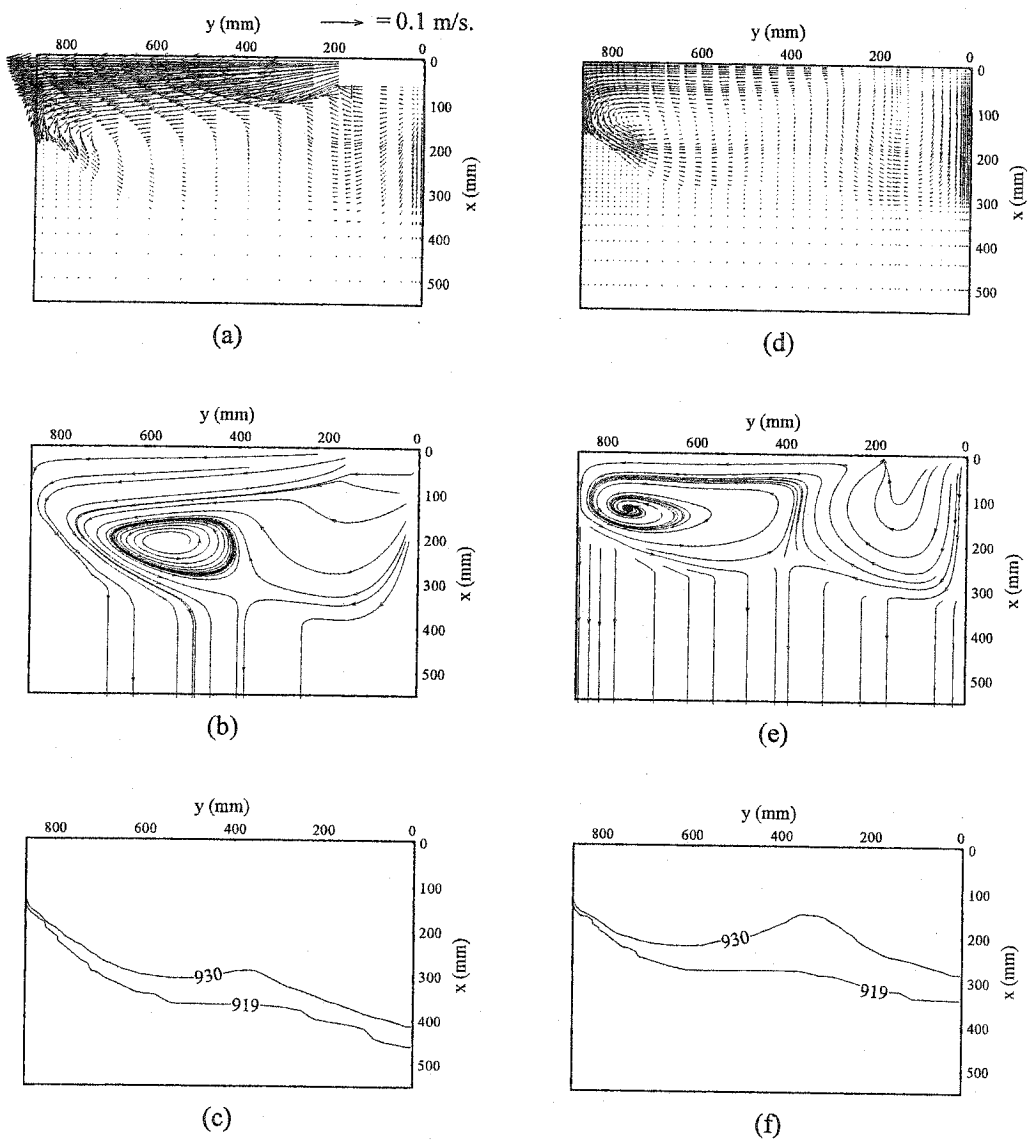

Figure 6.3: Computed results parallel to the slab rolling face using the long channel bag, casting speed = 40 mm/min, temperature superheat = 32 °C, (a-c) wide symmetry plane, (d-f) z = 109 mm, (a,d) vector plot, (b,e) streamlines, (c,f) temperature contours in Kelvin.

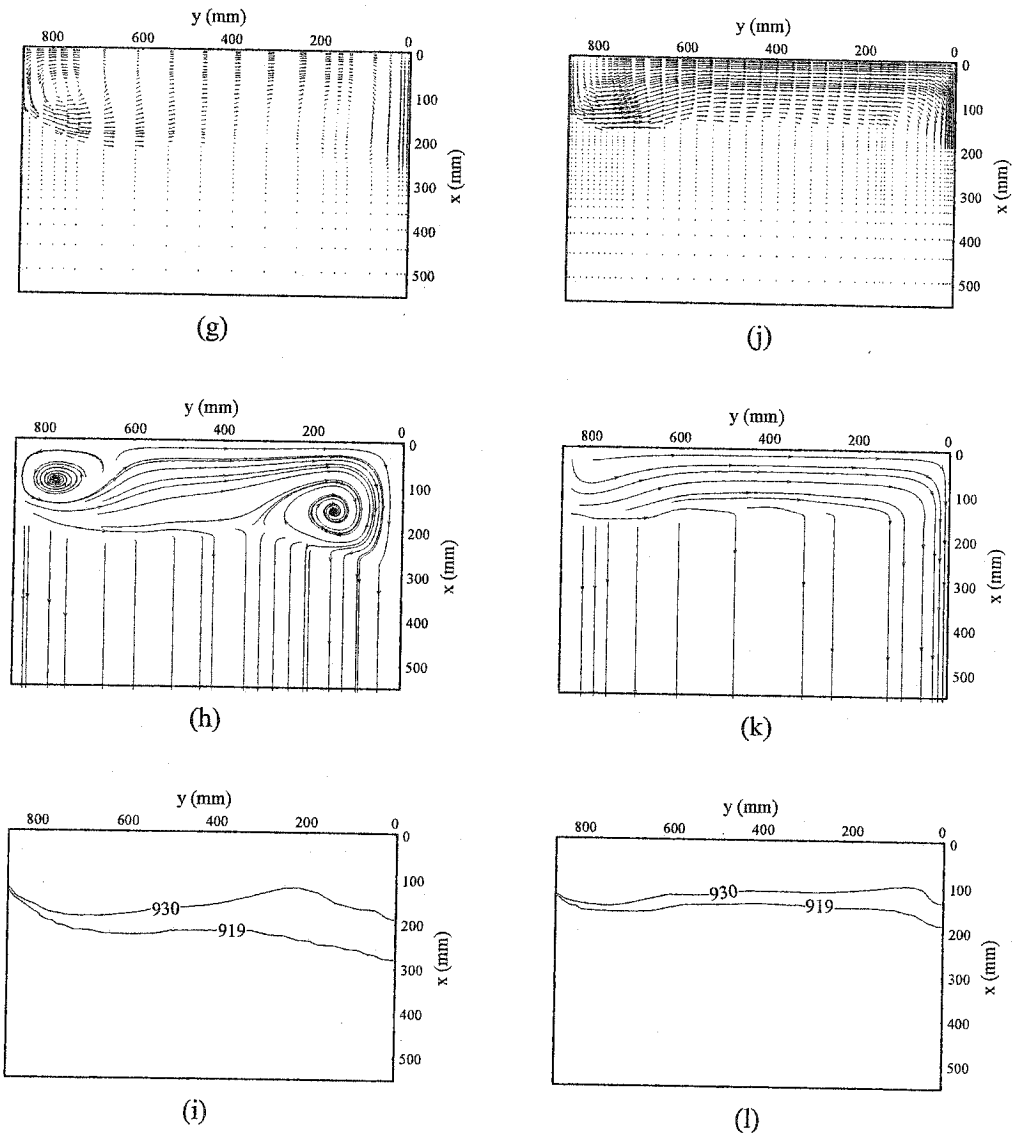

Figure 6.3 (continue): (g-i) z = 147 mm,(j-l) z = 212 mm. (g,j) vector plot, (h,k) streamlines, (i,l) temperature contours in Kelvin.

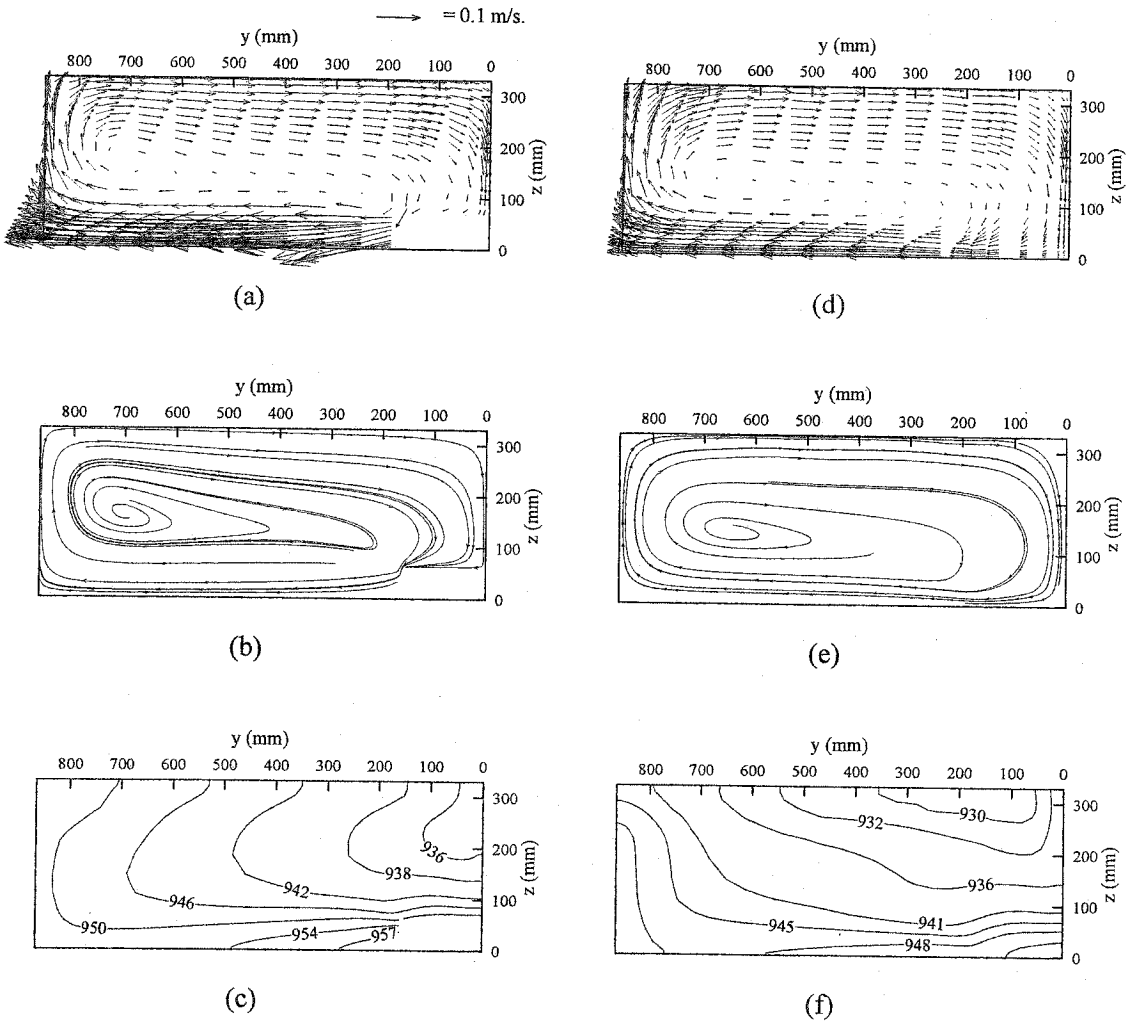

Figure 6.4: Computed results parallel to the slab free surface using the long channel bag, casting speed = 40 mm/min, temperature superheat = 32 °C, (a-c) slab free surface, (d-f) x = 75 mm. (a,d) vector plot, (b,e) streamlines, (c,f) temperature contours in Kelvin.

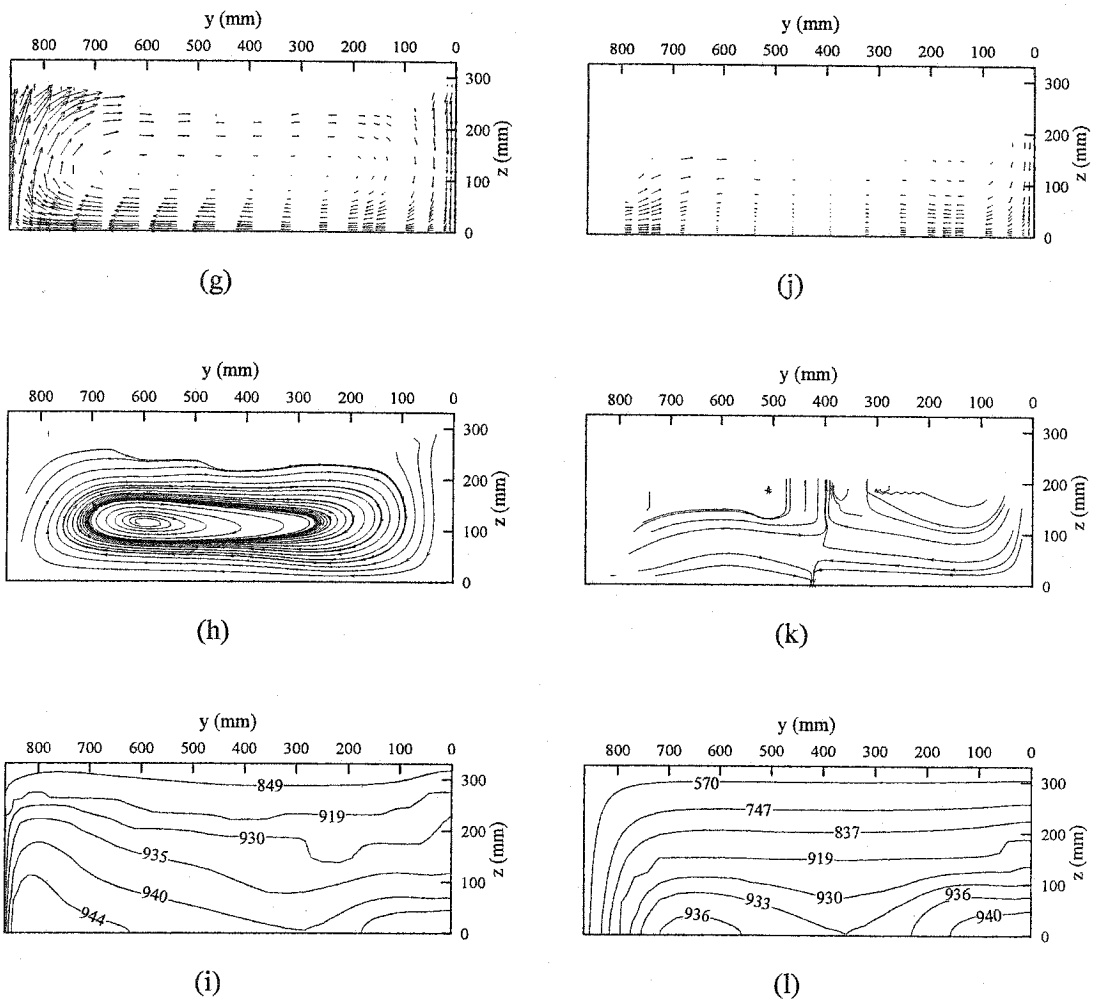

Figure 6.4 (continue): (g-i) x = 125 mm, (j-l) x = 215 mm, (g,j) vector plot, (h,k) streamlines, (i,l) temperature contours in Kelvin.

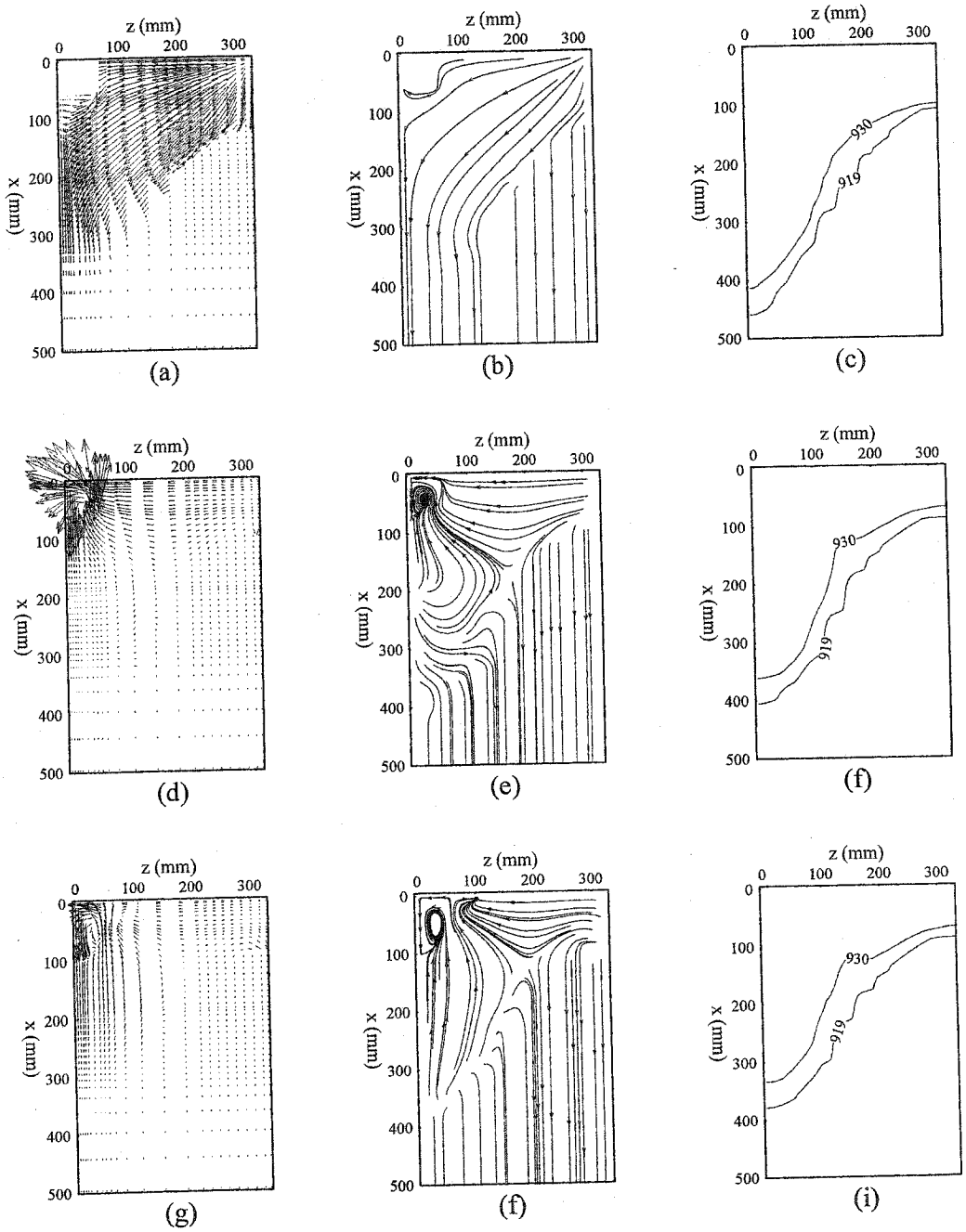

Figure 6.5: Computed results parallel to the slab narrow surface using the long channel bag, casting speed = 40 mm/min, temperature superheat = 32 °C, (a-c) narrow symmetry plane, (d-f) y = 173 mm, (g-i) y = 248 mm. (a,d,g) vector plot, (b,e,f) streamlines, (c,f,i) temperature contours in Kelvin.

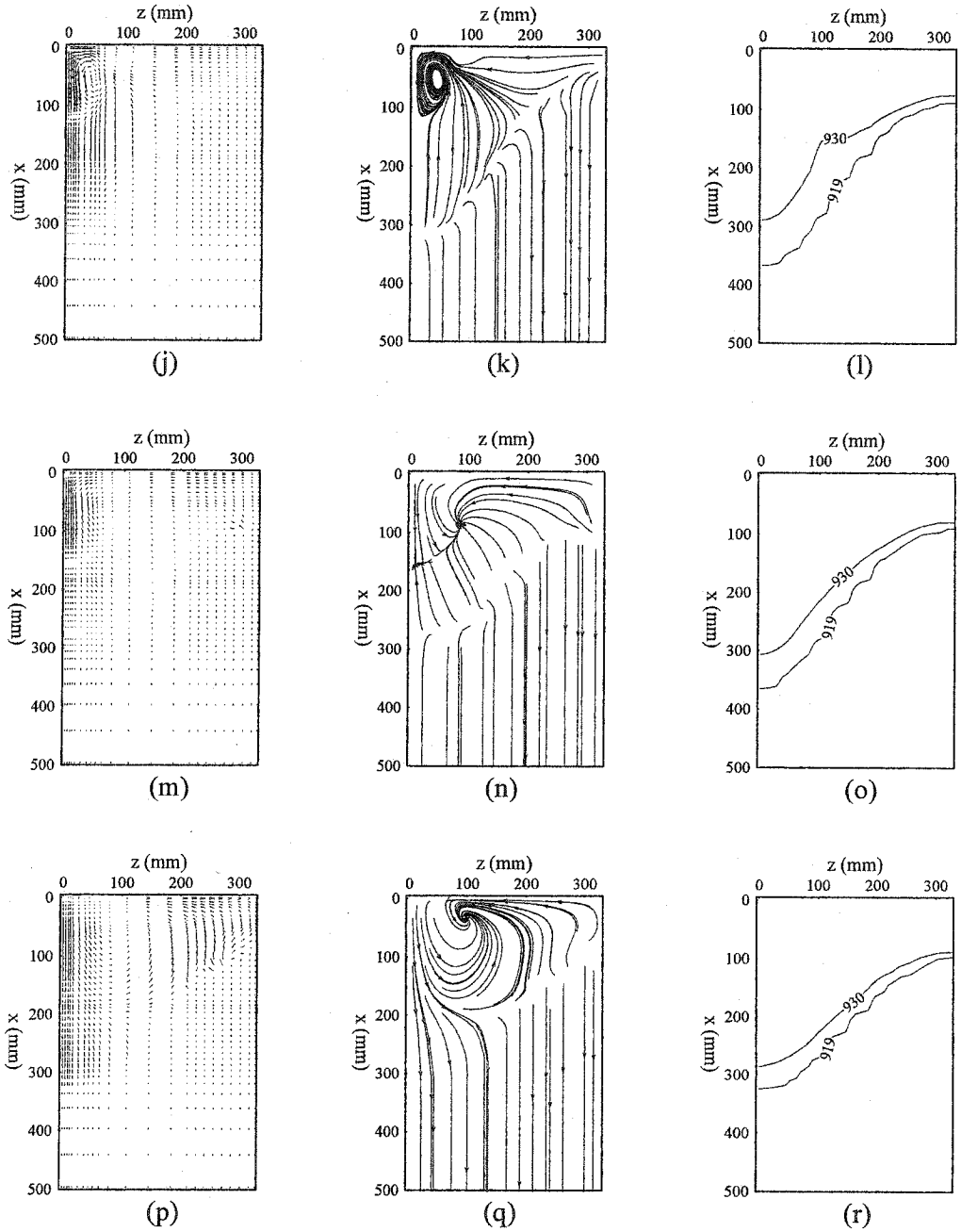

Figure 6.5 (continue): (j-l) y = 355 mm, (m-o) y = 503 mm, (p-r) y = 650 mm. (j,m,p) vector plot, (k,n,q) streamlines, (l,o,r) temperature contours in Kelvin.

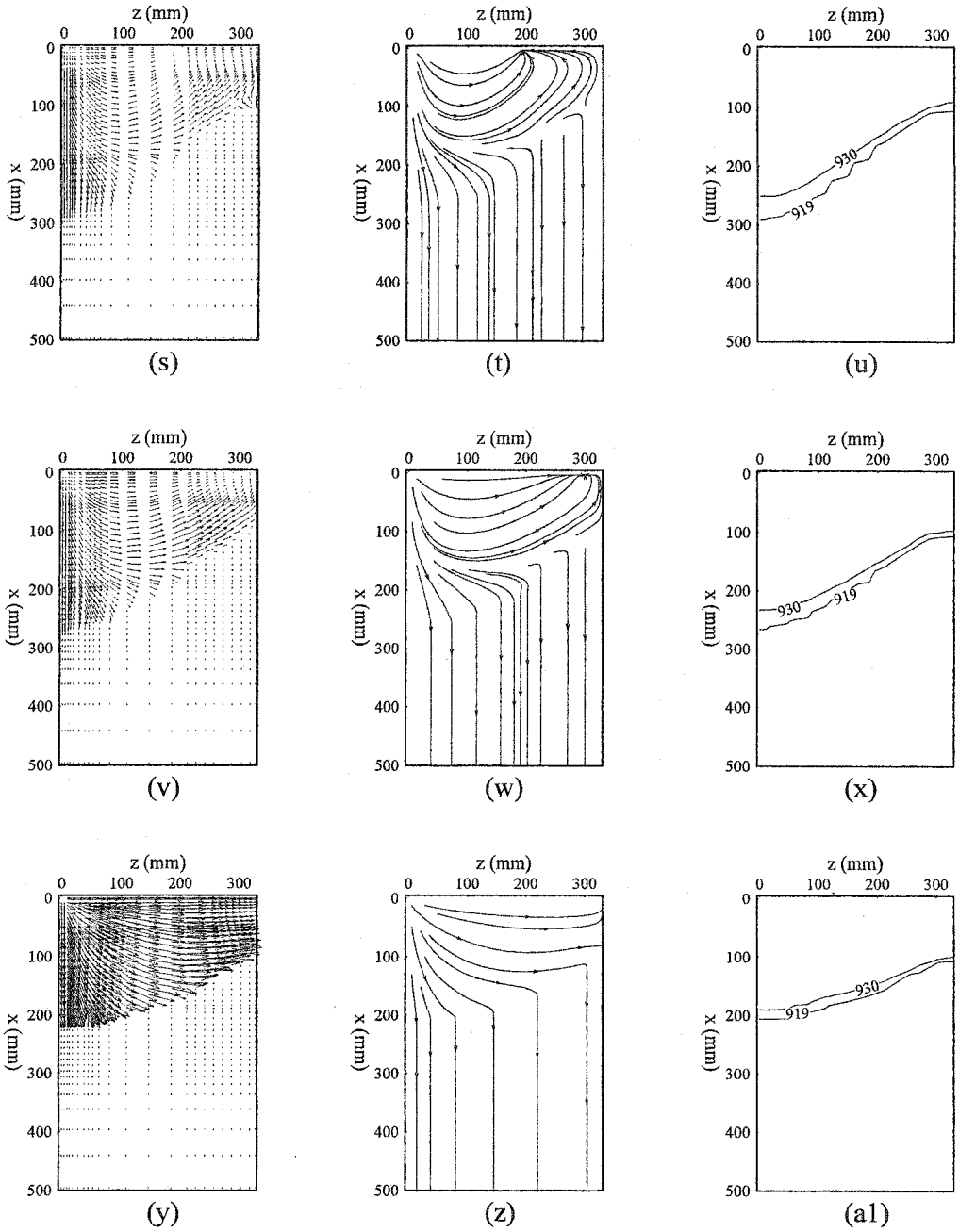

Figure 6.5 (continue): (s-u) y = 718 mm, (v-x) y = 742 mm, (y-a1) y = 806 mm. (s,v,y) vector plot, (t,w,z) streamlines, (u,x,a1) temperature contours in Kelvin.

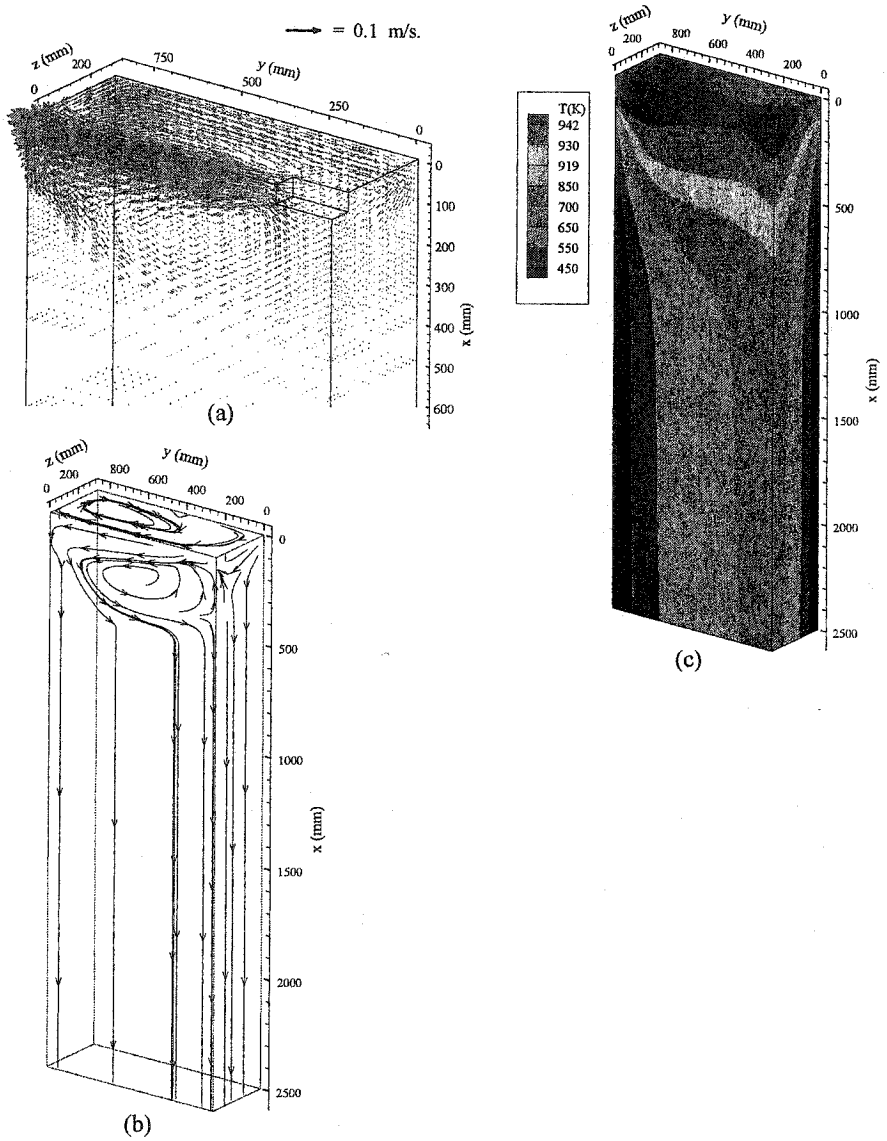

Figure 6.6: 3D-surface plot using the long-channel bag, casting speed = 50 mm/min, temperature superheat = 32 °C. (a) Vector field, (b) Streamlines, (c) Temperature contours.

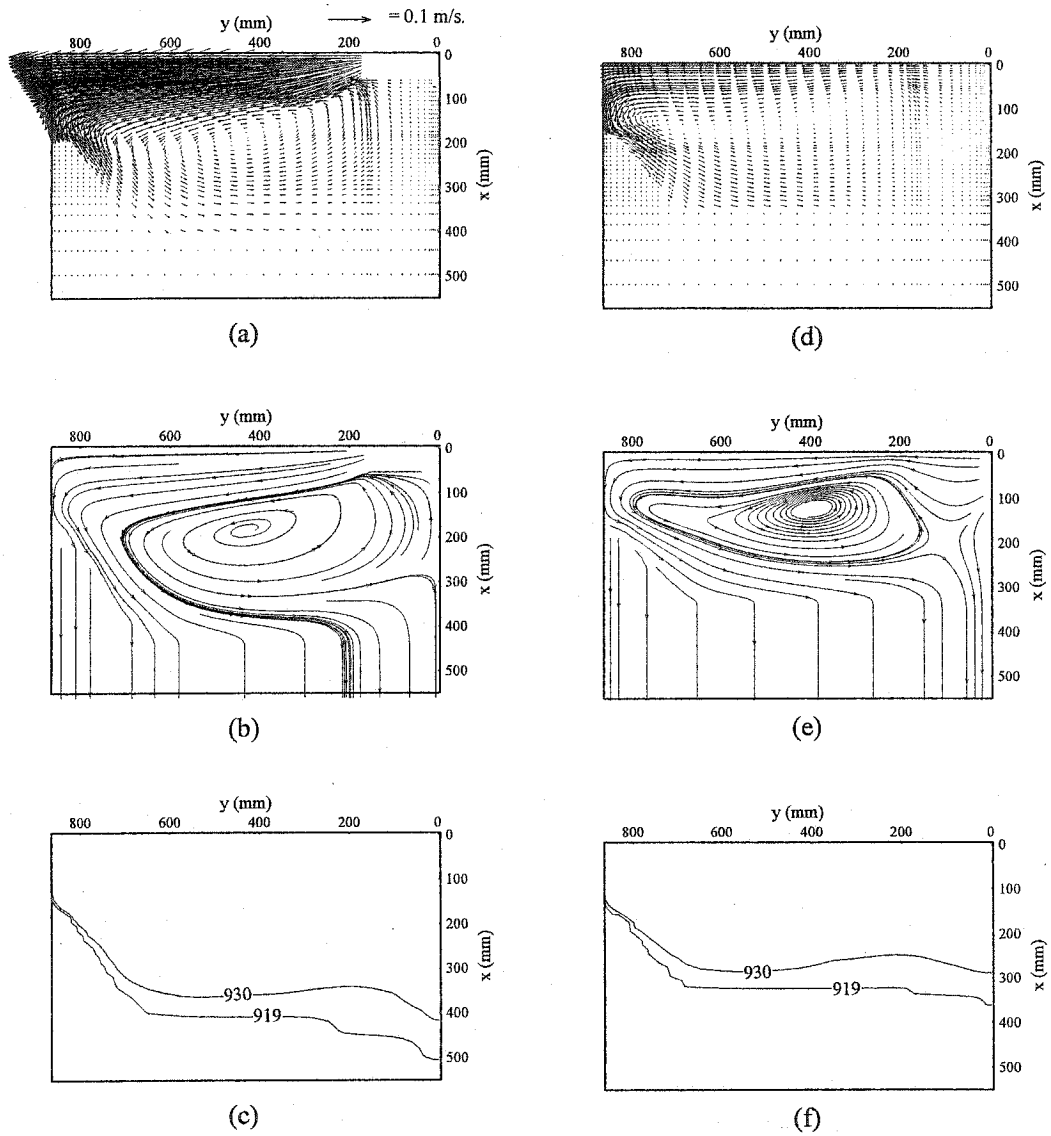

Figure 6.7: Computed results parallel to the slab rolling face using the long channel bag, casting speed = 50 mm/min, temperature superheat = 32 °C, (a-c) wide symmetry plane, (d-f) z = 109 mm. (a,d) vector plot, (b,e) streamlines, (c,f) temperature contours in Kelvin.

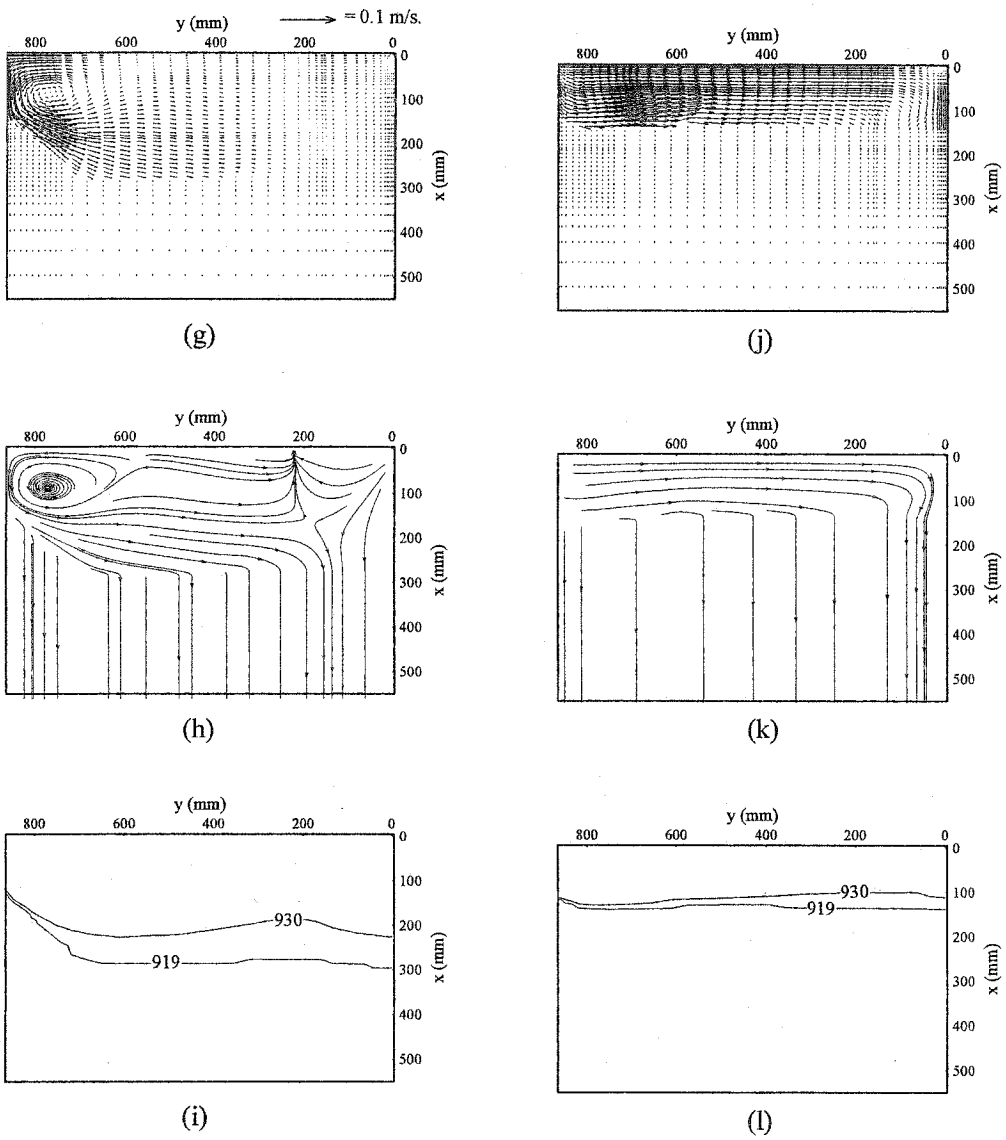

Figure 6.7 (continue): (g-i) z = 147 mm, (j-l) z = 257 mm. (g,j) vector plot, (h,k) streamlines, (i,l) temperature contours in Kelvin.

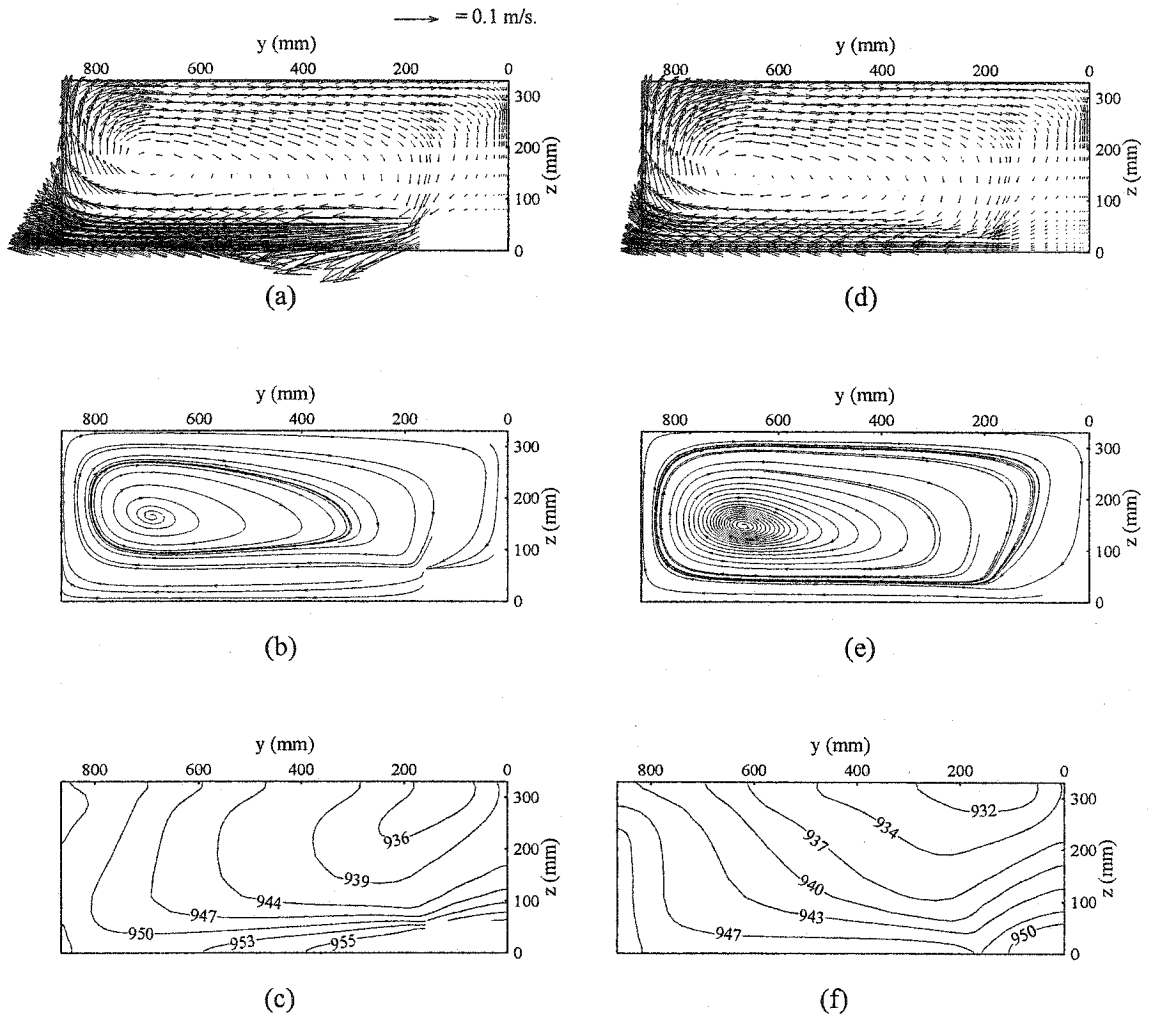

Figure 6.8: Computed results parallel to the slab Free surface using the long channel bag, casting speed = 50 mm/min, temperature superheat = 32 °C, (a-c) slab free surface, (d-f) x = 75 mm. (a,d) vector plot, (b,e) streamlines, (c,f) temperature contours in Kelvin.

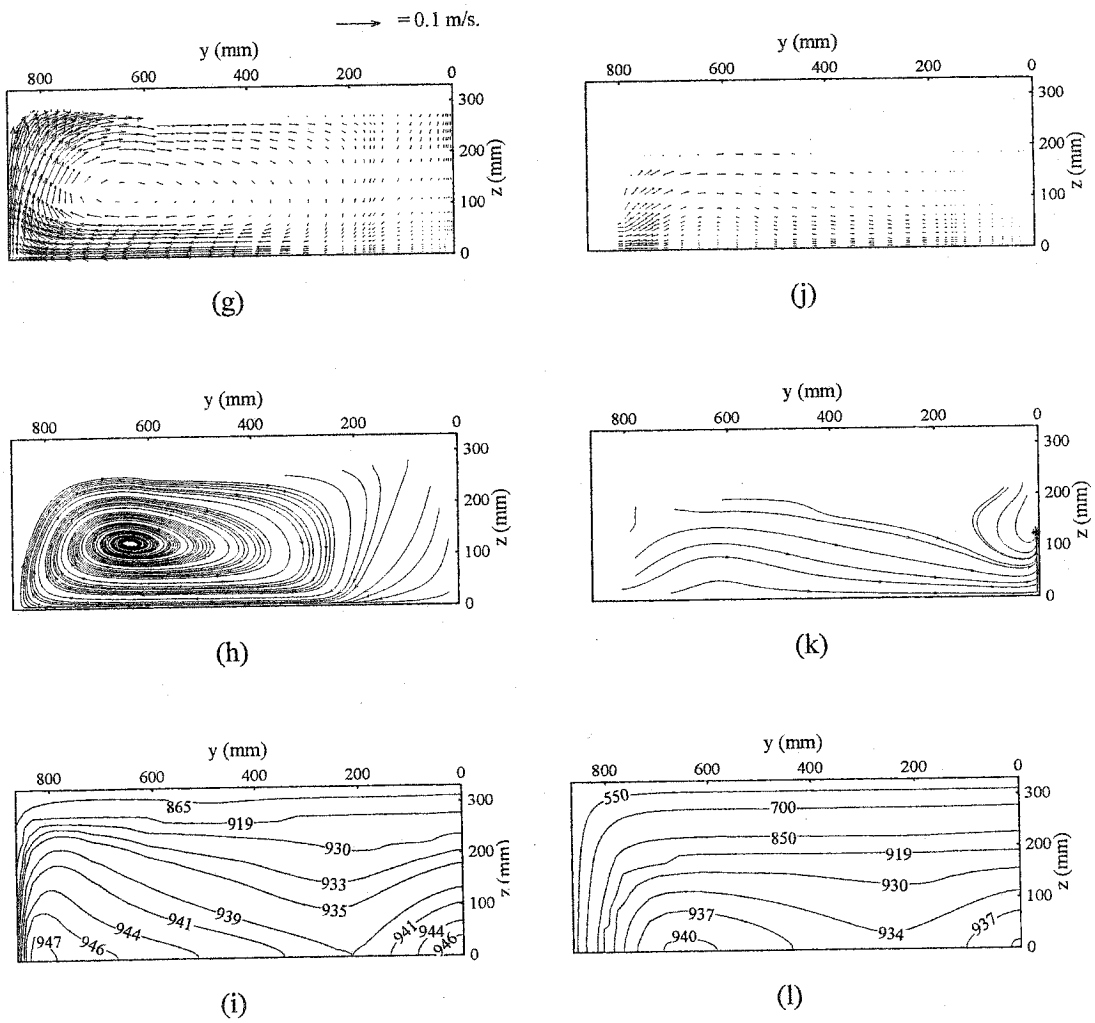

Figure 6.8 (continue): (g-i) x = 125 mm, (j-l) x = 215 mm. (g,j) vector plot, (h,k) streamlines, (i,l) temperature contours in Kelvin.

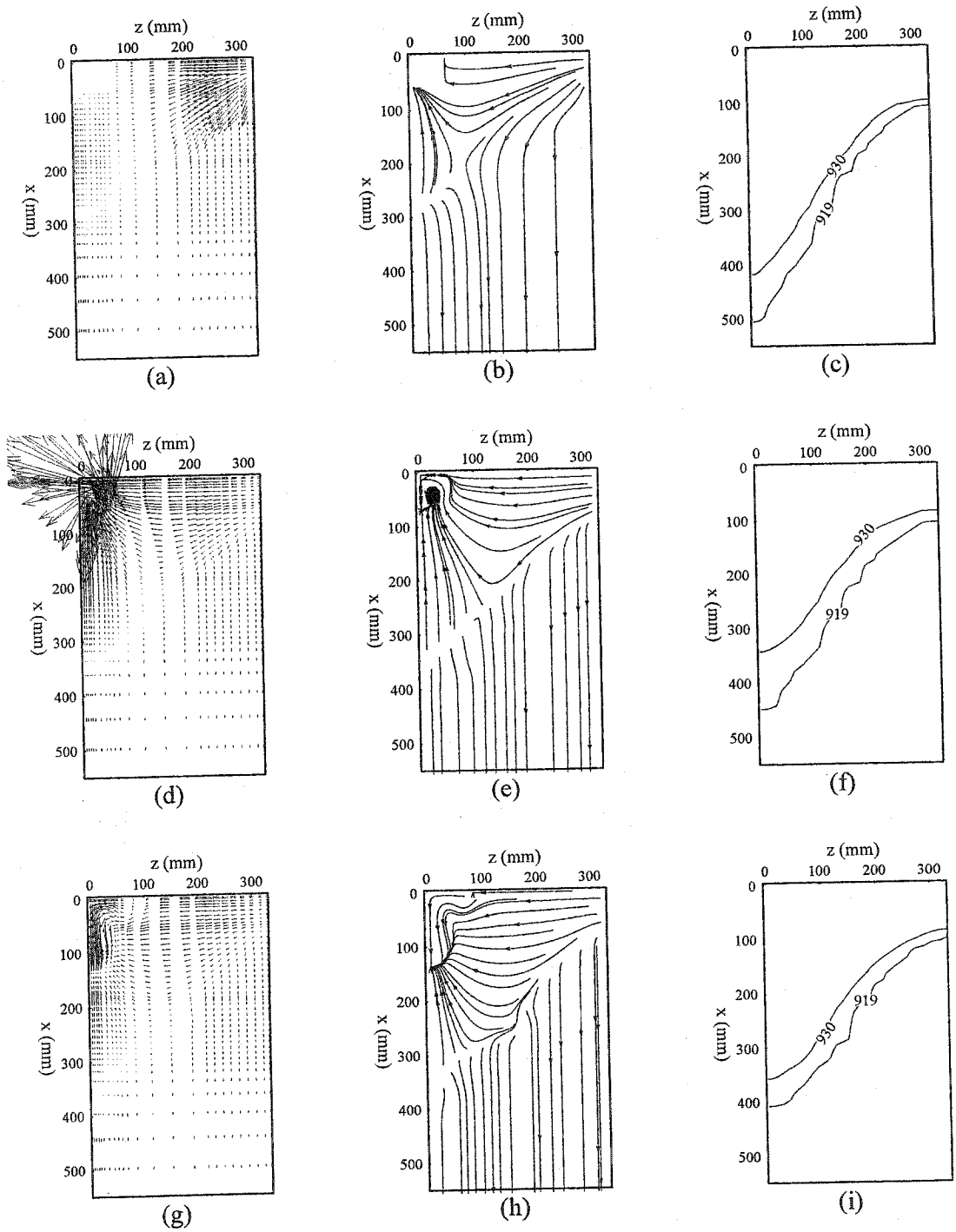

Figure 6.9: Computed results parallel to the slab narrow surface using the long channel bag, casting speed = 50 mm/min, temperature superheat = 32 °C. (a-c) narrow symmetry plane, (d-f) y = 173 mm, (g-i) y = 355 mm. (a,d,g) vector plot, (b,e,h) streamlines, (c,f,i) temperature contours in Kelvin.

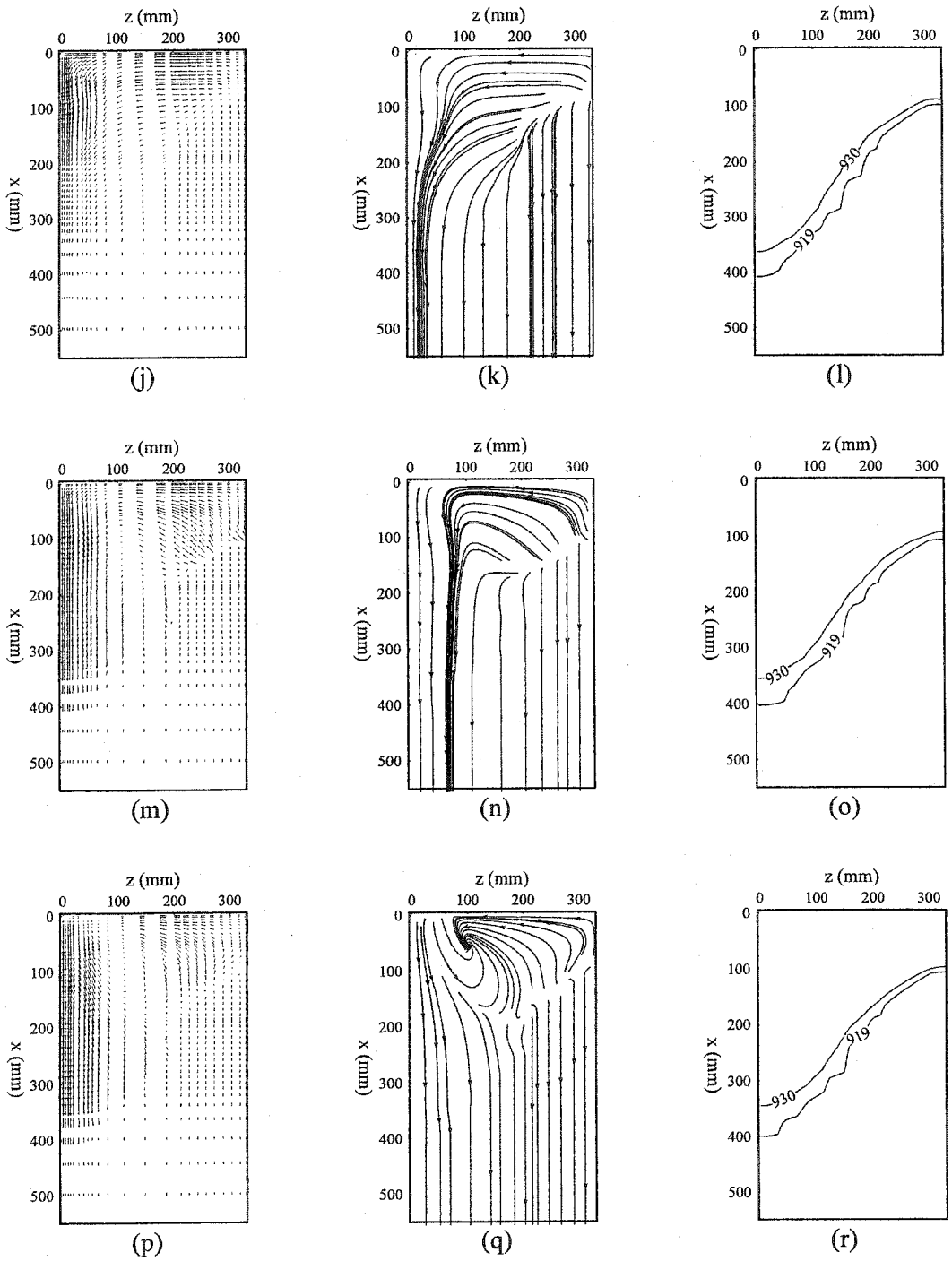

Figure 6.9 (continue): (j-l) y = 503 mm, (m-o) y = 613 mm, (p-r) y = 650 mm. (j,m,p) vector plot, (k,n,q) streamlines, (l,o,r) temperature contours in Kelvin.

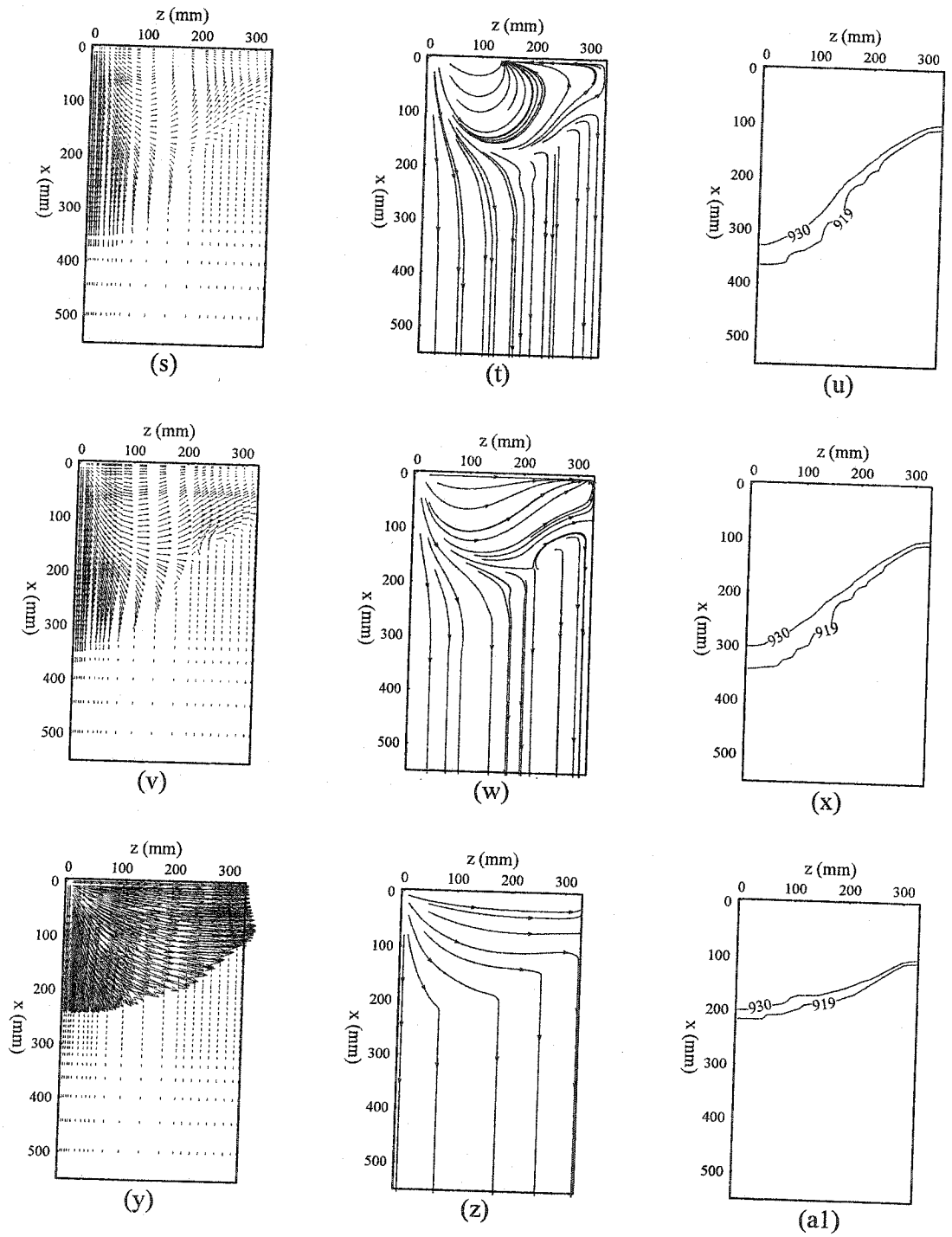

Figure 6.9 (continue): (s-u) y = 718 mm, (v-x) y = 742 mm, (y-a1) y = 806 mm. (s,v,y) vector plot, (t,w,z) streamlines, (u,x,a1) temperature contours in Kelvin.

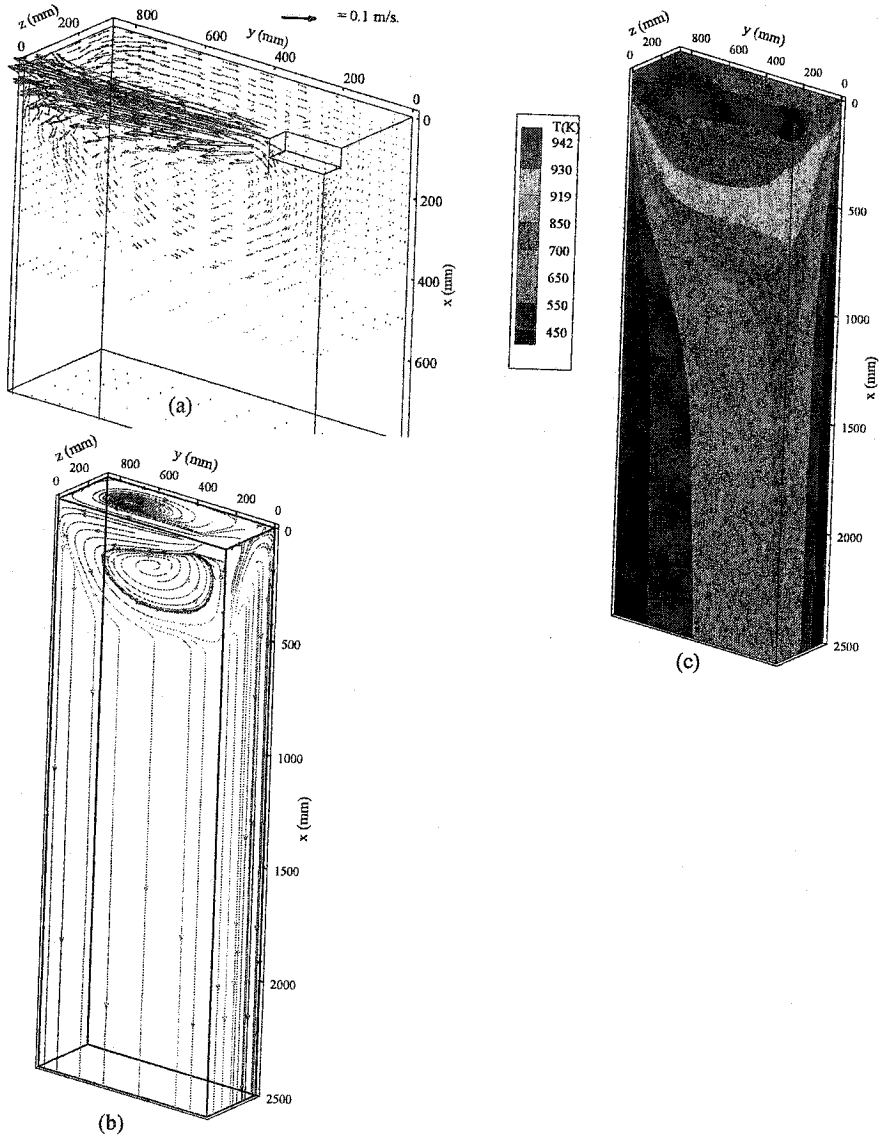

Figure 6.10: 3D-surface plot using the long-channel bag, casting speed = 60 mm/min, temperature superheat = 32 °C. (a) Vector field, (b) Streamlines, (c) Temperature contours.

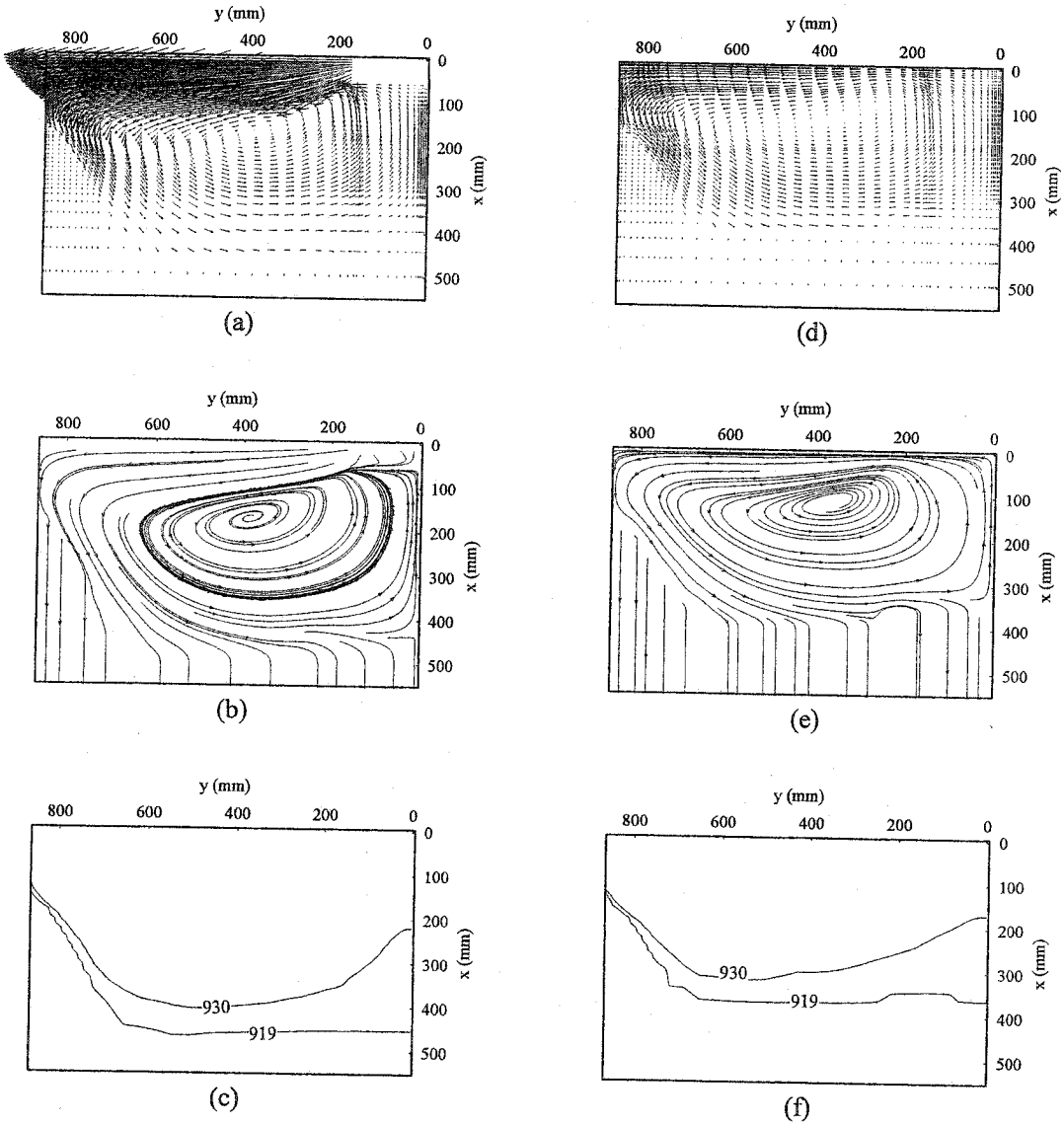

Figure 6.11: Computed results parallel to the slab rolling face using the long channel bag, casting speed = 60 mm/min, temperature superheat = 32 °C, (a-c) wide symmetry plane, (d-f) z = 109 mm. (a,d) vector plot, (b,e) streamlines, (c,f) temperature contours in Kelvin.

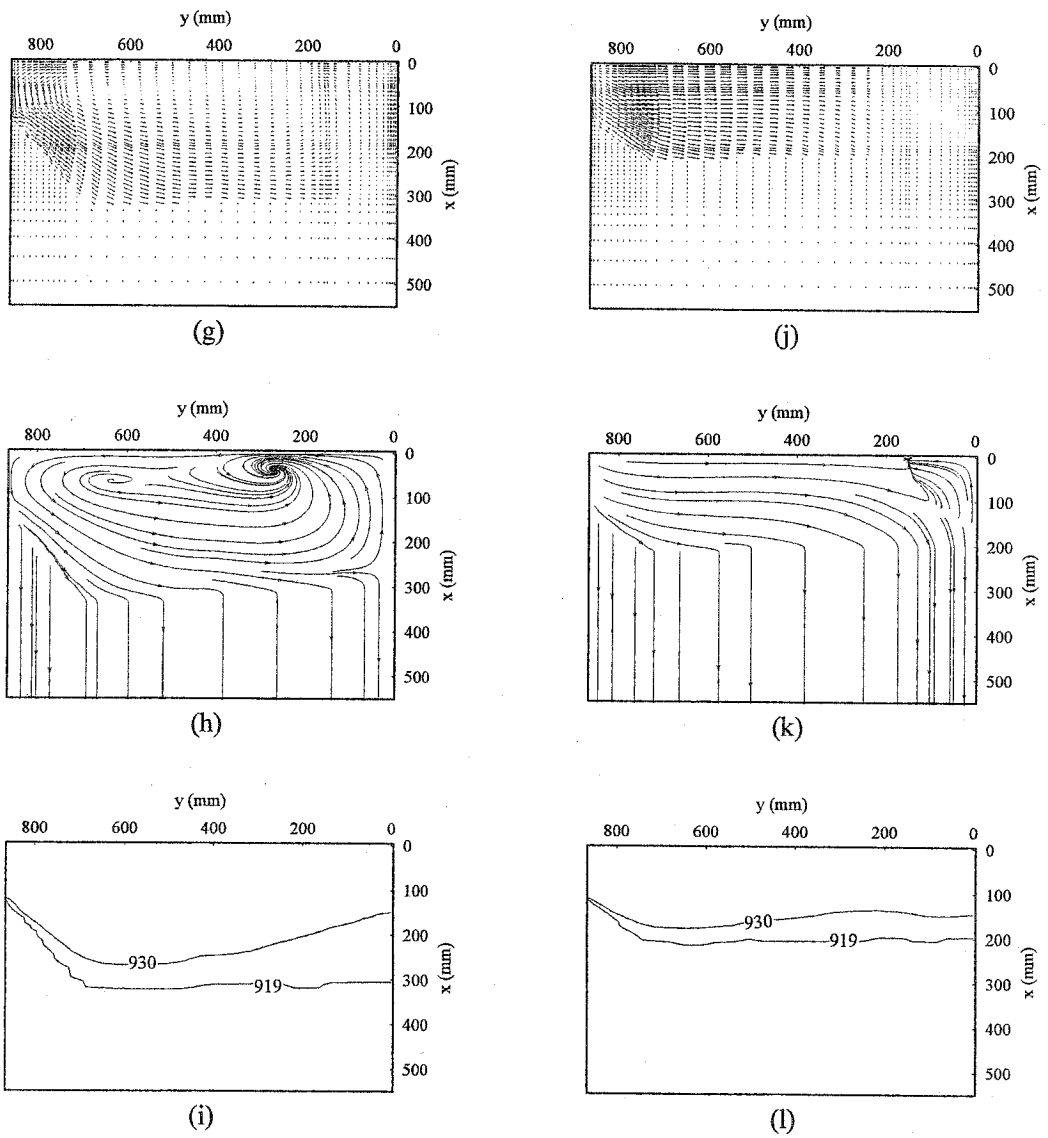

Figure 6.11 (continue): (g-i) z = 147 mm, (j-l) z = 212 mm. (g,j) vector plot, (h,k) streamlines, (i,l) temperature contours in Kelvin.

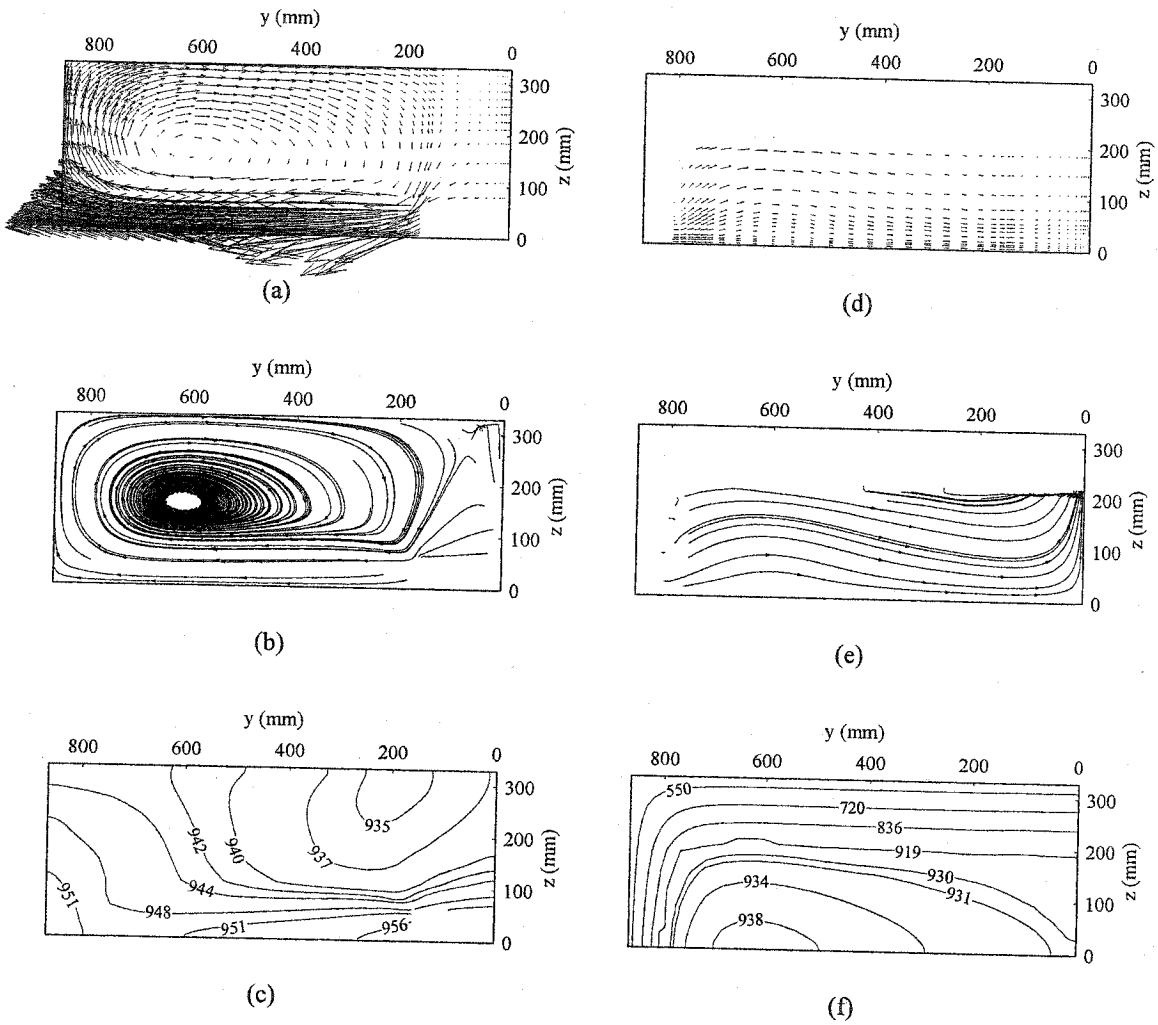

Figure 6.12: Computed results parallel to the slab-free surface using the long channel bag, casting speed = 60 mm/min, temperature superheat = 32 °C, (a-c) slab free surface, (d-f) x = 215 mm. (a,d) vector plot, (b,e) streamlines, (c,f) temperature contours in Kelvin.

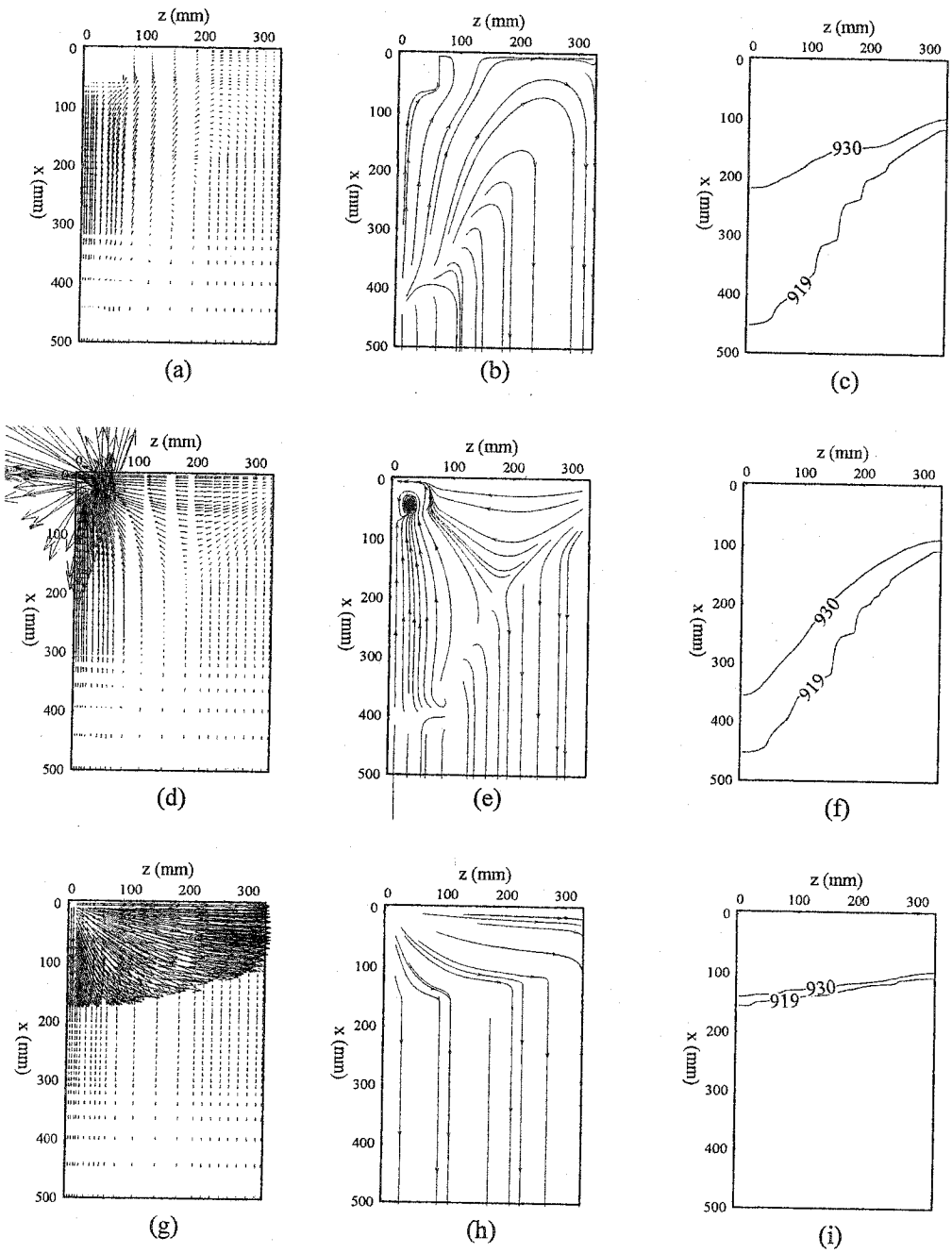

Figure 6.13: Computed results parallel to the slab narrow surface using the long channel bag, casting speed = 60 mm/min, temperature superheat = 32 °C. (a-c) narrow symmetry plane, (d-f) y = 173 mm, (g-i) y = 858 mm. (a,d,g) vector plot, (b,e,h) streamlines, (c,f,i) temperature contours in Kelvin.

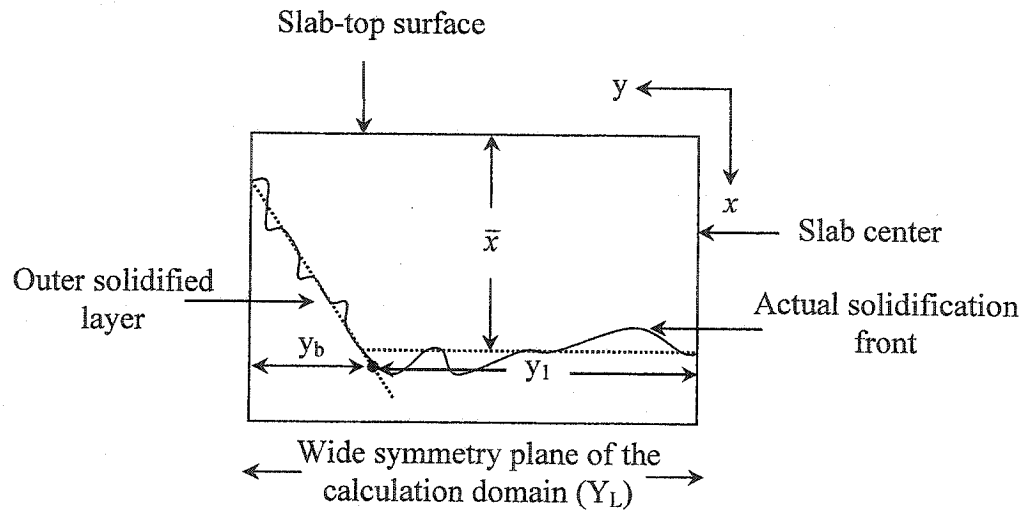

Figure 6.14: Schematic explaining how the average sump depth is calculated.

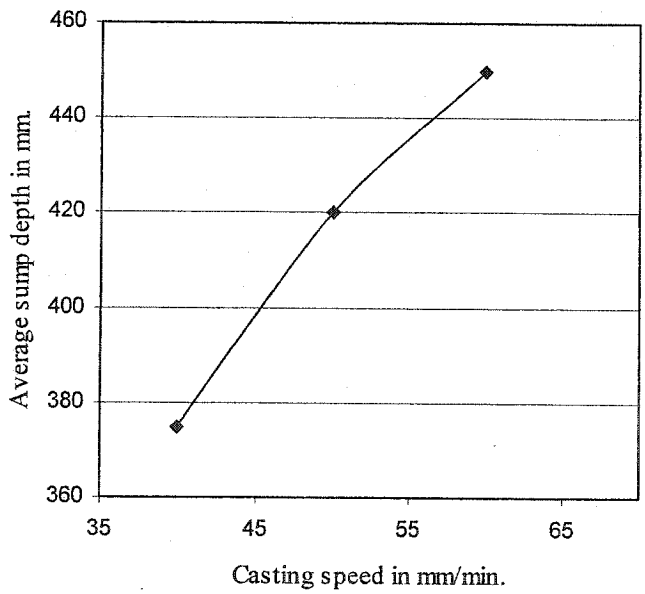

Figure 6.15: Effect of casting speed on sump depth using the long channel bag and temperature superheat of 32°C.

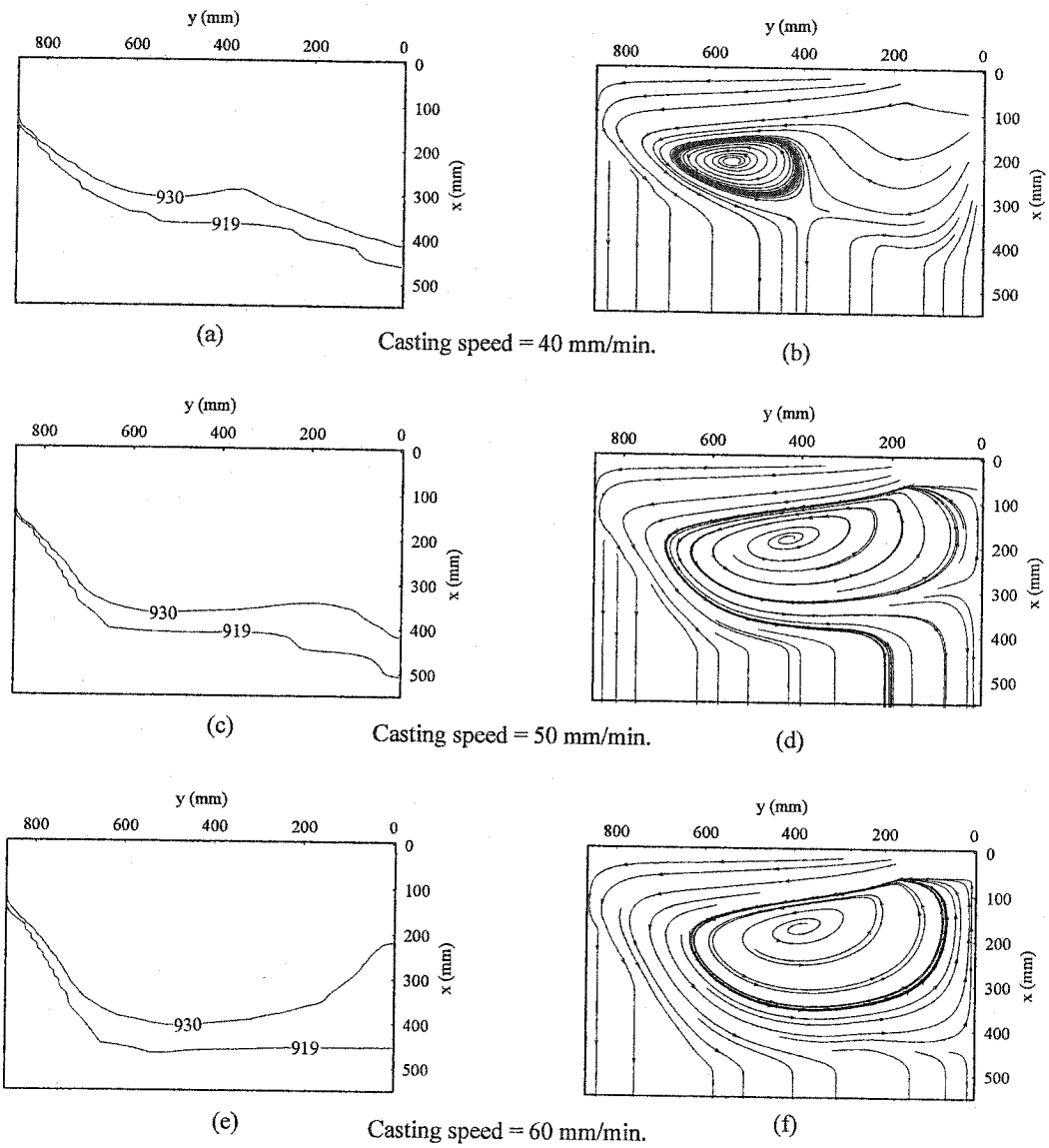

Figure 6.16: Effect of casting speed on the mushy layer and streamlines at the wide symmetry plane using long channel bag and 32°C temperature superheat. (a,c,e) liquidus and solidus temperatures in Kelvin, (b,d,f) streamlines.

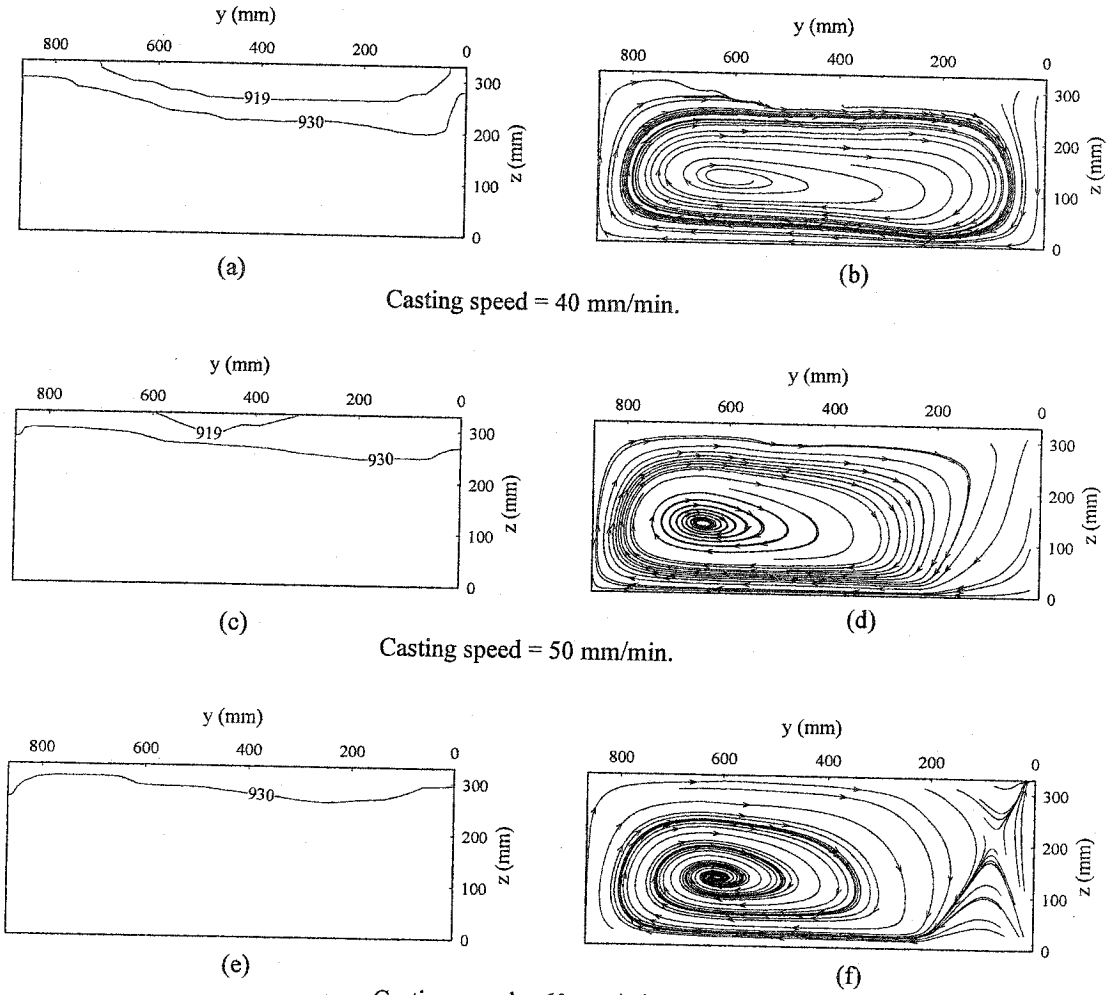

Figure 6.17: Effect of casting speed on the mushy layer and streamlines at the ingot free surface using long channel bag and 32°C temperature superheat. (a,c,e) liquidus and solidus temperatures in Kelvin, (b,d,f) streamlines.

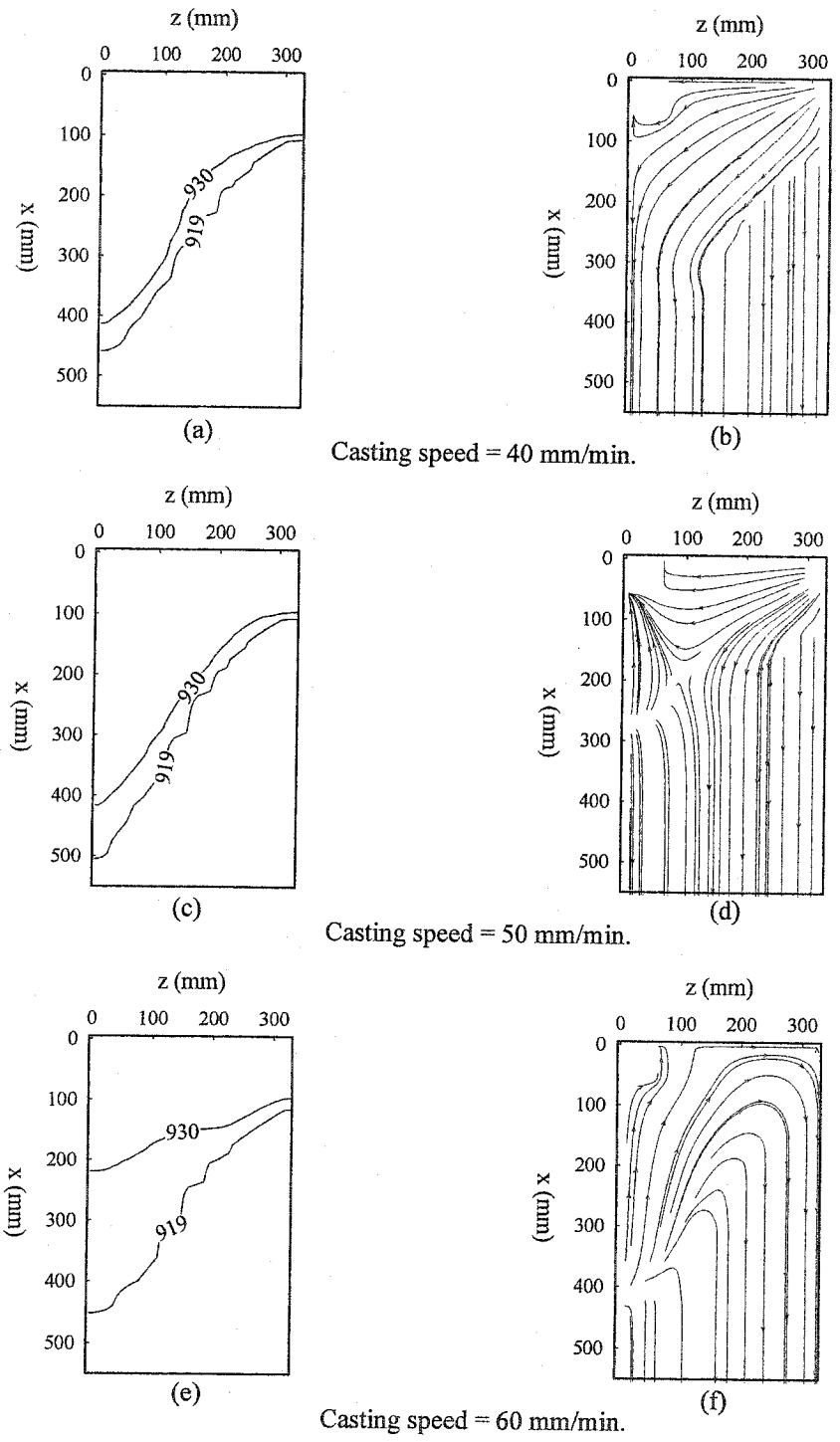

Figure 6.18: Effect of casting speed on the mushy layer and streamlines at the narrow symmetry plane using long channel bag and 32°C temperature superheat. (a,c,e) liquidus and solidus temperatures in Kelvin, (b,d,f) streamlines.

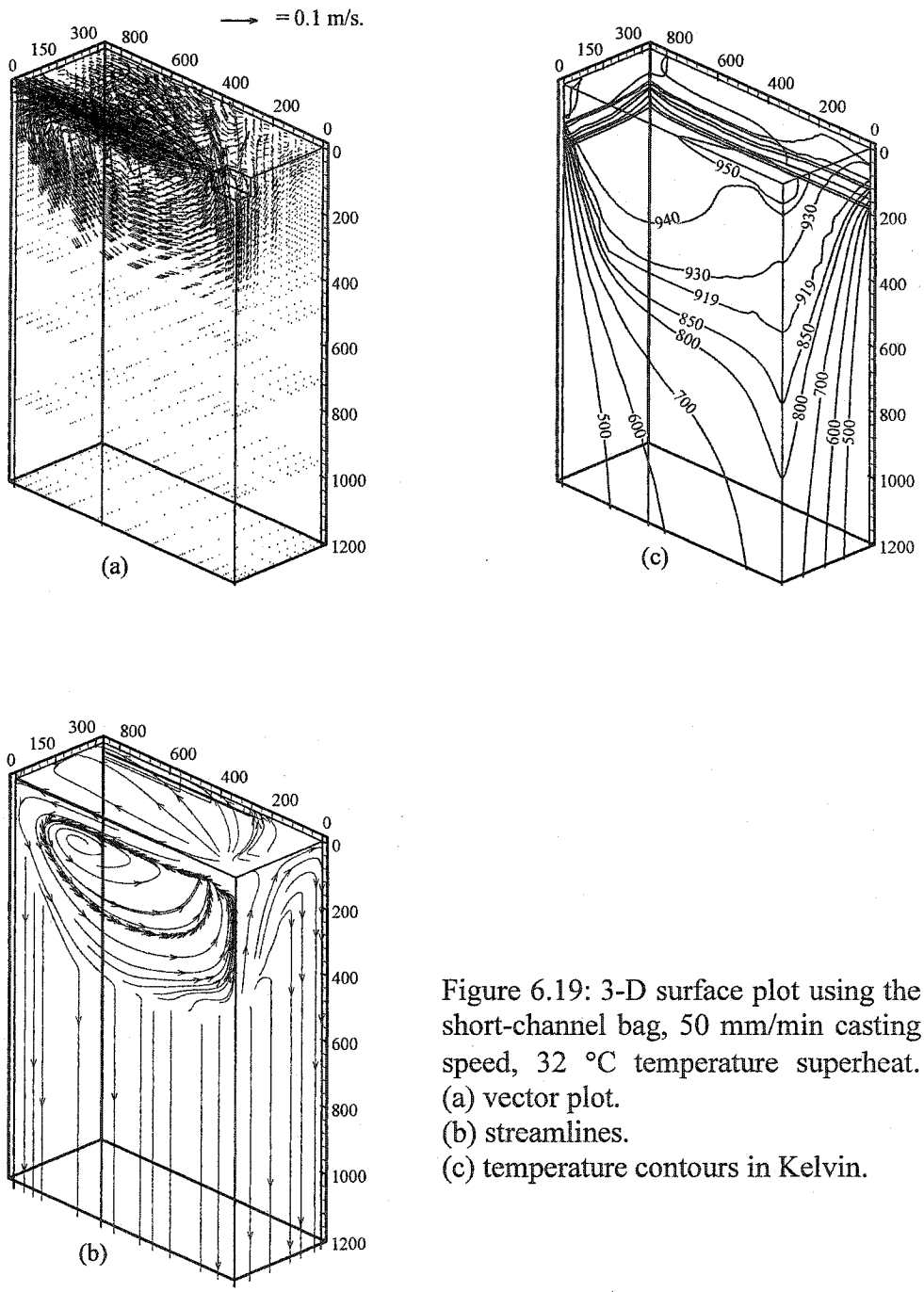

Figure 6.19: 3-D surface plot using the short-channel bag, 50 mm/min casting speed, 32 °C temperature superheat.
(a) vector plot.
(b) streamlines.
(c) temperature contours in Kelvin.

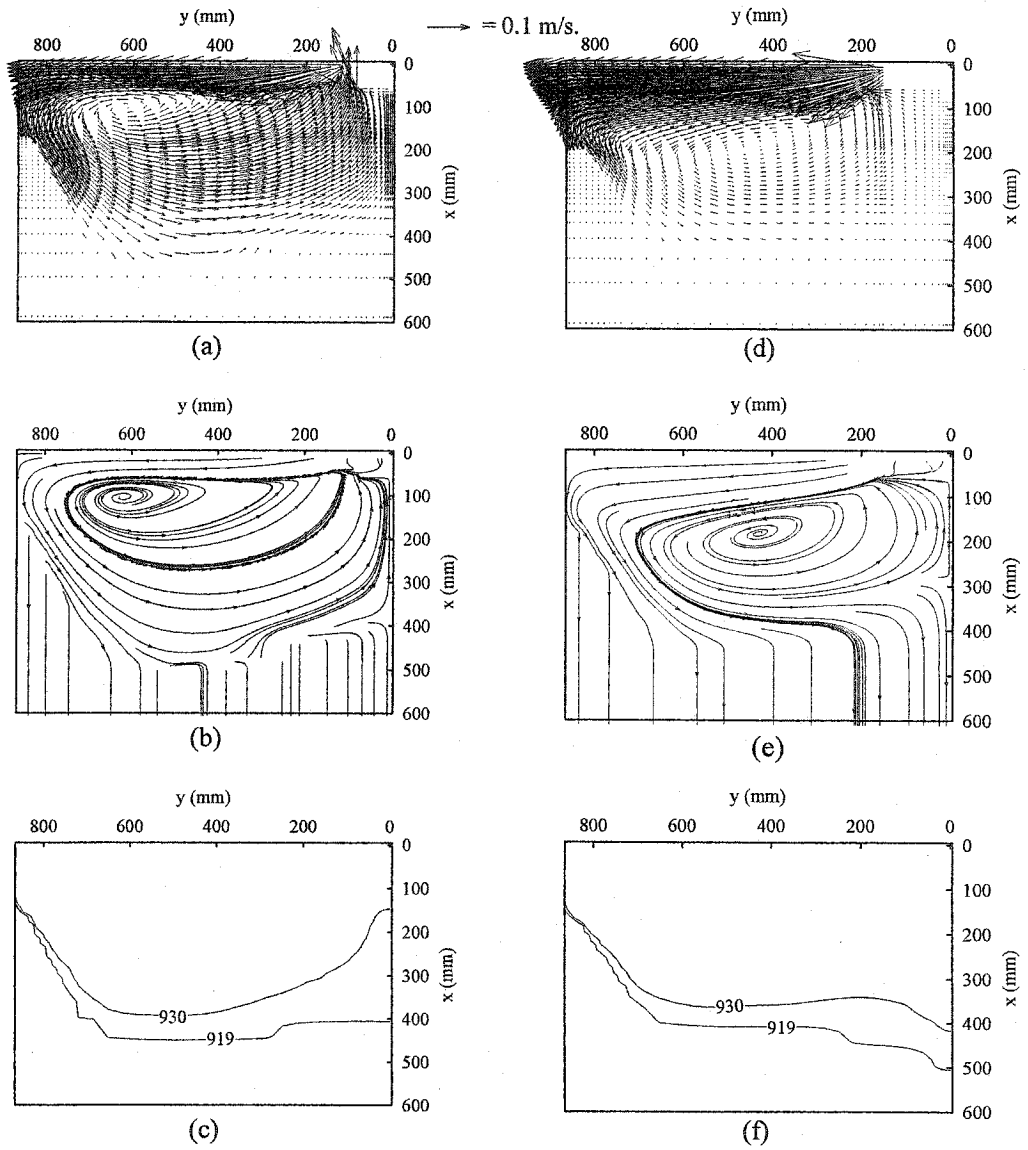

Figure 6.20: Computed results at the wide symmetry plane for 50 mm/min casting speed, 32°C temperature superheat. (a,b,c) representing vector, streamlines, temperature contours in Kelvin for the short channel bag. (d,e,f) representing vector, streamline, and temperature contours in Kelvin for the long channel bag.

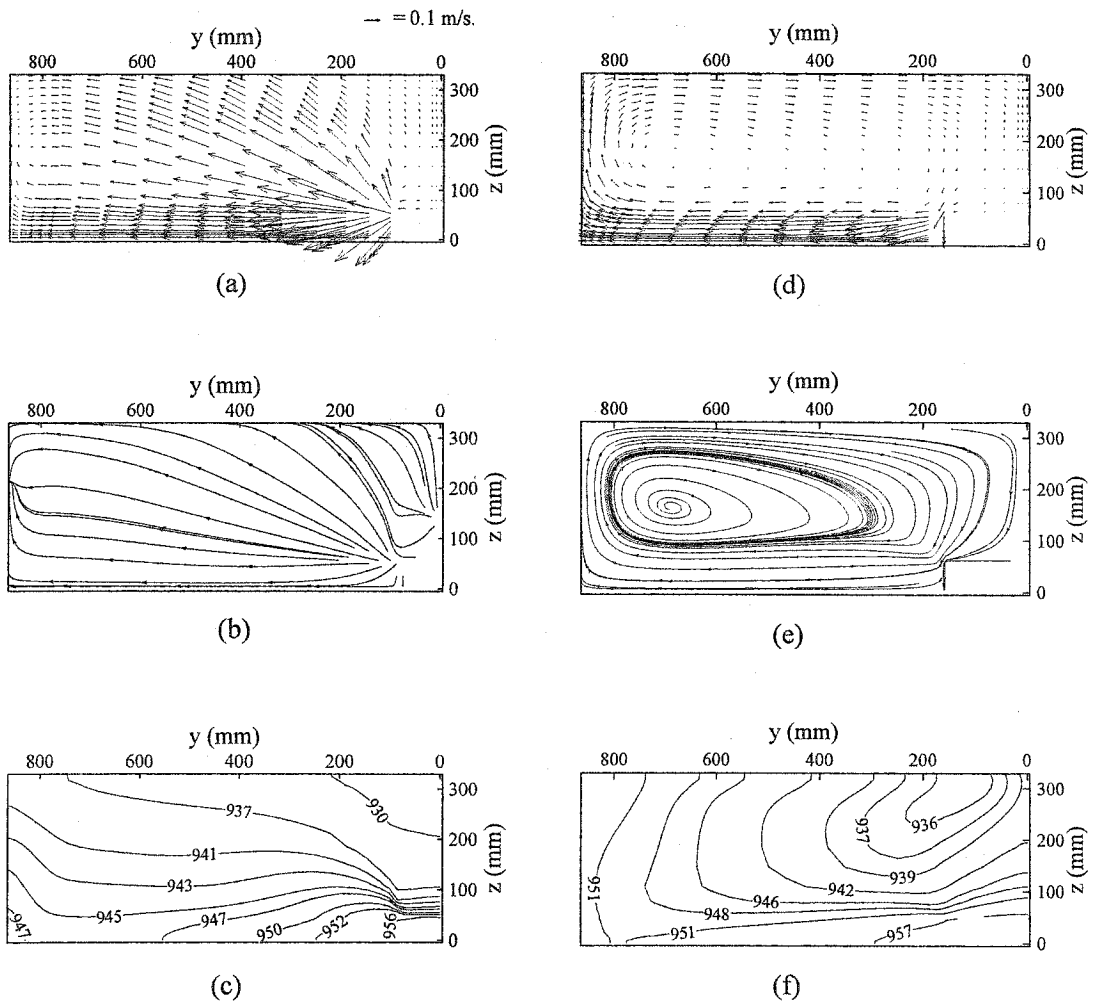

Figure 6.21: Computed results at the ingot free surface for 50 mm/min casting speed, 32°C temperature superheat. (a,b,c) representing vector, streamlines, temperature contours in Kelvin for the short channel bag. (d,e,f) representing vector, streamline, and temperature contours in Kelvin for the long channel bag.

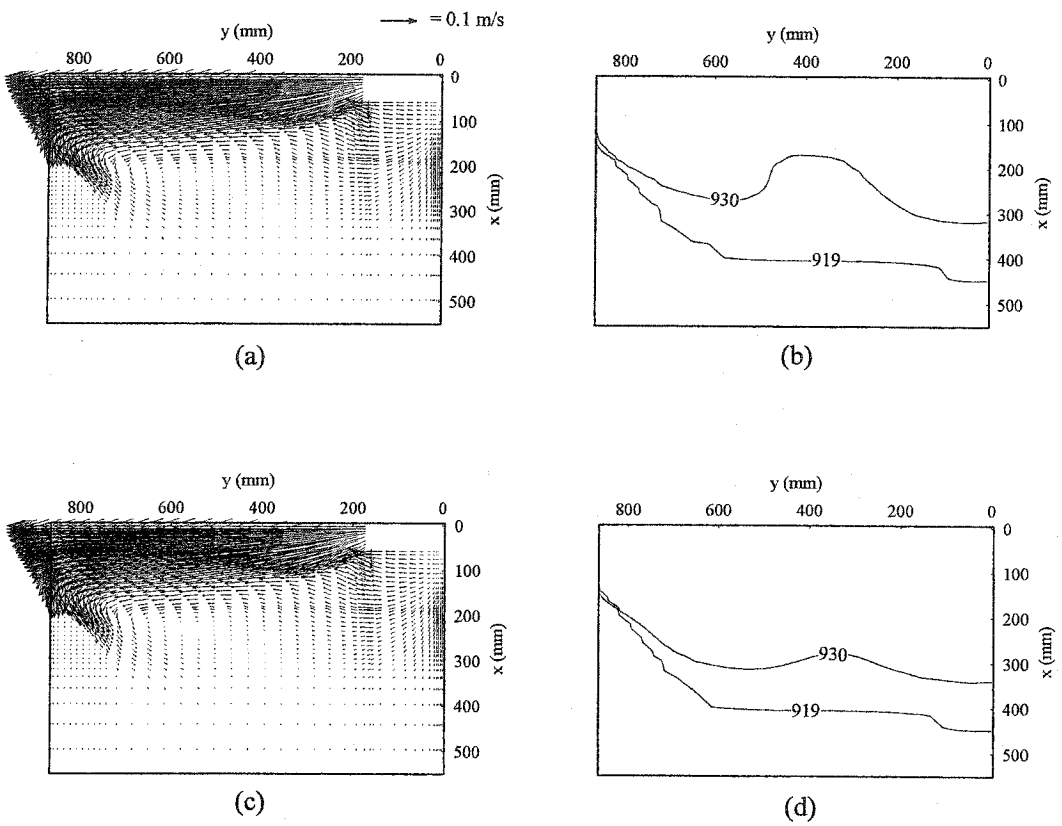

Figure 6.22: Computed results at the wide symmetry plane for 60 mm/min casting speed using the long-channel bag, (a,b) temperature superheat is 16°C, (c,d) temperature superheat is 60°C.

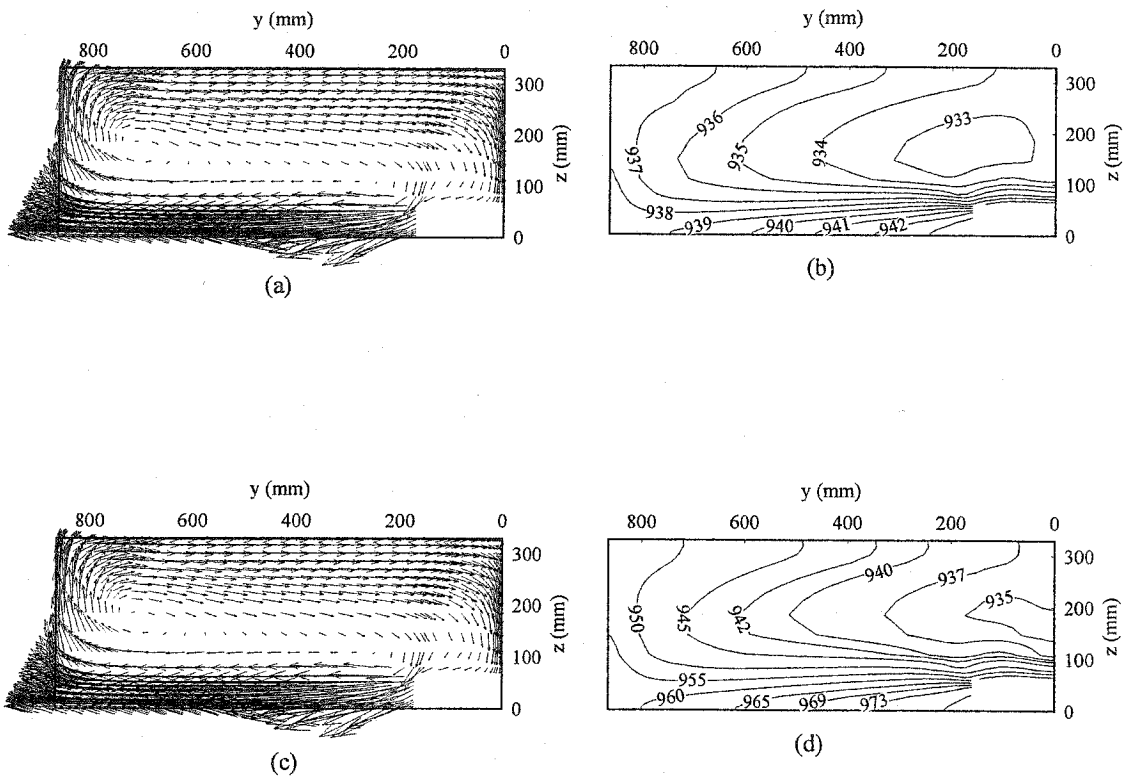

Figure 6.23: Computed results at the ingot free surface for 60 mm/min casting speed using the long channel bag. (a,b) vector and temperature contours in Kelvin for the 16°C superheat. (c,d) vector and temperature contours in Kelvin for the 60°C superheat.

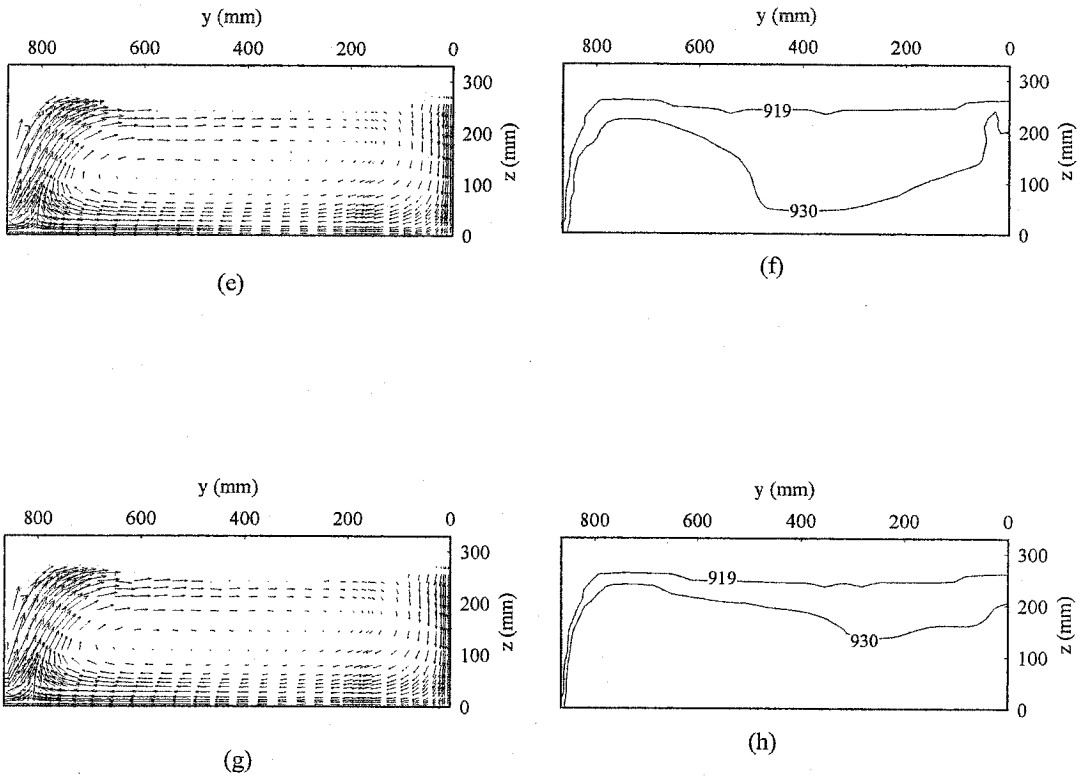

Figure 6.23 (continue): Computed results at x = 145 mm from the ingot free surface for 60 mm/min casting speed using the long channel bag. (e,f) vector and temperature contours in Kelvin for the 16°C superheat. (g,h) vector and temperature contours in Kelvin for the 60°C superheat.

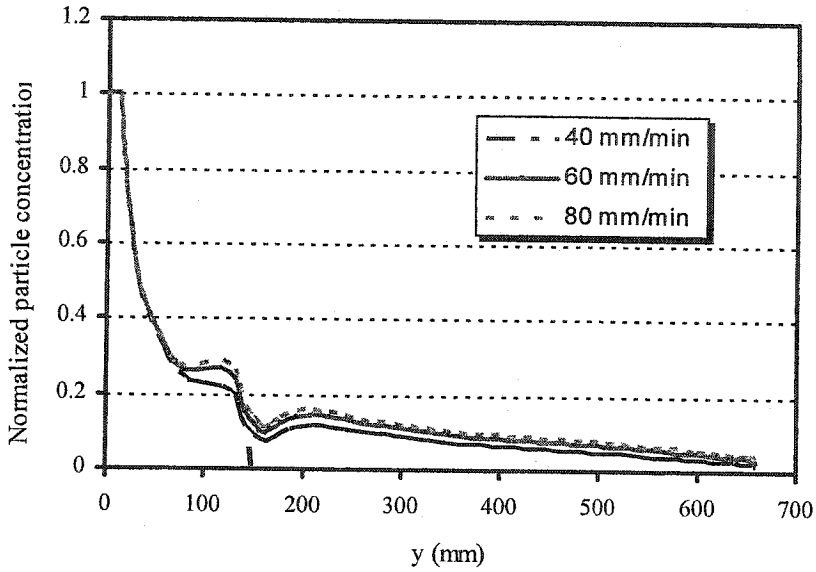

Figure 6.24: Effect of casting speed on the transverse particle distribution using the standard combo bag, particle diameter = 50μm, superheat = 65°C, (x,z) = (37,0) mm.

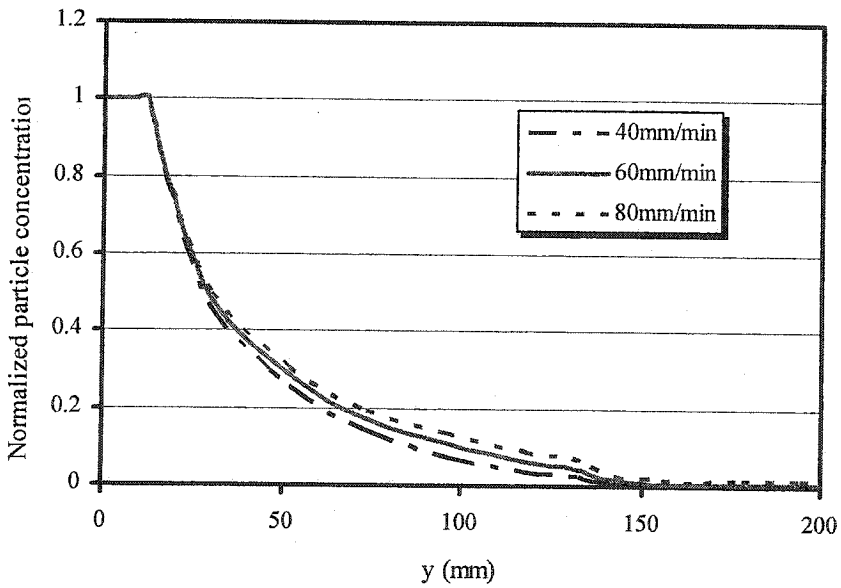

Figure 6.25: Effect of casting speed on the transverse particle distribution using the standard combo bag, particle diameter = 250μm, superheat = 65°C, (x,z) = (37,0) mm.

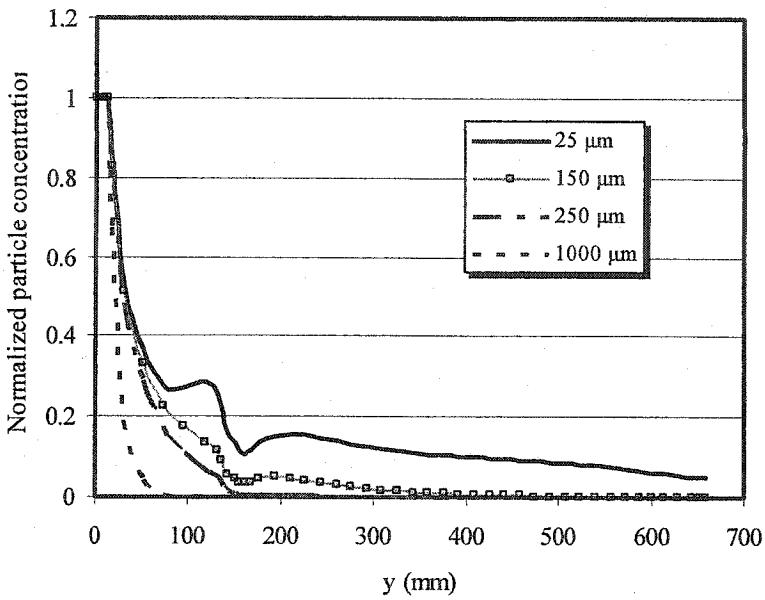

Figure 6.26: Effect of particle size on the transverse particle distribution using the standard combo bag, casting speed = 60 mm/min, superheat = 65°C, (x,z) = (37,0) mm.

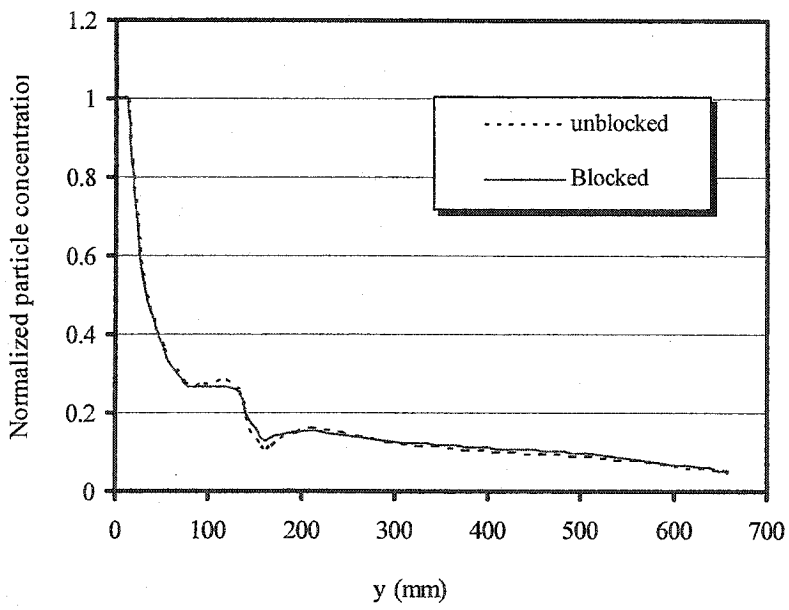

Figure 6.27: Effect of bottom-windows blockage on the transverse particle distribution using the standard combo bag, particle diameter = 25 µm, casting speed = 60 mm/min, superheat = 65°C, (x,z) = (37,0) mm.

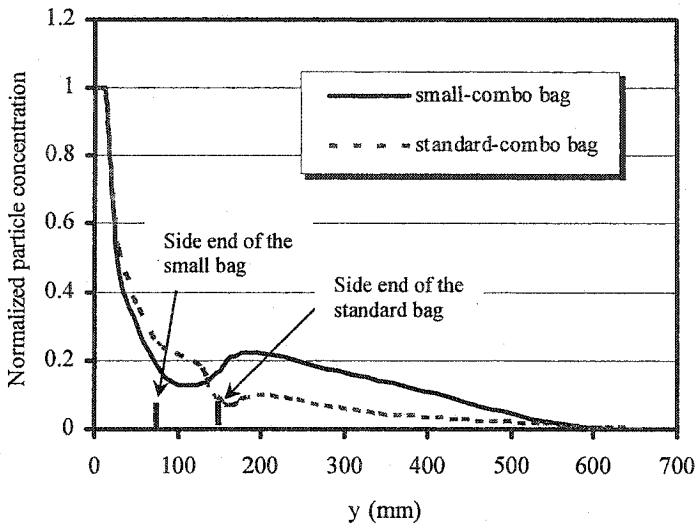

Figure 6.28: Effect of bag dimensions on the transverse particle distribution at the wide symmetry plane, particle diameter = 100 μm, casting speed = 60 mm/min, superheat = 65°C, x = 37 mm.

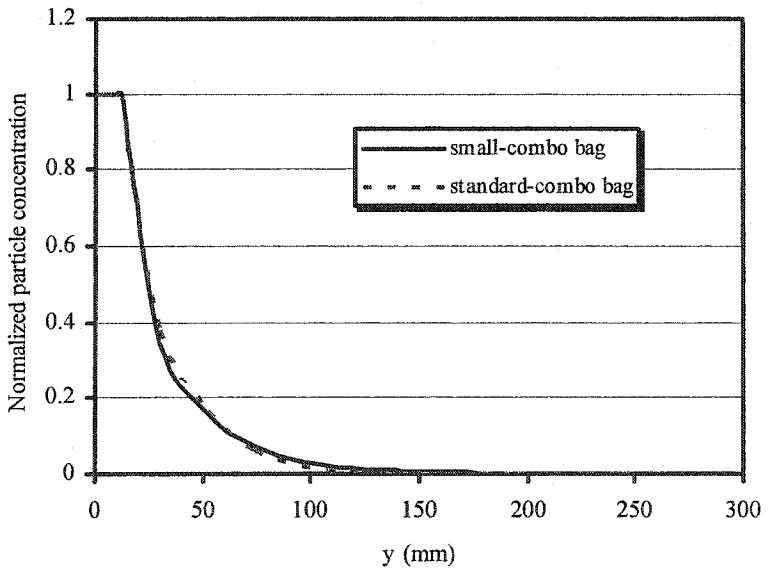

Figure 6.29: Effect of bag dimensions on the transverse particle distribution at the wide symmetry plane, particle diameter = 500 μm, casting speed = 60 mm/min, superheat = 65°C, x = 37 mm.

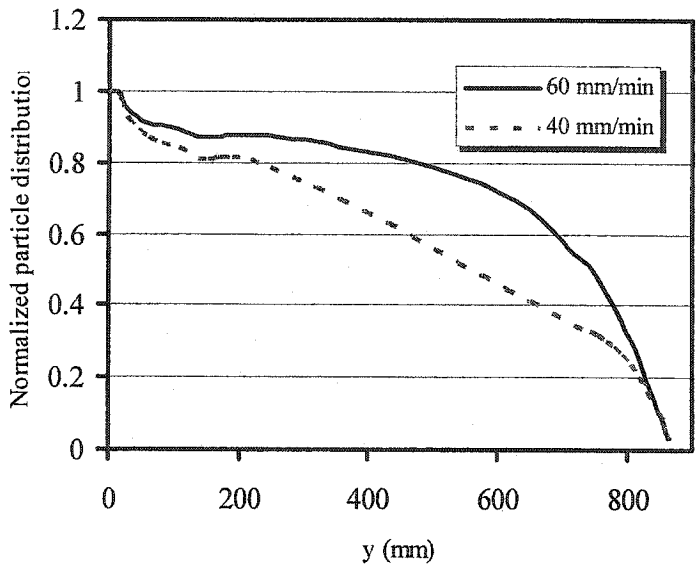

Figure 6.30: Effect of casting speed on the transverse particle distribution at the wide symmetry plane using the long channel, particle diameter = 100 μm, superheat = 32°C, x = 37 mm.

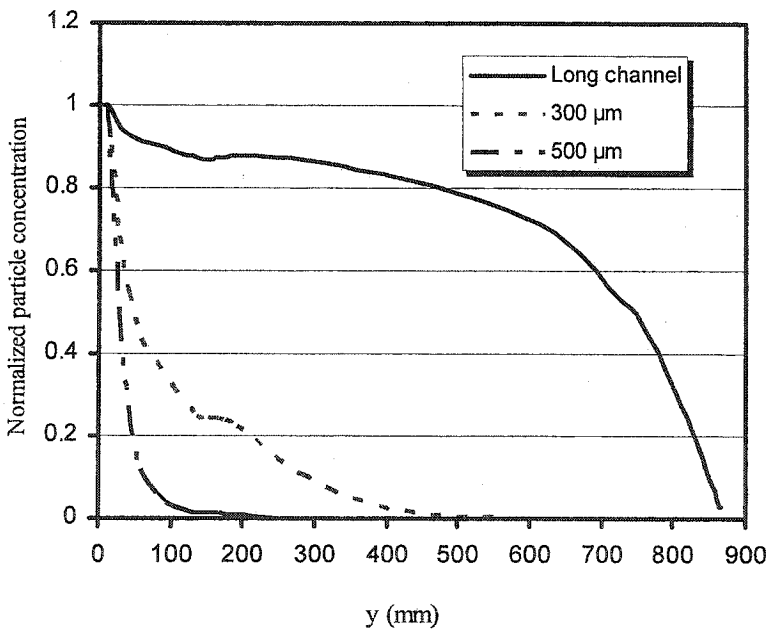

Figure 6.31: Effect of particle diameter on the transverse particle concentration distribution at the wide symmetry plane using long channel bag, casting speed = 60 mm/min, superheat = 32°C, x = 37 mm.

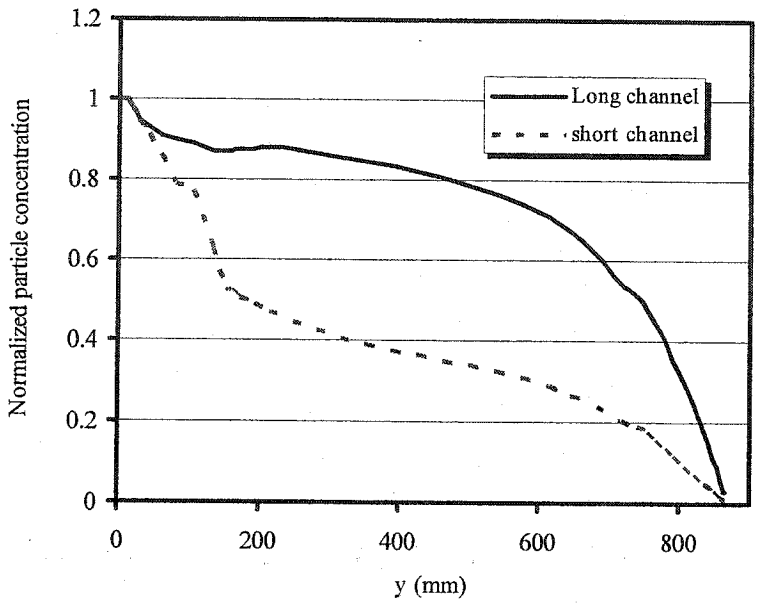

Figure 6.32: Effect of bag dimensions on the transverse particle concentration distribution at the wide symmetry plane, particle diameter = 100 μm, casting speed = 60 mm/min, superheat = 32°C, x = 37 mm.

CHAPTER
SEVEN

Conclusions, Originality, and Suggested Future Work

7.1 Overall Conclusions

A comprehensive 3D-numerical model for the simulation of steady state vertical DC casting of aluminum alloys process has been developed. The equations solved in the model are the continuity, momentum and energy equations. The momentum equations are modified with Darcy-type source terms to simulate the fluid motion in the mushy regions which develop during the solidification process. The two-equation k-ϵ model of Launder and Sharma [29] is included in the model to account for the turbulent aspect of the flow. The mathematical model has been verified both qualitatively and quantitatively by comparing the predicted results with those of the velocity field of a physical water model and the sump depth result of a real casting experiment, respectively. Considering the unknown factors in the experiment, the comparison showed a good agreement. The quantitative agreement with the available results is enhanced with the inclusion of the thermal buoyancy effect in the mathematical model. Upon verification, the developed mathematical model is used in carrying out an extensive parametric study of two vertical industrial size DC casters of different aspect ratios and for two different melt delivery distribution systems; namely, the combo bag and the channel bag. The physical properties of aluminum Al-3104 alloy are used in carrying out the simulation of the small aspect ratio caster, whereas, the properties of aluminum alloy Al-1050 are employed in the large aspect ratio caster.

In the study involving the small aspect ratio caster, the combo bag (which is used commercially) is considered for the melt distribution system. The studied parameters include casting speed, primary cooling rate, melt superheat, and combo-bag dimensions. Also studied are the effects of complete blockage of the bottom windows of the

distribution bag. The last studied parameter demonstrates the ability of the developed model as an efficient tool that can be used not only in the early stages of DC caster design, but also in analyzing the effects of possible scenarios that may occur after some period the caster in operation. The conclusions drawn from the study of the small aspect ratio caster can be summarized as follows:

- The issue of increasing and/or decreasing the mushy layer at the slab center has been clarified by the current model in terms of two factors; the upward component of the vertical recirculation, and the angle flow. If the momentum of the upward component of the vertical recirculation at the wide symmetry plane overwhelms the angle flow, the mushy region becomes thicker. On the other hand, if the angle flow overcomes the upward component of the vertical recirculation, then the mushy layer becomes thinner.
- The melt stream issued from the bottom window of the bag is found to be responsible to a certain extent for controlling the position of the vertical recirculation in a manner such that in the instance of a strong stream, the vertical recirculation is pushed axially downward.
- The position of the vertical recirculation within the sump is responsible for accelerating and/or decelerating the melt stream that is confined between the outer edge of this recirculation and the surface of the outer solidified layer of the slab. The depth and the uniformity of the solidification front are strong functions of the strength of this confined stream. The higher the momentum of this confined-hot stream, the deeper and more uniform the solidification front becomes.
- Having stated above the role played by the stream of melt issued from the bottom window of the bag, some care must be exercised in specifying the location of this window in order to prevent the reverse flow of melt from the sump into the bag. The reverse flow is predicted by the model and is observed when using the small combo bag. It is attributed to the location of the bottom window being in the positive pressure gradient region of the flow field. A similar flow behavior was reported by Jones et al. [16] in their physical experiments with water, but no explanation was reported as to why it occurred.

- The current model is able to quantify the relationship between the outer solidified layer and the casting speed. An increase in the casting speed causes the solidified-layer thickness to decrease almost linearly. This would benefit the cast engineer in specifying the upper and lower limits of the casting speed for the designed caster.
- It is found that the difference between the average thickness of the solidified layer at the rolling face and at the narrow face of the ingot is decreasing with the increase in the casting speed. Therefore, increasing the casting speed will result in the heat transfer rate at the ingot surfaces, especially the wide and narrow faces becoming more uniform.
- It is found from the plotting of the v-component of velocity vector of the melt stream issued from the side window of the bag at the wide symmetry plane that the velocity of approach to the narrow side of the mold is independent of the blockage of the bottom window and is dependent on the bag dimensions. The velocity of approach of the long distribution bag is higher than that of the small bag.

In the case of the large aspect ratio slab, the channel bag is used as the melt distribution system. The parameters studied are casting speed, bag dimensions and temperature superheat. Conclusions resulting from this case study can be summarized in the following points:

- An extension in the mushy layer from the liquidus side is found to occur in the region where upward flow exists, while the downward flow causes the mushy layer to thin, and may push the solidification front deeper or cause it to be horizontally uniform.
- Casting speed, being the most important independent parameter in vertical DC casting, must be optimized to achieve the following goals:
  - Avoiding turbulence at the slab free surface, such as those developed when using the long channel bag for a casting speed of 60 mm/min. The turbulence at the top free surface is found to be responsible for aluminum oxide detachment from the free surface. These oxides, once detached, will form inclusions that are distributed within the ingot. In addition, avoiding turbulence at the slab free surface reduces the oxidation rate by decreasing the melt surface area to volume ratio.

- Alleviating both the problems of negative segregation at the ingot center and the positive segregation at the slab surface by reducing the momentum of the flow traveling along the solidification front.
- Generally, a shallow sump under steady state condition is favorable in a vertical DC casting process.
- Considering the above mentioned points, the casting speed of 50 mm/min for the short channel distribution bag appears to be the optimum speed for this particular caster.

➢ Temperature superheat must be kept moderate, especially when using a graphite lining as insulation at the upper region of the mold. Keeping the superheat low would result in less wetting of the graphite surface by the molten aluminum, and hence reduce the possibility of formation of carbide-salt inclusions.

➢ The computed results show the possibility of obtaining similar solidification front profiles for using different parameter combinations. This has been demonstrated in the similarity of the solidification-front profile attained in the case of the long-channel bag with a casting speed of 60 mm/min to the profile obtained using the short bag with the casting speed of 50 mm/min. This will permit the cast engineers a degree of freedom in specifying the operational conditions that best suite the requirements of the production firm.

The mathematical model is extended to solve the non-dimensional mass concentration equation in 3D by utilizing the previously computed vector fields as input data into the program. The following conclusions can be drawn:

➢ Uniform concentration profile is an indication of good mixing within the melt, and the latter is an indication of a high degree of turbulence.

➢ Large particles are hardly affected by the working parameters such as casting speed, bag dimensions and/or type. These particles are mainly found to be concentrated around the center of the sump.

➢ For the standard combo bag, small particles are more uniformly distributed within the sump.

- The greater the casting speed, the higher the concentration of inclusion across the sump.
- Combo bags are found to distribute inclusions across the slab cross-sections more uniformly than the channel bags.

Present trends in research and development of aluminum casting technology is seen in the new developments and simulations of various phenomena taking place during solidification. The challenge today is not only in the development of certain stand-alone models for some specific phenomena, but also in the integration of existing models into the whole process chain model. As a result, metal production, solidification, homogenization, extrusion, rolling, properties of final products, and recycling should be studied and linked mainly by computer modeling in the future. In other words, the integrated process chain model will replace to a large extent the now dominating approach of trial-and-error and will help establish computer modeling as the leading tool for research and development (R&D) in the future by all major casting companies worldwide. Knowing that each unit is somehow dependent on the results from other units, the integrated process chain model must be built out of specialized and verified computer models or units in order to assure the efficiency and reliability of the whole package. Building the integrated chain model from general commercial packages would render questionable efficiency and reliability of this model.

7.2 Statement of Originality

A verified and specialized 3-dimensional mathematical model of fully coupled turbulent flow and solidification for the simulation of steady-state vertical DC casting of aluminum alloys is developed in this study. The reliability of the model is partly proven through its verification with physical and real casting experimental results that were conducted by independent researchers, and partly through the extensive and detailed parametric study carried out on two casters. The latter study has resulted in an in-depth understanding and clarification of the transport phenomena taking place during steady state in a vertical DC casting process. Some of these phenomena are reported in literature but have never been explained. Some have never been reported altogether. Hence,

besides the development of this reliable and specialized model, the clarification of both types of phenomena can be considered as original contributions to the field. These phenomena can be summarized in the following:

(1) Specifying the factors controlling the mechanism of expanding and/or contracting of the mushy layer at the slab center. The responsible factors are angle flow and upward component of the vertical recirculation.

(2) Combo bags are used widely in vertical DC casters. The author is not aware of any other study, be it experimental or numerical, whereby the role played by the bottom window is well analyzed and explained in the manner presented by the current study. To be more specific, the role of the bottom window is well explained. This role is played by melt stream issued from the bottom window of the bag. This stream is found to be controlling the axial position of the vertical recirculation. The outer moving edge of the later recirculation and the inner surface of the outer solidified layer are acting as a diverging converging channel with moving edges. The melt in between these two edges is accelerated by both the nature of the mentioned diverging-converging channel and by the fact that these edges are moving downward. The solidified layer is moving with the casting speed, while the outer edge of the vertical recirculation is moving with a different speed that can be derived from measuring the vector length. The accelerated hot stream of melt traveling downward in between the two edges causes the solidified front at/and around the slab center to be pushed deeper, flatter, and to extend horizontally along the wide symmetry plane of the slab.

(3) The model was able to identify a faulty design scenario wherein the bottom window is located in an unfavorable position within the short distribution bag. Identification of this window's location is important since it causes what is called 'reverse flow' to take place. It is interesting to mention that Jones et al. [16], in his physical water experiment using a similar combo bag, reported that only one stream was observed coming out of the side and bottom windows of the small combo bag, and they explained that a merger between the two streams into one stream had taken place. The vector field measured by the PIV technique does not show any merger but one stream. Considering the fact that it is not possible for the researchers to analyze what is

happening inside the bag, there is therefore a high probability that what happened in Jones et al. experiment is due to what has been predicted by the current study, i.e. the reverse flow, since only one stream from the side window is observed when this phenomenon occurs. It is recommended from this study that the bottom windows be shifted away from the inlet nozzle, and be placed towards the edges of the bag so that these windows would not be located in the axially positive pressure gradient region. To the author's knowledge, prediction and explanation of the reverse-flow phenomenon is original and is credited to the present study.

(4) The model has been extended to solve the steady state 3D-mass concentration equation in an effort to explain the inclusions distribution patterns in a vertical DC casting process.

7.3 Suggested Future Work

Some suggestions can be built on as a continuation and development of the present work. It is recommended that the future research work should consider the following points:

1) Extend the current mathematical model to cover the startup and end of a DC casting process. This development could be done by incorporating the current program to other programs that are not necessarily built on the basis of finite volume technique but rather on the mesh adjustable and flexible computational technique such as the finite element method.
2) Include the effect of surface morphology in the imposed heat transfer coefficient since this has a major effect on heat transfer and hence defect formation at the ingot surface.
3) In the model, allow for variation of the heat transfer coefficient in the transverse direction.
4) Connect the model to existing or newly developed computer codes to predict thermal stresses, microsegregation and microstructure of aluminum slabs. These codes can make use of the current model in the following manner; in the case of thermal stress analysis, isotherms in the solid and the shape of the solid are of interest. To predict the microstructure one requires detailed information about

isotherms in the mushy zone. Therefore, the information needed for stress and microstructure analysis could be found using the presently developed model with a moderate modification of the code.

5) Build a graphic user interface to facilitate the use of the code for DC casting designers and operators.
6) Study the inert flow patterns that will originate from bag defects, such as the ones that may occur as a result of human error. An example of such an error may be the misplacement and/or tilting of the distribution bag.
7) Since the current model uses the popular k-ε turbulence model equations, the model can therefore be used in future studies to optimize distribution bag design for the sake of minimizing the turbulence generated within the distribution bag itself. These turbulence effects are believed to be the principle cause in generating oxide inclusions.

REFERENCES

1- Weckman, D. C. and Niessen, P., "Mathematical Models of the DC Continuous Casting Process," *Canadian Metallurgical Quarterly*, vol. 23, No. 2, pp. 209-216, 1984.

2- L. Katgerman, "Developments in Continuous Casting of Aluminum Alloys ," *Cast Metals*, vol. 4, No. 3, pp. 133-139, 1991.

3- S. Flood, "Modeling of Aluminum Casting," *Materials Science and Technology*, 151- 152, 1992.

4- S.C Flood, L. Katgerman, A. H. Langille, S. Rogers, C. M. Read,"Modelling of Fluid Flow and Stress Phenomena During DC Casting of Aluminum Alloys," *Light Metals*, pp. 943-947, 1989.

5- E. D. Tarapore, "Thermal Modeling of DC Continuous Billet Casting," *Light Metals*, pp. 875- 880, 1989.

6- P. N. Hansen and P. R. Sahm, "A 3-D Geometric Modeller-Implicit FDM Solver Package for Simulation of Shaped Casting Solidification in Modeling of Casting and Welding Processes II," *Met. Soc. AIME*, pp. 243- 250, 1983.

7- C. Devadas and J. F. Grandfield, "Experience with Modeling DC Casting of Aluminum," *Light Metals*, pp. 883-892, 1991.

8- Ch. Raffourt, Y. Fautrelle, JL. Meyer, B. Hannart, "Liquid Metal Distribution in a Slab DC Casting: Experiments and Modeling Approach," *Light Metals*, pp. 877-882, 1991.

9- M.F. El-Demerdash, "Modeling of Temperature Distribution During DC Casting of Aluminum Alloys," *Light Metals*, pp. 949-954, (1993).

10- P. A. Davidson and S. C. Flood, "Natural Convection in Aluminum Ingot," *Metallurgical and Materials Transactions B*, vol. 25B, pp. 293- 302, 1994.

11- T.S. El-Raghy, M.F. El-Demerdash, H.A. Ahmed, and A.M. El-Sheikh, "Modeling of the Transient and Steady State Periods During Aluminum DC Casting," *Light Metals*, pp. 925-929, 1995.

12- A. Buchholz, M.-S. Ji, W. Schmitz, S. Engler, "Investigation of the Effect of Different Metal Feeding Systems on Cast Structures Using a Water Model," *Light Metals*, pp. 1043- 1049, 1997.

13- Christopher J. Vreeman, Frank P. Incropera, "The Effect of Free-Floating Dendrites and Convection on Macrosegregation in Billet DC Cast Aluminum Alloys Part I: Model Development," *Int. J. Heat and Mass Transfer*, vol. 43, pp. 677-686, 2000.

14- Christopher J. Vreeman, Frank P. Incropera, "The Effect of Free-Floating Dendrites and Convection on Macrosegregation in Billet DC Cast Aluminum Alloys Part II: Predictions for Al-Cu and Al-Mg Alloys," *Int. J. Heat and Mass Transfer*, vol. 43, pp. 687-704, 2000.

15- Dong Xu and J. W. Evans, "Physical Modeling (by Particle Image Velocimetry) and Mathematical Modeling of Metal Delivery Devices for EM and DC Casting of Aluminum," *Light Metals*, pp. 1051-1058, 1997.

16- Dong Xu, W. K. Jones, Jr., and J. W. Evans," The use of Particle Image Velocimetry in the Physical Modeling of Flow in Electromagnetic or Direct-Chill Casting of Aluminum Part I. Development of the Physical Model," *Metallurgical and Materials Transactions B*, vol. 29B, pp. 1281- 1288, 1998.

17- Dong Xu, W. K. Jones, Jr., and J. W. Evans, "The use of Particle Image Velocimetry in the Physical Modeling of Flow in Electromagnetic or Direct-Chill Casting of Aluminum Part II. Results of the Physical Model, Including Bag Geometry, Blockage, and Nozzle Placement," *Metallurgical and Materials Transactions B*, vol. 29B, pp. 1289- 1295, 1998.

18- Dong Xu, W. K. Jones, Jr., and J. W. Evans, "Physical Modeling of the Effects of Thermal Buoyancy Driven Flows in EM and DC Casters," *Light Metals*, pp. 835-839, 1999.

19- W. K. Jones Jr., D. and J. W. Evans, "Physical Modeling of the Effects of Non-Symmetric Placement of Flow Control Bags used in Semi-Continuous Casting of Aluminum," *Light Metals*, pp. 1051- 1057, 1998.

20- W. K. Jones Jr., D. Xu, J. W. Evans, E. Williams and D. P. Cook,"Effects of Combo-Bag Geometry on the Thermal History and Sump Profile of a 3104 DC Cast Ingot," *Light Metals*, pp. 841-845, 1999.

21- G.-U. Grun, I. Eick, and D. Vogelsang, "3D-Modeling of Fluid Flow and Heat Transfer for DC Casting of Rolling Ingots," *Light Metals*, pp. 863-869, 1994.

22- Gerd-Ulric Gruen, Andreas Buchholz, and Dag Mortensen, "3D-Modeling of Fluid Flow and Heat Transfer During the DC Casting Process- Influence of Flow Modeling Approach-," *Light Metals*, pp. 573- 578, 2000.

23- Gary Patrick Grealy, J. Lee Davis, Einar Kristian Jensen, Per Arne Tondel Jurgen Moritz, "Advances for DC Ingot Casting: Part 1- Introduction and Metal Distribution," *Light Metals*, pp. 805-811, 2001.

24- Gary Patrick Grealy, J. Lee Davis, Einar Kristian Jensen, Per Arne Tondel Jurgen Moritz, "Advances for DC Ingot Casting: Part 1- Heat Transfer and Casting Results," *Light Metals*, pp. 813-821, 2001.

25- Bjorn Rune Henriksen and Einar K. Jensen, "Modeling the Effect of Casting Speed and Metal Level on the Surface Segregation of AA5182," *Light Metals*, pp. 969-977, 1993.

26- Frank E. Wagstaff, Robert B. Wagstaff, K. Dean Bowles, and J. Martin Ekenes, "An Improved DC Casting Technology," *Light Metals*, pp. 709-714, 1993.

27- Yves Caron, Denis Bernard, Guy LeBlanc, "A New Advanced Mould Technology for Sheet Ingot Casting," *Light Metals*, pp. 991-998, 1994.

28- J. O. Hinze, "Turbulence," Second edition, *McGraw Hill*, New York, 1975.

29- Launder B. E., and Sharma B. I., "Application of the Energy Dissipation Model of Turbulence to the Calculation of the Flow Near a Spinning Disk," *Letters in Heat and Mass Transfer*, vol. 1, pp. 131-138, 1974.

30- Lam, C. K. G., and Bremhorst, K., "A Modified Form of the k-ε Model for Predicting Wall Turbulence," *J. Fluids Eng., Trans. ASME*, vol. 103, pp. 456-460, 1981.

31- Hollworth, B. R. and Berry, R. D., "Heat Transfer From Arrays of Impinging Jets with Large Jet-to-Jet Spacing," *ASME paper No. 78*, GT-117, 1978.

32- Van Driest, E. R., "On Turbulent Flow Near a Wall," *Journal of the Aeronautical Sciences*, vol. 23, pp. 1007-1011, 1956.

33- V. C. Patel, and G. Scheuerer, "Turbulence Models for Near-Wall and Low-Reynolds Number Flows: A Review," *AIAA Journal*, vol. 23, No. 9, pp. 1308-1319, 1985.

34- Y. Nagano, and M. Hishida, "Improved Form of the k-ε Model for Wall Turbulent Shear Flows," *Transactions of ASME*, vol. 109, pp. 156-160, 1987.

35- C. G. K. Lam, and K. Bremhorst, "A Modified Form of the k-ε Model for Predicting Wall Turbulence ," *Transactions of ASME*, vol. 103, pp. 456-460, 1981.

36- Kuei-Yuan Chien, "Predictions of Channel and Boundary-Layer Flows with a Low-Reynolds-Number Turbulence Model," *AIAA Journal*, pp. 33-38, January 1982.

37- R. Henkes and C.J. Hoogedoom, "Comparison of Turbulence Models for the Natural Convection Boundary Layer Along a Heated Vertical Plate," *Int. J. Heat and Mass Transfer*, vol. 32, No. 1, pp. 157-169, 1989.

38- Minakawa S., Samarasekera I. V. and Weinberg F., "Centerline Porosity in Plate Castings," *Metall. Trans.*, vol. 16B, pp. 245-255, 1987.

39- D. C. Weckmann, P. Niessen, "A Numerical Simulation of the D.C. Continuous Casting Process Including Nucleate Boiling Heat Transfer," *Metallurgical and Material Transactions B,* vol. *13B*, pp. 593-602, 1982.

40- J. W. Evans, "The Use of Electromagnetic Casting for Al Alloys and Other Metals," JOM, pp. 38-41, 1995.

41- Hans-Erik Ekstrom, Joacim Hagstrom and Lars Ostensson, "Particle Size Distributions in a DC-Cast and Rolled AA3104 Alloy," *Materials Science Forum*, vols. 331-337, pp. 179-184, 2000.

42- Michael J. Lessiter, "Understanding Inclusions in Aluminum Castings: Inclusion Assessment, Control and Separation Techniques Provide a Guided Path for Solving Frustrating Casting Problems," *Modern Casting*, pp. 29-31, 1993.

43- Masanori Tsunekawa, Shinichi Tani, Hajime Okazaki, and Nurifumi Hayashi, "Mechanism of Oxide Generation and Mixing into Aluminum Ingot in Cast Start Phase," *Light Metals*, pp. 831-837, 2001.

44- Wagstaff, Inc. "News Cast, Macrosegregation in DC Cast Aluminum," vol. 10 No. 2, April 2001.

45- Sylvain P. Tremblay, Martin Lapointe, "The Manufacturing, Design and Use of A New Reusable Molten Metal Distributor for Sheet Ingot Casting," *Light Metals*, pp. ,2002.

46- Patnkar, S. V. and Spalding, D. B., "A Calculation Procedure for Heat, Mass and Momentum Transfer," *Int. J. Heat and Mass Transfer*, vol. 15, pp. 1787-1806, 1972.

47- Caretto, L. S., Curr, R. M., and Spalding, D. B., "Two Numerical Methods for Three-Dimensional Boundary Layers," *Comp. Methods in Appl. Mech. Eng.*, vol. 1, pp. 39-48, 1972.

48- Patankar, S. V., "Numerical Prediction of Three-Dimensional Flows," in B. E. Launder (ed.) *Studies in Convection: Theory, Measurment and Applications*, vol. 1, Academic, New York, 1975.

49- Suhas V. Patankar, "Numerical Heat Transfer and Fluid Flow," *Hemisphere Publishing Corporation*, 1980.

50- H. K. Versteeg and W. Malalasekera, "An Introduction to Computational Fluid Dynamics, The Finite Volume Method," *Longman Scientific & Technical*, 1995.

51- Katgerman, L., "Heat Transfer Phenomena During Continuous Casting of Aluminum Alloys," *Proceedings of the Tenth International Heat Transfer Conference, Brighton, UK*, vol. 1, pp. 179-187, August, 1994.

52- Kamal R. Ragel, "A Numerical Study of 3D Turbulent Flow and Heat Transfer of Confined Slot Jets in A Crossflow," *M. Eng. Thesis*, Schulich Science Library, McGill University, Montreal, Quebec, Canada, Call Number: AS42 M3, 1995.

53- Z.N. Getselev et al. US patent 3467166, 1969.

54- J. L. Meyer, "Electromagnetic Process in Aluminum Casthouses and Foundries: An Overview," Light Metals, pp. 1215- 1231, 1992.

APPENDIX A

The program DCCAST, which was used in the present research work concerning 3-D CFD modeling of a commercial vertical DC (Direct-Chill) casting process, is an extension of the earlier version of the copy-righted code CONCAST. The FORTRAN source code of the DCCAST program is available upon request and after payment of a fraction of the development cost of the code through Professor Mainul Hasan at the following address:

Professor Mainul Hasan
Mining, Metals and Materials Engineering
McGill University
M.H. Wong Building, 3610 University Street
Montreal, Quebec, CANADA H3A 2B2

Tel: (514) 398 2524
Fax: (514) 398 4492
E-mail: mainul.hasan@mcgill.ca